UNIVERSITI TEKNOLOGI MARA

HETEROMORPHIC-NANOCHANNEL ACTINOMORPHIC STRUCTURED NICKEL OXIDE/GRAPHENE IN NANOCERAMIC-BASED HYDROGEL FOR ENERGY HARVESTING FROM HUMIDITY AND PIEZOELECTRICITY

NURUL SYAFIQAH BINTI MOHAMED MUSTAKIM

PhD

April 2026

UNIVERSITI TEKNOLOGI MARA

HETEROMORPHIC-NANOCHANNEL ACTINOMORPHIC STRUCTURED NICKEL OXIDE/GRAPHENE IN NANOCERAMIC-BASED HYDROGEL FOR ENERGY HARVESTING FROM HUMIDITY AND PIEZOELECTRICITY

NURUL SYAFIQAH BINTI MOHAMED MUSTAKIM

Thesis submitted in fulfilment
of the requirements for the degree of
Doctor of Philosophy
(Electrical Engineering)

Faculty of Electrical Engineering

April 2026

CONFIRMATION BY PANEL OF EXAMINERS

I certify that a Panel of Examiners has met on 6 January 2026 to conduct the final examination of Nurul Syafiqah binti Mohamed Mustakim on her Doctors of Philosophy thesis entitled "Heteromorphic-Nanochannel Actinomorphic Structured Nickel Oxide/Graphene in Nanoceramic-Based Hydrogel for Energy Harvesting from Humidity and Piezoelectricity" in accordance with Universiti Teknologi MARA Act 1976 (Akta 173). The Panel of Examiners recommends that the student be awarded the relevant degree. The Panel of Examiners was as follows:

Nur Emileen Abdul Rashid, PhD
Professor
Faculty of Electrical Engineering
Universiti Teknologi MARA
(Chairman)

Shafinaz Sobihana Shariffudin, PhD
Senior Lecturer
Faculty of Electrical Engineering
Universiti Teknologi MARA
(Internal Examiner)

Mohd Ambri Mohamed, PhD
Professor
Pusat Pengurusan Penyelidikan dan Instrumentasi
Universiti Kebangsaan Malaysia
(External Examiner)

PROFESSOR DR HJH ZURAEDA IBRAHIM
Dean
Institute of Postgraduates Studies
Universiti Teknologi MARA

Date 21 April 2026

AUTHOR'S DECLARATION

I declare that the work in this thesis was carried out in accordance with the regulations of Universiti Teknologi MARA. It is original and is the results of my own work, unless otherwise indicated or acknowledged as referenced work. This thesis has not been submitted to any other academic institution or non-academic institution for any degree or qualification.

I, hereby, acknowledge that I have been supplied with the Academic Rules and Regulations for Post Graduate, Universiti Teknologi MARA, regulating the conduct of my study and research.

Name of Student	:	Nurul Syafiqah binti Mohamed Mustakim
Student ID. No.	:	2022636964
Programme	:	Doctor of Philosophy (Electrical Engineering) – CEEE950
Faculty	:	Electrical Engineering
Thesis Title	:	Heteromorphic-Nanochannel Actinomorphic Structured Nickel Oxide/Graphene in Nanoceramic-Based Hydrogel for Energy Harvesting from Humidity and Piezoelectricity
Signature of Student	:	……..
Date	:	April 2026

ABSTRACT

Actinomorphic-structured nickel oxide (NiO)/graphene (Gr) nanoarchitectures embedded within a nanoceramic cobalt–zinc (Co–Zn) hydrogel matrix constitute an emerging class of hygroscopic nanomaterials for next-generation humidity gradient power generation (HGPG) platforms. These engineered hybrids exhibit exceptional hygroscopic uptake; however, their ability to sustain spatially non-equilibrated moisture profiles—crucial for continuous humidity-to-electricity transduction—is inherently constrained by unoptimized surface chemistry and structural anisotropy. Such deficiencies compromise the sequential ionization cascade required to establish persistent electrochemical potential gradients, thereby attenuating current and voltage outputs. Compounding these limitations, state-of-the-art HGPG devices frequently rely on intricate, resource-intensive fabrication routes, hindering industrial scalability and real-world deployment. To address these barriers, this study introduces a heteromorphic nanochannel framework wherein actinomorphic NiO/Gr (NG) assemblies are immobilized within a nanoceramic hydrogel matrix and subsequently functionalized via stearic acid (SA) surface treatment to engineer stable, self-sustaining moisture gradients. The NG composites were fabricated through a facile, low-energy sonicated solution immersion process, followed by doctor-blade deposition onto a cellulose substrate. Material optimization was carried out by varying the Gr contents (0.5 wt.%-2.0 wt.%), as well as by modifying SA content (i.e., 1 - 4 wt.%), immersion temperature (i.e., 30 °C, 60 °C, and 90 °C), and immersion duration (i.e., 2, 4, 6, and 8 hours) to enhance the hydrophilic properties through SA treatment. Further enhancement was achieved by incorporating hematite and applying a Co-Zn hydrogel layer, significantly improving the composite's moisture absorption and charge generation from ambient humidity. The synthesized hygroscopic materials were comprehensively characterized. The HGPG device with 1.0 wt.% Gr loading (S-NG-1.0) demonstrated the highest humidity response, yielding an output voltage of 2.24 ± 0.03 mV, a current density of 0.2 ± 0.0 nA/cm^2, and an output power of 0.50 ± 0.01 pW. Notably, the device maintained stable performance for over 400 days, indicating excellent long-term durability. Subsequently, an HGPG device incorporating SA-treated hematite/NiO/Gr composites with a Co-Zn hydrogel film exhibited improved output voltage of 11.5 ± 0.2 mV, a current density of 0.92 ± 0.02 nA/cm^2, and an output power of 13.2 ± 0.2 pW. Moreover, the NG composite integrated with hematite and Co-Zn hydrogel also showed promise in piezoelectric nanogenerator (PENG) applications, achieving an average peak-to-peak output voltage (V_{PP}) of 12 V. Finally, a hybrid HGPG-PENG device was successfully developed by integrating a waste-derived material with the composite film, producing a V_{PP} of 13 V and a power density of 65 μW/cm^2. This work delineates a scalable, material-agnostic strategy for engineering multifunctional hygroscopic–piezoelectric nanocomposites, elucidates the structure–property–performance relationships underpinning moisture-driven energy transduction, and validates their long-term operational resilience. The novel approach of integrating NG with hematite and Co-Zn hydrogel in HGPG and PENG devices highlights significant potential for the development of scalable and reliable energy harvesting technologies.

ACKNOWLEDGEMENT

All praise and gratitude to ALLAH S.W.T. for granting me the courage and determination to successfully complete this challenging PhD journey.

I would like to express my deepest gratitude to my supervisor, Professor Ir. Ts. Dr. Mohamad Hafiz Mamat, for his unwavering support and continuous inspiration throughout my studies. He has always been attentive, providing guidance and valuable insights that have enabled me to complete this research. May Allah reward him for his kindness.

My profound gratitude also goes to my co-supervisors, Ir. Ts. Dr. Mohd Hanapiah Abdullah (Centre for Electrical Engineering Studies, UiTM Pulau Pinang), Ts. Dr. Mohd Firdaus Malek (Institute of Science, UiTM Shah Alam), and Ts. Dr. Fararyanti Parimon (Faculty of Engineering, UMS). Their invaluable efforts and support have significantly contributed to my success. This research was funded by the Fundamental Research Grant Scheme (FRGS/1/2022/TK07/UITM/02/7). I would also like to extend my gratitude to the Ministry of Higher Education Malaysia and the Faculty of Electrical Engineering, UiTM Shah Alam for their continuous support. I sincerely appreciate the opportunities that have been given to me.

I am also deeply grateful to be surrounded by many wonderful people and would especially like to acknowledge my dear research colleagues: Dr. Dayana Kamaruzaman, Mr. Wan Muhammad Dzhahirul, Mr. Yousif, Dr. A. Shamsul Rahimi, and Ir. Dr. Musa, for their support and encouragement, which enabled the successful completion of this thesis. I also take this opportunity to thank all the technical staff at NANO-Electronic Centre (NET), particularly Mr. Suhaimi, Mr. Norsham, Mr. Asrul, and Ms. Nurul Fakhirah, for their invaluable assistance in handling the material characterization equipment in the laboratory.

My deepest gratitude and heartfelt appreciation go to my beloved parents, [redacted] and Mohamed Mustakim Osman, as well as my parents-in-law, [redacted] and Annas Goh, for their unwavering encouragement and continuous prayers, which have allowed me to accomplish this important life milestone. I also want to express my sincere appreciation to my dear spouse, Arif Farhan Annas Goh, for his unconditional support in every way. My lovely children, Arif Khaleed and Ariana Khadeeja, have always been my source of strength. Many thanks to my siblings, Nurul Syazmeen, Mohamed Aiman Syakeer, and Nurul Syafeera, for their constant support, advice, and unconditional love.

Lastly, I want to extend my sincere thanks to everyone who has supported me and provided valuable advice, both directly and indirectly, in helping me complete this research. I am incredibly grateful to have such a strong support system. May Allah always bless and protect you all.

TABLE OF CONTENTS

LIST OF TABLES

LIST OF FIGURES

LIST OF SYMBOLS

Symbols

A	Current (Ampere)
$A \cdot cm^{-2}$	Ampere Per Square Centimetre (Current Density)
a	Lattice Constant
Å	Ångström (Length)
β	Full Width at Half Maximum (FWHM)
c	H^+ Concentration
cm^2	Square Centimetre (Area)
$cm^2/V \cdot s$	Mobility
cm^3/C	Hall Coefficient
cm^{-3}	Carrier Concentration
Cu-Kα	Copper K-Alpha (Characteristic X-Ray Wavelength Used In XRD)
d	Interplanar Spacing
dc	Charge Density
d_{33}	Piezoelectric Coefficient
D	Crystallite Size
D_C	Diffusion Coefficient
Δc	Difference in H^+ Concentration Between the Top and Bottom Layers

ΔE_p	Potential Separation
°	Degree (Angle)
°C	Degree Celsius (Temperature)
E	Electric Field
E_i	Induced Electric Field Intensity
eV	Electronvolt (Unit of Energy)
ε	Strain
F	Faraday Constant / Farad (Capacitance) — Specify in Context
g/g	Grams of Water Absorbed Per Gram of Dry Material
γ_l	Surface Tension of The Liquid
γ_s^d	Dispersive Component of Solid Surface Tension
h	Hour
Hz	Hertz (Frequency)
I_{sc}	Short-Circuit Current
J_{Dif}	Diffusion Current Density
J_{Dri}	Drift Current Density
K	Shape Factor (Constant)
λ	X-Ray Wavelength
m^2/g	BET Surface Area
mJ/m^2	Surface Energy
min	Minute

mm	Millimetre (Length)
mL	Millilitre
M	Molarity
μm	Micrometre (Length)
N	Number of Electrons Transferred / Newton (Force) — Specify In Context
nm	Nanometre (Length)
Ø	Diameter
$Ø_{avg}$	Average Diameter
Ω	Ohm (Resistance)
Ω/sq	Sheet Resistance
P_d	Power Density
%	Percent (Dimensionless Ratio × 100)
pC/N	Picocoulomb Per Newton (Unit of Piezoelectric Charge Coefficient, D_{33})
Q	Electric Quantity (Elementary Charge) / Total Charge — Specify in Context
rpm	Revolutions Per Minute (Rotational Speed)
S	Humidity Response
S/cm	Siemens Per Centimeter (Electrical Conductivity)
σ	Conductivity
T	Thickness of Hygroscopic Film / Stress — Specify in Context
θ	Diffraction Angle

θ_{CA}	Water Contact Angle
V	Volt
V_i	Induced Voltage
V_{OC}	Open-Circuit Voltage
V_{PP}	Peak-To-Peak Voltage
W	Watt (Power)
wt.%	Weight Percentage
x	Distance to The Surface of Hygroscopic Layer

LIST OF ABBREVIATIONS

Abbreviations

2D	Second-Order Overtone of The D Vibration
2LO	Second-Order Longitudinal Optical
3D	Three-Dimensional
AC	Alternating Current
Ag	Silver
Al	Aluminium
A	Active Area
Ar	Argon
$BaTiO_3$	Barium Titanate
BET	Brunauer-Emmett-Teller
BJH	Barrett-Joyner-Halenda
C	Carbon
C=O	Carbonyl Carbon
C–O	Oxygen-Containing Functional Groups
$CH_3(CH_2)_{16}COOH$ (SA)	Stearic Acid
$(CH_2)_{16}CH_3$ (R)	Alkyl Group in Stearic Acid
$(CH_3COO)_2Co{\cdot}4H_2O$	Cobalt (II) Acetate Tetrahydrate
$C_6H_{12}N_4$ (HMT)	Hexamethylenetetramine

CNF	Cellulose Nanofiber
Co	Cobalt
Cu	Copper
CV	Cyclic Voltammetry
DI	Deionized
EAB	Effective Absorption Bandwidth
EDX	Energy-Dispersive X-Ray Spectroscopy
Fe	Iron
$Fe(NO_3)_3 \cdot 9H_2O$	Iron (III) Nitrate Nonahydrate
FGG	Fowkes-Girifalco-Good
FP	Filter Paper
FTIR	Fourier Transform Infrared Spectroscopy
FWHM	Full Width at Half Maximum
Gr	Graphene
HDF	Humidity Digestion Framework
HGPG	Humidity Gradient Power Generation
HGPG-PENG	Humidity Gradient Power Generation and Piezoelectric Nanogenerators
HMT	Hexamethylenetetramine
HNG	Hematite/NiO/Gr
HRTEM	High-Resolution Transmission Electron Microscopy
HyNG	Hybrid Nanogenerators

I–V–t	Current–Voltage–Time
IoT	Internet of Things
IR4.0	Fourth Industrial Revolution
JCPDS	Joint Committee on Powder Diffraction Standards
$KNbO_3$	Potassium Niobate
$KxNa_{1-x}NbO_3$	Lithium Sodium Niobate
LCDs	Liquid Crystal Displays
LEDs	Light-Emitting Diodes
$LiNbO_3$	Lithium Niobate
LO	First-Order Longitudinal Optical
MEMS	Microelectromechanical Systems
MSW	Municipal Solid Waste
MXene ($Ti_3C_2T_x$)	Mxene
N_2	Nitrogen
NG	NiO/Gr
Ni	Nickel
$NiFe_2O_4$	Nickel Ferrite
$Ni(NO_3)_2 \cdot 6H2O$	Nickel Nitrate Hexahydrate
NiO	Nickel Oxide
NKEA	National Key Economic Area
O	Oxygen

PAM	Polyacrylamide
P(AAm-co-AAc)/PPy	Poly(Acrylamide-Co-Acrylic Acid)/Polypyrrole
PENGs	Piezoelectric Nanogenerators
PET	Polyethylene Terephthalate
Pt	Platinum
PVDF	Polyvinylidene Fluoride
PVA	Polyvinyl Alcohol
PZT	Lead Zirconate Titanate
RH	Relative Humidity
RP	Recycled Paper
RT	Room Temperature
SA	Stearic Acid
SAED	Selected Area Electron Diffraction
SDG	Sustainable Development Goals
SEM	Scanning Electron Microscopy
SO_3H	Sulfonic Acid Groups
TENGs	Triboelectric Nanogenerators
TiO_2	Titanium Dioxide
WH-UDM	Williamson-Hall Uniform Deformation Model
WCA	Water Contact Angle
XPS	X-Ray Photoelectron Spectroscopy

XRD	X-Ray Diffraction
Zn	Zinc
$Zn(CH_3COO)_2 \cdot 2H_2O$	Zinc Acetate Dihydrate
ZnO	Zinc Oxide

CHAPTER 1
INTRODUCTION

1.1 Research Background

Atmospheric humidity, an omnipresent yet underexploited renewable resource, offers immense potential as a sustainable feedstock for electrical energy generation. Comprising water molecules in the vapor phase, humidity represents a clean, inexhaustible, and geographically ubiquitous energy carrier, accessible across diverse environments, including rural, isolated, and even arid regions. Unlike solar irradiance, which is inherently diurnal, atmospheric humidity persists continuously and often intensifies under nocturnal low-temperature conditions, enabling round-the-clock energy harvesting. This unique advantage positions humidity as an ideal complement to established renewable technologies.

Humidity gradient power generation (HGPG) is an emerging transduction paradigm that converts the chemical potential gradient of ambient water vapor into electrical energy, offering synergistic integration with mature green technologies such as photovoltaics [1] and nanogenerators [2, 3]. For example, a hybrid humidity-solar panel can operate dually, harvesting solar photons during daylight and exploiting ambient vapor at night to ensure continuous electrical output. Since the pioneering work of Qu et al. [4] in 2015, which demonstrated the first HGPG device, the field has witnessed a surge in research activity, driving the discovery of novel hygroscopic and ion-conductive materials optimized for this application. Given that relative humidity at most locations fluctuates within a relatively narrow band, HGPG systems can, in principle, deliver stable and predictable electrical output with minimal intermittency. Accordingly, advancing the design of high-performance humidity sorbents and transduction materials is essential to unlocking the full potential of humidity as a renewable, globally accessible, and sustainable energy source.

On the other hand, mechanical energy harvesting is another form of renewable energy (RE) that can be achieved through several mechanisms, including electromagnetic induction, electrostatic storage, and the piezoelectric effect. Among these, piezoelectric nanogenerators (PENGs) have emerged as particularly attractive

due to their high energy conversion efficiency, mechanical flexibility, and adaptability for integration into portable and wearable devices [5]. With the latest advancements, PENGs are viewed as crucial in the development of self-sustaining nanotechnology suitable for green energy applications [6]. This is due to their exceptional characteristics and capabilities, allowing them to serve as a highly efficient energy source for nanoscale devices, eliminating the need for potentially harmful power sources like chemical batteries.

In this thesis, the development of advanced nanomaterials comprising porous, actinomorphic-structured nickel oxide (NiO) and nanoporous graphene (Gr) architectures, deposited onto a cellulose-based substrate is reported and discussed. The selection of NiO and Gr is predicated on their intrinsic properties, exceptional moisture adsorption capacity, mechanical robustness, chemical durability, and high electronic conductivity which collectively ensure the long-term reliability and functional stability of humidity-driven devices [4, 7, 8]. Furthermore, cellulose-derived materials inherently exhibit hierarchical gradient structures [9-13], with cellulose fibers renowned for their characteristic adsorption–desorption dynamics in response to ambient moisture [14-16]. These synergistic attributes render NiO-Gr (NG) /cellulose hybrids ideal candidates for sustained humidity-to-energy conversion.

Despite the recent progress in HGPG technologies, the scalability of existing hygroscopic materials remains severely constrained by the high cost of precursors and the intricacy of multistep synthesis protocols. To overcome these barriers, the author employs a facile, low-energy sonicated solution immersion route to synthesize NG nanocomposites with an intrinsically high nanopore density, followed by a stearic acid (SA) surface modification to optimize the adsorption–desorption kinetics of water molecules. This approach is anticipated to induce the formation of heteromorphic nanochannels within the hygroscopic matrix, thereby enabling a novel charge-generation mechanism that sustains high humidity-to-electricity conversion efficiency over extended operational lifetimes. The NG architecture is further functionalized through hematite incorporation and encapsulation within cobalt–zinc (Co–Zn) nanoceramic hydrogel films, designed to enlarge the electroactive interface and accelerate interfacial reaction kinetics [22]. This hierarchical modification is anticipated to enhance both hygroscopic uptake and charge generation from ambient humidity.

Equally critical to HGPG device performance is the choice of substrate, which dictates moisture retention dynamics and, consequently, the device's humidity response. Cellulose-based substrates, such as paper, offer intrinsically high-water absorption capacity, rendering them attractive candidates for hygroscopic material deposition [17-19]. Nevertheless, the environmental burden of the paper industry, particularly its contribution to solid waste streams, remains a pressing sustainability challenge. Waste-to-energy paradigms offer a route to mitigate this impact by converting waste materials into useful energy, thereby advancing circular economy principles. In this context, repurposing wastepaper or recycled paper (RP) as a substrate for energy harvesting represents an unexplored but compelling opportunity. To the author's knowledge, no prior studies have demonstrated HGPG devices utilizing RP as a structural and functional substrate platform. This research advances a sustainable energy paradigm by engineering hematite/NiO/Gr (HNG) composites, encapsulated within Co–Zn nanoceramic hydrogel films, onto RP substrates and realizing a synergistic integration of RE harvesting, waste valorisation, and eco-conscious materials engineering [20].

The investigation was extended to evaluate the piezoelectric performance of HNG composites embedded within Co–Zn nanoceramic hydrogel. The multifunctional nature of the composite opens the possibility for hybrid energy harvesting configurations, achieving performance levels on par with, or complementary to, more established RE systems. Intriguingly, the engineered material also exhibits mechano-responsive electrical output, suggesting its suitability for mechanical-to-electrical energy transduction. This dual-mode assessment enables comprehensive elucidation of the coupled mechanisms governing both humidity-to-electricity and piezoelectric transduction within the same material platform. To the best of the author's knowledge, the synthesis and integration of heteromorphic-nanochannel, actinomorphic-structured NG composites with hematite on Co–Zn nanoceramic hydrogel-based cellulose substrates for HGPG and PENG has not yet been reported. The transformation of the study's material into an energy-harvesting resource is significant from both economic and environmental perspectives, as it promotes the advancement of RE through sustainable and green innovation.

The novelty of the current study lies in the development of novel composite films comprising NiO/graphene, hematite, and a Co–Zn hydrogel. In addition, this work

demonstrates a scalable and reliable energy-harvesting system that integrates two RE sources into a single platform. The synthesis process employed in this study further contributes to its novelty, as SA treatment and a sonicated solution-immersion method, which have not been reported in existing HGPG and PENG systems, are introduced. Moreover, the use of recycled paper derived from waste materials as a functional component has not been previously explored in HGPG applications, thereby adding to the originality of this work. Notably, to the best of the author's knowledge, this study is the first to report an experimental investigation of HGPG in Malaysia, which further strengthens the novelty and contribution of the research.

1.2 Problem Statement

The significant challenges and issues relevant to this study are outlined in the following points:

Problem statement 1 (PS 1): In the field of humidity-to-energy conversion, the ability of a material to sustain a moisture gradient is of paramount importance. Self-sustained moisture gradient materials are particularly valuable as they enable continuous water absorption, which is a fundamental requirement for driving the energy generation process in hygroscopic systems. This continuous absorption not only enhances the efficiency of energy conversion but also ensures the long-term operational stability of the device. Based on the literature, only protein nanowires extracted from microorganism Geobacter Sulfurreducens were reported to have self-sustained moisture gradient [21, 22]. However, the protein nanowire from microorganism, which is organic source, has short lifetime and not resisted to high temperature condition. Consequently, this organic material is not reliable for applications in humidity-to-energy conversion devices in the long term. Therefore, it is important to develop synthetic self-sustained moisture gradient hygroscopic nanomaterials, which are durable, high temperature resistant, stable, and robust that can function properly in the long period.

Problem statement 2 (PS 2): The current humidity-to-energy conversion based on existing synthetic hygroscopic materials can only produce brief bursts of power in the ambient environment, due to the lack of a sustained conversion mechanism [23-26]. The limitations also stem from the intrinsic structural configuration and surface characteristics of existing hygroscopic materials, which fail to sustain the moisture

gradient required to establish a chemical potential difference across the material for effective charge carrier transport. Consequently, current synthetic-material-based technologies are unable to deliver stable, high-density energy output from ambient humidity.

Problem statement 3 (PS 3): Paper is derived from cellulose, and in recent years, research related to cellulose has gained considerable global attention due to its excellent properties, including its ability to attract water molecules which is particularly beneficial for HGPG applications [27-29]. However, the high demand for paper for a wide range of purposes and applications has significantly contributed to waste generation. This presents a serious global concern, as paper waste is a major environmental issue that leads to air pollution, landfill accumulation, deforestation, and increased energy consumption, all of which contribute to the worsening planetary crisis [30, 31]. To date, various studies have addressed the issue of waste generation, including the implementation of waste-to-energy approaches aimed at mitigating key environmental and societal challenges. Nevertheless, more impactful research is needed to develop energy-generation methods that promote sustainable, green solutions and innovative strategies with long-term environmental benefits.

Problem statement 4 (PS 4): The mechanism of energy conversion from atmospheric humidity remains poorly understood, primarily due to the limited number of successful studies in this emerging field [32]. Furthermore, the development of materials for humidity-to-energy conversion has progressed slowly and is still in its early stages. Interestingly, these materials exhibit promising potential for integration into other energy harvesting technologies, either to match the performance of well-established systems or to enable hybrid configurations. However, given their nascent development, no definitive reports have yet demonstrated such integration. This gap presents significant opportunities for breakthrough research, particularly in designing and developing composite materials capable of efficiently generating electrical energy in hybrid systems. Therefore, extensive investigations into hygroscopic materials especially when combined with other energy-harvesting components are essential. At the very least, proof-of-concept studies conducted under controlled laboratory conditions are necessary to validate their feasibility and performance potential.

1.3 Research Objectives

Based on the problems outlined in the preceding section, the objectives of this study are defined as follows to address the identified challenges:

a) To investigate the structural attributes, surface morphology, wettability, and HGPG performance of novel composite films comprising actinomorphic-structured NG functionalized via SA treatment, incorporating heteromorphic nanochannels fabricated through a sonicated solution-immersion method.**(PS 1)**
b) To determine the optimal parameters for SA-treated NG on filter paper cellulose-based substrates through a comprehensive evaluation of their structural characteristics, surface morphology, wettability, chemical composition, and HGPG performance. **(PS 2)**
c) To evaluate the impact of incorporating hematite into the NG composite on its surface morphology, structural and chemical properties, and HGPG performance. **(PS 1 and 2)**
d) To access the humidity-to-energy conversion performance of HGPG-based HNG composites integrated with Co-Zn-based nanoceramic hydrogel films synthesized via the sol-gel method on filter paper and recycled paper cellulose-based substrates. **(PS 2 and 3)**
e) To characterize the performance of the HNG composite integrated with Co-Zn-based nanoceramic hydrogel films for application in PENG and HGPG-PENG hybrid device. **(PS 4)**

1.4 Scope and Limitation of Study

Based on the research objectives, this study focuses on the development of a hygroscopic material comprising HNG composite embedded with Co-Zn based nanoceramic hydrogel films. The goal is to achieve a stable and self-sustained moisture gradient for HGPG with potential integration into PENG applications. This research was confined to a defined scope and certain limitations.

Pristine NiO and NG composite materials were synthesized at low temperatures using a simple sonicated solution immersion method. The Gr content was varied at 0.5 wt.%, 1.0 wt.%, 1.5 wt.%, and 2.0 wt.% to study its influence on the material properties. The maximum immersion temperature during the synthesis process was limited to 95 °C

due to equipment constraints. A cellulose-based substrate of filter paper (FP) was employed in the fabrication of the HGPG device to produce films with moisture gradient characteristics. To enhance the hydrophilicity of the NG composites, surface modification was conducted using SA treatment. Parameters such as SA concentration, immersion temperature, and immersion duration were investigated for their influence on surface properties.

Further enhancement of the NG composite was achieved by incorporating hematite and Co-Zn based nanoceramic hydrogel, aiming to improve the material's moisture absorption and charge generation capabilities. The HNG composite was synthesized using the same methodology as the pristine NiO and NG composites. A nanoceramic Co-Zn based hydrogel was prepared using a sol-gel method, maintaining fixed concentrations of Zn and Co precursors across all samples. For comparative analysis and to introduce a sustainable innovation, a cellulose-based substrate derived from RP was also integrated with the HNG composite to fabricate hygroscopic films for HGPG applications. The RP was prepared using a simple, home-based method using unused printing papers. Furthermore, the output performance of the fabricated HGPG devices were evaluated under varying relative humidity (RH) levels, ranging from 40% to 90% RH. In addition, the potential of the developed materials for PENG applications was examined under low-frequency mechanical vibration which corresponds to energy typically generated by human motion.

This study emphasized several optimizations, including the effect of varying Gr content, the impact of SA treatment, the role of hematite addition, variations in synthesis temperature, and the utilization of hydrogel and RP substrates. The overarching objective was to match or exceed the performance of existing HGPG systems by optimizing output performance and demonstrating the material's potential in PENG as well as in hybrid device applications.

1.5 Significance of Study

As energy generation from nanomaterials remains an emerging field, this research is anticipated to deliver novel materials and transformative insights, including: (1) the design and fabrication of innovative nanomaterials comprising heteromorphic nanochannels and actinomorphic-structured NG embedded within a nanoceramic

hydrogel, engineered for robustness, durability, high conductivity, and long-term operational stability; (2) the development of advanced hygroscopic nanomaterials with self-sustaining capabilities for continuous energy generation from ambient humidity; (3) the integration of these developed nanomaterials onto RP substrates to enable clean energy production while advancing sustainable waste-to-energy strategies; and (4) the enhancement of hybrid energy harvesting systems through the incorporation of humidity-based energy conversion to complement and amplify PENG performance.

Malaysia is a tropical nation with persistently high humidity and is well-positioned to harness this technology for advancing sustainable green energy production. The societal impact includes increased public awareness of the importance and advantages of various RE sources, particularly humidity as a novel source for clean energy. From an academic perspective, this study contributes to the body of knowledge on humidity-to-energy conversion using advanced hygroscopic materials and devices. For industry, the findings present an opportunity to explore and invest in new green technologies, including the development of equipment for energy generation and performance evaluation. For the government, this research introduces an alternative energy production method that can support existing power systems, particularly in rural and remote areas where access to conventional energy sources may be limited.

Finally, by harnessing green energy from atmospheric humidity, this study promotes environmental sustainability, particularly in efforts to reduce carbon emissions. It aligns closely with several national and international goals, especially the Sustainable Development Goals (SDG) (SDG 7–Affordable & Clean Energy, SDG 9 – Industry, Innovation, & Infrastructure, and SDG 12–Responsible Consumption & Production), all of which emphasize the importance of innovative materials and diverse RE sources in advancing a circular economy and sustainable society. Furthermore, this work aligns with key national priorities, including Malaysia's National Key Economic Area (NKEA) for green technology and the strategic objectives outlined in the Fourth Industrial Revolution (IR4.0) policy framework.

1.6 Chapter Summary

Hygroscopic nanomaterials serve as moisture-absorbing components in diverse applications, including energy harvesting, humidity sensing, precision agriculture, and

protective coatings. Meanwhile, piezoelectric materials are known for their ability to convert mechanical energy into electrical energy. Driven by the increasing emphasis on sustainable product design and the escalating demand for high-performance functional materials, nanomaterials are gaining traction across multiple industrial sectors. Nevertheless, the direct generation of electrical energy from nanomaterials remains an emerging technology, requiring substantial optimization to enhance both material properties and energy conversion efficiency. This research seeks to pioneer innovative strategies for the development of next-generation nanomaterials capable of harvesting energy from atmospheric humidity and piezoelectricity. The outcomes are expected to facilitate the creation of locally engineered composite materials for RE applications, thereby fostering the advancement of indigenous green energy technologies.

CHAPTER 2
LITERATURE REVIEW

2.1 Introduction

This chapter provides an overview of the existing research relevant to the development of novel composite materials, particularly focusing on NG and HNG composites embedded with Co-Zn-based nanoceramic hydrogel films for HGPG and nanogenerator applications. It explores alternative RE strategies, with a specific emphasis on utilizing atmospheric humidity to generate electricity, including the application of PENGs. The chapter outlines the fundamental principles of humidity-to-electricity conversion, reviews current hygroscopic materials, and highlights the use of cellulose-based substrates in humidity-related applications. It further explores how composite material design and surface modification strategies can enhance HGPG performance metrics. The chapter also discusses the overview of PENGs and the piezoelectric effect in energy harvesting. The chapter concludes by addressing waste-to-energy concepts, underscoring the untapped potential of wastepaper as a sustainable substrate for innovative energy harvesting systems. This perspective integrates materials science, RE engineering, and circular economy principles, offering insights for future research directions and deepening the understanding of these rapidly emerging technologies.

2.2 Energy Harvesting from Humidity

Humidity-to-energy technology has emerged as a promising alternative energy source, leveraging the abundance of water molecules present in the vapor phase of ambient air. Harvesting energy from humidity has gained significant attention as a novel strategy in RE development and may also serve as a significant auxiliary energy source supporting other well-established technologies such as solar cells [33-35], nanogenerators [3, 36], and biofuels [37, 38]. This technology primarily generates electricity by absorbing water molecules through hygroscopic materials [39-41]. Research in this area began as early as 2013 and continues to progress to this day. Initial studies reported electricity generation from bacterial spores that respond to changes in

humidity [42]. Subsequent reports in 2014 introduced evaporation-driven engines that successfully generated electrical power from water evaporation due to changes in surrounding humidity [43]. Further research in 2015 demonstrated HGPG utilizing graphene oxide [4]. These pioneering works specifically focused on converting humidity into electricity, opening new opportunities for RE research and development. To date, only a few studies have successfully demonstrated electricity generation from humidity, as summarized in Table 2.1.

Table 2.1
Several Studies on Energy Harvesting from Humidity

Material	Application	Method	Outcome	Stability	Ref.
Carbon nitride	Moisture-enabled electric generator	Chemical vapor deposition	V_{OC} = 0.28 V, I_{SC} = 1.8 μA	600 hours	[32]
MXene ($Ti_3C_2T_x$) aerogel and polyacrylamide (PAM) ionic hydrogel	Moisture-electricity generators	Gelation process	V_{OC} = 600 mV, J_{SC}, = 1160 μA cm^{-2}, power density = 24.8 μW cm^{-2}	360 hours	[44]
PAM-LiCl/CMC	Moisture electricity generator	Chemical cross-linking	Power density = 113 μW·cm^{-2}	120 hours	[45]
Carbon black/polyvinylidene fluoride (PVDF) mixture onto foam Ni	Water-electricity cogeneration	Freeze-drying, spraying method	V_{OC} = 400 mV	10 hours	[46]
Two-Dimensional unilamellar titanium oxide ($Ti_{1-\delta}O_2$) nanosheets	Hydrovoltaic technology	Solid-state calcination method	V_{OC} = 1.32 V	250 hours	[47]
$Ti_3C_2T_x$/ cellulose	Self-powered Triboelectric Nanogenerators	Delignification and depressurized impregnation processes	High sensitivity =0.8/1%	150 s	[48]
PSSH-Pd/Pd_xO_y @C- Bi_2Te_3	Humidity-thermoelectric bimodal energy harvester	Air Electrothermal Wave (ETW) synthesis	Output power = 0.41 μW	16 hours	[49]
Cellulose acetate	Moist-Induced Electricity Generation	Electrospinning	Output voltage = 0.3 V, current density = 80 nA cm^{-2}	24 hours	[50]
S-HNiO/Gr on hydrogel/FP	Humidity energy harvesting	Sonicated solution immersion	Current density = $0.2 \pm 3.0\times10^{-3}$ nA/cm^2	9,600 hours	This study

One notable example is the work by Liu et al., who demonstrated humidity-to-energy conversion using conductive protein nanowires extracted from the microorganism Geobacter Sulfurreducens [21]. They achieved a power density of 4 mW/cm^2 by establishing a self-sustained moisture gradient within a 7-μm-thick protein nanowire film. As water molecules are adsorbed onto the surface of the protein nanowires, ionized water molecules donate charges to the nanowires. This exchange of

charge carriers generates a current flow, driven by the electrical potential that develops in response to the moisture gradient.

The working principle of humidity-to-energy conversion technology involves two main components, which are humidity absorbing materials or hygroscopic materials and water digestor [41, 51, 52]. The water digestor consists of humidity digestion framework (HDF), which convert water to electrical energy. The water will be supplied through the humidity absorbing materials, which capture water molecules from atmosphere humidity. There are few types of HDF technology which include hydroelectric, moisture battery, and atmospheric water splitting. Among these, the hydroelectric HDF-based technology remains one of the most challenging due to its working mechanism which need instant and dramatic humidity variation in hygroscopic materials to produce electrical energy from chemical potential energy.

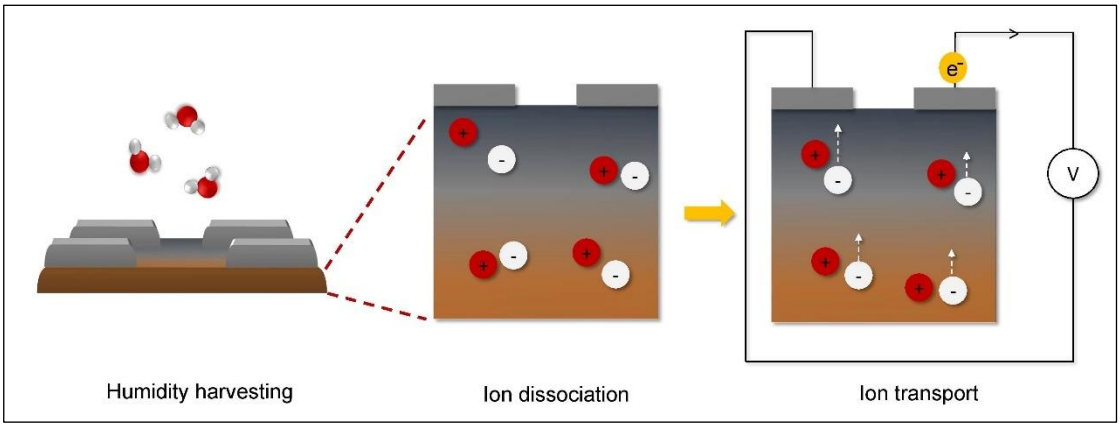

Figure 2.1 Humidity-To-Energy Device Configuration and the Working Principle of Humidity-To-Energy Conversion Based on Hydration-Induced Ionization Effect

The working principle of this technology is based on hydration induced ionization effect, as illustrated in Figure 2.1. When hygroscopic or humidity absorption materials are embedded along with metal electrodes and expose to atmospheric humidity, absorption of water molecules occurs spontaneously, and successive hydration of the materials produces free-charge carriers by ionization effect. The gradient configuration in the hygroscopic materials will induce the diffusion of charge carriers, which promote an electric potential between the electrodes and generate current flow. Therefore, the power generation by hygroscopic materials is very promising for future technological applications and the selection of hygroscopic materials is very crucial to achieve high energy conversion output.

2.3 Hygroscopic Material

Power generation via hygroscopic materials has emerged as a promising avenue for advanced energy-harvesting technologies. Daripa et al. demonstrated a power density of 0.7 $\mu W/cm^2$ using block copolymer–modified reduced Gr oxide for moisture-induced electricity generation [53]. Their approach exploited a potential gradient generated by spatially varying concentrations of oxygen-containing functionalities, specifically sulfonic acid groups ($-SO_3H$) within the active layer, thereby accelerating charge carrier transport and enhancing electrical output. Shen et al. reported a strongly hydrophilic titanium dioxide (TiO_2) nanowire network film, 10 μm in thickness, incorporating three-dimensional (3D) nanochannels to facilitate the diffusion of atmospheric water vapor; this architecture achieved a power density of 4 $\mu W/cm^2$ [54]. Similarly, other group has harnessed Gr or carbon-based hygroscopic materials functionalized with vertically heterogeneous hydroxyl groups to generate humidity-driven electrical power [24].

Despite these advances, the output power of most synthetic hygroscopic systems remains low, with operational lifetimes often below 50 s and prolonged self-recharging intervals before output recovery. Such performance limitations stem largely from the inability of existing materials to sustain a stable moisture gradient, which is critical for continuous, high-power generation from humidity sources. Microorganism-derived protein nanowires have demonstrated comparatively high humidity-to-energy conversion efficiencies; however, their application is constrained by the intrinsic instability of organic materials. Protein nanowires are susceptible to thermal degradation and are poorly suited for harsh environmental conditions, thereby compromising the long-term durability and reliability of energy-harvesting devices fabricated from such materials.

Thus far, the prevailing mechanism of humidity-induced energy generation in HGPG devices can be described as follows [21]. Upon absorbing atmospheric moisture, the hygroscopic material undergoes proton dissociation, generating a concentration gradient of H^+ ions across its structure. This ionic gradient drives a diffusion process, quantitatively expressed by:

$$J_{Dif} = -qD_C \frac{\delta c}{\delta x} \tag{2.1}$$

In this equation, J_{Dif} denotes diffusion current density, q is electric quantity of elementary charge, D_c is diffusion coefficient, c represents H^+ concentration and x are the distance to the surface of hygroscopic layer. As H^+ ions migrate within the hygroscopic layer exhibiting a gradient distribution, a drift-induced electric field is established between two layers, described by:

$$J_{Dri} = \sigma E_i \tag{2.2}$$

In this equation, J_{Dri}, σ and E_i denote drift current density, conductivity and induced electric field intensity, respectively. During thermodynamic equilibrium, an equation could be derived as shown below:

$$J_{Dif} + J_{Dri} = 0 \tag{2.3}$$

By substituting equations (2.1) and (2.2) into equation (2.3), a following equation could be established:

$$E_i = \frac{qD}{\sigma} \frac{\delta c}{\delta x} \tag{2.4}$$

Then, the induced voltage, V_i could be defined as follows:

$$V_i = \int \frac{qD}{\sigma} \frac{\delta c}{\delta x} \tag{2.5}$$

Here, the x-axis is oriented perpendicular to the hygroscopic layer's surface. Assuming that absorbed water molecules provide sufficient transport channels within each hygroscopic layer to maintain uniform diffusion coefficients and ionic conductivities, equation (2.5) can be further simplified as follows:

$$V_i = \frac{qD}{\sigma} \int \frac{\delta c}{\delta x} \tag{2.6}$$

For sufficiently thin hygroscopic films, the concentration gradient $\frac{\delta c}{\delta x}$ can be approximated as $\frac{\Delta c}{t}$, where Δc denotes the difference in H^+ concentration between the top and bottom layers, and t is the film thickness. Considering that $V_i = \frac{Voc}{t}$, where V_{oc} is the open-circuit voltage, equation (2.6) can be reformulated to yield the open-circuit voltage expression:

$$V_i = \frac{qD}{\sigma} \Delta c \tag{2.7}$$

This relationship reveals that the induced voltage intensity in a hygroscopic material is directly proportional to the H^+ concentration gradient across its thickness. Consequently, the voltage output can be amplified by engineering multilayered hygroscopic architectures to maximize and sustain the ionic concentration differential.

2.3.1 Heteromorphic Nanochannel, Actinomorphic Structured NiO/Gr Composites

In hygroscopic materials, the conventional energy conversion mechanism is governed by a self-sustained moisture gradient, as described in equations (2.1) to (2.7). Beyond this established process, the present work introduces a distinct humidity-to-energy conversion pathway by engineering heteromorphic nanochannels within an actinomorphic-structured NG composite. In this architecture, the porous, heteromorphic nanochannel network formed by the intimate integration of NiO and Gr, functions as an efficient trapping medium for positive ions. The zeta potentials of NiO have been reported in the range of approximately –6 mV to –18 mV, while Gr exhibits values between –30 mV and –40 mV [55, 56]. Such negative surface potentials promote the electrostatic attraction of positively charged species, predominantly proton, onto the surfaces of NiO and Gr.

Reported studies have shown that NiO nanomaterials exhibit outstanding performance in humidity sensing applications, with sensitivity values surpassing those of other oxide-based sensors such as zinc oxide (ZnO) and TiO_2 [57-59]. This superior performance is attributed to the high surface area generated by their low-dimensional morphology and the abundance of nanopores distributed across the surface [60]. These nanopores promote efficient permeation and diffusion of water molecules, enabling rapid and effective moisture adsorption. Furthermore, NiO nanomaterials possess intrinsic charge storage capability, which can enhance the performance of humidity-to-energy conversion systems [61, 62]. In parallel, Gr exhibits exceptional physicochemical properties, including pronounced edge effects, a tuneable non-zero band gap, and quantum confinement phenomena, that render it highly promising for energy harvesting applications [63]. Moreover, its surface can be functionalized via both wet- and dry-processing routes, enabling tailored modification of its structural and surface chemistry to optimize performance.

Based on the literature studies, the adoption of porous, actinomorphic-structured NiO is expected to further improve water absorption capacity due to its ultrathin geometry and high density of dangling bonds. These dangling bonds contribute to elevated surface energy, fostering strong molecular interactions and facilitating rapid water adsorption. Additionally, Gr is incorporated to boost the electrical conductivity of the hygroscopic nanocomposite, thereby supporting higher current generation. The low-dimensional morphology of both NiO and Gr, manifested as ultrathin, flake-assembled actinomorphic networks, maximizes atomic-level surface exposure which in turn enhances the diffusivity of water molecules across the material interface [64, 65]. The actinomorphic topography, coupled with the high-density nanoporous architecture, is schematically illustrated in Figure 2.2, underscoring its potential to revolutionize scalable HGPG material platforms.

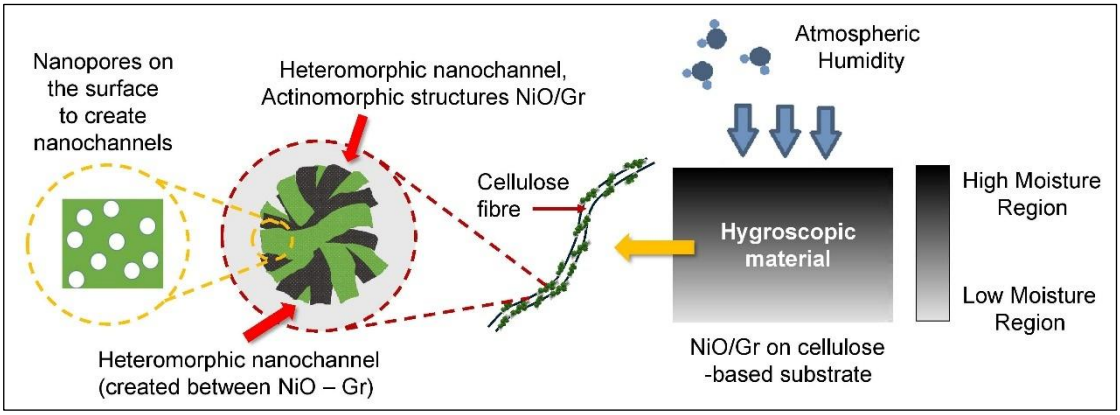

Figure 2.2 Synthetic Hygroscopic Nanomaterials Based on Heteromorphic Nanochannel, Actinomorphic Structured NG

The high density of heteromorphic nanochannels generated at NiO-Gr interfaces facilitates directional water molecule diffusion. Within these confined capillary pathways, electrostatic-induced water dissociation yields H^+ ions that preferentially adsorb onto the NiO and Gr surfaces. As water molecules penetrate deeper into the nanochannel network, the selective transport properties of the structure permit H^+ migration while impeding OH^- ion flow. This asymmetric ion transport results in spatial charge separation, thereby establishing an electric field along the nanochannel axis. The resulting electrostatic potential difference manifests as an output voltage, enabling direct energy harvesting from ambient humidity.

2.3.2 Nanoceramic Co-Zn-based hydrogel

In general, hydrogels are composed of crosslinked, hydrated polymer chains with an intrinsically high porosity that enables the entrapment of substantial quantities of water molecules. According to the literature, the water retention capacity of certain hydrogels can reach up to 2,000 times the dry weight of their polymer framework [66]. Hydrogel fabrication typically involves introducing both hydrophilic and hydrophobic functional groups into a water-soluble polymer with a reticular crosslinking architecture. The hydrophilic moieties bind water molecules and immobilize them within the three-dimensional hydrogel network, while the hydrophobic segments undergo volumetric expansion upon water exposure, contributing to the material's swelling behaviour.

Co-containing hydrogels have demonstrated superior water absorption capabilities, with water uptake values of approximately 4.6 g/g, exceeding the performance of most hydrogels reported to date [67]. Their preparation process is straightforward, requiring no stringent synthesis conditions, thereby enabling cost-effective and scalable production. Beyond their hygroscopic properties, Co-based hydrogels can serve as electrolytic media, reducing interfacial resistance, facilitating ion transport, and enhancing electrical output. These combined attributes position Co-based hydrogels as promising platforms for HGPG devices and other functional applications [68-75].

A promising strategy to further enhance water adsorption is the incorporation of materials with high water affinity, such as Zn-based nanoparticles [76]. These nanoparticles exhibit broad utility in analytical chemistry and can be synthesized using simple, low-cost methods [77-82]. Leveraging the complementary properties of Co and Zn, Co–Zn hybrid hydrogels are anticipated to deliver improved HGPG performance through enhanced water permeability, reduced power losses, and favourable dielectric and resistive characteristics. Such properties have rendered Co–Zn systems attractive across diverse industrial sectors. Table 2.2 summarizes representative studies on Co–Zn materials synthesized via different methodologies. Extensive prior investigations into Zn–Co nanoparticles provide strong evidence supporting the use of Co–Zn-based hydrogels as high-performance active layers for humidity gradient power generation [83].

Table 2.2
Several Studies on Co-Zn by Different Synthesis Techniques in Various Applications

Material	**Application**	**Synthesis method**	**Outcome**	**Ref.**
$Co_xZn_{1-x}Fe_2O_4$	Environmental and biomedical	-	• Highest absorption rate: x (Co) = 0.4. • Adsorption capacity = 24.7 mg/g. • crystallite size ranging from 5 - 9 nm.	[84]
$Co_{0.5}Zn_{0.5-x}Gd_xFe_2O_4$	Electromagnetic wave (EMW) absorption	Hydrothermal method	• The average particle size = 26 to 50 nm. • The reflectivity absorbance = -2.11 to -27.94 dB. • Effective absorption bandwidth (EAB) = 4.08 GHz.	[85]

$Co_{0.5}Zn_{0.5}Fe_2O_4$	Microwave absorbers	Solvothermal	• EAB = 4.3 GHz (11.7–16.0 GHz) • Thickness = 2.1 mm.	[86]
$Co_xZn_{1-x}Fe_2O_4$	Pb (II) adsorption and magnetic hyperthermia	Honey-mediated synthesis	• x(Zn) = 0.6, loss power = 2.56 W/g. • Crystallite size around 14 ±2 nm. • Adsorption capacity values = 23.10 mg/g (for $Co_{0.8}Zn_{0.2}Fe_2O_4$) to 289 mg/g (for $ZnFe_2O_4$).	[87]
O-$Co_xV_{1-x}Se_2$ nanostructures	Zinc–cobalt batteries	Hydrothermal and subsequent controlled selenization process.	• Ultrahigh specific capacity of ≈ 461.8 mAh g^{-1} at a current density of 1 A g^{-1}.	[88]
Co-Zn-S nanoarrays	Supercapacitors	Facile electrochemical deposition	• Specific capacity of 317.03 $C.g^{-1}$ at 1.76 $A.g^{-1.}$ • Energy and power densities (25.71 $Wh.kg^{-1}$ and 8.73 $kW.kg^{-1}$	[89]
Zn/CoN-C	Zn-air battery	Atomic dispersion	• Maximum power density = 230 mW cm^{-2}. • Specific surface area (1343 m^2/g). • Average pore width = 2.46 nm.	[90]
$ZnFe_{0.8}Co_{0.4}O_{2.4}$ nanoparticles	Water purification	Sol-gel combustion method	• Diameters = 20 to 60 nm.	[91]
$Mn_xCo_{0.5-x}Zn_{0.5}Fe_2O_4$	Supercapacitor electrode	Sol-gel auto combustion technique	• Crystallite size = 35.4–43.6 nm.	[92]
Zn-Co-S@N-C is	Lithium-ion storage	Sulfidation and thermal annealing	• Cycling stability = 667.7 mAh g^{-1} after 300 cycles at 1000 mA g^{-1}. • Rate capability (332.2 mAh g^{-1} at 5000 mA g^{-1}). • Average particle size = ~90 nm, thickness = ~15 nm.	[93]

Therefore, in this study, a Co–Zn-based hydrogel is employed as the primary humidity-trapping medium in the HGPG device. Its integration is anticipated to significantly enhance the moisture uptake capacity of the hygroscopic composite, enabling efficient water molecule to capture even under low-humidity conditions. Furthermore, the incorporation of heteromorphic nanochannels and actinomorphic-structured NG within the hydrogel matrix is expected to modulate ion transport

dynamics and interfacial charge separation, thereby influencing and potentially amplifying the overall performance of the HGPG device, a relationship systematically investigated in this work.

2.3.3 The Utilization of Cellulose-Based Substrates in Energy Harvesting Applications

Cellulose, most commonly sourced from wood, originates from a hierarchical assembly of structural units. Wood itself comprises numerous cells, whose walls are built from microfibril bundles that can be further resolved into microfibrils, nanofibrils, elementary fibrils, and molecular chains at progressively smaller length scales, as illustrated in Figure 2.3. The three principal lignocellulosic constituents of wood, namely cellulose, hemicellulose, and lignin, are widely utilized in energy-conversion technologies, including nanogenerators, photovoltaic cells, and related devices [27-29].

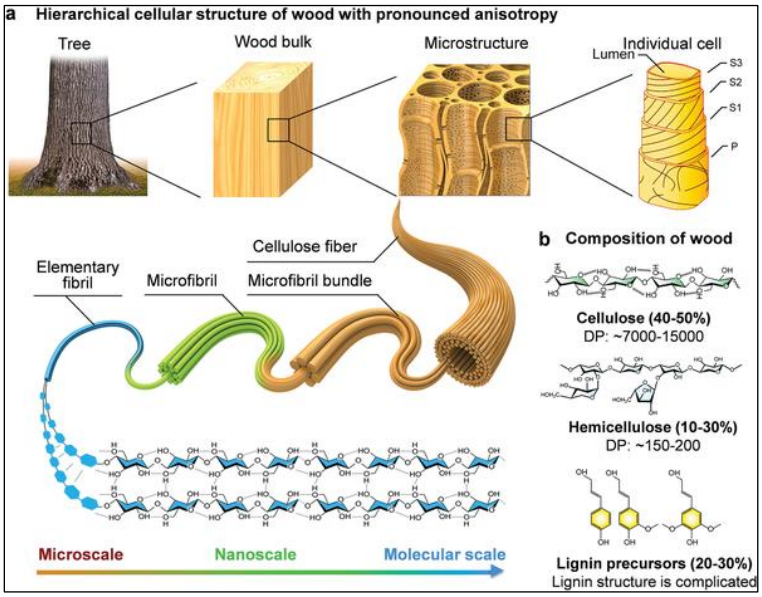

Figure 2.3 Wood's Structure and Compositions. Reproduced Permission from Reference [94]. Copyright 2020, John Wiley and Sons.

As the most abundant natural polymer on Earth, cellulose represents a green, cost-effective, biocompatible, and renewable resource [95, 96]. Its structural versatility allows it to be engineered into mesoporous frameworks, flexible thin films, high-strength fibers with excellent thermal stability, and three-dimensional open-network architectures with high aspect ratios—configurations well suited for accommodating additional functional materials [97, 98]. These tuneable structural and physicochemical

attributes make cellulose an ideal platform for enhancing the performance of power-conversion systems. Table 2.3 summarizes representative studies on cellulose-based materials, highlighting diverse synthesis strategies and application domains.

Table 2.3
Comparison of Cellulose-Based Materials Synthesized via Different Methods and Their Corresponding Applications

Material	**Application**	**Synthesis method**	**Outcome**	**Ref.**
Cellulose nanocrystals and polyvinyl alcohol composite films	Moisture-electric converter	Self-assembly method	• Output voltage = 200–700 mV	[99]
Cellulose nanofibers	Moisture-enabled electric generator	Drop casting	• Output voltage = 0.7 V, output current = 807 nA	[100]
Cellulose-PVDF-KNN	PENG	-	• Power density = 12.81 μW cm^{-2}	[101]
Polydopamine@ barium titanate/cellulose acetate nanofiber films	Hybrid nanogenerators	Electrospinning	• Output voltage = 44V	[102]
Cellulose membranes/fluorinated cellulose membranes	Triboelectric nanogenerators	Electrospinning	• 94 V, 8.5 μA, and 0.15 W/m^2	[103]
Microcrystalline cellulose/carbon black/carbon nanotubes, cellulose nanofibers/carbon nanotubes	Triboelectric and piezoelectric nanogenerators	Filtration	• MCC-0.2%CNT Triboelectric = 39 V CNF-0.3%CNT Piezoelectric = 0.75 V	[104]
Cellulose nanocrystal	Pyro-piezoelectric nanogenerator	3D Printing	• Output voltage ~ 5−15 V, short-circuit current ~ 0.04−0.2 μA	[105]
Cellulose nanofiber/graphene oxide	Moisture-driven electricity generator	Vacuum-assisted filtration, surface imprinting technique.	• Output voltage = 286 mV	[106]
Cellulose nanofibrils	Triboelectric Nanogenerator	Aminosilane modification	• Output voltage = 195 V, output current = 13.4 μA	[107]
Cyanoethyl cellulose/poly-tetra-fluoroethylene (PTFE)	Triboelectric nanogenerator	-	• Charge density at 95%RH is 533 μC/m^2	[108]
Cellulose fiber	Battery	Hydrothermal and calcination	• Capacitance = 476 mA h g^{-1}	[109]
Cellulose nanopaper	Organic solar cells	Dimethylacetamide filtration and vacuum-dried	• Efficiency = 16.17%, J_{SC} = 21.18 mA cm^{-2}	[110]
Nanowire cellulose/ MXene	Sensor	Vacuum filtration and foaming	• Sensitivity = 419.7 kPa^{-1}	[111]

Ge et al. [99] successfully developed a moisture-electric converter capable of transforming moisture signals into electrical signals by using cellulose nanocrystals and polyvinyl alcohol (PVA) composite films. The fabricated device responded to environmental humidity changes by producing a stable output voltage ranging from 200 to 700 mV for over 100 hours, demonstrating its potential for long-term operation in high-humidity conditions. In a related study, Thakur et al. [100] fabricated a bilayer moisture-enabled electric generator. The system, produced via a drop-casting technique, employed chemically modified cellulose nanofibers functionalized with carboxylate and quaternary ammonium groups. The resulting device generated an output of 0.7 V and 0.8 μA without requiring an external power source.

Cellulose, being the primary component of lignocellulose, has recently gained attention as a promising material for nanogenerator applications due to its biodegradability and chemical modifiability. Upon contact or friction, cellulose tends to transfer electrons to materials with higher electron affinity. According to Cao et al. [103], cellulose can serve as a tribo-positive material in triboelectric nanogenerators (TENGs), due to the abundance of hydroxyl groups and oxygen atoms on its surface, which are prone to electron loss. Furthermore, González et al. [104] demonstrated the potential of cellulose in PENGs, achieving an output voltage of 0.75 V using cellulose nanofibers combined with carbon nanotubes. Their study emphasized that the crystallinity and crystal orientation of cellulose significantly influence the performance of PENGs. Lu et al. [102] conducted a significant study on harvesting mechanical energy by developing a flexible hybrid nanogenerator. This device integrated polydopamine and piezoelectric barium titanate nanoparticles within a cellulose acetate matrix via electrospinning. The resulting device achieved an output voltage of 44 V and demonstrated excellent durability, withstanding over 15,000 operation cycles, effectively detecting a wide range of human motions. The study highlights its potential for use in advanced, self-powered wearable biosensors capable of precise and reliable motion monitoring.

2.3.4 The Development of Hygroscopic Material Via Various Synthesis Methods

Hygroscopic materials can be broadly categorized into several classes, including hydrogels, aerogels, composites, and related hybrids. Hydrogels are polymer-based, 3D networks with exceptional water retention capacity, capable of absorbing and immobilizing large quantities of water molecules from the surrounding environment. Aerogels, in contrast, are distinguished by their ultra porous architecture, extremely low density, and exceptionally high surface area. Composite hygroscopic materials comprise hybrid systems in which nanoparticles or other functional fillers are embedded within hygroscopic matrices to enhance structural, surface, and moisture absorption properties. A wide range of synthesis strategies has been employed to fabricate hygroscopic materials with tailored properties. Representative techniques include 3D printing for precise structural control, chemical or physical cross-linking to stabilize polymeric networks, and drying methods such as ambient drying and freeze-drying to achieve desired porosity and morphology [112]. According to Du et al. [113], the choice of synthesis strategy significantly influences the development of highly hydrophilic materials with desirable properties such as enhanced water uptake, optimal dehydration temperature, electrical conductivity, mechanical stability, swelling behaviour, and heat transfer coefficient. These characteristics directly impact the performance of assemblies, devices, and instruments in various applications.

For instance, Zhu et al. [114] developed cellulose nanofiber (CNF) aerogels via a water bath and freeze-drying process for moisture-enabled electricity generation. By incorporating Al(III) into the CNF aerogels, they successfully enhanced moisture absorption and stability, achieving a maximum open-circuit voltage of 950 mV, a short-circuit current density of 112.9 $\mu A \cdot cm^{-2}$, and a power density of 106.1 $\mu W \cdot cm^{-2}$. On the other hand, Ghaffarkhah et al. [115] demonstrated an effective atmospheric water harvesting system using aerogels composed of biobased materials particularly cellulose nanofibers and sodium alginate integrated with metal-organic frameworks (MOFs) and hygroscopic salts. Their study employed a cost-effective ambient drying method, avoiding the need for freeze-drying while preserving the aerogels' structural integrity and functionality. The developed material enhanced water capture under low RH and facilitated ambient drying, promoting efficient water transport and absorption. The

material achieved a competitive water uptake of 0.32 g/g at 25% RH and 3.52 g/g at 90% RH within 12 hours.

Table 2.4 summarizes representative studies on the development of hygroscopic materials synthesized via diverse methodologies. However, many of these preparation techniques are inherently complex, which constrains their scalability and broader technological deployment [116]. Contemporary research is increasingly directed toward the design of high-performance hygroscopic materials that exhibit rapid responsiveness, long-term stability, and superior water absorption rate and capacity, while simultaneously emphasizing environmentally benign, cost-effective, and industrially scalable fabrication strategies.

Table 2.4
Summary of Hygroscopic Materials Used in Various Applications and Their Fabrication Methods

Material	**Application**	**Synthesis method**	**Synthesis Process (Steps/Conditions)**	**Ref.**
Cellulose nanofibers	Moisture-enabled electric generator	Drop casting	• Drop-casting suspensions • Drying for 24 h at RT	[100]
Cellulose nanofiber/graphene oxide	Moisture-driven electricity generator	Vacuum-assisted filtration, surface imprinting technique.	• Solution mixing (cellulose nanofibers, 1 mg·mL−1) and Gr oxide solution (1 mg·mL−1) • Ultrasonic treatment at RT for 60 min • Vacuum-filtered the mixture • patterning using nylon mesh • Drying at RT	[106]
Nano fibrillated cellulose + hydroxypropyl cellulose hydrogel encapsulating LiCl	Atmospheric water harvesting	Gelation followed by LiCl loading	• Solution mixing • Ultrasonication for 15 min • Stir in an ice−water bath for 1 h • Further ultrasonicated for 10 min • thermally polymerized at 50 °C for 4 h • Soaked in LiCl solution for 48 h • Frozen at −80 °C for 12 h and • Freeze-drying for 24 h	[117]
Cellulose nanofiber aerogels	Moisture-enabled electricity generation	Water bath, freeze-dry	• Cellulose nanofiber /water suspension • Directional freezing • AlCl3 solution dropping, allowed to stand for > 0.5 h • Bath for 12 h • Sample washing at a shaking speed of 90 rpm • Freeze-dry below − 90 ◦C and 5.0 Pa for 40 h	[114]
Diatomaceous	Water adsorption	Uniaxial	• Ball-milled for 15 min	[118]

earth/boehmite porous ceramics		Pressing and Sintering	• Pressing sample into 5 mm thick samples at 30 MPa for 30 min • Dry at 100 °C • Sintering process at 300 °C for 90 min, ramping to 950 °C for 120 min, holding for 120 min, and cooling naturally	
Cellulose nanofibers and sodium alginate/aerogel	Atmospheric water harvesting	Ambient drying	• Solution mixing • Stir for 10 min at 10 000 rpm for 10 min • Centrifuge at 1500 rpm for 5 min • Frozen overnight at −30 °C • Dry under ambient conditions for 24 h	[115]
Porous silico-aluminophosphate-34/ Gr-based sheets	Atmospheric water harvesting	Crosslinking of alginate	• Crosslinking • Drying process	[119]
Polyacrylamide /LiCl	Various absorption applications	One-pot approach, freeze drying	• Solution mixing • Stirring for 10 min • Crosslinking • Curing process at RT • Dry for 3 days at 60 °C in an oven at RH of ≈0%	[120]

2.4 The Enhancement of Humidity Gradient Energy Harvesting through Hematite Composite Strategy

Hematite (α-Fe_2O_3) is widely recognized as a highly promising and low-cost photoanode material, with the ability to absorb part of the visible light spectrum due to its band gap of 1.9–2.2 eV [121]. It is earth-abundant, non-toxic, and known as a stable catalyst for electrochemical water oxidation [122]. However, its application is limited by its low electrical conductivity, which is attributed to its short minority carrier diffusion length and low mobility (~10^{-2} to 10^{-4} S/cm) [123]. Recently, hematite has been investigated in humidity-related studies, though reports remain limited. According to Zou et al. [124], upon moisture absorption, hematite provides an abundance of adsorption sites and its surface chemistry facilitates the development of ionic charge carriers which making it suitable for humidity-sensing applications. Ahmad et al. [125], studied the effect of annealing temperature on hematite for humidity sensor performance. The study found that an annealing temperature of 400 °C yielded the highest humidity response (S = 177.78).

Ahmed et al. [126] demonstrated that introducing hematite into chitosan significantly enhances moisture uptake, ionic transport, and charge separation. Their findings showed that increased hematite loading led to improved ion mobility and ionic conductivity, indicating that hematite plays a key role in forming conductive channels that facilitate ion dissociation and migration within the material. Meanwhile, Kok et al. [127] emphasized the potential of hematite as a novel humidity-reactive material, citing its high availability, abundant active sites, and porous structure. These characteristics are valuable in improving humidity sensitivity, surface area, stability, and selectivity.

Hematite has also found application in TENGs. Wei et al. [128] developed a TENG-driven self-powered water splitting system using titanium-modified hematite as the photoanode, demonstrating its ability to convert mechanical energy into electricity. While the use of hematite in humidity-based nanogenerators remains relatively underexplored, its intrinsic ionic conductivity and hygroscopic characteristics suggest considerable potential for such applications. These properties highlight a promising avenue for future research, particularly in leveraging the moisture-responsive behaviour of hematite to enhance humidity-based nanogenerator performance. Table 2.5 summarizes several studies involving hematite in different applications.

Table 2.5
Summary of Reported Studies on Hematite and Its Applications

Material	Application	Role of hematite	Key enhancements	Ref.
Hematite/ iridium oxides	Water splitting	Stable absorber	• Steady photocurrent density of 1.71 mA cm^{-2} at 1.23 V versus reversible hydrogen electrode (RHE)	[121]
Al-doped hematite	Water splitting	Photoanode material and a catalyst in water oxidation	• Overpotential value of 0.96 V	[123]
Hematite-hercynite	Solar Water Splitting	Absorber and electron conductor on alloy interface	• Photocurrent density of 1.24and 1.53 mA cm^{-2} at 1.23 V versus RHE	[122]
Hematite/CuO-Sb_2O_5-SnO_2 ceramics	Solar Water Splitting	Light absorber over conductive substrate	• Photocurrent density of 0.63 mA cm^{-2} at 1.23 V versus RHE	[129]
Co-MOF/ Ti:Fe_2O_3	Water Splitting	Base semiconductor	• Photocurrent density of 1.80 mA cm^{-2} at 1.23 V	[130]
Eu, Nb co-doped Fe_2O_3	Solar Water Splitting	Photoanode material	• J_{ph} of 3.49 mA cm^{-2} and a V_{on} of 0.67 V_{RHE}	[131]

Si and Sn co-doped hematite with the reduced Sn	Battery	Photoanode material	• Achieve a 3.0 mA cm^{-2} photocurrent density at 1.23 V_{RHE},	[132]
Ti-Fe_2O_3	Water splitting system/TENG	Photoanode material	• 0.12 mA under illumination	[128]
Fe_2O_3@NiO	Supercapacitor	Base semiconductor	• Specific capacitance of 530.87 F/g at a current density of 7 mA/cm^2	[133]
Fe_2O_3/NiO/rGO	Supercapacitor	Base semiconductor	• Specific capacitance of 747 F g^{-1} at a current density of 1 A g^{-1}	[134]

2.5 The Enhancement of Humidity Gradient Energy Harvesting through Surface Modification Strategy

The water contact angle (θ_{CA}) measurement is a common method used to evaluate the hydrophilic properties and water absorption capacity of a material. This measurement essentially reflects a liquid's tendency to spread on a flat surface. Surface classifications based on θ_{CA} include super hydrophilic (5°-10°), hydrophilic ($10° \leq \theta < 90°$), hydrophobic ($90° \leq \theta < 150°$), and superhydrophobic (150°-180°) [135]. Optimizing the effectiveness of humidity-to-energy devices requires the maintenance of appropriate hydrophilicity.

Several alternative techniques have also been reported for achieving tuneable surface wettability, including plasma treatment and laser texturing [136]. Plasma treatment is a widely used surface modification method that alters the chemical and physical properties of a material's surface using ionized gas or plasma, without affecting its bulk characteristics. It is particularly effective for modifying surface wettability and adjusting surface energy. Mehmood et al. [137] performed plasma treatment using argon (Ar) thermal plasma on bismuth surfaces, which resulted in a reduction of the material's θ_{CA}. Similarly, Shu et al. [138] employed Ar plasma treatment to enhance the surface hydrophilicity of cellulose-based paper. In their study, the improved hydrophilicity was attributed to the formation of surface pores by the Ar plasma jet, which increased the material's surface permeability. Furthermore, oxygen plasma treatment, which introduces oxygen-rich functional groups, is another effective method for reducing θ_{CA} and modifying the nano topography of the material [139, 140]. In contrast, laser texturing is a method that creates micro- and nano-scale surface structures, enabling precise control over texture, roughness, and wettability. This

technique allows rapid and reversible tuning between hydrophilic and hydrophobic states [141]. Laser-induced morphologies significantly increase the contact angle of surfaces and laser exposure may also induce localized oxidation or redeposition, further altering the surface chemistry [142, 143].

Based on recent literatures, SA treatment outperforms other conventional methods by offering a robust and long-lasting solution for stable wettability control [144, 145]. It is recognized for its simplicity, cost-effectiveness, and the absence of complex procedures or specialized equipment, such as plasma and laser systems. Yang et al. [146], demonstrated that material wettability can be tailored through SA surface chemistry, wherein the long alkyl chain of SA primarily relies on the central carbon atom in the $–CH_3$ group to acquire electrons in various spatial directions from the surrounding hydrogen atoms. This, in turn, influences the Coulombic repulsion with the oxygen atoms in water molecules, thereby inducing specific hydrophobic or hydrophilic effects. Meanwhile, according to the study conducted by Qu et al. [147], surface modification through SA treatment has a pronounced impact on the overall performance of energy-harvesting devices. Their findings indicate that applying 3 wt% SA effectively controlled the wettability of the developed materials, resulting in voltage and current outputs of the TENG that were 3.7 and 3.6 times higher, respectively, than those of the untreated device.

The wettability of a material generally has a strong correlation with surface energy. Water tends to spread across a material with a high surface energy and strong attraction to water, resulting in a low θ_{CA}. From here, we know that θ_{CA} is a crucial parameter that is commonly used to evaluate surface energy. According to Chen et al. [148], the surface energy of a material can be calculated using the Fowkes-Girifalco-Good (FGG) theory in combination with Young's equation, which can be simplified as follows:

$$\gamma_s^d = \frac{1}{4}\gamma_l(\cos\theta_{CA} + 1) \tag{2.8}$$

In this equation, γ_s^d represents the dispersive component of the solid surface tension and is referred to as the surface energy. Meanwhile, γ_l denotes the surface tension of the liquid.

Table 2.6 summarizes several studies that have employed SA treatment on materials relevant to the present work. Literature reports consistently highlight SA's efficacy in enhancing particle dispersion and modulating surface wettability, while preserving the engineered interfacial properties over time [149-151]. Informed by these demonstrated advantages, SA treatment was adopted in the present study to modify the developed composite surfaces. Notably, both excessive and insufficient hydrophilicity can compromise the performance of HGPG devices [152]. To achieve an optimally balanced hydrophilic profile that promotes controlled water adsorption without impairing charge transport, SA treatment was applied as a robust and reproducible surface-engineering strategy [153, 154]. The degree of surface hydrophilicity is dictated by a synergistic interplay between surface roughness and chemical composition, both of which govern surface energy. These parameters, when finely tuned, enable precise control over moisture adsorption kinetics which is an aspect critically aligned with the objectives of the current investigation [155, 156].

Table 2.6
Summary of Reported Studies on SA-Treated Materials Relevant to the Present Work

Material	Application	Role of SA	Key enhancements	Ref.
NiO	Cellular Toxicity Studies	Surface shield coating	• Surface charge value = 13 ± 1 mV	[157]
reduced-graphene oxide (rGO)/Ni	Self-cleaning and anticorrosion	Superhydrophobic coating	• WCA = 162.7° ± 0.8°	[158]
NiO	Adsorbent	Surface modification	-	[159]
NiO-Al_2O_3	Self-cleaning and removal of dyes	Forming a carboxylate layer on oxide surface	• WCA > 90°	[149]
Ni-Graphene	Various	Superhydrophobic modification	• WCA = 161.4°	[160]

Table 2.7 presents a selection of reported studies employing SA surface treatment in nanogenerator applications. The literature predominantly emphasizes the use of SA to impart strong hydrophobicity, a modification often correlated with enhanced device performance. However, investigations targeting optimized wettability, particularly those that leverage or tailor the inherent hydrophilic characteristics of certain nanogenerator materials, remain comparatively scarce. Moreover, systematic studies on SA-mediated surface engineering specifically for HGPGs and PENGs are exceedingly limited. This gap underscores a compelling research opportunity, which

the present work seeks to address through the strategic integration of SA treatment into composite systems designed for dual mode energy harvesting.

Table 2.7
Summary of Reported Studies that have Employed SA Treatment in Nanogenerator Applications

Material	SA Content	Application	Key enhancements	Ref.
Polystyrene waste/ZnO	0.025 g/ml	TENG	• Output voltage = 8.2 V, power density = 28.1 μW/cm^2	[3]
Polytetrafluoroethylene/ PVDF-hexafluoropropylene (HFP)	3.0 wt%	TENG	• WCA = 133° • V_{OC} = 145 V, power density = 2.6 W m^{-2}, I_{SC} = 18 μA	[147]
PVDF-HFP	3.0 wt%	TENG	• Power density = 1681 mW/m^2	[161]
PVDF-HFP/ poly[styrene-b-(ethylene-co-butylene)-b-styrene]	1.5 wt%	TENG	• V_{oc} = 101 V, I_{sc} = 1.88 μA	[162]
PVC film	5.0 wt%	TENG	• High stability with 82% of wear rate	[163]
Bromobutyl rubber	0.192 g	TENG	• Output voltage = 40 V under • force of 40 N	[164]

2.6 Piezoelectric Nanogenerator

Essentially, PENGs are composed of piezoelectric materials as their core element, which generate electrical energy when exposed to mechanical forces. PENGs offer numerous advantages in small electronic technologies, being both environmentally friendly and efficient, as well as adaptable to a wide range of components and systems. They are resistant to various environmental factors, such as air, temperature, and humidity [165]. Moreover, external mechanical stimuli such as compression, tension, vibration, and twisting can produce electrical output [166]. Recent studies have extensively explored flexible PENGs that can harvest energy from the environment or from human activity. It has been shown that their electrical output performance is sufficient to power devices such as wireless signal transmitter, liquid crystal displays (LCDs), and light-emitting diodes (LEDs).

2.6.1 Piezoelectricity

PENGs are designed to efficiently gather mechanical energy from the surrounding environment. Piezoelectricity is the process through which mechanical

energy is continuously transformed into electrical energy using the piezoelectric effect. This effect describes the creation of electric charge in specific materials when subjected to mechanical pressure. The term "piezo" originates from the Greek word for "pressure" and was introduced by Hankel in 1881 [167]. The "direct" piezoelectric effect is the core concept of converting mechanical energy into electricity and was first identified by French physicists Jacques Curie and Pierre Curie in 1880 [168]. Conversely, the “inverse" effect, initially explained by Lippmann in 1881, converts electrical energy into mechanical energy.

Piezoelectric materials, also known as PENG materials, experience a change in length due to mechanical strain or stress induced by an electric current when an electrical voltage is applied. In 1882, the Curie brothers conducted an experiment to validate this [167]. These materials find application in a wide range of fields, including accelerometers, actuators, fuel injectors, engines, resonators, sensors, transducers, energy harvesters, and more [169]. As illustrated in Figure 2.4, the direct piezoelectric effect manifests when a force is exerted on a material placed between two electrodes, generating a current through a circuit. Conversely, the inverse piezoelectric effect involves the deformation of the same piezoelectric device in response to an applied electric field. Equation (2.9) represents a simplified method to describe the direct and converse piezoelectricity [170]. The mechanical domain (stress, T, and strain, ε) and the electrical domain (electric field, E, and charge density, d_c) are interrelated through constitutive equations as follows:

$$\begin{cases} d_c = dT + \varepsilon E \\ \varepsilon = sT + dE \end{cases} \tag{2.9}$$

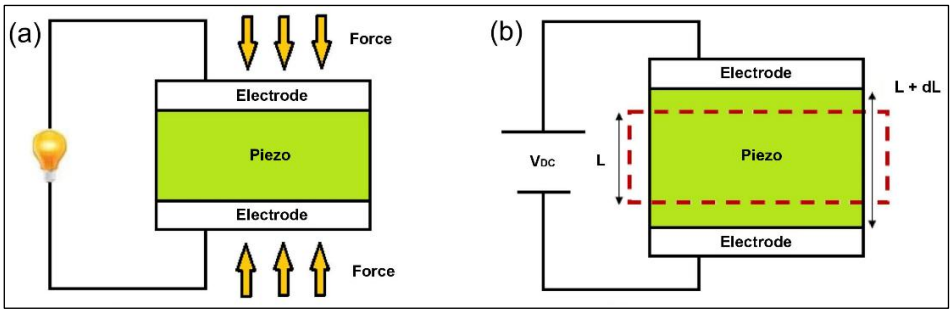

Figure 2.4 Schematic Diagram of a) the Direct and b) the Inverse Piezoelectric Effects

2.6.2 Piezoelectric Applications

The initial discovery of PENGs occurred in 2006 by Wang, where ZnO nanowires were employed to convert mechanical energy into electrical energy [171]. Over time, the performance of PENGs has improved significantly due to continuous advancements in piezoelectric composites, processing techniques, and technical systems. However, despite this progress, the widespread application of PENGs is restricted by their limited power capacity, even though the output voltage has exceeded 100 V. The piezoelectric coefficient (d_{33}) remains small, but compatible with current process technology, making PENGs suitable for various applications, including biomedical, aerospace, industrial ambient, and wearable electronics. The flexibility and nontoxic nature of PENGs further enhance their appeal. In 2010, PENGs achieved a maximum short-circuit current (I_{sc}) of 28.8 nA and a maximum open-circuit voltage (V_{oc}) of 1.26 V, surpassing the electrical output of typical batteries [172]. Unlike conventional batteries, PENGs offer a sustainable and environmentally friendly energy source.

Current developments in piezoelectric energy harvester technology are aimed at producing self-powered, flexible, and long-lasting devices. Piezoelectric materials are increasingly utilized in a variety of fields, such as biomedicine, portable electronics, actuators, nanogenerators, and microelectromechanical systems (MEMS) devices. Numerous studies have reported on the various applications of PENGs. These include energy harvesters powered by human activity for implantable and wearable medical technology, the use of piezoelectric materials in aerospace, vibrational energy harvesting in self-propelled wireless sensors and vehicles, and health monitoring. Table 2.8 summarizes recent advancements in piezoelectric energy harvesting based on research across various application domains highlighting performance improvements achieved through the integration of diverse materials and fabrication techniques.

Table 2.8
Several Recent Progress and Studies in PENG Applications

Piezoelectric material	Fabrication method	Sample size	Performance	Application	Ref.
PVDF/ high crystallization hβ-PVDF nanosheets	Solution method	-	High J_{sc} = 145 nA cm^{-2}.	Acceleration sensor	[173]

PVDF/ PEDOT-C_4:DS; PEDOT-C_6:DS; PEDOT: PSS-CNT	Spin-coating	35×35 mm^2	PEDOT-C_4: DS = 1.54V, 166.0nA, 63.0nW; PEDOT-C_6:DS = 1.49V, 159.0nA, 59.9nW	Self-powered piezoelectric sensor	[174]
PDMS/ SnS monolayers	Liquid metal-based technique	50×20 mm^2	Voltage output of ~150 mV at 0.7% strain.	Wearable device	[175]
Silicone rubber/ Samarium/titanium doped $BiFeO_3$ (BFO)	Freeze-drying method	1.5×3 cm^2	V_{OC} = 16V; I_{SC} = 2.8μA.	Self-Powered Mechan sensation System	[166]
Polylactic acid (PLA) / $Ba_{0.85}Ca_{0.15}Zr_{0.10}Ti_{0.90}O_3$	Sol-gel method; Single-step hydrothermal synthesis	1.5×1.3 cm^2	V_{OC} = 14.4V, I_{SC} = 0.55μA, P_d = 7.54mW/cm^3	Biomechanical energy harvesting	[176]
PMDS/ MoS_2 and Au-$MoSe_2$	$MoSe_2$: Solvothermal reaction method MoS_2: Atmospheric pressure chemical vapor deposition method	-	Voltage output = 26 mV; V_{OC} increases as strain increases from 0.25% - 0.60%.	Gas sensor	[177]
PDMS/ P(VDF-TrFE)	Electrospinning	4 cm × 2.5cm × 3mm	Maximum P_d = 8.75μW/cm^2; 150 V (fingers pressure/ release cycle)	Self-powered wearable devices	[178]
PVDF-TrFE/ ZnO @ PA @ PFOES	Spin-coating	-	Voltage output = 2.40 V	Wearable flexible electronic	[179]
Au electrode on polyethylene terephthalate (PET) substrate / MoS_2	CVD method	-	Increased to 100 pA and 22 mV	Potential: Stretchable/wearable electronics	[180]
PVDF-HFP / Graphene quantum dot	Spin coating	-	Voltage output = 6 V, current output = 25 nA	Self-powered human breathing. Finger movement sensors	[181]
PET substrate / SnSe	Sputtering	-	Voltage output = 760 mV; P_d = 28 mW/m^2	Self-powered electronic tongue. Electronic skin. Photoelectric devices	[182]
PVDF	Electrospinning	-	-	E-skin (sense body's mechanical movement)	[183]

Wood sponge	Simple delignification process	15×15×14 mm^3	Voltage output = 0.69 V, Current = 7.1 nA	Wearable sensor for monitoring human motions	[184]
PDMS and PVDF/ Graphene quantum dot (GQD) and TiO_2 nanoparticles	Spin coating	-	V_{OC} = 14.3 V; I_{SC} = 5.1 μA.	Potential: Flexibility display. Electronic skin. Wearable electronic products. Self-powered sensors.	[185]
PMMA/PDMS/ Organic nanowires (ONW) - Au - ZnO	Plasma enhanced chemical vapor deposition (PECVD)	1.5×4.5 cm^2	Current = 15 nA, voltage output = 105 mV.	Potential: Energy harvesting device	[186]
Piezoelectric Ceramic / PMMA	Microfluidic drive technology	3×3×18mm ^{3}	Voltage output = 150V.	Microfluidics technology	[187]

2.6.3 Piezoelectric Materials and Device Structure

Numerous flexible PENGs have been developed to capture waste energy from the body or its environment. Much research has focused on modelling, operational principles, and output enhancements, with the introduction of innovative nanogenerator devices. As shown in Figure 2.5, PENG devices are commonly designed in a layered structure comprising a piezoelectric material layer, electrodes, and a protective film. Platinum (Pt) [188], silver (Ag) [189], aluminium (Al) [190] and copper (Cu) [191] have been widely employed as electrodes in PENG applications. Additionally, a polymer layer like polyethylene terephthalate (PET) is often included in PENG devices for insulation and protection, ensuring the stability of the structure.

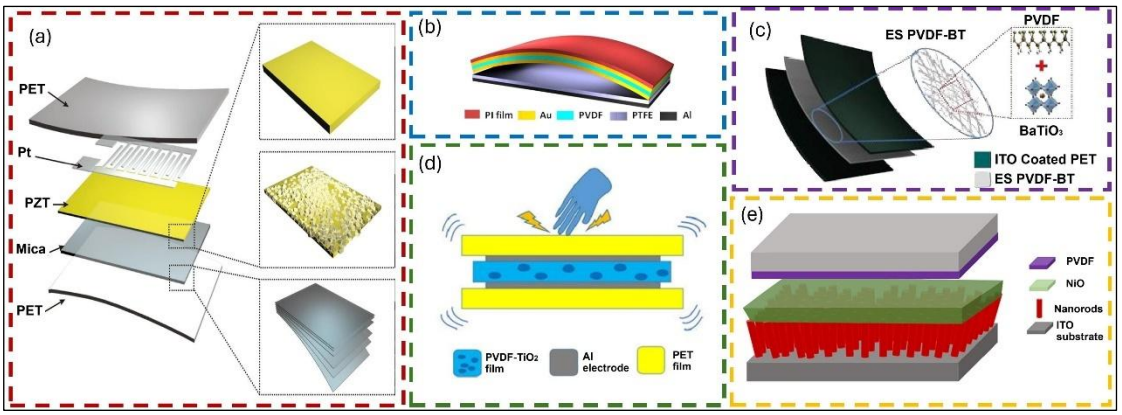

Figure 2.5 Structure of the PENG (a) PET/Pt/PZT/Mica/PET, Reproduced with Permission from Reference [192]. Copyright 2020, American Chemical Society Publisher (b) 3D Schematic View of the Arch-Shaped

Piezo/Triboelectric Hybrid Generator, Reproduced with Permission from Reference [193]. Copyright 2015, Springer Nature Publisher (c) PVDF/$Batio_3$/PET/ITO, Reproduced with Permission From Reference [194]. Copyright 2022, American Chemical Society Publisher (d) Al/PVDF-Tio_2/PET, Reproduced with Permission from Reference [190]. Copyright 2023, Elsevier Publisher (e) Al/Zno/Nio/PVDF, Reproduced with Permission from Reference [195]. Copyright 2023 Elsevier Publisher

Significant progress has been made in reducing the energy consumption of electronic systems and devices over the past decade, largely due to the wide range of piezoelectric applications in advanced and portable devices across various fields. However, energy supply and consumption remain the primary obstacles to the advancement of flexible technologies [196]. Consequently, the selection of piezoelectric materials is critical in the design of PENGs, as increasing the output current of PENGs remains a significant challenge in this domain. Enhancing the conversion efficiency of PENGs necessitates the development of materials with superior piezoelectric properties, manipulation of the nano- and microscopic surface morphology of piezoelectric materials, incorporation of chemical substances during doping, and fabrication of composite thin-film materials. It is anticipated that PENGs will ultimately achieve exceptional flexibility and performance. Nevertheless, exploration and efforts toward further improvements are ongoing. The main categories of piezoelectric materials include ceramics, single crystals, polymers, and organic-inorganic hybrid composites [169]. These materials, including paper and hydrophobic substances, have traditionally been used in piezoelectric applications. Figure 2.6 illustrates the classifications and commonly used piezoelectric materials in PENGs.

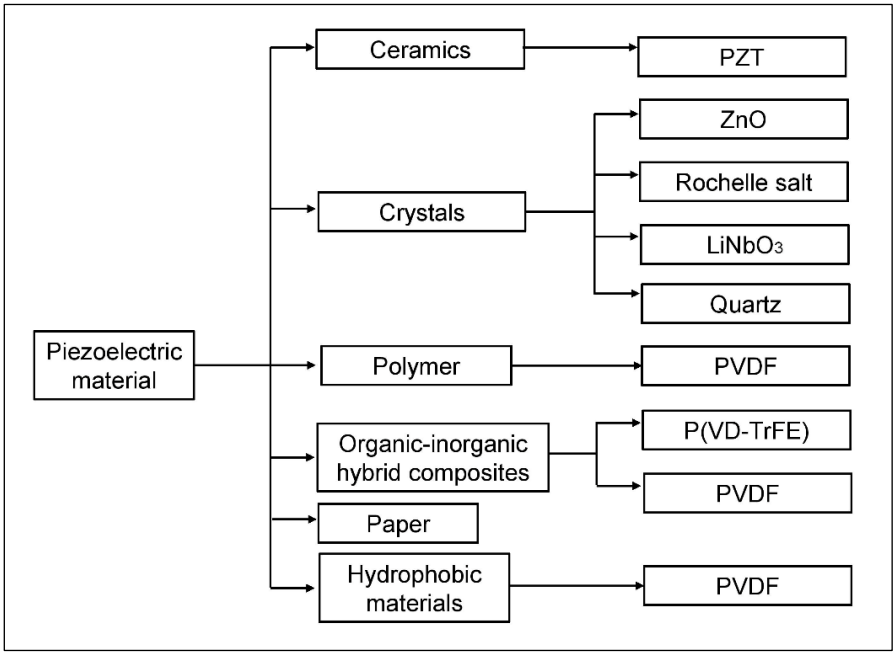

Figure 2.6 Piezoelectric Materials in PENGs Applications

PENGs commonly utilize various inorganic nanomaterials, including lithium sodium niobate ($KxNa1\text{-}xNbO_3$) [197], barium titanate ($BaTiO_3$) film [198], lead zirconate titanate (PZT) [199], and lithium niobate ($LiNbO_3$) [176]. However, most nanogenerators based on these nanomaterials require complex manufacturing processes, which complicate the development and growth of PENGs. Additionally, producing PENGs that combine both ultralightweight properties and high-output power proves to be exceedingly challenging. Inorganic materials have been shown to exhibit relatively high dielectric constant values and d_{33} coefficients.

Paper is a promising option in certain applications due to its convenience and suitability for environmentally friendly, biodegradable devices. Moreover, the cellulose crystallites within paper contribute to its shear piezoelectric constants, which are comparable to those of quartz [200]. Currently, significant research is focused on developing lead-free composites with high performance. These composites incorporate paper alongside other piezoelectric materials, such as potassium niobate ($KNbO_3$) and $BaTiO_3$ and meet the specific demands of the biomedical sector.

2.7 Waste-to-energy

Despite the increasing focus on the Internet of Things (IoT), paper consumption remains one of the most in-demand products globally. In Malaysia, statistics indicate that approximately 25% of landfill waste consists of paper, posing significant challenges for waste disposal and contributing to environmental and health problems [30, 31]. Additionally, it is reported that over 4 billion tons of municipal solid waste (MSW) are generated annually worldwide, with projections estimating an increase from 2.01 billion tons in 2016 to 3.40 billion tons by 2050 [201]. Wastepaper which is a major component of MSW, represents a critical issue with global paper consumption reaching approximately one million tons annually [202].

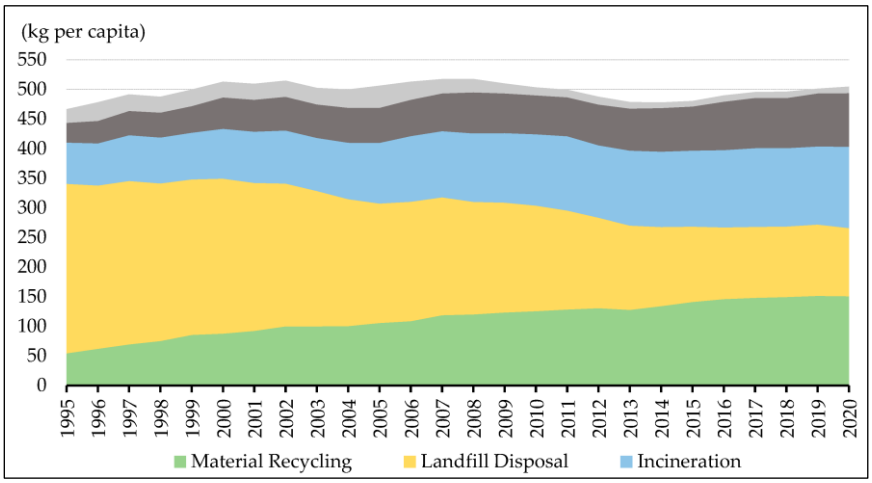

Figure 2.7 Main MSW Treatment Methods from 1995 To 2020. Reproduce with Permission from Reference [203]. Copyright 2022, MDPI.

Recycling is one of the most effective strategies to address these challenges, offering a sustainable solution to reduce wastepaper volumes [204-206]. As illustrated in Figure 2.7, recycling is a common MSW treatment method that has shown a consistent year-over-year increase. Studies reveal that recycling one ton of paper can prevent the felling of approximately 17 trees [207, 208]. Another promising approach adopted in many countries is waste-to-energy technology, which is now widely recognized as a viable option for treating residual waste and supporting long-term waste management strategies [209]. Various technologies are available to convert waste into valuable energy products, such as heat and electricity, thereby reducing the volume of waste sent to landfills [210]. Interestingly, this study adopts a combined approach of

wastepaper recycling and waste-to-energy conversion. This integrated strategy offers complementary benefits for managing paper waste, contributing to a more sustainable circular economy and ensuring optimal utilization of waste components within the MSW stream.

2.8 Hybrid Devices Integrated with Humidity Gradient Energy Harvesting

In 2009, Wang et al. [126] successfully developed the first hybrid energy cell. The concept of hybridized nanogenerators has garnered significant scholarly interest due to the advantages of integrating multiple nanogenerators into a single microsystem capable of generating electric either independently or simultaneously from various energy sources. For instance, generating wind energy in still air is impractical, and solar energy cannot be harvested indoors or during cloudy weather. Thus, hybridization represents a fundamental approach to addressing the challenge of utilizing available ambient energy at any given moment.

HGPGs are harvesting energy from humidity. PENGs, TENGs, and electromagnetic generators are viable options for acquiring mechanical energy, while solar and electrochemical cells can generate energy from solar radiation and chemical reactions, respectively. Thermoelectric and pyroelectric nanogenerators, on the other hand, are specifically designed to extract thermal energy. Both piezoelectricity and triboelectricity are commonly utilized in the fabrication of nanogenerators [128]. Extensive research and development have focused on hybridization structures and the enhancement of piezo/triboelectric nanogenerators, which have recently shown the ability to generate high power and sensitivity with a single mechanical motion. Additionally, hybridization allows the device to adapt and function under various conditions. As detailed in Table 2.9, numerous comprehensive reviews have been conducted on alternative hybridized nanogenerators, such as piezoelectric/photovoltaic hybrid nanogenerators (HyNG) and triboelectric/electromagnetic hybridized devices.

Table 2.9
Comparison of Reported Hybrid Devices Integrated with Piezoelectric Nanogenerator

Nanogenerator type	**Developed material**	**Voltage**	**Current**	**Ref.**
Piezoelectric/triboelectric HyNG	$MAPbBr_3$ SCs-PVDF	256 V	0.04mA/ cm^2	[211]

Piezoelectric/triboelectric HyNG	PVDF/$BaTiO_3$ composite nanofibers	444 V	19.02 mA m^{-2}	[212]
Piezoelectric/triboelectric HyNG	Doku & PVDF/SWCTs NFs	19.5 V	6 μA	[213]
Piezoelectric/triboelectric/electromagnetic HyNG	CZF NPs @PDMS composite film	35 V	4.5 μA	[214]
Piezoelectric/triboelectric HyNG	MoS_2-PVDF/PDMS	35.3 V	20.8μA	[215]
Piezoelectric/triboelectric HyNG	SbSeI NWs	2.71 V	-	[216]
Piezoelectric/triboelectric/electromagnetic HyNG	PVDF stripe	-	-	[217]
Piezoelectric/triboelectric HyNG	PDMS/(PVDF-TrFE) nanofiber	13.1 V	46 nA	[218]
Solar-thermal-pyroelectric HyNG	P(VDF-TrFE-CFE), P(VDF-TrFE)	-	-	[219]
Piezoelectric/photovoltaic HyNG	PVDF Polymer-Based Leaf	5.071 V	1.282 mA	[220]
Piezoelectric/triboelectric HyNG	PVDF/ PTFE layer and Nylon layer	-	-	[221]
Piezoelectric/triboelectric HyNG	PDMS@ Ag/ZnO	20 V	0.2 μA	[222]
Piezoelectric/triboelectric HyNG	VDF/KNN-ZS nanofibrous web	~25 V	~2.11mA	[223]
Piezoelectric/triboelectric HyNG	MWCNTs/PVDF-TrFE/PDMS	34.4 V	1.74 μA	[224]
Piezoelectric/triboelectric HyNG	BTO-PDMS composite/Al	100 V	980 nA	[225]

Researchers are continually striving to improve the performance of materials used in energy harvesting, enhance the convenience and flexibility of hybridized energy harvesting technologies, and optimize energy conversion efficiency to develop high-output power devices. Despite these advances, significant opportunities for further development remain, particularly in hybridized technologies involving HGPG, as it is extremely rare for HGPG to be integrated with other energy-harvesting systems. Table 2.10 presents a comparison of reported hybrid devices with humidity-driven applications.

Table 2.10
Comparison of Reported Hybrid Devices with Humidity-Driven Application

Hybrid device	**Material**	**Outcome**	**Ref.**
Electromagnetic-moisture energy	P(AAm-co-AAc) hydrogel/PPy	• I_{SC} = 0.045 μA at 0.1Hz, 0.65 μA at 100Hz	[226]
Hydrovoltaic-Photovoltaic	Photosystem II (PSII)/ Geobacter Sulfurreducens (G.S)	Output power with a high density = 1.24 W/m^2	[227]
Photocatalysis-enhanced hydrovoltaic	Photosensitized carbon nitride (P-CN)	• V_{OC} = 0.28 V, I_{SC} = 1.8 μA	[32]

		Stability = 600 h after short-term illumination	
Photocatalysis-atmospheric water energy	Hydrogel-Cu_2O@$BaTiO_3$	Output = 224.3 μA cm^{-2} under 10 mW cm^{-2} illumination	[228]
Solar cell-moisture energy	$BaTiO_3$@$BiVO_4$/Co-Zn hydrogel	Output = 0.4 mA/cm^2 under an illumination of 10 mW/cm^2	[229]
Solar cell-moisture energy	TiO_2/Zn hydrogel	240μA/cm^2 under ambient indoor light	[230]

For example, Gao et al. [226] successfully developed an electromagnetic-moist coupled wireless energy interactive system based on poly(acrylamide-co-acrylic acid)/ polypyrrole (P(AAm-co-AAc)/PPy)-polyelectrolyte/conjugated conductive polymer ionic diode films to synergistically harvest electromagnetic and moisture energy. The study anticipated that this technology could be beneficial for automated and intelligent electromagnetic stealth and protection, contributing to future applications in wireless charging, information encryption, and self-powered radiation monitoring. Meanwhile, Ren et al. [227] reported the successful development of hybrid hydrovoltaic–photovoltaic power generators capable of capturing energy from both sunlight and moisture. Their system, integrating photosystem II with Geobacter Sulfurreducens, achieved a high-power density of 1.24 W/m^2, consistently generating hygro-electricity from moisture absorption while producing a photovoltaic electric field that further enhanced electricity generation under sunlight.

To date, there has been no reported study on the hybridization of HGPG and PENG within a single system. This unexplored combination presents significant opportunities, as HGPG–PENG hybrid devices could serve a wide range of applications, including self-powered environmental monitoring systems that harvest both humidity and wind/vibration from the ambient environment. Such hybrid devices also hold strong potential for wearable electronics, particularly smart clothing or health-monitoring devices powered by sweat (humidity) and body motion as well as for IoT devices and automotive systems that can harvest ambient humidity and mechanical vibrations and convert them into useful energy.

2.9 Chapter Summary

From the literature analysis, recent progress in humidity-based energy harvesting and PENGs has catalysed innovative strategies aimed at simultaneously

enhancing energy conversion efficiency and advancing sustainability through the incorporation of waste-derived materials. The development of humidity-to-energy conversion platforms with exceptional stability and self-sustained moisture gradients has enabled the introduction of a new class of hygroscopic materials for HGPGs, which also demonstrate strong potential for integration into PENG architectures. In this context, the incorporation of SA-treated composites with nanoceramic hydrogel films into HGPG and PENG devices is designed to address persistent performance limitations in hygroscopic-material-based energy systems. By leveraging waste-derived substrates, this approach not only mitigates environmental impact but also aligns with sustainable, eco-conscious energy generation practices. This targeted use of recycled and waste materials represents a significant advancement in materials science, facilitating the fabrication of high-performance energy harvesting devices with improved efficiency and simplified manufacturing processes. Through the synergistic integration of advanced composite architectures, surface functionalization techniques, and waste valorisation strategies, the fields of humidity-driven energy harvesting and nanogenerator technology continue to evolve, opening new pathways toward scalable, sustainable, and environmentally responsible energy solutions.

CHAPTER 3
RESEARCH METHODOLOGY

3.1 Introduction

The experimental processes of this investigation were systematically organized into six distinct phases, each meticulously designed to sequentially address specific research objectives. In the initial phase (Phase 1), heteromorphic nanochannels, actinomorphic structured NG powders were synthesized and subsequently integrated with a cellulose-based substrate to develop NG composite films for HGPG. The synthesis of pristine NiO and NG was performed using a low-temperature sonicated solution immersion method, marking the starting point of the experimental workflow. The synthesized pristine NiO and NG were subsequently functionalized with SA, and the resulting composite films were fabricated using the doctor-blade technique. Comprehensive characterization experiments were conducted to evaluate the structural properties, surface morphology, and wettability of the pristine NiO and NG composite films with varying Gr loadings.

Phase 2 focused on the strategic enhancement of the NG composite films through surface treatment with SA to optimize their hydrophilic properties. In Phase 3, hematite was incorporated into the NG composites to further enhance their humidity-to-electricity conversion performance. Phase 4 and phase 5 involved the integration of the optimized HNG composite into a Co-Zn-based nanoceramic hydrogel film and RP substrate, respectively. Extensive characterization analyses were carried out to investigate the wettability, surface morphology, and structural properties of the synthesized composite materials. The performance of these materials in HGPG applications was then evaluated. In the final phase (Phase 6), additional characterization was conducted to evaluate the d_{33} of the developed materials for their potential application in PENGs and hybrid HGPG-PENG device application. The materials were incorporated into HGPG and PENG devices by combining various composites (NiO, NG, and HNG) with the Co–Zn nanoceramic hydrogel film and RP substrate. This integration enabled a comprehensive evaluation of the devices' humidity-to-energy conversion efficiency under ideal conditions, as well as their overall nanogenerator

performance. Figure 3.1 presents a schematic illustration of the entire experimental procedure.

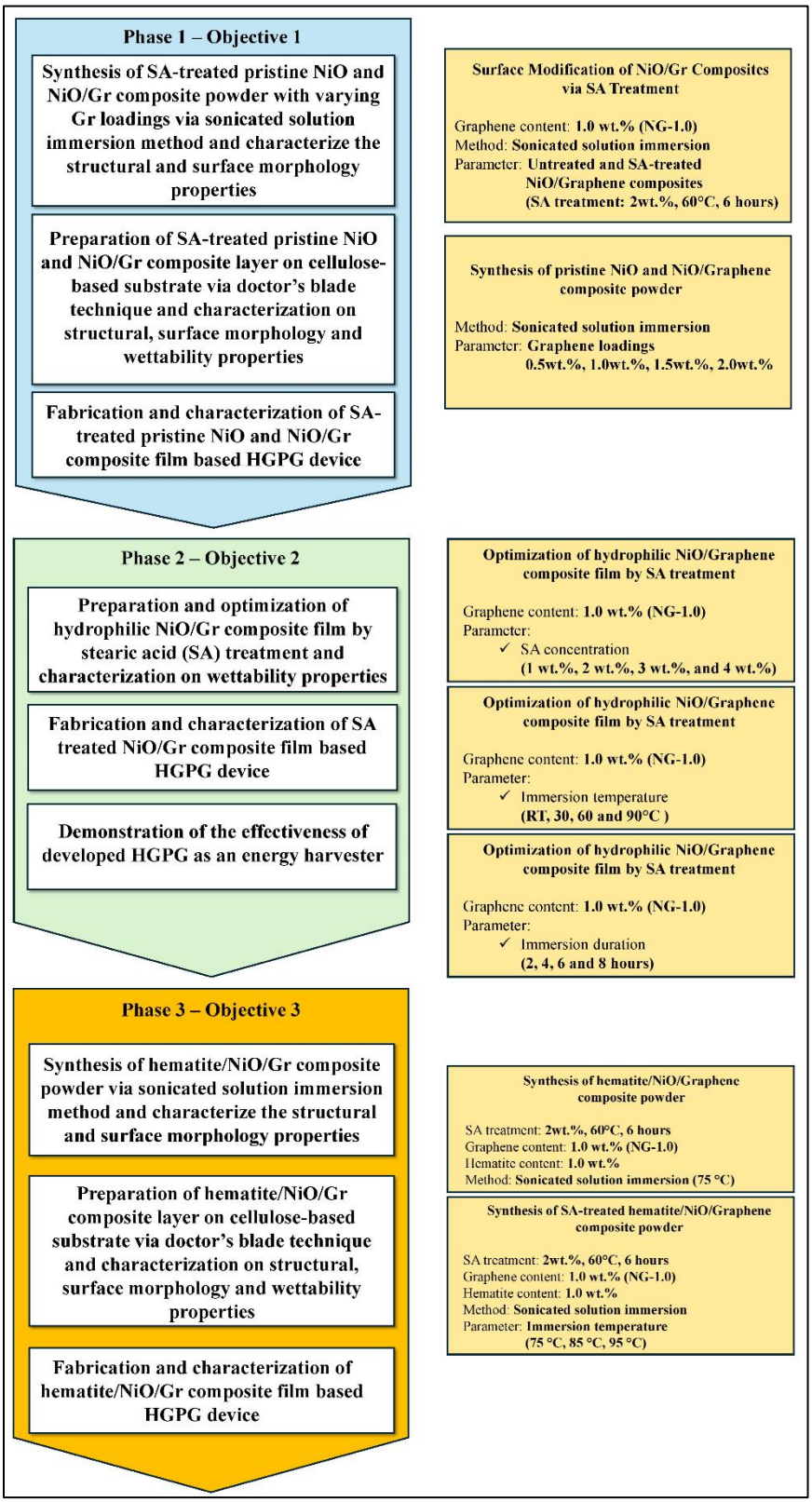

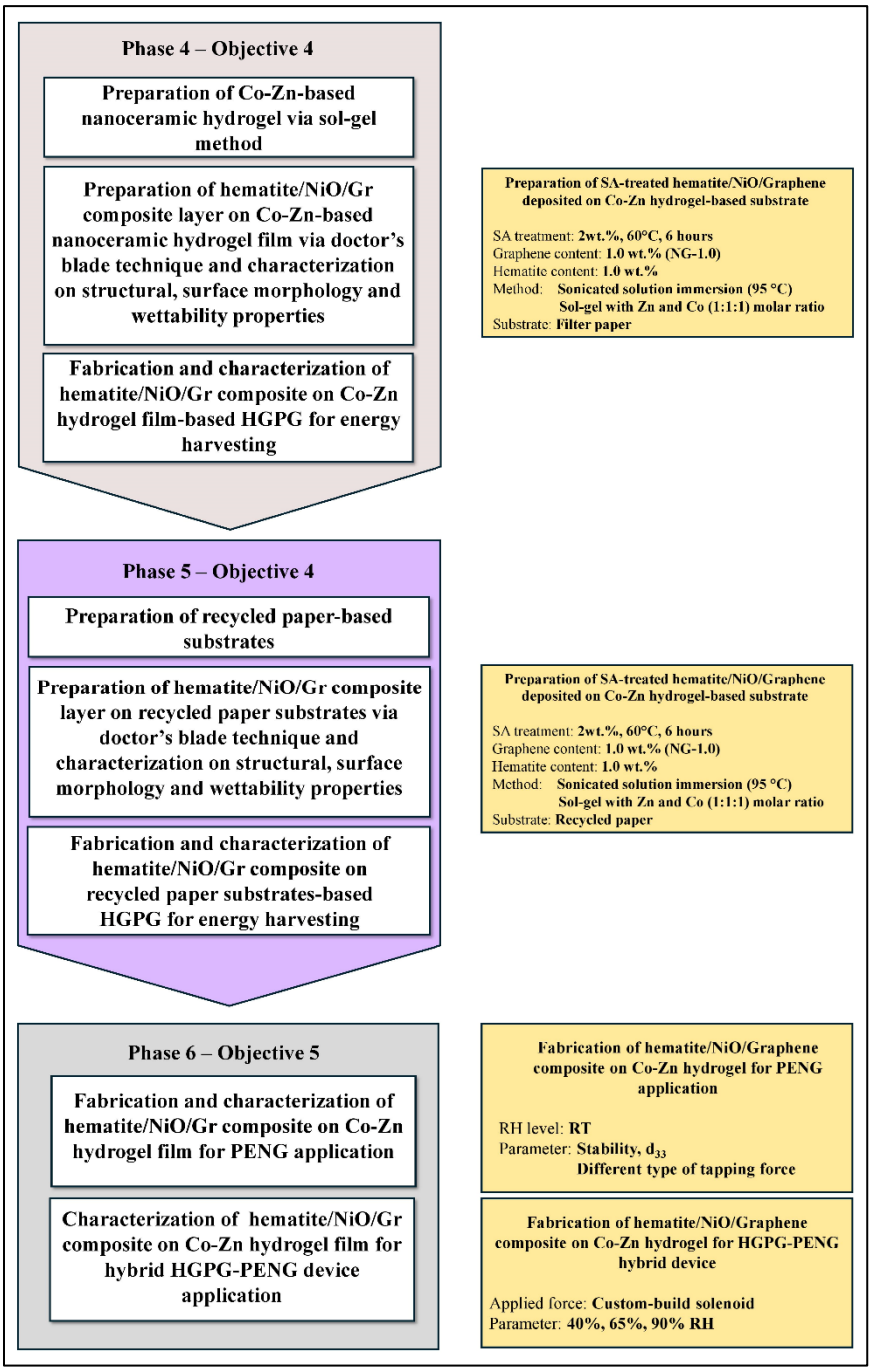

Figure 3.1 An Overview of Research Methodology That Aligns with the Research Objectives

3.2 Synthesizing of Composite Powder Based on NiO with Gr via Sonicated Solution Immersion Method at Different Amount of Gr Loading

To synthesize the NG composites powder, Gr nanoplatelets (99.98%, Techinstro) with varying weight percentages (wt.%) of 0.5 wt.%, 1.0 wt.%, 1.5 wt.%, and 2.0 wt.% were added along with hexamethylenetetramine (HMT, $C_6H_{12}N_4$, 99.0%, ACS reagent, Sigma-Aldrich), and 0.2 M of nickel nitrate hexahydrate ($Ni(NO_3)_2 \cdot 6H_2O$, 94.5-105.5%, EDTA titration, Sigma-Aldrich) to deionized water (DI) water. To enhance the chemical blending and uniformity, the solution was sonicated in an ultrasonic bath (Hwashin Technology Powersonic 405) for 1 hour, followed by stirring process at 500 rpm for 1 hour. Then, the homogeneous solution was transferred into Schott bottle (Duran, 100 mL). The bottle was securely sealed prior to immersion in a water bath (Memmert) set to 75°C for 1 hour. Following the immersion, the precipitates that were produced were gathered and filtered through Whatman Qualitative Grade 1 FP (diameter: 110 mm). To eliminate superfluous water molecules, the resulting nanomaterials were dried at 36°C in oven (Memmert) for an entire night. To improve its crystallinity, the dried sample was then annealed in a chamber furnace (Protherm) for 1 hour at 500°C in an ambient environment. Figure 3.2 illustrates the overall process. Subsequently, all samples were treated with a fixed 2 wt.% SA concentration at 60 °C for an immersion duration of 6 hours. The SA-treated NG (S-NG) powders were labelled as S-NG-0.5, S-NG-1.0, S-NG-1.5, and S-NG-2.0, whereby the number indicates the respective Gr weight percentages. Untreated NG sample with 1.0 wt.% Gr also prepared for reference and labelled as U-NG-1.0. Additionally, SA-treated pristine NiO was synthesized following the same procedures described above, but without any Gr content, and was designated as S-PN. All prepared samples were subjected to a comprehensive suite of characterization techniques to evaluate their structural and morphological features, hydrophilicity and wettability, chemical states and elemental composition, surface area and porosity, as well as electrical performance. The complete characterization framework is presented in detail in Table 3.1.

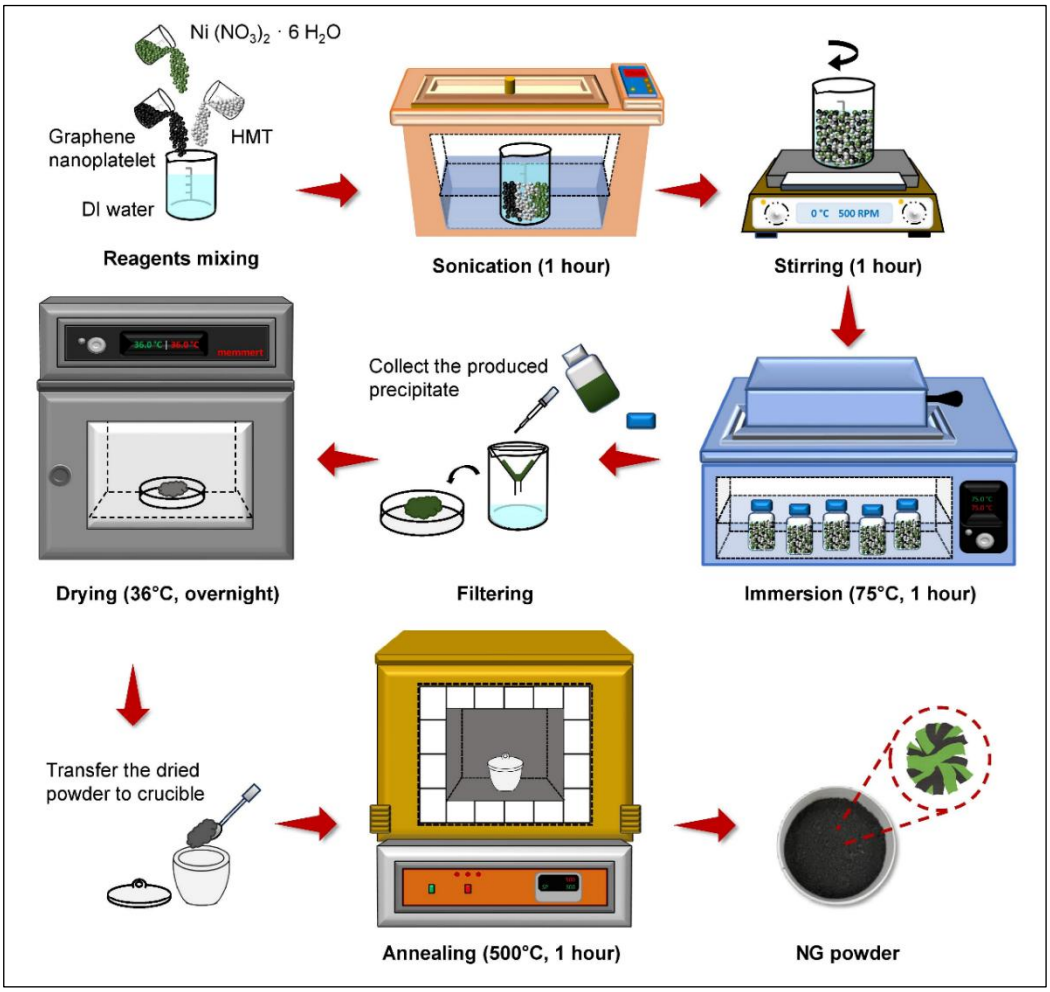

Figure 3.2 Synthesis of the NG Composites Powder Through the Sonicated Solution Immersion Method

Table 3.1
Synthesis Parameters and Characterization Techniques for S-NG Powder

Growth solution preparation	Precursor material	• Nickel nitrate hexahydrate ($Ni(NO_3)_2 \cdot 6H_2O$) • Graphene nanoplatelets, 1.0 wt.%
	Stabilizer	Hexamethylenetetramine, HMT ($C_6H_{12}N_4$)
	Solvent	Deionized water
	Volume	100 mL
	Molar concentration	0.2 M
	Sonicating process	RT, 1 h
	Stirring process	RT, 1 h, 500 rpm
Immersion process	Reaction temperature	75°C
	Reaction time	1 h
Drying process	Drying temperature	36°C
	Drying time	Overnight
	Ambient	Air
Annealing process	Annealing temperature	500°C
	Annealing time	1 h
	Ambient	Air
Characterization	Structural analysis	XRD (Rigaku Ultima IV)
	Morphology analysis	• FESEM (JEOL JSM-7600F) • HRTEM

		(FEI TECNAI G2 F20 X-TWIN)
	Elemental analysis	EDX (EDAX AMETEK)
	Hydrophilic analysis	WCA (VCA-3000)
	Molecular vibrational spectroscopy analysis	Raman (Horiba Scientific Xplora Plus)
	Chemical composition analysis	XPS (Ulvac-PHI Quantera II)
	Surface area and porosity analysis	BET (Micromeritics ASAP 2060)
Label	U-NG-1.0, S-PN, S-NG-0.5, S-NG-1.0, S-NG-1.5, S-NG-2.0	

3.3 Preparation of Pristine NiO and NiO/Gr on Cellulose Based Substrate for Humidity Gradient Energy Harvesting Application

S-PN paste was prepared by dispersing 1 g of S-PN powder in 15 ml of transparent paper glue (Chunbe 6603), which served as a binder. In this study, FP (Whatman Qualitative Grade 1, 110 mm in diameter) was used as the cellulose-based substrate. A homogeneous thin layer of the hygroscopic material was deposited onto FP using the doctor-blade technique, with Kapton tape employed to ensure uniform layer thickness across all samples. The coated FP was then dried on a hot plate at 90 °C for 1 hour. After drying, the S-PN-coated FP which denoted as S-PN-FP, was cut into square pieces measuring 15 mm × 15 mm. Subsequently, a commercial Ag conductive paste (Mechanic, MCN-DJ002) was applied to the pristine S-PN-FP as the working electrode, forming contact areas of 5 mm × 5 mm with a spacing of 5 mm between them. The fabrication process of the humidity-to-energy device is illustrated in Figure 3.3. The same procedure was repeated for the S-NG composite on the cellulose-based substrate. The resulting sample was labelled as S-NG-FP. The experimental parameter and characterization technique involved are presented in Table 3.2.

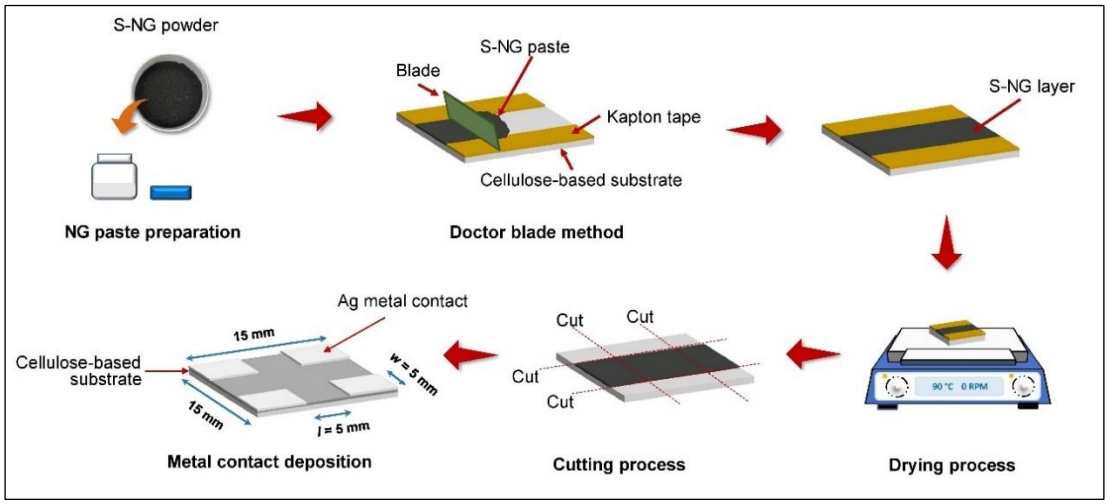

Figure 3.3 Fabrication Process and the Image of The HGPG Device Based on S-NG-FP Through Doctor-Blade Technique

Table 3.2
Synthesis Parameters and Characterization Techniques for S-PN and S-NG Composite on Cellulose-Based Substrate

Paste preparation	Composite powder	1 g
	Binder	15 ml, Glue, Chunbe 6603
Substrate	FP (Whatman Qualitative Grade 1)	
Drying	Temperature	90 °C
	Duration	1 hour
	Ambient	Air
Working electrode	Material	Ag
	Size	5 mm × 5 mm
	Drying	90 °C, 1 hour
Characterization	Structural analysis	XRD (Rigaku Ultima IV)
	Morphology analysis	FESEM (Thermo Scientific Apreo 2S)
	Elemental analysis	EDX (BRUKER XFLASH 6/100)
	Hydrophilic analysis	WCA (VCA-3000)
	Electrical characterization	• Hall effect (ezHEMS Controller) • Cyclic voltammetry (Autolab)
	Humidity-to-electricity conversion analysis	I–V–t measuring system (Keithley 2400)
Label	S-NG-FP, S-NG-0.5-FP, S-NG-1.0-FP, S-NG-1.5-FP, S-NG-2.0-FP	

3.4 Surface modification of Composite Powder Based on NiO with Gr through SA Treatment

To identify the optimal NG composites with the best hydrophilic properties, the materials were treated with SA under different concentrations, immersion temperatures, and immersion durations. Ethanol (99.8%, Systerm) was used to dissolve SA (95%, Sigma-Aldrich) at varying concentrations ranging from 1 to 4 wt.%. The solution was

then sonicated for 10 minutes. Next, the synthesized NG composites powder was added to the solution, and the mixture was agitated at fixed speed of 300 rpm for different immersion temperatures (i.e., 30°C, 60°C, and 90°C) and immersion durations (i.e., 2, 4, 6, and 8 hours). After the treatment, the treated samples were filtered and left to dry overnight at 36°C in oven (Memmert). The SA treatment procedure is illustrated in Figure 3.4.

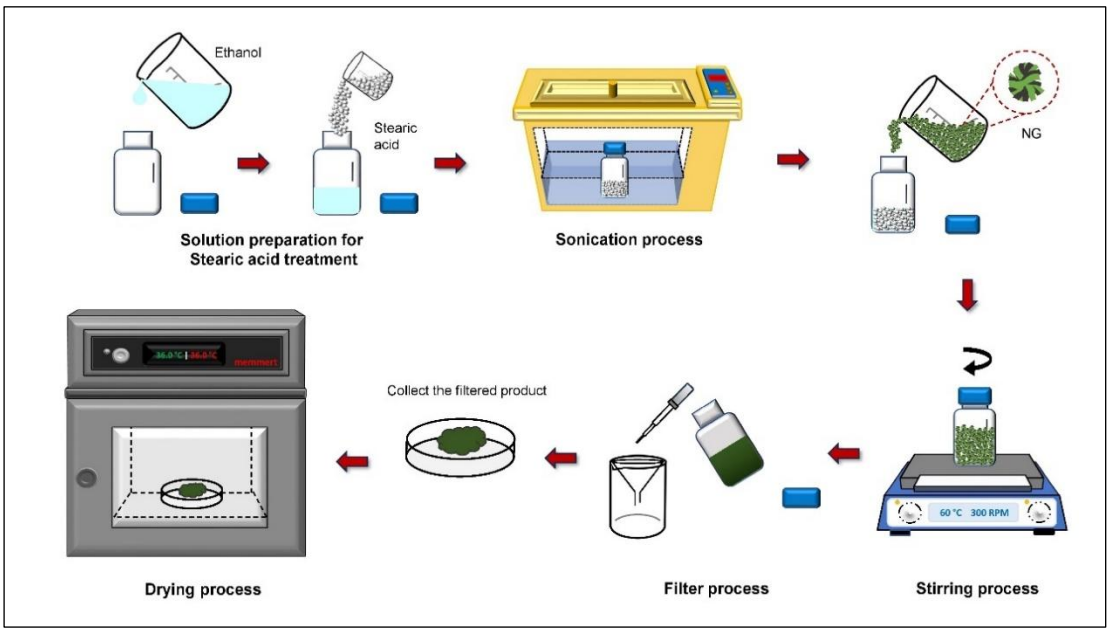

Figure 3.4 SA Treatment Process on NG Composite

3.4.1 SA Treatment at Various Stearic Acid Concentration

SA (95%, Sigma-Aldrich) was dissolved in ethanol (99.8%, Systerm) at varying wt.% ranging from 1 wt.% to 4 wt.%. The solution was then sonicated for 10 minutes. Subsequently, synthesized NG-1.0 composite powders were added to the solution, and the mixture was stirred at fixed speed of 300 rpm for 6 hours at 60°C. After the treatment, the treated sample was filtered and dried at 36°C overnight in oven (Memmert). The SA-treated samples were labelled as S1%-NG-1.0, S2%-NG-1.0, S3%-NG-1.0 and S4%-NG-1.0, whereby the number indicates the respective SA weight percentages. Untreated sample was labelled as U-NG-1.0. The experimental parameter and characterization technique involved are presented in Table 3.3.

Table 3.3
SA Treatment at Various SA Concentration and Characterization Techniques for S-NG Composite Powder

Treatment solution	Ethanol	30 ml

preparation	Stearic acid	1 wt.%, 2 wt.%, 3 wt.%, 4 wt.%.
Sonication process	Time	10 min
	Temperature	RT
SA treatment	Immersion time	6 h
	Immersion temperature	60°C
	Stirring speed	300 rpm
Drying process	Drying temperature	36°C
	Drying time	Overnight
	Ambient	Air
	Structural analysis	• XRD (Rigaku Ultima IV) • FTIR (Perkin Elmer Spectrum One)
	Morphology analysis	FESEM (JEOL JSM-7600F)
	Elemental analysis	EDX (EDAX AMETEK)
	Hydrophilic analysis	WCA (VCA-3000)
	Humidity-to-electricity conversion analysis	I–V–t measuring system (Keithley 2400)
Label	S1%-NG-1.0, S2%-NG-1.0, S3%-NG-1.0 and S4%-NG-1.0	

3.4.2 SA Treatment at Different Immersion Temperature

SA (95%, Sigma-Aldrich) was dissolved in ethanol (99.8%, Systerm) at a concentration of 2 wt.%. The solution was then sonicated for 10 minutes. After the addition of powdered NG-1.0 composite, the mixture was stirred for 6 hours at fixed speed of 300 rpm at 3 different immersion temperatures (i.e., 30°C, 60°C, and 90°C). After the treatment, the treated sample was filtered and dried overnight at 36°C in oven (Memmert). The SA-treated samples were labelled as S30-NG-1.0, S60-NG-2.0 and S90-NG-1.0 whereby the number indicates the respective immersion temperatures. The experimental parameter and characterization technique involved are presented in Table 3.4.

Table 3.4
SA Treatment at Different Immersion Temperature and Characterization Techniques for S-NG Composite Powder

Treatment solution preparation	Ethanol	30 ml
	Stearic acid	2 wt.%
Sonication process	Time	10 min
	Temperature	RT
SA treatment	Immersion time	6 h
	Immersion temperature	30°C, 60°C, 90°C
	Stirring speed	300 rpm
Drying process	Drying temperature	36°C
	Drying time	Overnight
	Ambient	Air
Characterization	Structural analysis	XRD (Rigaku Ultima IV)
	Hydrophilic analysis	WCA (VCA-3000)
	Humidity-to-electricity conversion analysis	I–V–t measuring system (Keithley 2400)
Label	S30-NG-1.0, S60-NG-1.0, S90-NG-1.0	

3.4.3 SA Treatment at Different Immersion Time

SA (95%, Sigma-Aldrich) was dissolved in ethanol (99.8%, Systerm) at a concentration of 2 wt.%. The solution was then sonicated for 10 minutes. After the synthesized NG-1.0 composite powder was added, the mixture was stirred at 60°C for varying immersion durations of 2, 4, 6, and 8 hours at fixed speed of 300 rpm. Following the treatment, the mixture was filtered and dried at 36°C overnight in oven (Memmert). The SA-treated samples were labelled as S2h-NG-1.0, S4h-NG-1.0, S6h-NG-1.0 and S8h-NG-1.0, where the numeral denotes the corresponding immersion duration in hours. The experimental parameter and characterization technique involved are presented in Table 3.5.

Table 3.5
SA Treatment at Different Immersion Time and Characterization Techniques for S-NG Composite Powder

Treatment solution preparation	Ethanol	30 ml
	Stearic acid	2 wt.%
Sonication process	Time	10 min
	Temperature	RT
SA treatment	Immersion time	2 h, 4 h, 6 h, 8 h
	Immersion temperature	60°C
	Stirring speed	300 rpm
Drying process	Drying temperature	36°C
	Drying time	Overnight
	Ambient	Air
Characterization	Structural analysis	XRD (Rigaku Ultima IV)
	Hydrophilic analysis	WCA (VCA-3000)
	Humidity-to-electricity conversion analysis	I–V–t measuring system (Keithley 2400)
Label	S2h-NG-1.0, S4h-NG-1.0, S6h-NG-1.0, S8h-NG-1.0	

3.5 Synthesizing of Composite Powder Based on NiO/Gr and Hematite via Sonicated Solution Immersion Method

To synthesize the SA-treated HNG (S-HNG) composite powder, a straightforward sonicated solution immersion process was employed. Initially, 0.2 M of $Ni(NO_3)_2 \cdot 6H_2O$, 0.2 M of HMT, and 1.0 wt.% of Gr nanoplatelets were mixed in DI water, followed by the addition of 1.0 wt.% of iron (III) nitrate nonahydrate ($Fe(NO_3)_3 \cdot 9H_2O$, ACS reagent, ≥98%, Sigma-Aldrich) to the solution. The resulting mixture was sonicated for 1 hour using a sonication chamber (Hwashin Technology, Powersonic 405), then stirred at 500 rpm for an additional hour to ensure complete mixing. The homogeneous solution was transferred into a 100 mL Schott bottle (Duran), sealed tightly, and placed in an immersion bath (Memmert) at varying temperatures of

75°C, 85°C, and 95°C for 1 hour. After immersion, the resulting precipitates were filtered and dried overnight in oven (Memmert) at 36°C to remove excess water. The dried sample was then annealed in a chamber furnace (Protherm) at 500°C for 1 hour to enhance its crystallinity. Subsequently, all samples were treated with a fixed 2 wt.% SA concentration at 60 °C for an immersion duration of 6 hours. The SA-treated powders were designated as S-H75/NG, S-H85/NG and S-H95/NG, where the numeral denotes the corresponding immersion temperature in °C. The overall procedure is illustrated in Figure 3.5. The experimental parameter and characterization technique involved are presented in Table 3.6.

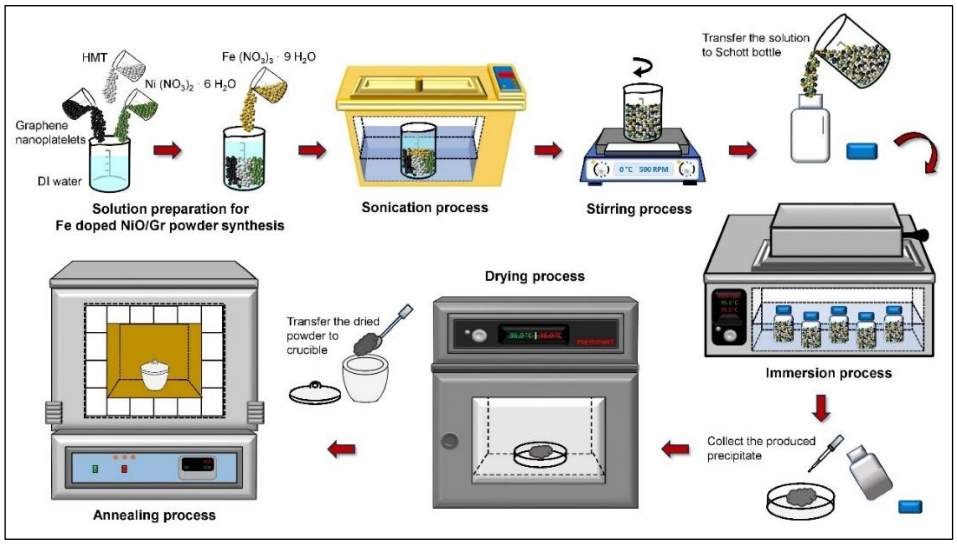

Figure 3.5 Synthesis of the HNG Composites Powder Through the Sonicated Solution Immersion Method

Table 3.6
Synthesis Parameters and Characterization Techniques for S-HNG Composites Powder

Growth solution preparation	Precursor material	• Nickel nitrate hexahydrate ($Ni(NO_3)_2 \cdot 6H_2O$) • Graphene nanoplatelets, 1.0 wt.%
	Additional component	Iron (III) nitrate nonahydrate ($Fe(NO_3)_3 \cdot 9H_2O$), 1.0 wt.%
	Stabilizer	Hexamethylenetetramine, HMT ($C_6H_{12}N_4$)
	Solvent	Deionized water
	Volume	100 mL
	Molar concentration	0.2 M
	Sonicating process	Room temperature (RT), 1 h
	Stirring process	RT, 1 h, 500 rpm
Immersion process	Reaction temperature	75°C, 85°C, 95°C
	Reaction time	1 h
Drying process	Drying temperature	36°C
	Drying time	Overnight
	Ambient	Air

Annealing process	Annealing temperature	500°C
	Annealing time	1 h
	Ambient	Air
Substrate	FP (Whatman Qualitative Grade 1)	
Characterization	Structural analysis	XRD (Rigaku Ultima IV)
	Morphology analysis	• FESEM (Thermo Scientific Apreo 2S) • HRTEM (FEI TECNAI G2 F20 X-TWIN)
	Elemental analysis	EDX (BRUKER XFLASH 6/100)
	Surface area and porosity analysis	BET (Micromeritics TriStar II Plus)
	Chemical composition analysis	XPS (Ulvac-PHI Quantera II)
	Electrical characterization	Hall effect (ezHEMS Controller)
Label	S-HNG, S-H75/NG, S-H85/NG and S-H95/NG	

3.5.1 Preparation of Hematite/NiO/Gr on Cellulose Based Substrate for Humidity Gradient Energy Harvesting Application

S-HNG paste was prepared by dispersing 1 g of S-HNG composite powder in 15 ml of transparent paper glue (Chunbe 6603), which served as a binder. The FP (Whatman Qualitative Grade 1, 110 mm in diameter) was used as the cellulose-based substrate. A homogeneous thin layer of the hygroscopic material was deposited onto FP using the doctor-blade technique, with Kapton tape employed to ensure uniform layer thickness across all samples. The coated FP was then dried on a hot plate at 90 °C for 1 hour. After drying, the S-HNG-coated FP which denoted as S-HNG-FP, was cut into square pieces measuring 15 mm × 15 mm. Subsequently, a commercial Ag conductive paste (Mechanic, MCN-DJ002) was applied to the S-HNG-FP as the working electrode, forming contact areas of 5 mm × 5 mm with a spacing of 5 mm between them. The same procedure was repeated for the S-H75/NG, S-H85/NG and S-H95/NG composite on the cellulose-based substrate. The resulting samples were labelled as S-H95/NG-FP, S-H95/NG-FP and S-H95/NG-FP, respectively, where the numeral denotes the corresponding immersion temperature in °C. The experimental parameter and characterization technique involved are presented in

Table 3.7.

Table 3.7
Synthesis Parameters and Characterization Techniques for S-HNG Composite on Cellulose-Based Substrate

Paste preparation	Composite powder	1 g
	Binder	15 ml, Glue, Chunbe 6603
Substrate	FP (Whatman Qualitative Grade 1)	
Drying	Temperature	90 °C
	Duration	1 hour
	Ambient	Air
Working electrode	Material	Ag

	Size	5 mm × 5 mm
	Drying	90 °C, 1 hour
Characterization	Structural analysis	XRD (Rigaku Ultima IV)
	Morphology analysis	FESEM (Thermo Scientific Apreo 2S)
	Elemental analysis	EDX (BRUKER XFLASH 6/100)
	Hydrophilic analysis	WCA (VCA-3000)
	Surface area and porosity analysis	BET (Micromeritics TriStar II Plus)
	Electrical characterization	• Hall effect (ezHEMS Controller) • Cyclic voltammetry (Autolab)
	Humidity-to-electricity conversion analysis	I–V–t measuring system (Keithley 2400)
Label	S-HNG-FP, S-H75/NG-FP, S-H85/NG-FP, S-H95/NG-FP	

3.5.2 Preparation and Fabrication of Hematite/NiO/Gr on Hydrogel-based FP for Humidity Gradient Energy Harvesting Application

The Co-Zn-based nanoceramic hydrogel film was prepared using the sol-gel method with a 1:1:1 molar ratio of zinc acetate dihydrate ($Zn(CH_3COO)_2 \cdot 2H_2O$, ACS reagent, ≥ 98%, Sigma-Aldrich), cobalt (II) acetate tetrahydrate [$(CH_3COO)_2Co \cdot 4H_2O$, ACS reagent, > 98.0%, Sigma-Aldrich], and ethanolamine (ACS reagent, ≥ 99.0%, Sigma-Aldrich) in anhydrous 2-methoxyethanol (99.8%, Sigma-Aldrich). The solution was stirred at 80°C for 3 hours at 300 rpm and then allowed to age at RT for 24 hours. Commercial Whatman Qualitative Grade 1 FP was subsequently dipped into the gel-like solution for 1 minute and dried at 150°C for 10 minutes. The overall procedure is illustrated in Figure 3.6.

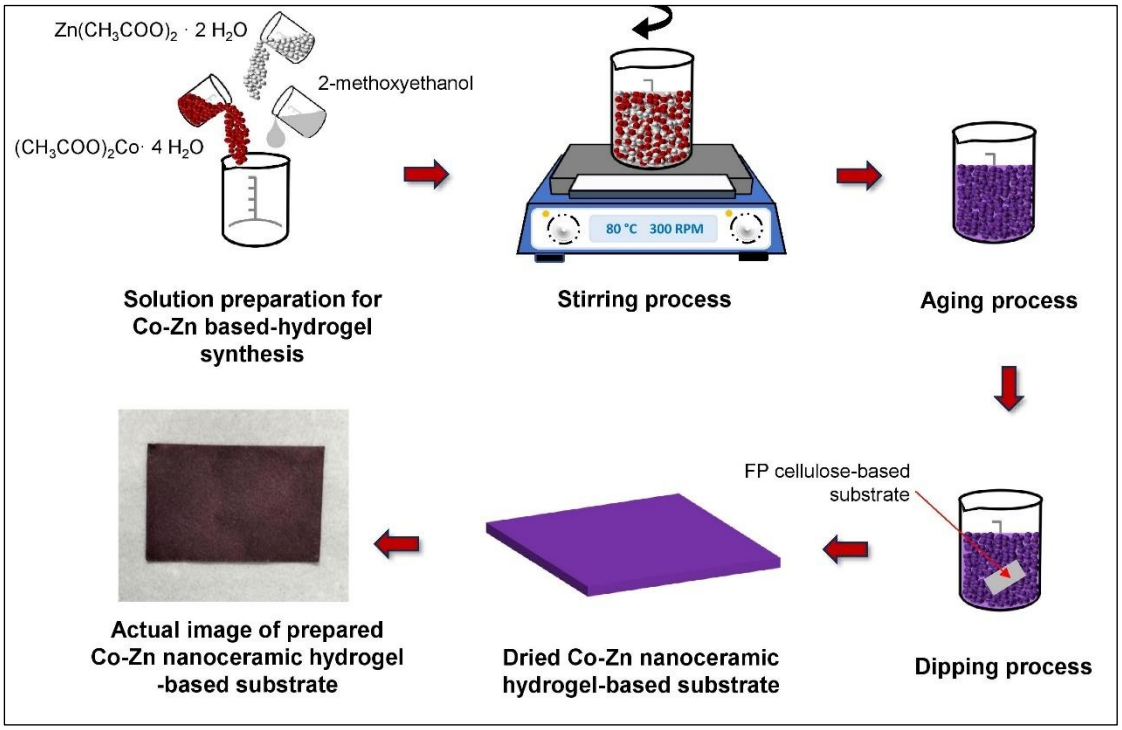

Figure 3.6 Co-Zn-Based Nanoceramic Hydrogel Film via Sol-Gel Method

S-HNG paste was prepared by dispersing 1 g of S-HNG composite powder in 15 ml of transparent paper glue (Chunbe 6603), which served as a binder. A homogeneous thin layer of the hygroscopic material was deposited onto the Co-Zn-based nanoceramic hydrogel film using the doctor-blade technique, with Kapton tape employed to ensure uniform layer thickness across all samples. The coated hydrogel film was then dried on a hot plate at 90 °C for 1 hour. After drying, the HNG-coated hydrogel film which denoted as S-HNG-hydrogel/FP, was cut into square pieces measuring 15 mm × 15 mm. Subsequently, a commercial Ag conductive paste (Mechanic, MCN-DJ002) was applied to the S-HNG-hydrogel/FP as the working electrode, forming contact areas of 5 mm × 5 mm with a spacing of 5 mm between them. The experimental parameter and characterization technique involved are presented in Table 3.8.

Table 3.8
Synthesis Parameters and Characterization Techniques for S-HNG Composite on Hydrogel-Based Film

Sol-gel process	Solution preparation (1:1:1) molar ratio	• Zinc acetate dihydrate, $(Zn(CH_3COO)_2 \cdot 2H_2O)$ • Cobalt (II) acetate tetrahydrate, $[(CH_3COO)_2Co \cdot 4H_2O]$ • Ethanolamine
	Solvent	2-methoxyethanol, 30 ml

	Stirring process	80°C, 3 h, 300 rpm
	Aging process	RT, 24 h
	Dipping process	1 min
	Drying process	150°C for 10 min
Substrate	Co-Zn-based nanoceramic hydrogel-based FP	
Paste preparation	Composite powder	1 g
	Binder	15 ml, Glue, Chunbe 6603
Drying	Temperature	90 °C
	Duration	1 hour
	Ambient	Air
Working electrode	Material	Ag
	Size	5 mm × 5 mm
	Drying	90 °C, 1 hour
Characterization	Structural analysis	XRD (Rigaku Ultima IV)
	Morphology analysis	• FESEM (Thermo Scientific Apreo 2S) • HRTEM (FEI TECNAI G2 F20 X-TWIN)
	Elemental analysis	EDX (BRUKER XFLASH 6/100)
	Hydrophilic analysis	WCA (VCA-3000)
	Surface area and porosity analysis	BET (Micromeritics TriStar II Plus)
	Electrical characterization	Hall effect (ezHEMS Controller)
	Humidity-to-electricity conversion analysis	I–V–t measuring system (Keithley 2400)
Label	S-HNG-hydrogel/FP	

3.5.3 Preparation and Fabrication of Hematite/NiO/Gr on Hydrogel-based RP for Humidity Gradient Energy Harvesting Application

A straightforward procedure was employed to prepare RP. First, used paper was shredded into small pieces and blended with water until a mushy pulp was formed. The resulting pulp was transferred into a container. A separate basin was filled halfway with water, into which the pulp was added and mixed thoroughly. A mould and deckle were then immersed into the mixture and lifted, allowing a thin layer of pulp to settle on the mould. This pulp layer was then transferred onto a sheet of towel by flipping the mould, and a sponge was used to absorb excess moisture. The pulp sheet was then left to dry naturally. The overall process is illustrated in Figure 3.7 and the supplementary video (V 1) in the APPENDIX 1.

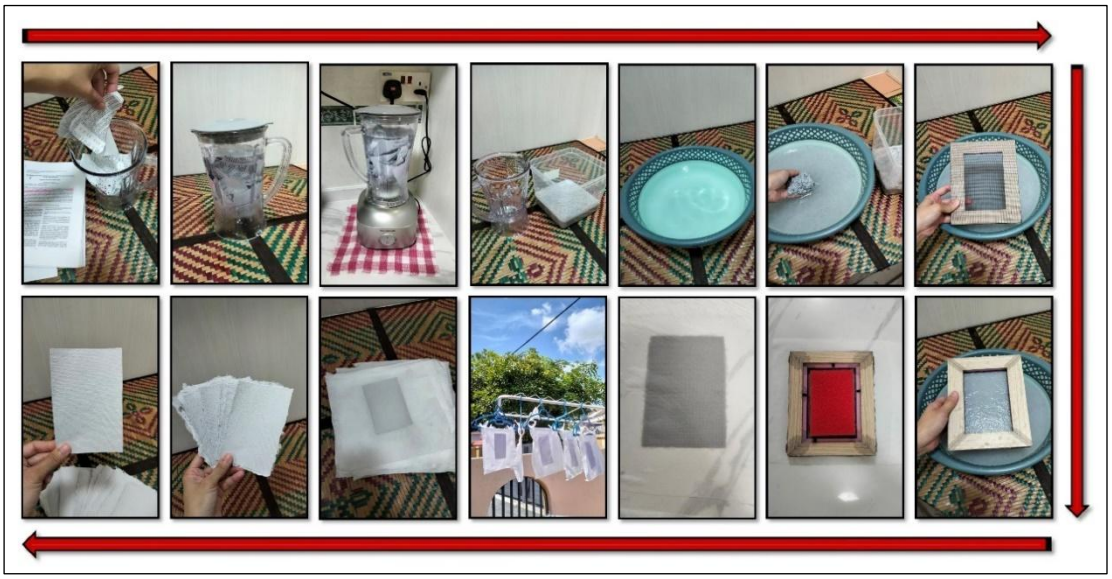

Figure 3.7 Overall Process of Preparing RP from Scratch using Unused Printing Paper

The resulting RP was subsequently immersed in a Co-Zn-based gel-like solution for 1 minute and then dried at 150 °C for 10 minutes. The final product was denoted as hydrogel/RP. A S-HNG paste was prepared by dispersing 1 g of S-HNG composite powder in 15 mL of transparent paper glue (Chunbe 6603), which acted as a binder. A homogeneous thin layer of the hygroscopic material was deposited onto the hydrogel/RP using the doctor-blade technique, with Kapton tape employed to ensure uniform layer thickness across all samples. The coated hydrogel/RP was then dried on a hot plate at 90 °C for 1 hour. After drying, the S-HNG-coated hydrogel/RP which denoted as S-HNG-hydrogel/RP, was cut into square pieces measuring 15 mm × 15 mm. Subsequently, a commercial Ag conductive paste (Mechanic, MCN-DJ002) was applied to the S-HNG-hydrogel/RP as the working electrode, forming contact areas of 5 mm × 5 mm with a spacing of 5 mm between them. The experimental parameters and characterization techniques employed are summarized in Table 3.9.

Table 3.9
Synthesis Parameters and Characterization Techniques for S-HNG Composite on Hydrogel/RP Film

Paste preparation	Composite powder	1 g
	Binder	15 ml, Glue, Chunbe 6603
Substrate	Co-Zn-based nanoceramic hydrogel film-based RP	
Drying	Temperature	90 °C
	Duration	1 hour
	Ambient	Air
Working electrode	Material	Ag
	Size	5 mm × 5 mm
	Drying	90 °C, 1 hour

Characterization	Structural analysis	XRD (Rigaku Ultima IV)
	Morphology analysis	FESEM (Thermo Scientific Apreo 2S)
	Elemental analysis	EDX (BRUKER XFLASH 6/100)
	Hydrophilic analysis	WCA (VCA-3000)
	Surface area and porosity analysis	BET (Micromeritics TriStar II Plus)
	Electrical characterization	Hall effect (ezHEMS Controller)
	Humidity-to-electricity conversion analysis	I–V–t measuring system (Keithley 2400)
Label	S-HNG-hydrogel/RP	

3.6 Preparation and Fabrication of Hematite/NiO/Gr on Hydrogel-based Cellulose Substrate for Piezoelectric Coefficient Measurement

A thin layer of S-HNG paste was deposited onto the Co-Zn nanoceramic hydrogel/FP substrate using the doctor-blade technique to fabricate a square-shaped PENG device measuring 15 mm × 15 mm. After deposition, the sample was dried on a hot plate at 90 °C for 1 hour. Commercial Ag paste was then applied to both the top surfaces of the film to form the working electrodes, each with dimensions of 5 mm × 5 mm, as illustrated in Figure 3.8. The same procedure was repeated for the PENG fabrication of the S-HNG-hydrogel/RP. The experimental parameters and characterization techniques employed are summarized in Table 3.10.

Table 3.10
Synthesis Parameters and Characterization Techniques for S-HNG Composite on Hydrogel-Based Cellulose Substrate for Piezoelectric Coefficient Measurement

Growth solution preparation	Precursor material	• Nickel nitrate hexahydrate ($Ni(NO_3)_2 \cdot 6H_2O$) • Graphene nanoplatelets, 1.0 wt.% • Iron (III) nitrate nonahydrate ($Fe(NO_3)_3 \cdot 9H_2O$), 1.0 wt.%
	Stabilizer	Hexamethylenetetramine, HMT ($C_6H_{12}N_4$)
	Solvent	Deionized water
	Volume	100 mL
	Molar concentration	0.2 M
	Sonicating process	RT, 1 h
	Stirring process	RT, 1 h, 500 rpm
Immersion process	Reaction temperature	75°C, 85°C, 95°C
	Reaction time	1 h
Drying process	Drying temperature	36°C
	Drying time	Overnight
	Ambient	Air
Annealing process	Annealing temperature	500°C
	Annealing time	1 h
	Ambient	Air
Sol-gel process	Solution preparation (1:1:1) molar ratio	• Zinc acetate dihydrate, ($Zn(CH_3COO)_2 \cdot 2H_2O$) • Cobalt (II) acetate tetrahydrate, [$(CH_3COO)_2Co \cdot 4H_2O$] • Ethanolamine
	Solvent	2-methoxyethanol, 30 ml
	Stirring process	80°C, 3 h, 300 rpm

	Aging process	RT, 24 h
	Dipping process	1 min
	Drying process	150°C for 10 min
	Substrate	• FP (Whatman Qualitative Grade 1) • RP
Characterization	Piezoelectric coefficient analysis	Piezometer (YE2730A, APC International Ltd.)
	Nanogenerator performance testing analysis	Oscilloscope (Keysight InfiniiVision DSOX2022A)
	Humidity-to-electricity conversion analysis	I–V–t measuring system (Keithley 2400)
Label	S-HNG-hydrogel/FP-based PENG, S-HNG-hydrogel/RP-based PENG	

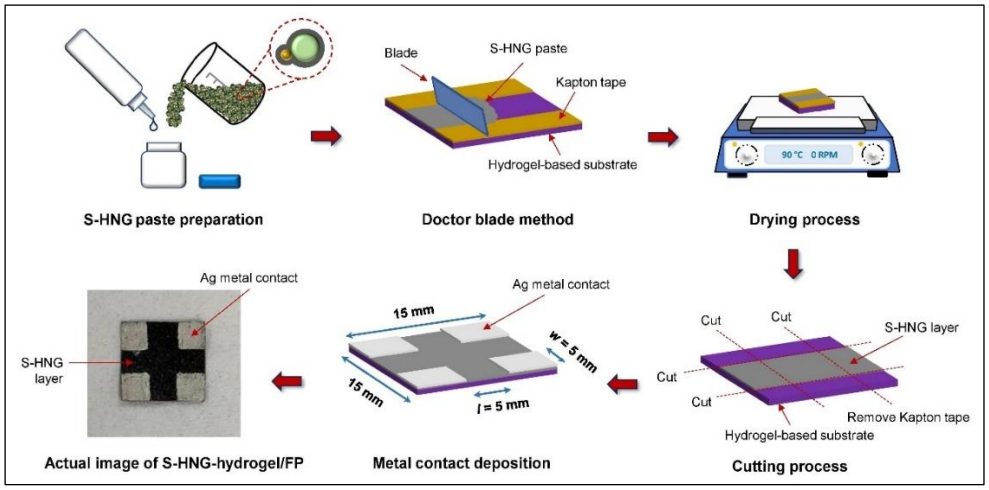

Figure 3.8 Fabrication Process and the Image of the HGPG Device Based on S-HNG-Hydrogel/FP Through the Doctor-Blade Technique

3.7 HGPG and PENG Device Configurations

In this study, the developed HGPG and PENG devices employ a planar electrode configuration, which is relatively rare in energy harvesting system. In a typical planar architecture, the working electrodes are arranged on the same plane and positioned side by side. As illustrated in Figure 3.9, the device consists of three key components: the working electrodes, the composite material, and the substrate. Notably, both the HGPG and PENG utilize the exact same fabricated device configuration, including the composite materials, substrate type, and electrode layout.

Table 3.11
List of Fabricated S-HNG-Hydrogel/FP and S-HNG-Hydrogel/RP Along with Their Respective Code Names

Conditions	**Description of fabricated HGPG and PENG**	**Code name**
Pistine NiO	SA-treated pristine NiO	S-PN
Different Gr loading	SA-treated NG with 0.5 wt.% Gr loading	S-NG -0.5
	SA-treated NG with 1.0 wt.% Gr loading	S-NG-1.0
	SA-treated NG with 1.5 wt.% Gr loading	S-NG-1.5

	SA-treated NG with 2.0 wt.% Gr loading	S-NG-2.0
	SA-treated NG with 0.5 wt.% Gr loading on FP	S-NG-FP
	SA-treated NG with 0.5 wt.% Gr loading on FP	S-NG-0.5-FP
	SA-treated NG with 1.0 wt.% Gr loading on FP	S-NG-1.0-FP
	SA-treated NG with 1.5 wt.% Gr loading on FP	S-NG-1.5-FP
	SA-treated NG with 2.0 wt.% Gr loading on FP	S-NG-2.0-FP
SA treatment with different SA content, treated at 60°C for 6 hours	Untreated NG with 1.0 wt.% Gr loading	U-NG-1.0
	NG with 1.0 wt.% Gr loading treated with 1 wt% SA	S1%-NG-1.0
	NG with 1.0 wt.% Gr loading treated with 2 wt% SA	S2%-NG-1.0
	NG with 1.0 wt.% Gr loading treated with 3 wt% SA	S3%-NG-1.0
	NG with 1.0 wt.% Gr loading treated with 4 wt% SA	S4%-NG-1.0
SA treatment with 2 wt.% SA, treated for 6 hours at different immersion temperature	NG with 1.0 wt.% Gr loading treated at RT	SRT-NG-1.0
	NG with 1.0 wt.% Gr loading treated at 30°C	S30-NG-1.0
	NG with 1.0 wt.% Gr loading treated at 60°C	S60-NG-1.0
	NG with 1.0 wt.% Gr loading treated at 90°C	S90-NG-1.0
SA treatment with 2 wt.% SA, treated at 30°C for different immersion duration	NG with 1.0 wt.% Gr loading treated at for 2 hours	S2h-NG-1.0
	NG with 1.0 wt.% Gr loading treated at for 4 hours	S4h-NG-1.0
	NG with 1.0 wt.% Gr loading treated at for 6 hours	S6h-NG-1.0
	NG with 1.0 wt.% Gr loading treated at for 8 hours	S8h-NG-1.0
Introduction of hematite in NG and different synthesis temperature	HNG with 1.0 wt.% Gr loading synthesized at 75°C	S-HNG
	HNG with 1.0 wt.% Gr loading synthesized at 75°C	S-H75/NG
	HNG with 1.0 wt.% Gr loading synthesized at 85°C	S-H85/NG
	HNG with 1.0 wt.% Gr loading synthesized at 95°C	S-H95/NG
	HNG with 1.0 wt.% Gr loading synthesized at 75°C on FP	S-HNG-FP
	HNG with 1.0 wt.% Gr loading synthesized at 75°C on FP	S-H75/NG-FP
	HNG with 1.0 wt.% Gr loading synthesized at 85°C on FP	S-H85/NG-FP
	HNG with 1.0 wt.% Gr loading synthesized at 95°C on FP	S-H95/NG-FP
Integration with hydrogel for HGPG and PENG devices	HNG with 1.0 wt.% Gr loading synthesized at 95°C on hydrogel/FP	S-HNG-hydrogel/FP
	HNG with 1.0 wt.% Gr loading synthesized at 95°C on hydrogel/RP	S-HNG-hydrogel/RP

Ag conductive paste was employed as the working electrode, while S-HNG was utilized as the composite active layer, serving dually as a hygroscopic material for the HGPG and a piezoelectric material for the PENG. The primary substrate was a cellulose-based FP, specifically standard, commercially available Whatman Qualitative Grade 1 (110 mm diameter). To promote innovation and sustainability, RP was introduced as an alternative to FP. The RP was produced entirely from unused printing paper via a simple, home-based preparation method. Both cellulose-based substrates (FP and RP) were subsequently integrated with a Co–Zn hydrogel to enhance water molecule uptake. The final HGPG and PENG devices were fabricated with dimensions of 5 × 5 mm^2, with a 5 mm separation between electrodes. Table 3.11 provides a summary of the fabricated HGPG and PENG configurations along with their corresponding sample codes for reference.

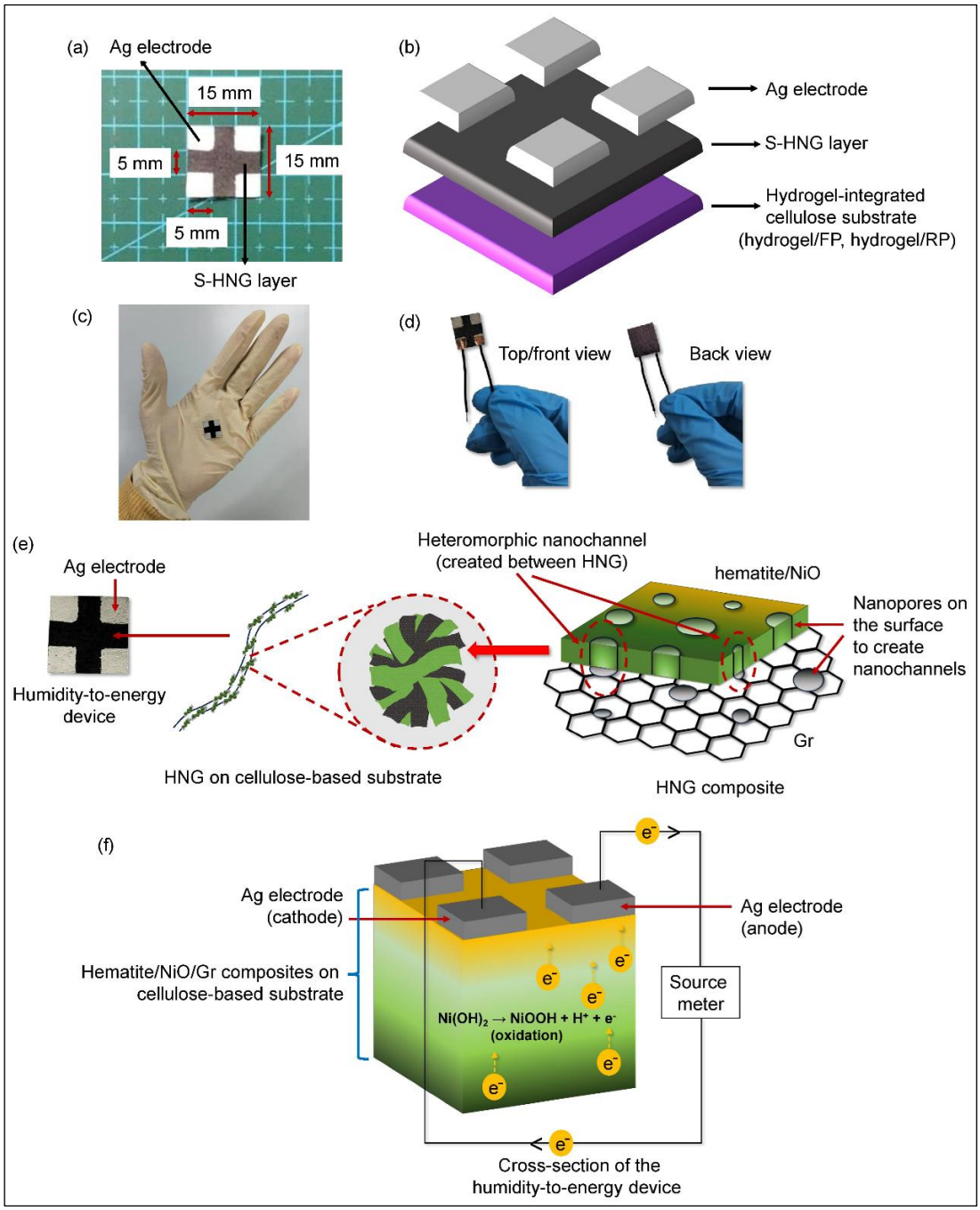

Figure 3.9 (a) Dimensions and (b) Detailed Illustration of the Fabrication Process for S-HNG-Hydrogel/FP- and S-HNG-Hydrogel/RP-Based HGPG and PENG Devices. (c) Actual Photograph of the Fabricated HGPG and PENG Devices Compared to a Human Palm. (d) Top/Front and Back Views of the Fabricated HGPG and PENG Devices. (e) Formation of Heteromorphic Nanochannels between Synthesized HNG. (f) Schematic Device Structure of Surface Reactions during Humidity Conversion that Enable Electricity Generation via the Developed Hygroscopic Materials

3.8 Characterization Techniques

The developed and synthesized materials were comprehensively characterized using a suite of advanced analytical techniques. The crystallographic structure and phase evolution were examined via X-ray diffraction (XRD), while elemental composition and morphological/atomic features were investigated using field emission scanning electron microscopy (FESEM), scanning electron microscopy (SEM) coupled with energy-dispersive X-ray spectroscopy (EDX), and high-resolution transmission electron microscopy (HRTEM). Raman spectroscopy was employed to study the vibrational modes of molecules, providing insights into the chemical bonding, composition, and related characteristics of the materials.

Composition of surface chemical species in the samples was further analyzed using X-ray photoelectron spectroscopy (XPS). Water contact angle (WCA) measurements were performed using a wafer surface analysis system to assess the surface wettability of the samples. Functional group identification was carried out by Fourier transform infrared spectroscopy (FTIR) on untreated and SA-treated samples. Meanwhile, the specific surface area of the materials was determined using the Brunauer-Emmett-Teller (BET) method. Cyclic voltammetry (CV) analysis was conducted to examine the redox behaviour of the samples. Electrical conductivity and the Hall coefficient were measured using the Van der Pauw method with a Hall measurement system. To further assess the device's response to humidity, measurements were conducted at controlled temperatures in a bench-top temperature and humidity chamber, equipped with a current–voltage–time (I–V–t) measurement system. The piezoelectric properties of the prepared samples were evaluated using a d_{33} tester by measuring the d_{33} constant.

The synthesized pristine NiO, NG, and HNG composites including SA-treated composite films and those integrated with various substrates such as FP cellulose-based substrate, Co-Zn-based nanoceramic hydrogel films, and RP cellulose-based substrate were comprehensively studied to understand their properties and how they influence the performance of the HGPG and PENG devices.

3.8.1 Structural and Morphological Analysis

3.8.1.1 XRD Analysis

In this study, XRD analysis was carried out using a Rigaku Ultima IV system to examine all synthesized samples, including S-PN, S-NG, and S-HNG composites. This also included those integrated with various substrates such as FP cellulose-based substrate, Co-Zn-based nanoceramic hydrogel films, and RP cellulose-based substrate. To assess the crystallinity of the materials, XRD measurements were performed in both powder and film modes using a Cu-Kα radiation source with a wavelength of 1.541 Å, covering a 2θ range from 5°/20° to 90°. The unique diffraction patterns obtained were used to identify the material phases.

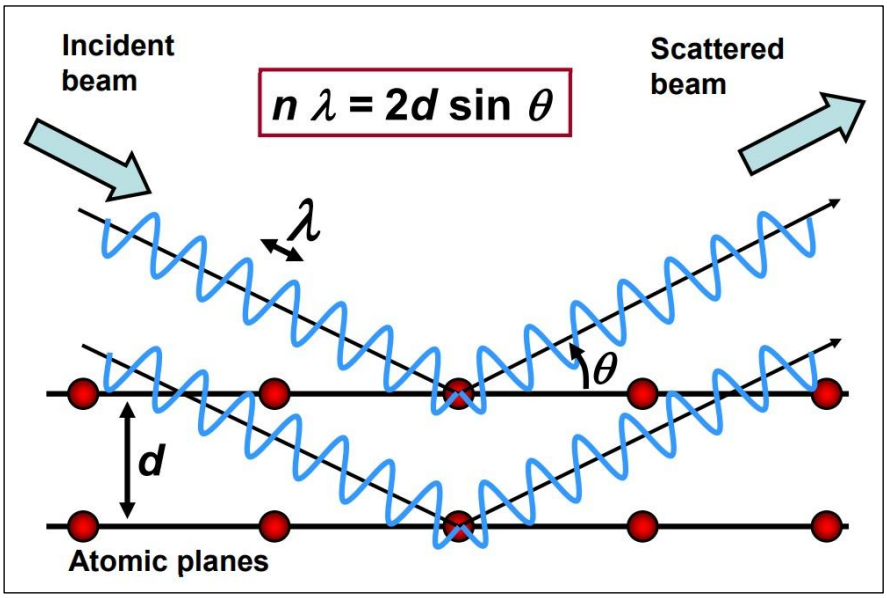

Figure 3.10 Principle of XRD. Reproduced Permission from Reference [231].

XRD characterization is crucial for identifying materials by determining their crystalline phases and orientations, as well as classifying their atomic-scale structure as crystalline, polycrystalline, or amorphous. The structure of the materials was determined by comparing the measured diffraction data with standard reference patterns from the internationally recognized Joint Committee on Powder Diffraction Standards (JCPDS) database.

The following JCPDS reference patterns were used in this study: NiO (JCPDS No. 01-071-4750), nickel (Ni) (JCPDS No. 00-004-0850), graphite (JCPDS No. 00-041-1487), hematite (JCPDS No. 00-033-0664), magnetite (JCPDS No. 01-073-9877), cellulose (JCPDS No. 00-056-1718) and SA (JCPDS No. 00-038-1923) as listed in APPENDIX 2. Figure 3.10 shows the basic principle of XRD. From the XRD data, important structural parameters such as lattice parameters, interplanar spacing, and D were calculated to provide further insight into the material properties.

The crystallite size (D) of all synthesized materials was calculated using the Debye-Scherrer formula [232, 233]:

$$D = \frac{K\lambda}{\beta\, cos\theta} \tag{3.1}$$

In this equation, D refers to the crystallite size, K is a constant which is commonly taken as 0.9, λ is the X-ray wavelength (1.541 Å), θ is the diffraction angle, and β is the full width at half maximum (FWHM) of the diffraction peak, which reflects broadening associated with the crystallite dimensions. To further analyze the structural characteristics of the materials, lattice parameters (a), interplanar spacing (d), and unit cell volume (V) were calculated. These calculations were based on Bragg's law equations:

$$a = d\sqrt{h^2 + k^2 + l^2} \tag{3.2}$$

$$d = \frac{n\lambda}{2\sin\theta} \tag{3.3}$$

$$V = a^2 \tag{3.4}$$

In these calculations, h, k, and l denote the Miller indices, λ is the X-ray wavelength, θ is the diffraction angle, and n is the order of diffraction, typically taken as 1.

3.8.1.2 FESEM analysis

The synthesized pristine NiO, NG, and HNG composites including SA-treated composite films and those integrated with various substrates such as FP cellulose-based substrate, Co-Zn-based nanoceramic hydrogel films, and RP cellulose-based substrate were examined for their surface morphology using FESEM. As illustrated in Figure 3.11, FESEM uses a field emission electron source, also known as a cold cathode field emitter. This technique generates electrons by applying a strong electric field between the anode and cathode, without relying on thermal energy. The filament is placed within a high electric potential gradient, allowing for the emission of a focused, high-brightness electron beam. The emitted electron beam interacts with the sample's surface, and the resulting signals contain information about the material's surface morphology, crystalline structure, orientation, and chemical composition. Due to the sharp tip of the field emitter, FESEM provides significantly higher resolution and greater magnification compared to conventional SEM. This allows for the detailed observation of surface features and the clear identification of closely spaced nanoparticles or structural details [234, 235].

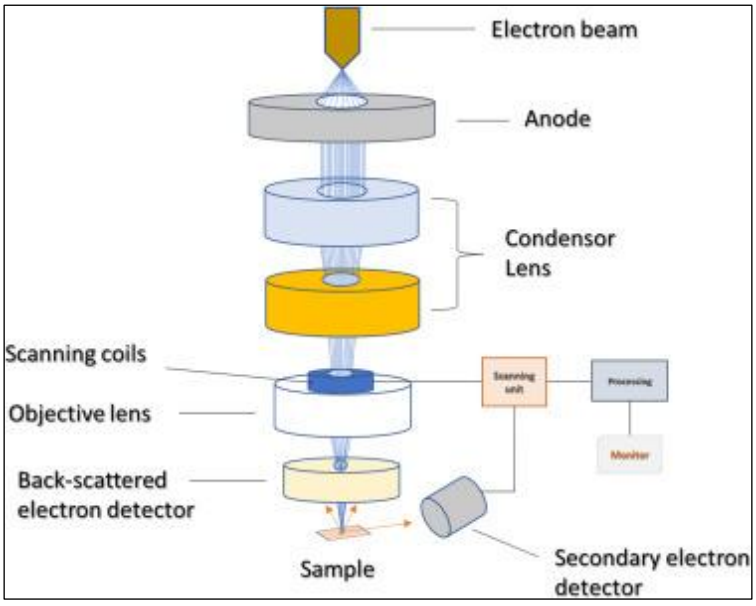

Figure 3.11 Schematic Representation of FESEM [236]

FESEM imaging was conducted using the Thermo Scientific Apreo 2S (Faculty of Applied Sciences, UiTM Shah Alam) and the JEOL JSM-7600F (NANO-Electronic Centre, Faculty of Electrical Engineering, UiTM Shah Alam). Prior to FESEM

characterization, samples were coated with either gold (Au) or Pt to minimize surface charging during imaging. Au coating was performed using a Bal-Tec SCD005 sputter coater (Faculty of Applied Sciences, UiTM Shah Alam), while Pt coating was applied using JEOL JFC-1600 auto fine coater (NANO-Electronic Centre, Faculty of Electrical Engineering, UiTM Shah Alam).

The acquired FESEM images were analyzed using ImageJ, an open-source image processing software. Each image was first calibrated using a known scale reference. Following scale calibration, all visible particles within the selected images were measured and analyzed. The average particle size was then calculated based on the mean of the measured particle sizes.

3.8.1.3 HRTEM analysis

HRTEM enables imaging of a sample's crystallographic structure down to the atomic level [237]. Due to its extremely high resolution, HRTEM is an ideal tool for investigating material properties at the nanoscale. It allows for the visualization of individual atoms, crystal structures, and crystal defects. Additionally, Selected Area Electron Diffraction (SAED) in TEM/HRTEM mode is commonly used to identify crystal structures and measure lattice parameters [238]. In this study, HRTEM analysis was performed using a FEI TECNAI G2 F20 X-TWIN microscope operated at 200 keV and equipped with a Gatan Orius SC1000B camera. Prior to structural analysis, the synthesized materials were dispersed and sonicated in ethanol to form colloidal solutions, which were then drop-cast and dried onto carbon-coated copper grids. To investigate the crystal structures and analyze the SAED patterns, the acquired HRTEM images were further processed using ImageJ software.

3.8.1.4 Molecular Vibrational Spectroscopy Analysis

Raman spectroscopy provides information about a molecule's vibrational energy levels [239]. This technique is widely used to determine the chemical bonding, molecular conformation, and intermolecular interactions of materials. It is a non-destructive analytical method suitable for identifying the phase composition of nanomaterials. A typical Raman system comprises a monochromator, detector, optical filter, sample cell, and laser light source, as illustrated in Figure 3.12. Among these

components, the laser light source is crucial, as it emits the laser beam that interacts with the sample via a fiber optic cable. The performance of the laser system in Raman spectrometers is primarily influenced by three parameters: the type of laser source, laser wavelength, and laser spot size [240].

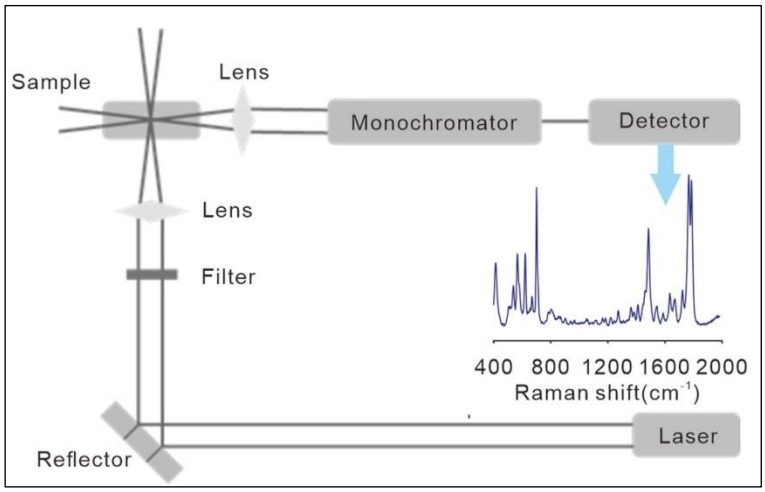

Figure 3.12 Diagram of a Typical Raman Spectrometer. Reproduced with Permission from Reference [240]

When the laser beam strikes the sample, it induces transitions in the vibrational energy levels of the molecules. The molecule momentarily enters a higher energy (virtual) state and then returns to a lower energy state by emitting photons [240]. Most of these scattered photons undergo only a change in their direction of propagation without transferring energy to the molecule. This phenomenon is known as Rayleigh scattering or elastic scattering, and it does not provide significant chemical information. However, a small fraction of the scattered photons interacts inelastically with the sample, transferring or gaining vibrational energy in the process. This is referred to as Raman scattering as illustrated in Figure 3.13(a). In this interaction, if the scattered photons have lower energy than the incident light, the process is termed Stokes scattering. Conversely, if they have higher energy, it is termed anti-Stokes scattering. These processes are depicted in Figure 3.13 (b).

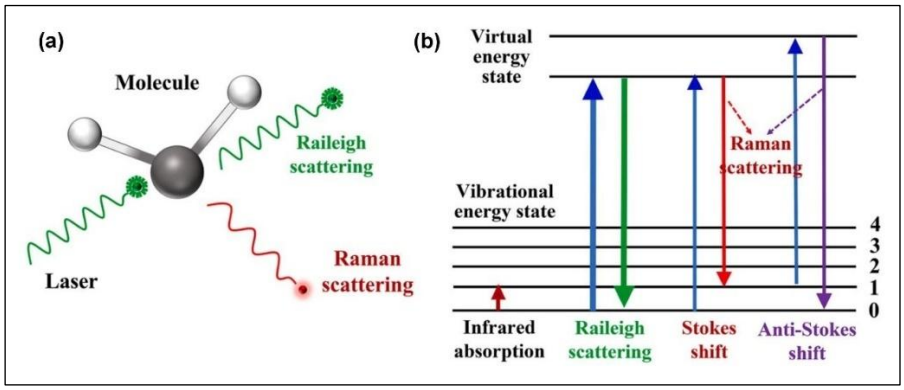

Figure 3.13 Schematic Diagram of Raman Spectroscopy Principles: (a) Light Scattering Modes of Molecules and (b) Energy-Level States Involved in Raman Spectra. Reproduced with Permission from Reference [241]. Copyright 2023, Elsevier.

In general, a Raman spectrum serves as a unique chemical fingerprint of a molecule or substance, enabling rapid identification or differentiation from other materials. The spectrum consists of multiple peaks, each representing the wavelength position and intensity of the Raman-scattered light. Each peak corresponds to a specific molecular bond vibration such as C−C, C=C, N−O, or C−H bonds as well as to collective vibrational modes, such as the breathing mode of a benzene ring, polymer chain vibrations, lattice modes, and other relevant structural features. These vibrational signatures provide valuable insights into the molecular composition and structural characteristics of the analyzed material. In this study, the Horiba Scientific Xplora Plus Raman spectrometer measuring system was used to perform the vibrational analysis at the Microelectronics and Nanotechnology-Shamsuddin Research Centre (MiNT-SRC), Universiti Tun Hussein Onn Malaysia.

3.8.2 Elemental, Chemical and Surface Analysis

3.8.2.1 EDX Analysis

EDX was employed to perform qualitative and quantitative elemental analysis, elemental distribution mapping, and chemical state assessments of the catalyst [242]. The EDX detector is commonly integrated into both SEM and TEM systems, enabling high-energy measurements. Basically, when high-energy electrons bombard the sample surface, they eject inner-shell electrons, creating vacancies. The transition of electrons from higher to lower energy levels to fill these vacancies results in the emission of characteristic X-ray photons, which are detected by the EDX system. These emitted X-

rays are specific to the elements present in the sample and can be presented in the form of elemental maps or spectra [243]. The EDAX AMETEK instrument (Faculty of Mechanical Engineering, UiTM Shah Alam) and BRUKER XFLASH 6/100 (Faculty of Applied Sciences, UiTM Shah Alam) were utilized in this investigation.

3.8.2.2 XPS Analysis

XPS was employed in this study as a surface analysis technique to determine the chemical composition of the developed samples. The XPS analysis was carried out at MIMOS Berhad and the Centre for Instrumentation using the Ulvac-PHI Quantera II. XPS is commonly used to ascertain the stoichiometry and ionic states of elements [244]. As shown in Figure 3.14, this technique involves irradiating the sample surface with X-ray photons under vacuum conditions which also known as photoemission process, causing the emission of electrons from the inner atomic orbitals. The binding energy of these emitted electrons is specific to the elements from which they originate. By analyzing the resulting energy spectrum of the photoelectrons, the elemental composition and concentration at the sample surface can be determined.

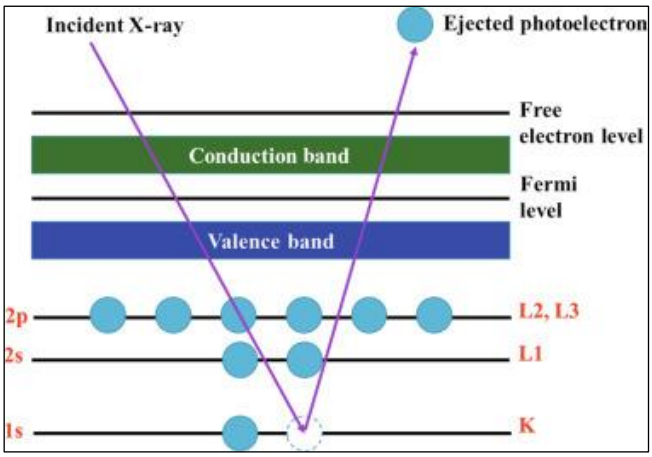

Figure 3.14 Schematic of the Photoemission Process [245]

3.8.2.3 WCA Analysis

One approach to determine surface wettability is by estimating the surface energy through the analysis of WCA measurements. A tangent was drawn at the base of a water droplet placed on the surface of the sample to determine the θ_{CA} of water. In this study, a 3 µL drop of DI water was deposited onto the surface of the fabricated

hygroscopic material films to evaluate their wettability. Each sample was measured multiple times, and the average value was reported as the final WCA.

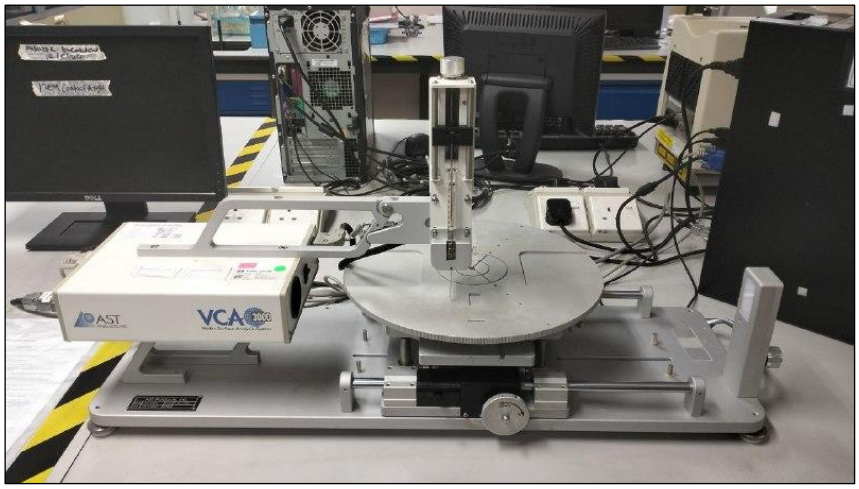

Figure 3.15 WCA Measurement Instrument: VCA-3000

Based on the WCA measurements, the surface energy of the samples was calculated using the FGG-Young's equation [Equation (2.8)], as previously described. In this equation, the surface tension of the liquid γ_l is approximately 72.8 mJ/m^2, corresponding to the DI water used in this study. The WCA measurements were conducted using a VCA-3000 instrument (AST Products, Inc.) at the Faculty of Chemical Engineering, UiTM Shah Alam, as shown in Figure 3.15

3.8.2.4 FTIR Analysis

FTIR is an absorption-based technique that measures the energy of molecular vibrations when a sample is exposed to infrared light [246]. In brief, an absorbance spectrum is produced when a continuous infrared light beam passes through the sample and is absorbed by target molecules at specific wavenumbers corresponding to the energy difference between molecular vibrational states, as shown in Figure 3.16. FTIR spectroscopy can detect the internal molecular structure of a material, as the functional groups and chemical bonds are constantly in a state of vibration [247]. The distinctive absorption bands observed in the resulting spectra serve as the chemical fingerprint of the sample. In this study, the FTIR analysis was conducted at the Faculty of Chemical Engineering, UiTM Shah Alam using a Frontier FTIR spectrometer (Perkin Elmer Spectrum One) to identify compounds and analyze the molecular structure of the

prepared hygroscopic materials, specifically to compare samples with and without SA treatment.

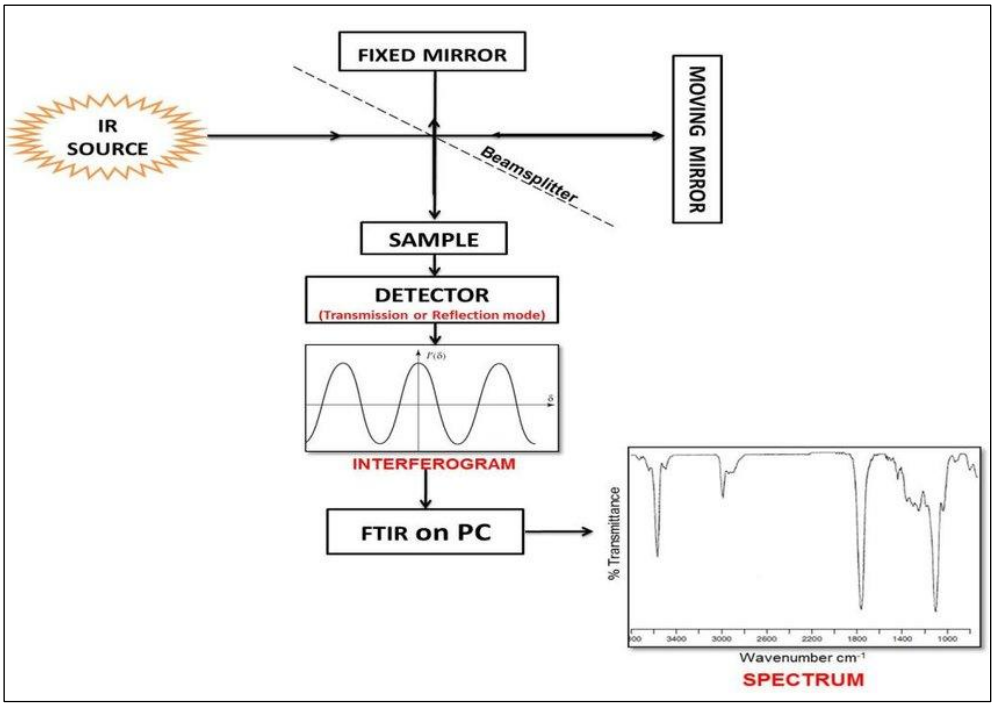

Figure 3.16 Brief Mechanism of FTIR for Detection [248]

3.8.2.5 BET Analysis

The porosity and specific surface area of microporous and mesoporous materials are commonly determined using the BET method, based on nitrogen adsorption isotherm studies [249]. These two parameters are crucial in HGPG applications, as they reveal the material's structural characteristics and may also indicate potential zones for foulant accumulation. The quantity and size distribution of pores influence not only the material's permeability but also its hydrophilicity [250]. Additionally, pore volume and pore size distribution can be obtained using the Barrett-Joyner-Halenda (BJH) method, which is applied to the desorption data derived from BET analysis [251].

In this study, BET analysis was carried out at the Faculty of Applied Sciences, UiTM Shah Alam, using a Micromeritics TriStar II Plus instrument and at the Institute of Nanoscience and Nanotechnology, Universiti Putra Malaysia, using a Micromeritics ASAP 2060 system, as depicted in Figure 3.17.

Figure 3.17 BET Instrument: Micromeritics ASAP 2060 System

3.8.3 Electrical Analysis

3.8.3.1 CV analysis

CV is a common and effective electrochemical technique that measures the current response to a linearly scanned potential [252]. From CV analysis, valuable information can be obtained, such as the electron transfer rate, diffusion coefficient, redox potential, and the amount of adsorbed species on the electrode surface [253]. Analyzing the shape and features of the resulting voltammogram is essential for understanding the electrochemical behaviour of the materials under investigation. Typically, CV curve shapes can be classified into three general types such as rectangular, rounded, or quasi-rectangular, which often accompanied by broad or distinct redox peaks. The shape of the CV curve varies depending on the charge storage mechanism involved, such as pseudo-capacitors or Faradaic (battery-like) systems.

Figure 3.18 illustrates a CV curve characteristic of a typical redox process. The presence and symmetry of redox peaks provide insights into the reversibility of the redox couple and the kinetics of electron transfer. The standard rate constant for electron transfer can be qualitatively inferred from the potential separation (Δ_{Ep}) between the oxidation and reduction peaks. In pseudo-capacitors, the shape of the CV curve typically denotes redox or Faradaic processes taking place at or close to the electrode surface. In contrast, discrete redox peaks are typically observed in Faradaic (battery-

like) systems, where charge storage entails electron transfer coupled with redox processes within the electrode material.

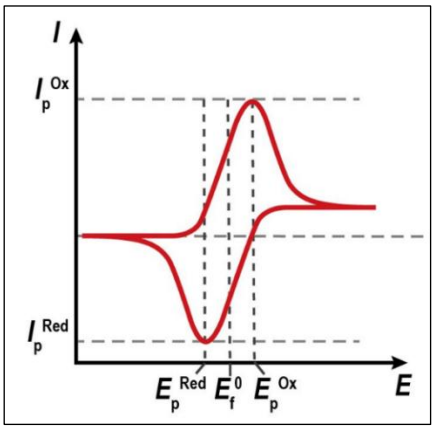

Figure 3.18 Typical Redox CV Curve Characteristic. Reproduce from Reference [254]

The charge stored is related to the area under the redox peaks. Faraday's law is fundamental for quantifying the electrochemical response in CV. The total charge (Q) involved in the redox process is given by:

$$Q = n \times F \tag{3.5}$$

In this equation, n is the number of electrons transferred, and F is the Faraday constant (96,485 C/mol). This relationship aids in evaluating the electrochemical activity of the developed materials.

Figure 3.19 CV Instrument: Autolab

In this study, CV analysis was primarily conducted to investigate the presence of redox activity in the developed material within the system. The analysis was

performed at the Faculty of Applied Sciences, UiTM Shah Alam, using an Autolab CV instrument, as shown in Figure 3.19. The potential was scanned from -1 V to 1 V at a scan rate of 0.1 V/s.

3.8.3.2 Hall Effect Analysis

The Hall effect is a phenomenon in which a Hall voltage is generated across a semiconductor when an electric current flows through it and a magnetic field is applied perpendicular to both the current and the voltage [255]. This voltage arises from the formation of an electric field due to the magnetic force that pushes charge carriers to one side of the semiconductor, resulting in charge imbalance. To perform Hall-effect measurements, a computer-controlled system was employed, typically consisting of a high-impedance voltmeter, an electrometer, and a constant current source. Sample was arranged in a Van der Pauw geometry of square configuration, which allows for accurate determination of electrical properties in thin films. Small-area metal contacts were deposited at the four corners of the sample to establish ohmic contacts on p-n type for the voltage ranges of interest. Ohmic behaviour is essential for Hall-effect measurements to avoid complications such as depletion-layer effects, which would otherwise necessitate corrections related to film thickness. By measuring the Hall coefficient and mobility, the electrical conductivity can be accurately estimated using following equation [256]:

$$\sigma = \frac{\mu}{R_H} \tag{3.6}$$

In this equation, σ is the electrical conductivity, μ is the mobility, and R_H is the Hall coefficient. In this study, the Hall effect analysis was carried out at the NANO-Electronic Centre, Faculty of Electrical Engineering, UiTM Shah Alam using Hall measurement system (ezHEMS Controller, Nanomagnetic Instruments), as depicted in Figure 3.20.

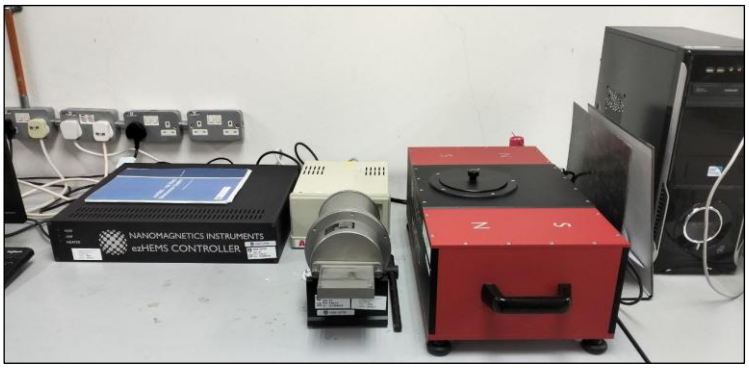

Figure 3.20 Hall Effect Measurement Instrument: Ezhems Controller, Nanomagnetic Instruments

3.8.3.3 Humidity-to-electricity conversion performance analysis

As HGPG is a type of energy harvesting device that utilizes humidity to generate electrical energy, it is essential to evaluate its response to varying humidity levels. A key parameter in analyzing the efficiency of humidity-to-electricity conversion is the output voltage. Since no external load or current path is connected to the HGPG device during this measurement, the output voltage represents the maximum potential difference the device can produce. It directly reflects the intrinsic ability of the fabricated HGPG device to convert humidity into electrical energy. Generally, a higher output voltage indicates a more efficient energy conversion process. In addition, Ohm's law was applied to examine the relationship between output voltage and load resistance, in order to determine the maximum output power of the HGPG device, where P denotes power, V the generated voltage, and R the load resistance:

$$P = \frac{V^2}{R} \tag{3.7}$$

In this study, the fabricated HGPG device, with an adsorption area of 1.25 cm^2, was tested under various RH levels at certain temperatures. The device was connected to a 10 MΩ resistor with no external bias applied. The analysis was carried out at the NANO-Electronic Centre, Faculty of Electrical Engineering, UiTM Shah Alam, using a bench-top temperature and humidity chamber (ESPEC-SH261) equipped with a current-voltage-time (I-V-t) measuring system (Keithley 2400), which functioned as a nanoammeter. Figure 3.21 illustrates the experimental setup used in this study.

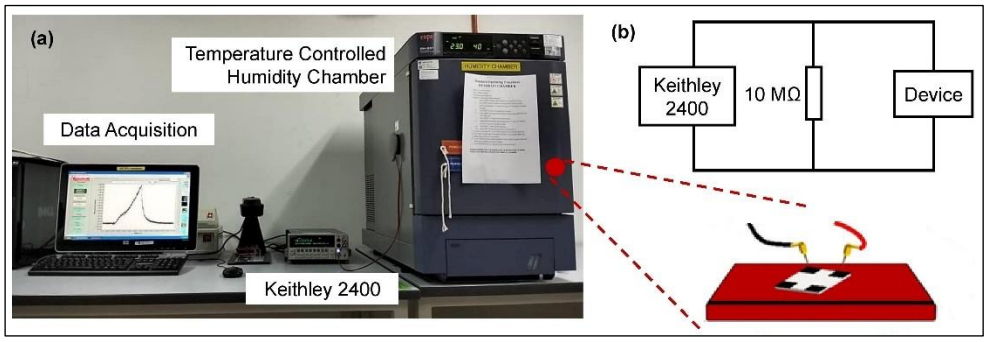

Figure 3.21 (a) Measurement Setup for Evaluating the Humidity-To-Electricity Performance of Developed HGPG Devices. (b) Circuit Block Diagram of HGPG Device Used for Voltage and Current Measurements

3.8.3.4 Piezoelectric Coefficient Analysis

In piezoelectric materials, the relationship between electrical charge and mechanical stress is characterized by piezoelectric coefficients [257]. These coefficients indicate either the amount of electric charge generated in response to applied pressure, or the degree of material deformation induced by an electric field. A commonly used device for this purpose is the d_{33} meter, which directly measures the d_{33} coefficient which representing the piezoelectric response along the same axis as the applied force. In this study, the d_{33} coefficient of the samples was measured at the Applied Physics Unit, Faculty of Science and Technology, Universiti Kebangsaan Malaysia using a piezometer (YE2730A, APC International Ltd.) as shown in Figure 3.22.

Figure 3.22 Piezometer: YE2730A, APC International Ltd

3.8.3.5 Nanogenerator Performance Testing Analysis

In this study, the output voltage produced by the S-HNG-based PENG composite incorporated with a Co-Zn-based nanoceramic hydrogel film was measured

using a homemade solenoid tapping device. The output voltage was recorded using a digital oscilloscope (Keysight InfiniiVision DSOX2022A). The output voltage provides a direct measure of the intrinsic capability of the fabricated PENG device to convert mechanical energy into electrical energy. Moreover, the power density (P_d) can be calculated based on Ohm's Law and the power dissipation formula, using the relation:

$$P_d = \frac{V^2}{R \times A} \tag{3.8}$$

In the equation, V represents the output voltage, R is the external load resistance, and A denotes the active area of the PENG. The PENG developed in this study adopts a planar electrode configuration, as illustrated in Figure 3.23. In this configuration, the active area is typically defined by the spacing between the electrodes and the area of the piezoelectric material situated between them [258, 259].

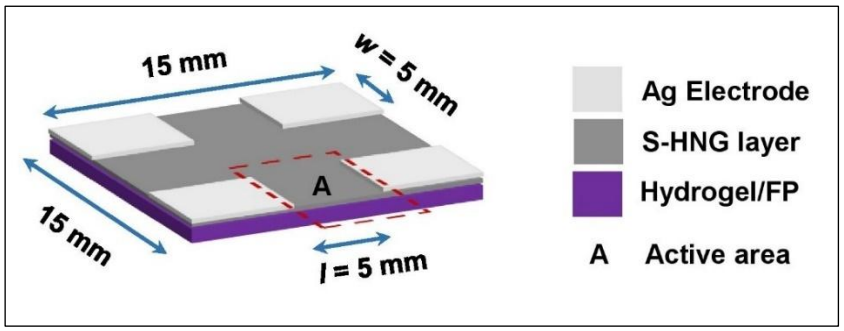

Figure 3.23 Basic Structure of the S-HNG-Hydrogel/FP-Based PENG with Planar Electrode Configuration

In this study, the solenoid tapping system functioned as an external mechanical actuation system to provide continuous mechanical input. As illustrated in Figure 3.24, the system consists of a push-pull solenoid (12 V, 250 mA), a power supply, a relay, an Arduino Uno, and a diode. This setup was designed to activate the PENG device by applying a repeated mechanical force, simulating real-world mechanical stimuli. By referring to the work done by D. Kamaruzaman et al. [3], the Arduino Uno microcontroller was programmed to generate a 10 Hz stroke frequency, operating at a force of approximately 2 N. The specific parameters used for testing the S-HNG-hydrogel-based PENG are summarized in Table 3.12.

Table 3.12
Parameter Setting for Measurement of Prepared S-HNG-Hydrogel-Based PENG

Sample size	1.5 cm × 1.5 cm
Active area	0.25 cm2
Working electrode	Ag
Operational frequency	10 Hz
Applied force	2 N
RH level	40%, 65%, 90%
Ambient temperature	RT

To evaluate its practical application in energy harvesting, the fabricated PENG device was also tested with LEDs, as depicted in the circuit block schematic in Figure 3.25. Once the capacitor within the circuit reached the required charge level, the switch was triggered to power the connected electronic devices.

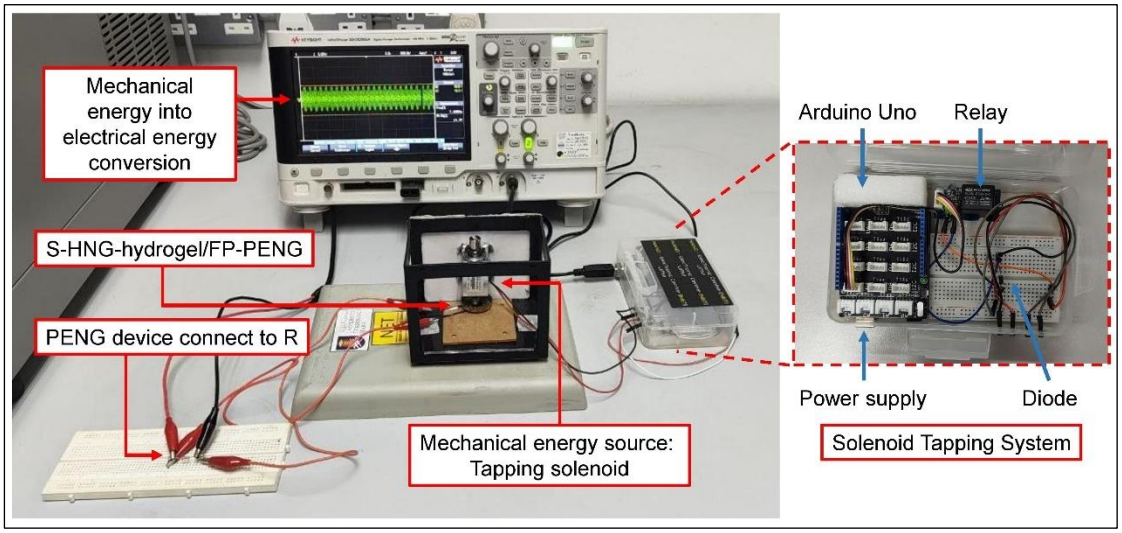

Figure 3.24 Electrical Performance Test for S-HNG-Hydrogel/FP-Based PENG Device with the Diagram of Solenoid Tapping System

Figure 3.26 illustrates the measurement setup used to evaluate the electrical performance of the developed HGPG–PENG hybrid device. The PENG component generates an alternating current (AC) signal under mechanical excitation, whereas the HGPG component produces a direct current (DC) output. For direct comparison within the HGPG–PENG hybrid configuration, the PENG waveform was converted to its DC equivalent using the following equation [260, 261]:

$$V_{DC,eq} = V_{rms} = \frac{V_{PP}}{2\sqrt{2}} \tag{3.8}$$

In this equation, V_{rms} represents the power-equivalent DC voltage, and and V_{PP} denotes the peak-to-peak voltage measured on the oscilloscope.

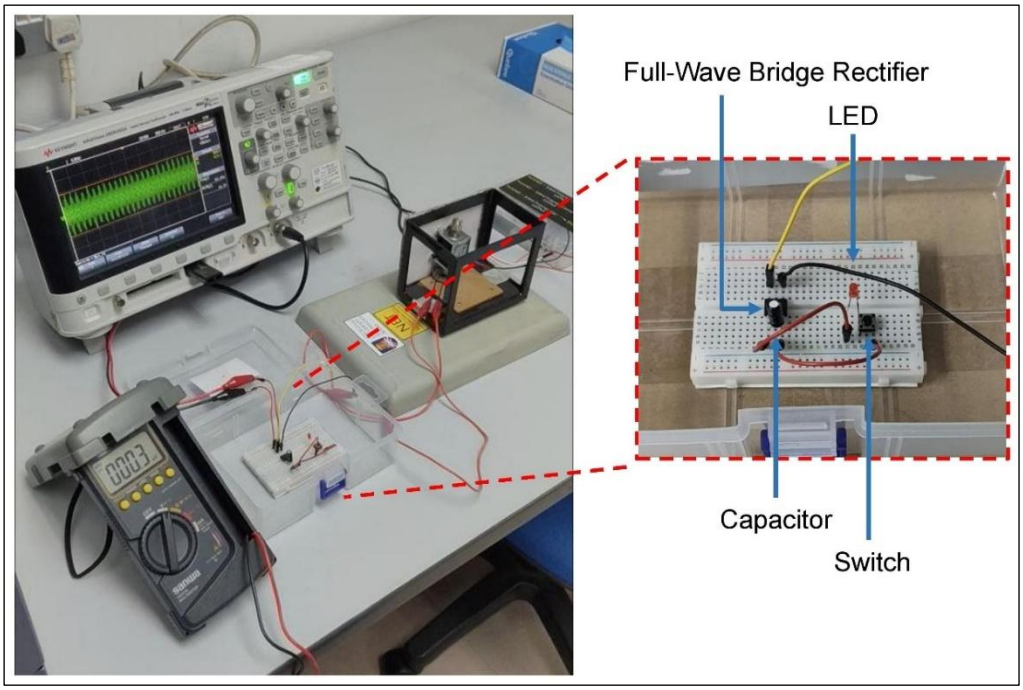

Figure 3.25 Diagram of Operating Electronic Devices through a Full-Wave Bridge Rectifier

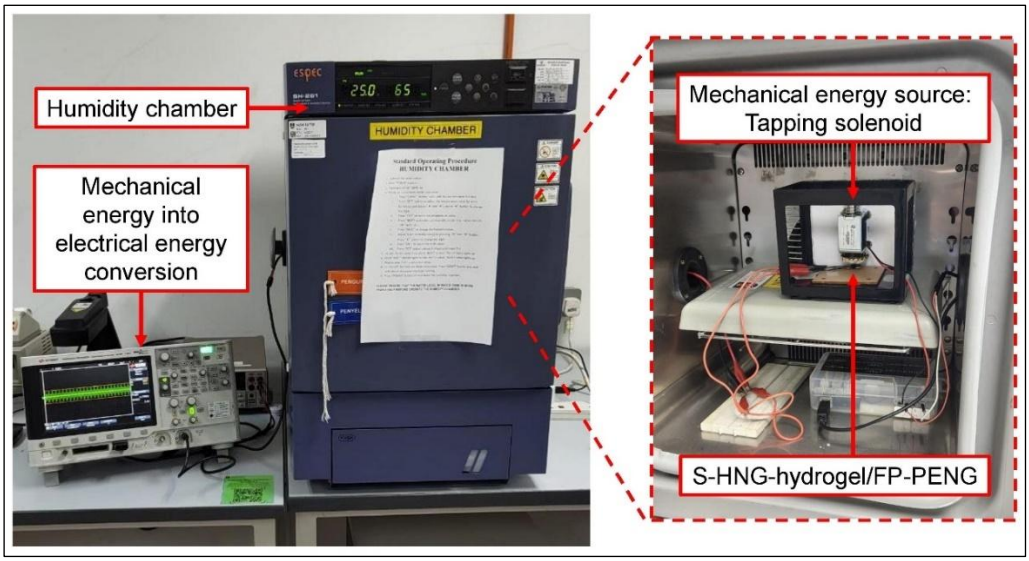

Figure 3.26 Measurement Setup for Evaluating the Mechanical-To-Electricity Performance of Developed HGPG-PENG Hybrid Device

3.9 Chapter Summary

This chapter presents the comprehensive experimental methodology employed in this study. It outlines the procedures for synthesizing S-PN, S-NG, and S-HNG composites using the sonicated solution immersion method. The deposition of these composites onto cellulose-based substrates via the doctor-blade technique is also described. Furthermore, the sol-gel method used to prepare the Co-Zn-based nanoceramic hydrogel film is explained, along with the process of converting wastepaper into RP for integration into the hygroscopic material film. The application of SA treatment and the investigation of optimization parameters are thoroughly discussed. Detailed descriptions of the complete fabrication processes and configurations of the HGPG and PENG devices are provided. Lastly, the chapter presents the characterization techniques used and elaborates on the testing procedures conducted to evaluate the performance of the HGPG and PENG devices.

CHAPTER 4
FABRICATION AND PERFORMANCE ANALYSIS OF HUMIDITY GRADIENT ENERGY HAVESTING BASED ON PRISTINE NICKEL OXIDE AND COMPOSITED WITH GRAPHENE AS HYGROSCOPIC MATERIALS

4.1 Introduction

Harvesting energy from ambient humidity has emerged as a promising frontier in RE technologies. This strategy exploits hygroscopic materials to adsorb water molecules from the surrounding environment and convert the resulting ionic gradients into electricity [39-41]. The careful selection of hygroscopic materials is pivotal, as their water-trapping capacity directly governs device humidity sensitivity and the stability of energy output [262-264]. In this study, NG composites are employed as the active hygroscopic medium. Gr is renowned for its exceptional electrical and thermal conductivities, coupled with tuneable surface chemistry, while NiO nanoparticles are valued for their low cost, chemical stability, and favourable electronic properties. The synergistic properties of NiO and Gr, particularly their favourable zeta potentials, facilitate efficient ion mobility, thereby enabling electric field generation and current output, and ultimately enhancing humidity-to-energy conversion efficiency. Despite these advantages, conventional synthesis routes for NG composites are often costly, technically demanding, and environmentally unsustainable [23, 265]. To the best of our knowledge, the application of NG composites in humidity-to-energy harvesting has not yet been reported [266]. In humidity-related contexts, NiO is widely recognized as a highly effective humidity absorber [267], whereas Gr has been extensively employed in humidity-sensing devices due to its exceptional sensitivity and strong surface interaction capabilities [268-270].

Water uptake behaviour is fundamentally determined by a material's hygroscopicity and hydrophilicity, typically driven by chemisorption mechanisms involving noncovalent interactions between hydrophilic functional groups and water molecules [271]. Upon exposure to ambient moisture, these functional groups engage in electrostatic interactions or hydrogen bonding with water vapor, thereby conferring high water adsorption capacity. Modulating surface wettability such as through SA

modification, offers an effective strategy to optimize this property. In the present work, SA-treated NG composites were designed as the primary hygroscopic medium, supported on a cellulose substrate whose abundant surface hydroxyl groups and intrinsic hydrophilicity further enhance water adhesion.

This study investigates the performance of cellulose-based HGPG devices incorporating NG composites synthesized via a simple, low-cost sonicated solution immersion method. The chapter is structured into two parts: (1) synthesis and characterization of untreated NG (U-NG) and S-NG composites on cellulose substrates for HGPG applications, and (2) synthesis and characterization of S-NG composites with varying Gr loadings on cellulose substrates for the same purpose. The overarching aim is to exploit the unique structural and surface attributes of these materials to achieve efficient humidity-to-electricity conversion. Through the adoption of an innovative synthesis approach, this work addresses key limitations in the fabrication of NG composites, paving the way for their seamless integration into self-sustaining, high-performance energy harvesting systems.

4.2 Surface Modification of NiO/Gr Composites via SA Treatment

NG composites were successfully fabricated via a facile sonicated solution immersion technique, followed by deposition onto a cellulose-based substrate as detailed in Sections 3.2 and 3.3. To elucidate the influence of SA treatment on the humidity-to-electricity conversion performance of the HGPG device, a series of comprehensive characterizations were undertaken. Throughout the investigation, the NG composite incorporating 1.0 wt.% Gr (NG-1.0) was employed as the reference formulation to identify the optimum SA-treated configuration. The assessment encompassed crystallographic and structural analyses, microstructural and morphological evaluations, wettability and hydrophilicity measurements, as well as electrical performance characterization, thereby enabling a holistic understanding of the SA treatment effects on device functionality.

4.2.1 Structural Properties of untreated and SA-treated NiO/Gr composite

Figure 4.1 presents the XRD patterns of the untreated NG-1.0 (U-NG-1.0) and SA-treated NG-1.0 (S-NG-1.0) nanostructures. The diffraction peaks at $2\theta = 37.04°$ and 44.50° are indexed to the ♣(1 1 1) and ♣(2 0 0) crystallographic planes of NiO (JCPDS

No. 01-071-4750), respectively. Characteristic reflections for Gr appear at 26.38° and 54.54°, corresponding to the ★(0 0 2) and ★(0 0 4) planes (JCPDS No. 00-041-1487). In addition, the diffraction features at 22.36° and 43.92° are assigned to the ●(2 0 0) and ●(2 3 1) planes of cellulose (JCPDS No. 00-056-1718). The ▲ at the peaks located at 44.51°, 51.85° and 76.46° correspond to the (1 1 1), (2 0 0) and (2 2 0) planes, respectively, as indexed to Ni (JCPDS No. 00-004-0850). For SA material, prominent peaks are observed at 21.63° and 24.18°, indexed to the ♦(3 1 1) and ♦(6 0 2) planes, respectively (JCPDS No. 00-038-1923). The inset image provides a magnified view of the XRD pattern, unequivocally confirming the successful SA functionalization on the S-NG-1.0 surface through the emergence of distinct SA characteristic diffraction features.

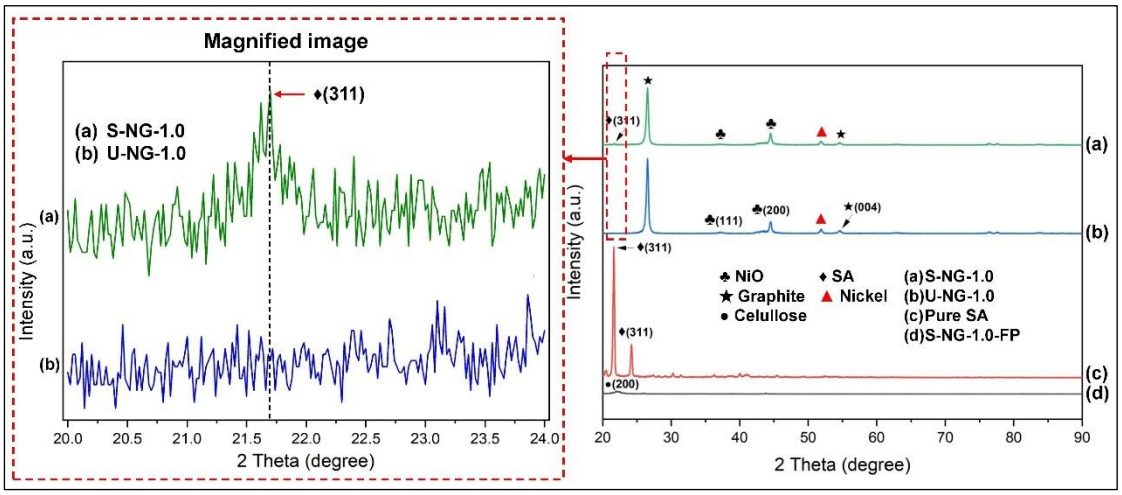

Figure 4.1 XRD Pattern for (a) S-NG-1.0, (b) U-NG-1.0, (c) Pure SA and (d) S-NG-1.0-FP. The Inset Image Presents a Magnified XRD Pattern, Clearly Illustrating the Successful SA Functionalization on the S-NG-1.0 Surface

Table 4.1
The FWHM, 2θ, Interplanar Spacing, Unit Cell Volume, and Crystallite Size of the NiO ♣(1 1 1) Plane for U-NG-1.0 and S-NG-1.0 samples

Sample	FWHM, β (rad)	2θ (°)	Interplanar spacing, d (nm)	Unit Cell Volume, V (nm^3)	Crystallite size, D (nm)
U-NG-1.0	0.0173	37.02	0.242	0.074	8.5
S-NG-1.0	0.0174	37.28	0.241	0.073	8.4

XRD analysis revealed that the D of the S-NG-1.0 nanostructures, derived from the ♣(1 1 1) diffraction peak of NiO via the Debye–Scherrer equation [Equation (3.1)], exhibited a subtle contraction from 8.5 nm to 8.4 nm following SA treatment. Concomitantly, refined broadening in the FWHM and slight peak position shifts were discerned, signifying lattice perturbations and microstructural reconfigurations induced

by the surface modification process. Using Equations (3.3) and (3.4), the interplanar spacing and unit cell volume were calculated, respectively. Since both parameters are directly dependent on the diffraction angle, any shift in peak position results in corresponding variations in their values. A comprehensive synopsis of the structural parameters extracted from XRD analysis is presented in

Table 4.1, providing a comparative framework for elucidating the crystallographic modifications induced by the treatment process.

The FTIR spectra presented in Figure 4.2 exhibit distinct vibrational features characteristic of pure SA, with absorption bands at 2913.45 cm^{-1} and 2847.80 cm^{-1} corresponding to the asymmetric and symmetric stretching modes of $–CH_2$ groups, respectively [272]. A sharp peak at 1699.18 cm^{-1} is attributed to the stretching vibration of the carbonyl (C=O) functional group, whereas the bands at 1462.95 cm^{-1}, 1429.48 cm^{-1}, and 1411.20 cm^{-1} are assigned to $–CH_2$ bending modes. In the S-NG-1.0 sample, a new absorption feature at 2345.59 cm^{-1} emerges, arising from the asymmetric stretching of ambient CO_2 molecules [273]. Notably, the Ni–O stretching band at 548.26 cm^{-1} undergoes a blue shift to 566.71 cm^{-1} upon SA treatment, indicating successful chemisorption of SA molecules onto the NiO nanoparticle surface.

In pure SA, the bands at 1297.11 cm^{-1} and 940.51 cm^{-1} correspond to $–CH_2$ bending and rocking vibrations, respectively; their absence in the SA-treated NiO spectrum suggests that these functional groups remain unbound or are sterically hindered, consistent with partial removal or non-reactivity of excess SA [274]. For the U-NG-1.0 sample, a distinct absorption band emerged at 3336.13 cm^{-1}, corresponding to the stretching vibrations of surface –OH functional groups, originating from hydroxylated sites and physisorbed moisture on the Gr surface. Upon SA functionalization, this band underwent a red shift to 3309.70 cm^{-1}, indicative of altered hydrogen-bonding environments and modified dipole–dipole interactions, thereby confirming the chemical interaction between SA moieties and the NG composite surface [275]. The FTIR analysis unequivocally confirms the successful surface functionalization of S-NG-1.0 sample by SA molecules, as evidenced by characteristic spectral shifts and the selective retention or disappearance of vibrational features. This modification is expected to influence both the hydrophilicity and humidity-to-energy conversion performance of the composite, as further discussed in subsequent sections.

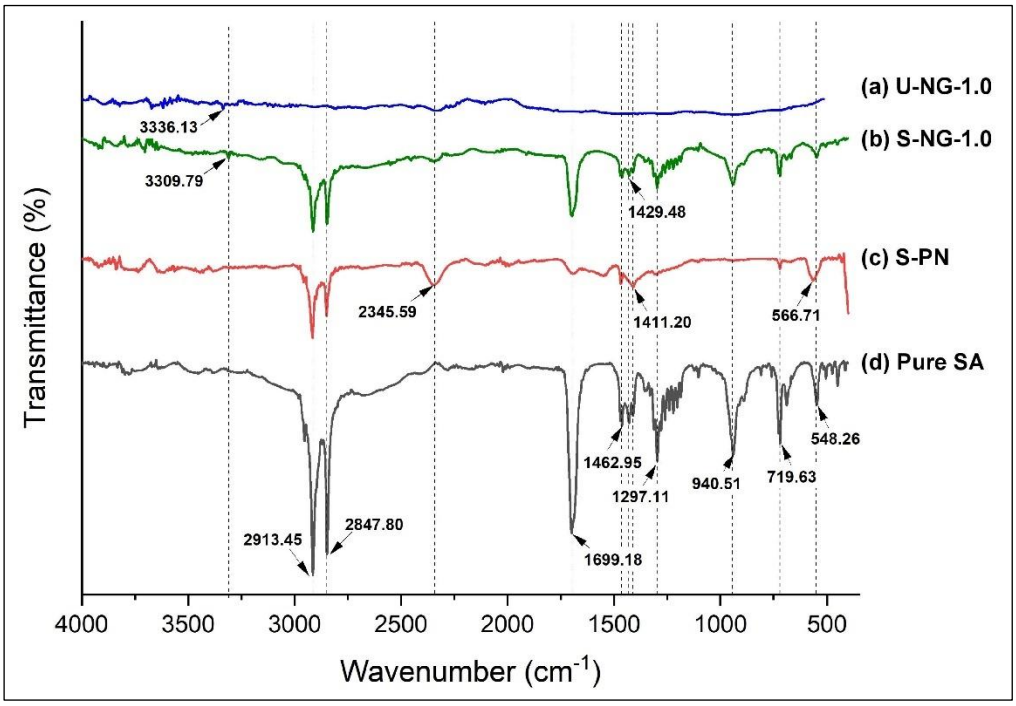

Figure 4.2 FTIR Spectra for Pure SA, S-PN, S-NG-1.0 and U-NG-1.0

4.2.2 Morphological Analysis of untreated and SA-treated NiO/Gr composite

Figure 4.3 (a–d) presents FESEM micrographs elucidating the intricate morphological evolution of the NG-1.0 composite powder pre- and post-SA functionalization. In the pristine U-NG-1.0 sample [Figure 4.3 (a–b)], the architecture is dominated by nanostructured aggregates with particle diameters (Ø) spanning 61–172 nm, forming loosely coalesced agglomerates with irregular intergranular boundaries. This topology suggests a kinetically driven nucleation–growth process, yielding high-surface-area features conducive to water molecule adsorption. Upon SA treatment [Figure 4.3 (c–d)], pronounced morphological reconfiguration is observed, manifesting as hierarchically layered, overlapping lamellae that emulate the quasi-periodic arrangement of piscine scales. These lamellae are interspersed with uniformly agglomerated nanoclusters (Ø ≈ 53–106 nm), indicative of constrained crystal growth and enhanced interfacial cohesion, possibly mediated by surface ligand coordination between SA functional groups and NG surface sites. Such architectural modulation is hypothesized to reduce surface energy anisotropy, thereby facilitating optimized water adsorption–desorption kinetics essential for high-efficiency humidity-to-energy transduction. The S-NG-1.0-FP micrograph [Figure 4.3 (e)] further reveals robust anchoring of the composite onto cellulose microfibers, enabled by strong hydrogen-

bonding interactions between cellulose hydroxyl moieties and the SA-functionalized NG surface. This intimate interfacial adhesion ensures minimal delamination under operational humidity gradients, thereby enhancing device stability.

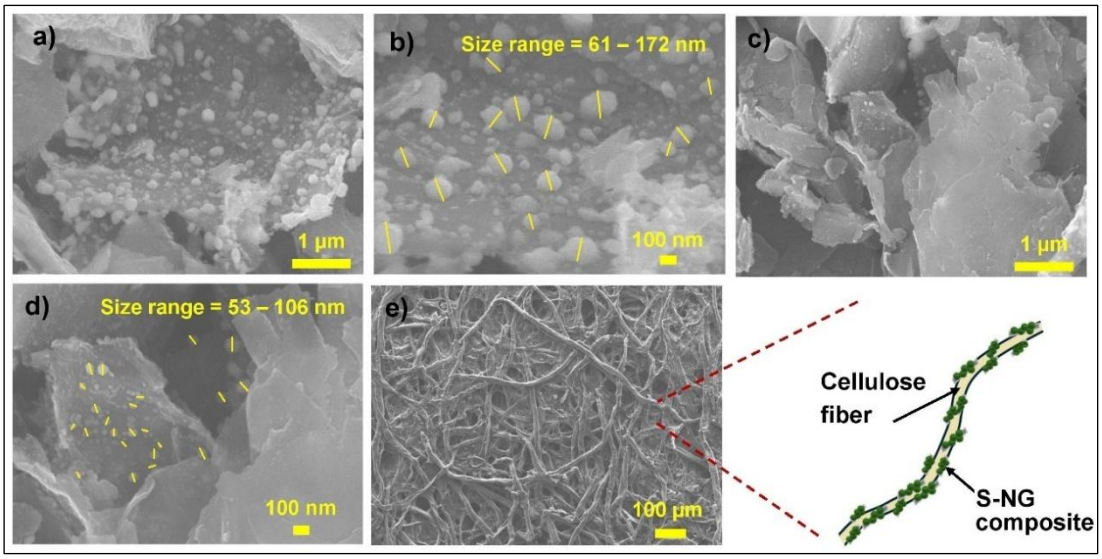

Figure 4.3 FESEM Images of U-NG-1.0, (b) Magnified FESEM Images of U-NG-1.0, (c) FESEM Images of S-NG-1.0 (d) Magnified FESEM Images of S-NG-1.0, and (e) Morphology of S-NG-1.0-FP

Elemental analysis via EDX shown in Figure 4.4 confirms the presence of carbon (C), oxygen (O), and Ni, with sharp peaks in the 0–10 keV range, devoid of extraneous elemental signatures. The compositional parity between U-NG-1.0 and S-NG-1.0 confirms that SA treatment primarily modulates morphology and surface chemistry without introducing contamination, in agreement with XRD observations. This structural–compositional synergy is anticipated to significantly augment charge carrier mobility and interfacial ion transport, thereby elevating HGPG performance metrics.

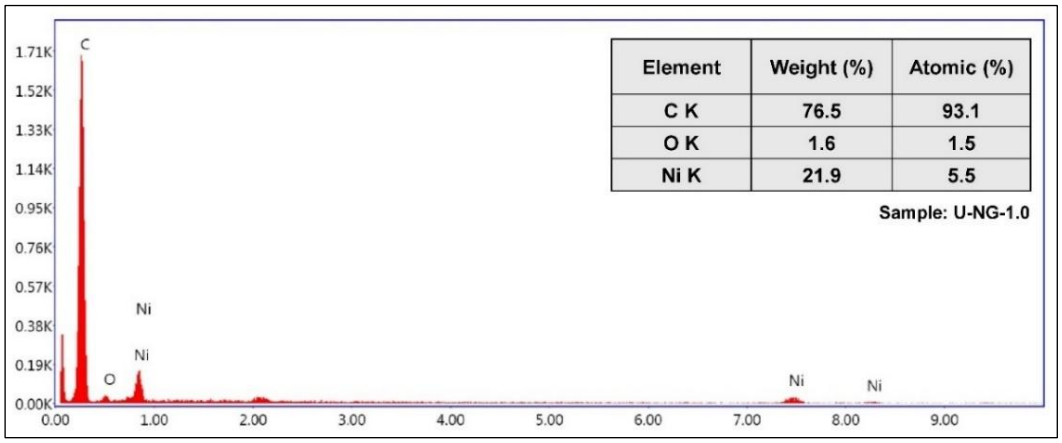

Figure 4.4 EDX Peaks with Inset Presenting the Analytic Elemental Composition of S-NG-1.0

4.2.3 Hydrophilicity Analysis of untreated and SA-treated NiO/Gr composite

Figure 4.5 presents optical images of sessile water droplets on the surface of S-NG-1.0-FP, revealing that SA functionalization markedly increases the θ_{CA} relative to the untreated counterpart. The measured θ_{CA} for the SA-treated sample is 65.3° ± 1.2°, which, while elevated, remains within the hydrophilic regime. Using Equation (2.8), the surface free energy of S-NG-1.0-FP was calculated to be 25.8 ± 0.3 mJ/m^2, significantly lower than that of the untreated sample (Table 4.2). This reduction in surface energy is indicative of enhanced interfacial water mobility, which can modulate adsorption–desorption kinetics and, in turn, influence the humidity-to-energy conversion efficiency of the HGPG device.

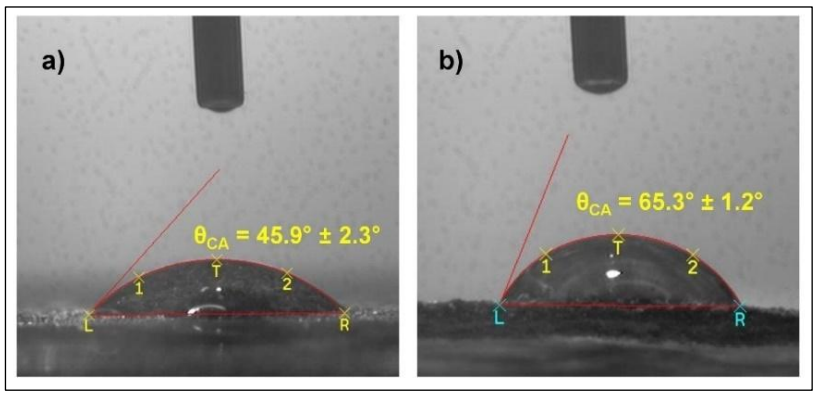

Figure 4.5 Water Contact Angle Measurements of the Prepared (a) U-NG-1.0-FP and (b) S-NG-1.0-FP

Table 4.2
Contact Angle Measurement Data of Samples U-NG-1.0-FP and S-NG-1.0-FP

Sample	WCA (°)	Surface Energy (mJ/m^2)
U-NG-1.0-FP	45.9° ± 2.3°	30.9 ± 0.5
S-NG-1.0-FP	65.3° ± 1.2°	25.8 ± 0.3

In general, a high surface energy indicates strong intermolecular attraction, facilitating rapid bond formation and enhanced water spreading across the surface, which manifests as a reduced θ_{CA}. Conversely, a lower surface energy diminishes molecular attraction, thereby increasing θ_{CA} [276]. The wettability behaviour of a surface is intrinsically linked to its morphological characteristics. SA functionalization promotes the adsorption of a higher density of SA molecules onto the composite surface, forming a more compact and orderly molecular arrangement [320, 321]. This is consistent with FESEM observations, which reveal a layered and overlapping morphology on the SA-treated substrate, trending toward increased surface roughness. Literature reports suggest that pronounced surface roughness can compromise hydrophilicity by trapping substantial volumes of air within the interstices of agglomerated nanostructures, thus impeding effective water–solid contact [148, 277].

Theoretically, the long hydrocarbon chains of the fatty acid reduce surface hydrophilicity, altering interfacial properties by increasing water resistance and limiting the penetration of water molecules into the composite structure. As illustrated in Figure 4.6, during SA treatment, Ni ions on the surface of the NG composites react with SA ($CH_3(CH_2)_{16}COOH$) in ethanol, forming a thin layer of Ni stearate. This surface modification alters the material's hydrophilicity and thus affects its surface energy [3]. The reaction can be simplified as:

$$Ni–OH + HOOC–R \rightarrow Ni–OOC–R + H_2O \quad (4.1)$$

where R represents the long alkyl chain of SA, $(CH_2)_{16}CH_3$. The modification occurs specifically at the NiO surface, likely involving a reaction between SA (HOOC–R) and Ni–OH groups formed through surface hydration.

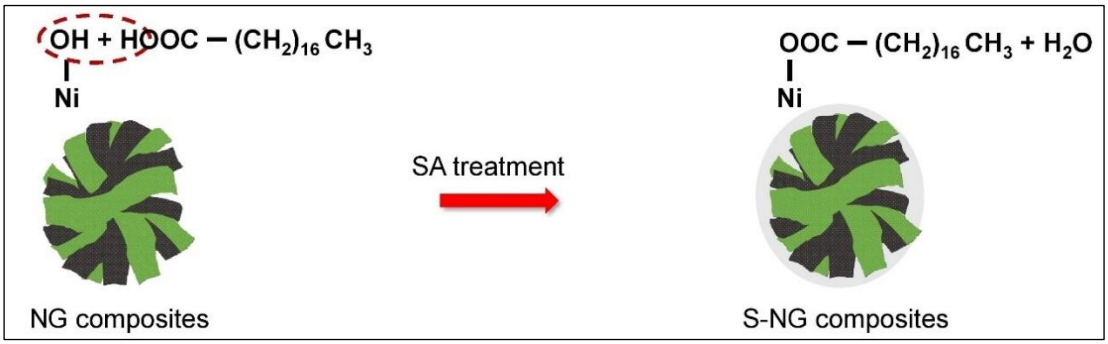

Figure 4.6 Chemical Reaction during the SA Treatment Process to produce Optimally Hydrophilic S-NG Composites Powder

4.2.4 Electrical Characterization of untreated and SA-treated NiO/Gr composite

To assess the device's humidity responsiveness and operational efficiency, zero-bias measurements were performed over an active adsorption area of 1.25 cm^2. The temporal voltage response at 75 % RH is depicted in Figure 4.7, whereas Figure 4.8 (a) and Figure 4.8 (b) illustrate the corresponding current–time profiles across the RH range of 40 % to 90 % for the untreated and SA-functionalized devices, respectively. A comprehensive summary of the humidity-to-energy conversion metrics for the fabricated devices is provided in Table 4.3.

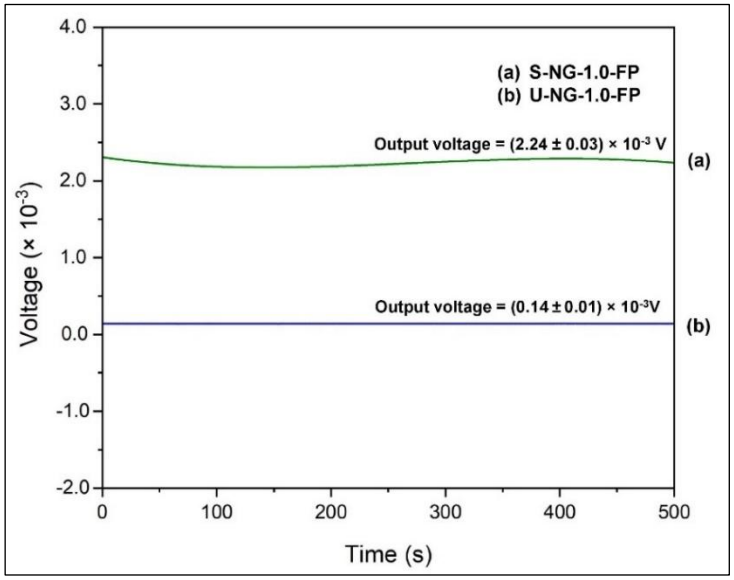

Figure 4.7 Humidity Response of U-NG-1.0-FP and S-NG-1.0-FP Humidity-To-Energy Device at 75% RH with 0 a Bias

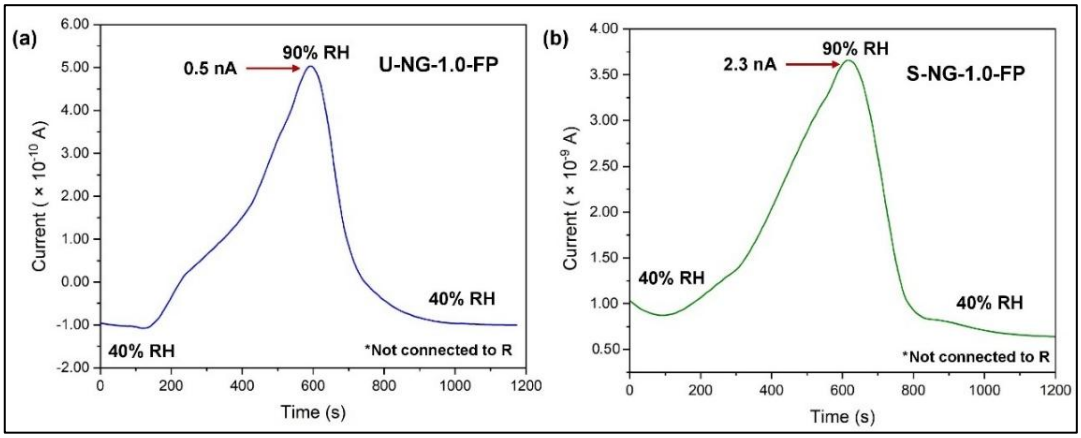

Figure 4.8 Humidity Response of Untreated and (c) SA-Treated Humidity-To-Energy Device from 40% to 90% RH with 0 V Bias

Table 4.3
The Humidity-To-Energy Performance of Fabricated U-NG-1.0-FP and S-NG-1.0-FP-Based HGPG Devices

Sample	RH (%)	R (MΩ)	Output voltage, V (V)	Current density, J (A/cm^2)	Power, P (W)
U-NG-1.0-FP	75	10	$(0.14 \pm 0.01) \times 10^{-3}$	$(11.12 \pm 0.07) \times 10^{-12}$	$(1.93 \pm 0.12) \times 10^{-15}$
S-NG-1.0-FP	75	10	$(2.24 \pm 0.03) \times 10^{-3}$	$(1.79 \pm 0.02) \times 10^{-10}$	$(5.02 \pm 0.13) \times 10^{-13}$

The experimental findings unambiguously substantiate the superior humidity-responsive performance of the SA-functionalized (S-NG-1.0-FP) HGPG device compared to its untreated (U-NG-1.0-FP) counterpart. At 75 % RH, the SA-treated device achieved an output voltage of $(2.24 \pm 0.03) \times 10^{-3}$ V, a current density of $(1.79 \pm 0.02) \times 10^{-10}$ A/cm^2, and an output power of $(5.02 \pm 0.13) \times 10^{-13}$ W, surpassing the performance of the untreated counterpart. This enhancement is attributed to the SA-modified hygroscopic composite's ability to trap a greater number of water molecules under high-RH conditions, thereby facilitating more efficient charge generation and significantly boosting voltage output [152]. The observed performance improvement directly correlates with the morphological evolution and reduced surface energy induced by SA treatment, which promotes optimized water adsorption–desorption dynamics while preserving sufficient hydrophilicity for rapid humidity-driven charge transfer.

Both fabricated devices exhibited excellent sensitivity to humidity variations. At 90% RH, the untreated HGPG device delivered a peak output current of 0.5 nA, whereas the SA-functionalized counterpart achieved a markedly higher output of 2.3 nA. These results substantiate that SA surface functionalization of the hygroscopic S-NG-1.0-FP composite significantly enhances humidity-to-energy conversion efficiency, yielding highly promising performance metrics.

4.3 Synthesis and Characterization of NiO/Gr Composites with Different Graphene Loading on Cellulose-based Substrate for Humidity Gradient Energy Harvesting Application

In alignment with the gradient configuration concept of the humidity-to-energy device, S-NG composites were successfully synthesized via a facile sonicated solution immersion method. The resulting composites were subsequently deposited onto a cellulose-based substrate, as detailed in Sections 3.2 and 3.3. To assess the suitability of the synthesized S-NG composite powder for HGPG device applications, a comprehensive suite of analyses was performed. These included crystallographic and structural characterization, morphological assessment, hydrophilicity and wettability evaluation, chemical state and elemental composition analysis, surface area and porosity measurements, as well as electrical performance characterization.

4.3.1 Structural Properties of NiO/Gr Composites

Figure 4.9 shows the XRD patterns of the S-PN and S-NG composites (in powder forms) with different Gr loadings within the angular range of 2θ from 20° to 90°. The XRD patterns clearly show the diffraction peaks at 37.33°, 43.04°, 62.49°, 74.93° and 78.89° were indexed to the ♣(1 1 1), ♣(2 0 0), ♣(2 2 0), ♣(3 1 1), and ♣(2 2 2) planes, respectively, corresponding to crystallized cubic NiO (JCPDS No. 01-071-4750) [278, 279]. Multiple distinctive peaks with sharp intensities suggest that the S-PN synthesized has highly crystalline structures and is polycrystalline in nature [280, 281]. The XRD patterns exhibit the planes of ♦(6 0 2) at diffraction peak of 24.18° corresponding to SA (JCPDS No. 00-038-1923).

In contrast, the planes of ★(0 0 2) and ★(0 0 4) correspond to the diffraction peaks that are significant for graphite (JCPDS No. 00-041-1487), which are positioned at 26.38° and 54.54°, respectively [282, 283]. The successful formation of the NG composites is confirmed by the presence of characteristic peaks associated with NiO and graphite in all composite samples. Following the hybridization of NiO with Gr, the ♣(2 0 0) peak is slightly shifted to a higher angle at 44.5°, indicating the effect of Gr incorporation on the peak position. This observation is consistent with the findings reported by Kiran et al [284]. Additionally, a strong characteristic peak of Gr was identified in all composite samples, most likely as a result of high Gr loading in the

composites. As expected, more Gr in sample contributes to higher diffraction signal, hence the intensity of Gr peaks increases as the amount of Gr loading increases from 0.5 wt% to 2.0 wt%. Subsequently, the weaker intensity of NiO peaks was observed as the Gr content rises, indicating a decrease in the relative contribution of NiO to the diffraction pattern.

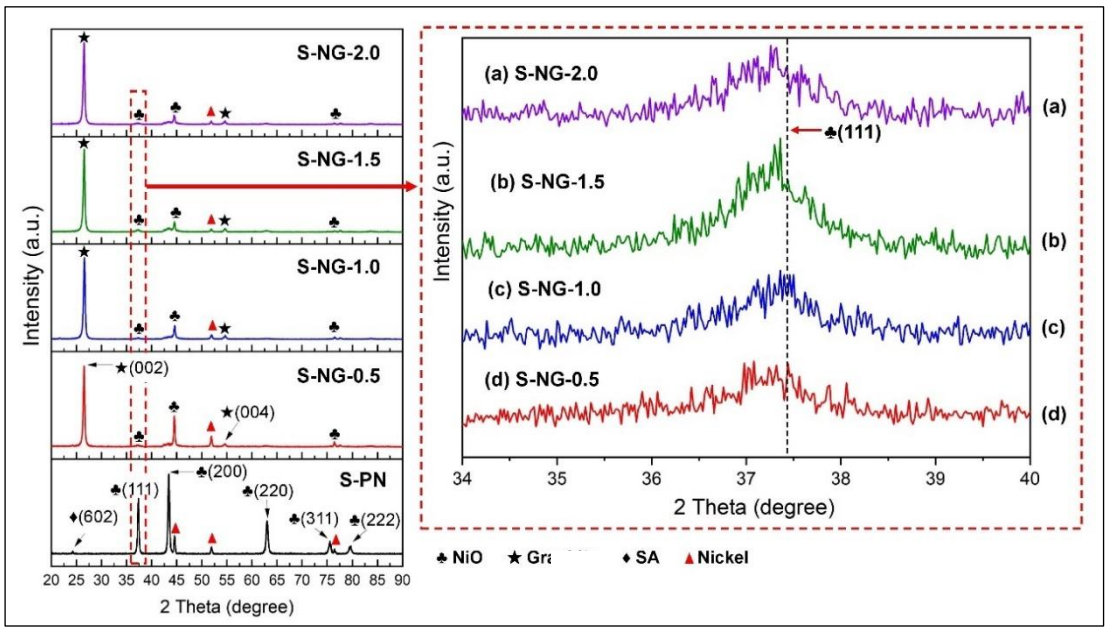

Figure 4.9 XRD Pattern of Synthesized S-NG Composites with Varying Gr Loading (wt. %) with Inset Shows the Magnified XRD Peak Corresponding to the ♣(1 1 1) Plane of NiO

The D was calculated using the Debye-Scherrer formula [Equation (3.1)]. The resulting crystallite sizes of the samples are tabulated in Table 4.4. The crystallite size of S-PN was approximately 19.8 nm. It was discovered that the addition of Gr reduced the size of the crystallites, and the D value continues to decrease as the Gr content rises. The presence of Gr may inhibit the growth of NiO crystals or cause strain in the NiO lattice, leading to smaller crystallites [28, 285]. This observation underscores the structural influence of Gr within the composite system and is consistent with the Scherrer equation, which relates crystallite size to XRD peak broadening. In addition, the interplanar spacing and unit cell volume were estimated using Equations (3.3) and (3.4), respectively, revealing closely comparable values among the samples, consistent with the minimal variations observed in their diffraction peak positions.

Table 4.4
The FWHM, 2θ, Interplanar Spacing, Unit Cell Volume and Crystallite Size of NiO ♣(1 1 1) Materials for Different Gr Loadings

Sample	FWHM, β (rad)	2θ (°)	Interplanar spacing, d (nm)	Unit Cell Volume, V (nm^3)	Crystallite size, D (nm)
S-PN	0.0074	37.31	0.241	0.073	19.8
S-NG-0.5	0.0165	37.23	0.242	0.073	8.9
S-NG-1.0	0.0174	37.28	0.241	0.073	8.4
S-NG-1.5	0.0178	37.24	0.241	0.073	8.2
S-NG-2.0	0.0189	37.22	0.242	0.073	7.7

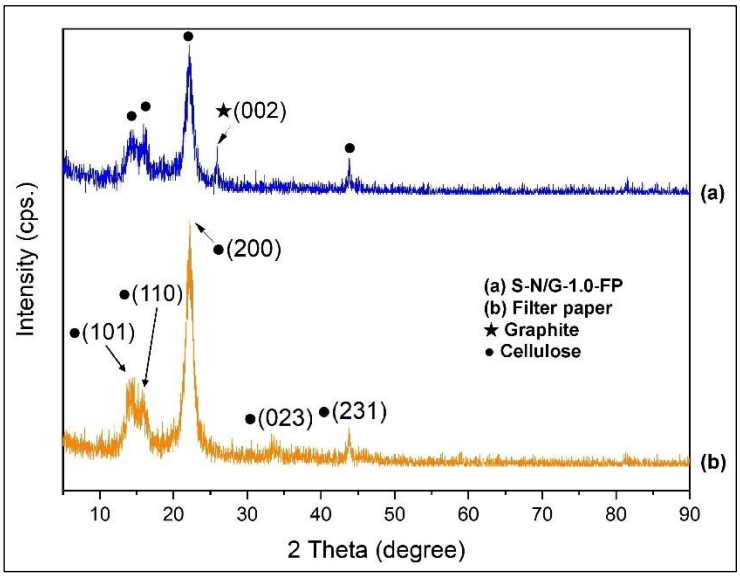

Figure 4.10 XRD Pattern of Prepared S-NG-1.0-FP

In this study, S-PN and S-NG composites were deposited onto FP substrates, and XRD patterns in Figure 4.10 unequivocally verified the successful formation of the S-NG-1.0 composite on the FP cellulose-based substrate (S-NG-1.0-FP). This confirmation is substantiated by the emergence of phase-specific, high-intensity Bragg reflections characteristic of NiO, Gr, and cellulose, indicating the coherent integration of all constituent phases within a unified composite architecture. Meanwhile, the XRD pattern of the pristine FP substrate, shown in Figure 4.9, distinctly displays Bragg reflections corresponding to the ●(1 0 1), ●(1 1 0), ●(2 0 0), ●(0 2 3), and ●(2 3 1) crystallographic planes, located at 2θ values of 14.46°, 15.94°, 22.12°, 33.54°, and 43.84°, respectively. These reflections are characteristic of the crystalline phase of cellulose with a monoclinic crystal structure (JCPDS No. 00-056-1718) [286, 287].

4.3.2 Morphological Analysis of NiO/Gr Composites

FESEM analyses were conducted to investigate the surface morphology and microstructure properties of the synthesized S-PN and S-NG composites. The FESEM image in Figure 4.11(a) revealed the aggregated particles with irregular spheroidal morphology of S-PN, approximately 1.9 ± 0.3 μm in size. The magnified image in Figure 4.11(c) provides a clearer view of the actinomorphic-structured NiO microspheres, which resemble flowers composed of numerous nanosheets. For the prepared S-NG-1.0 composites, the presence of Gr is evidenced from the FESEM image in Figure 4.11 (b), which shows Gr flakes with ripples and a wrinkled surface resulting from carbon compression. The average microstructure size is approximately 2.1 ± 0.3 μm. As observed in magnified image in Figure 4.11 (d), random dispersion of the NiO particles occurs throughout the Gr flakes, contributing to an electro-conductive and porous structure. The growth of NiO particles is nucleated by the defect sites and edge surfaces of Gr in the precursor solution, which causes the particles to reorganize on Gr flake to form heterostructures [288]. Similar results obtained by other reported studies as well [289-291]. The conductivity of Gr and the porosity of NiO in S-NG composites may enhance the hydrophilic properties of the composite's material, improving its water absorption capabilities and, consequently, its humidity harvesting performance.

The surface morphologies of S-PN and S-NG composites with 0.5 wt.%, 1.0 wt.%, 1.5 wt.%, and 2.0 wt.% of Gr loading deposited on FP were investigated. From the FESEM images in Figure 4.12, it is evidenced that FP consists of cellulose fibrils forming a highly porous fibrillar network. Figure 4.12 (a) shows agglomerated NiO microstructures attached to the surface of FP and spreading between the fibrils. The images reveal a randomly distributed, non-preferentially oriented fibril network reinforced with NiO microstructures. Additionally, FESEM observations indicate a rough morphological surface with noticeable porosity, which is expected to enhance water molecule adsorption.

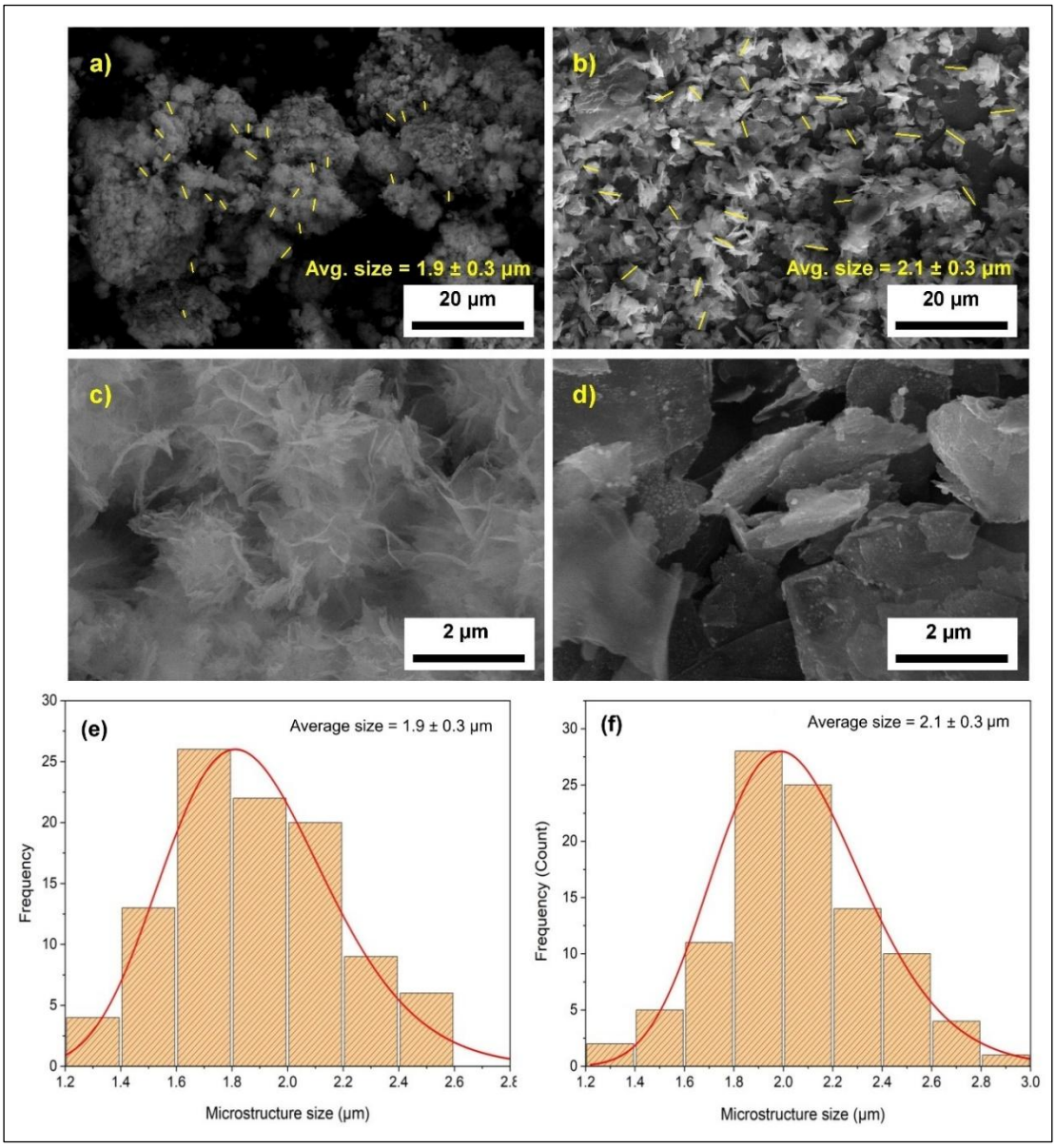

Figure 4.11 FESEM Morphology of the (a) S-PN Powder and (b) S-NG-1.0. Magnified FESEM Morphology of the (c) S-PN and (d) S-NG-1.0. Histograms of the Particle Size Distribution of the (e) S-PN and (f) S-N/G-1.0

Meanwhile, Figure 4.12 (b) to (e) demonstrate good dispersion of S-NG composites within the porous network of FP, with results showing relative consistency across the different Gr loadings. The S-NG composites appear effectively wrapped within the channels provided by the FP. Interestingly, as the Gr loading percentage increases, the S-NG composites particles become denser, forming a more tightly packed structure attached to the fibrils. With increasing Gr content, the cross-linking effect imparted by the intercalated S-NG composites particles could influence the surface roughness as well [292]. Additionally, all composites' samples exhibited a well-

maintained three-dimensional network structure that was both porous and interconnected. The rough and highly porous surface of the prepared composites is anticipated to provide active adsorption sites, facilitating effective water absorption.

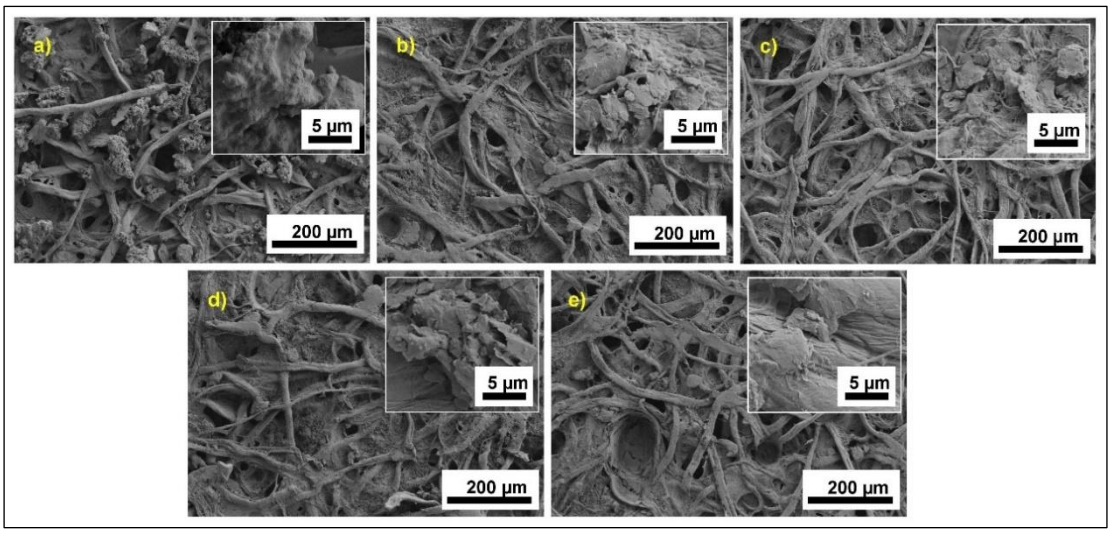

Figure 4.12 FESEM Morphology of the Prepared (a) S-PN-FP, (b) S-N/G-0.5-FP, (c) S-N/G-1.0-FP, (d) S-N/G-1.5-FP, and (e) S-N/G-2.0-FP with Inset Presenting the Corresponding Magnified FESEM Morphology

The presence and distribution of the elements in the S-NG-1.0-FP composites were further confirmed by EDX analysis. The EDX spectrum in Figure 4.13 (a) verified that elements such as C, O and Ni are presented in the composites, and Figure 4.13 (b) to (d) show the corresponding elemental mapping images. C element indicating the presence of Gr and cellulose-based FP. Significant dispersion of the C, O, and Ni elements was shown EDX mapping analysis, indicating that they are well distributed across the surface. Figure 4.14 (a) to (e) illustrates the EDX properties of specific spots for S-PN, S-NG-0.5, S-NG-1.0, S-NG-1.5, and S-NG-2.0, along with quantitative elemental analyses (inset). The EDX spectra of all samples display three distinct peaks corresponding to C, O, and Ni.

For the S-NG composites, the C content is observed to increase with the rising Gr content, which ranges from 0.5 wt.% to 2.0 wt.%. The EDX spectra reveal significant reductions in the peaks of O and Ni compared to pristine NiO. This reduction is attributed to the presence of Gr in the composites, which overshadows the signals of the other elements. Furthermore, the purity of the synthesized composites material is confirmed by the absence of any additional elemental peaks in the EDX spectra of the S-NG composites.

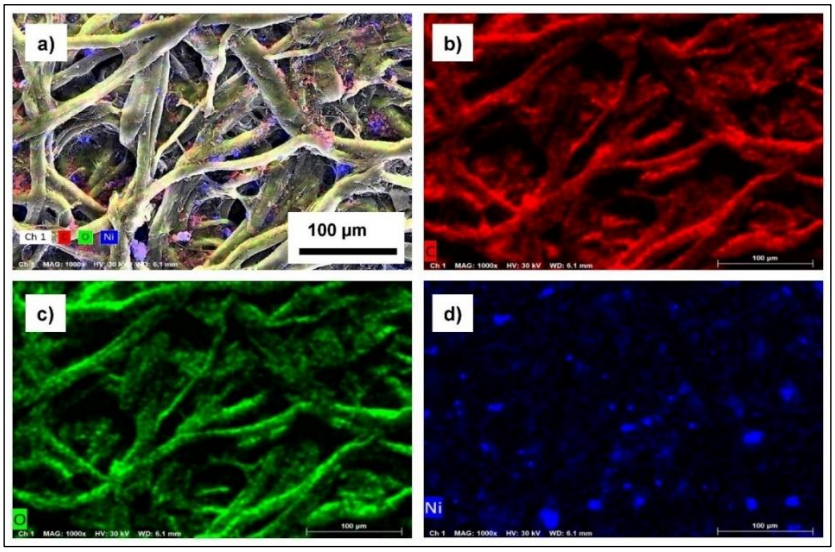

Figure 4.13 (a) Overall EDX Elemental Mapping of S-N/G-1.0-FP on the Same Spot: Corresponding to (b) C, (c) O, and (d) Ni Mapping

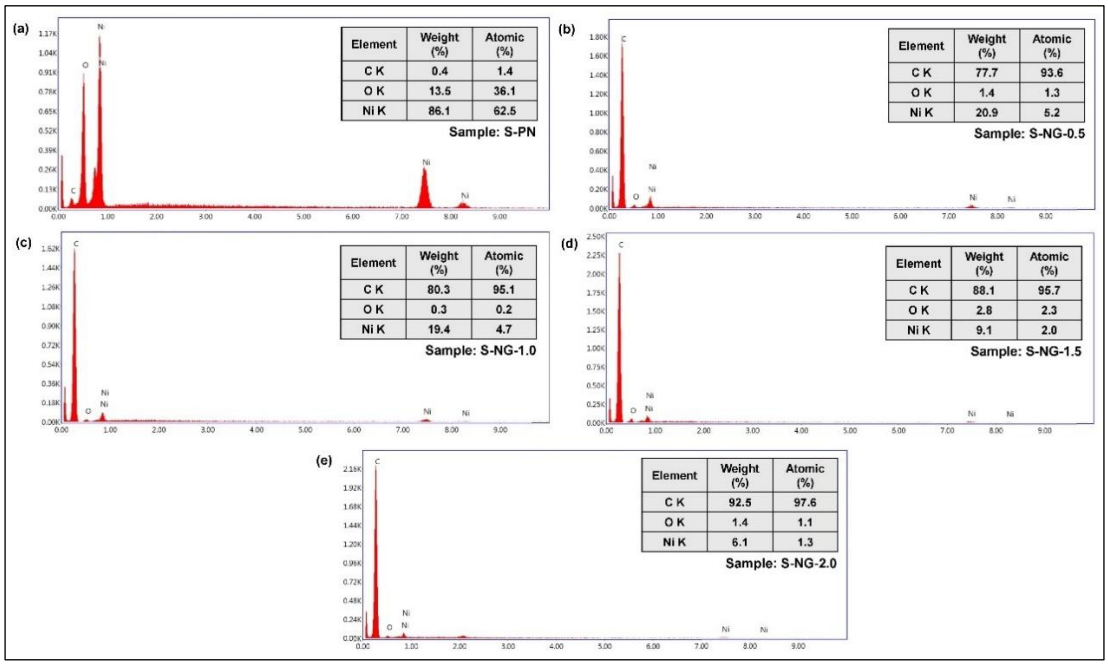

Figure 4.14 EDX Characteristic Peak of Composite Powder of (a) S-PN, (b) S-N/G-0.5, (c) S-N/G-1.0, (d) S-N/G-1.5, and (e) S-N/G-2.0 with Inset Presenting the Quantitative EDX Elemental Analysis of the S-NG Composites

To further study the morphology and microstructure of the hybridized Gr in the NiO crystal system, HRTEM and SAED analyses were conducted, with results shown in Figure 8. The HRTEM images of S-PN, containing aggregated nanoparticles of irregular size and spherical shape, are displayed in Figure 4.15(a). The HRTEM image

shown in Figure 4.15 (b) reveals clear crystal lattice fringes with a lattice spacing of 0.247 nm, corresponding to the ♣(1 1 1) crystal plane of the NiO phase. The SAED patterns shown in Figure 4.15 (c) indicating polycrystalline nature of the prepared S-PN and from the histogram of particle sizes of S-PN presented in Figure 4.15 (d), it is evident that most NiO nanoparticles range in size from 10 to 40 nm, with an average size of 25 ± 6 nm.

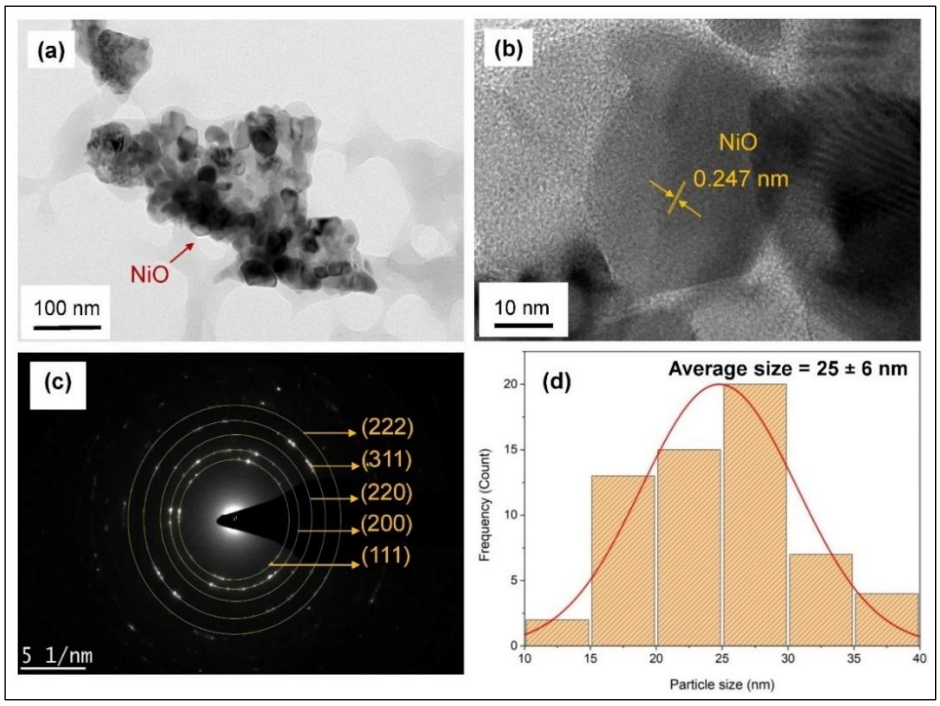

Figure 4.15 TEM Images of the S-PN: (a) Low Magnification, (b) High Magnification, (c) SAED Pattern and (d) the Histograms of the Particle Size Distribution of S-PN

Meanwhile, the S-NG-1.0 HRTEM image, displayed in Figure 4.16 (a), demonstrates that most NiO nanoparticles anchor to Gr, with some NiO nanoparticles overlapping, as shown in Figure 4.16 (b). Regarding the lattice fringes, lattice spacings of 0.308 nm and 0.246 nm have been identified based on the HRTEM image in Figure 4.16 (c). These values align with the calculated spacings of the (0 0 2) plane of Gr and the (1 1 1) plane of NiO, respectively. Additionally, the SAED patterns shown in Figure 4.16 (d) showcase typical polycrystalline rings, indicating polycrystalline nature of the prepared materials. The NiO nanoparticles in the hybridized system were observed to have a reduced size, ranging from 4 to 13 nm, with an average of 8 ± 2 nm, as depicted

in Figure 4.16 (e). The particle size provided by the HRTEM analysis is complementary to the information obtained from XRD analysis.

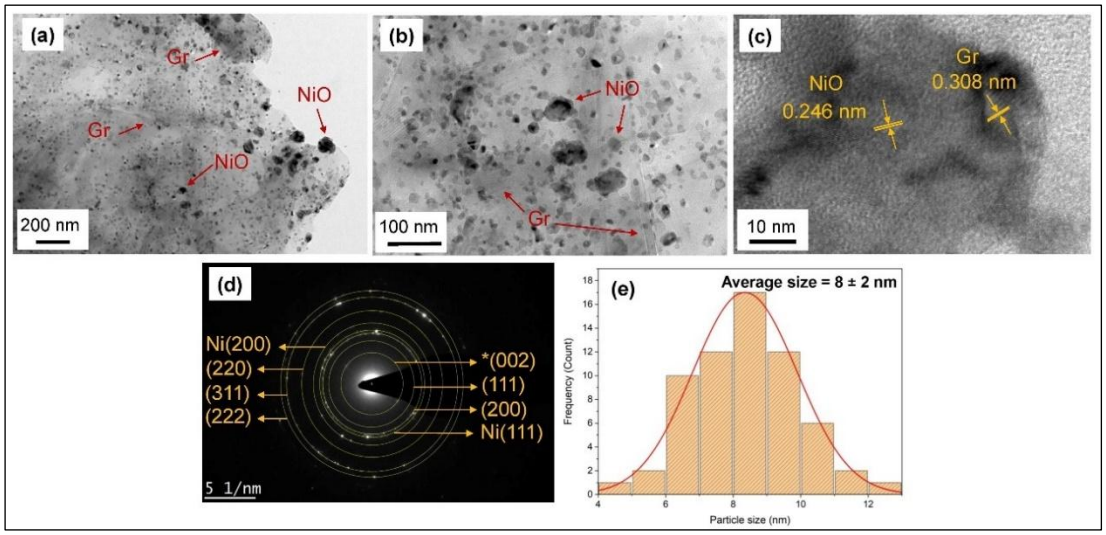

Figure 4.16 TEM Images of the S-NG-1.0: (a) Low Magnification, (b – c) High Magnification, (d) SAED Pattern and (e) the Histograms of the Particle Size Distribution of S-NG-1.0

4.3.3 Hydrophilicity Analysis of NiO/Gr Composites

WCA measurements were conducted to investigate the hydrophilic properties of samples S-PN, S-NG-0.5, S-NG-1.0, S-NG-1.5, and S-NG-2.0. The results, presented in Figure 4.17, confirm that all samples exhibit hydrophilic characteristics. The surface energy of each sample was calculated using Equation (2.8), and the sample details are summarized in Table 4.5. From the measurement, the θ_{CA} increased from 49.3° ± 0.6° for S-PN-FP to 64.5° ± 3.3° for S-NG-0.5-FP. This increase is likely due to the incorporation of Gr, which contributes to a higher θ_{CA}. Notably, S-PN-FP exhibited a higher surface energy of 30.1 ± 0.1 mJ/m^2 compared to 26.0 ± 0.9 mJ/m^2 for S-NG-0.5-FP, indicating stronger molecular interactions that promote bond formation and enhance water spreading on the S-PN-FP surface.

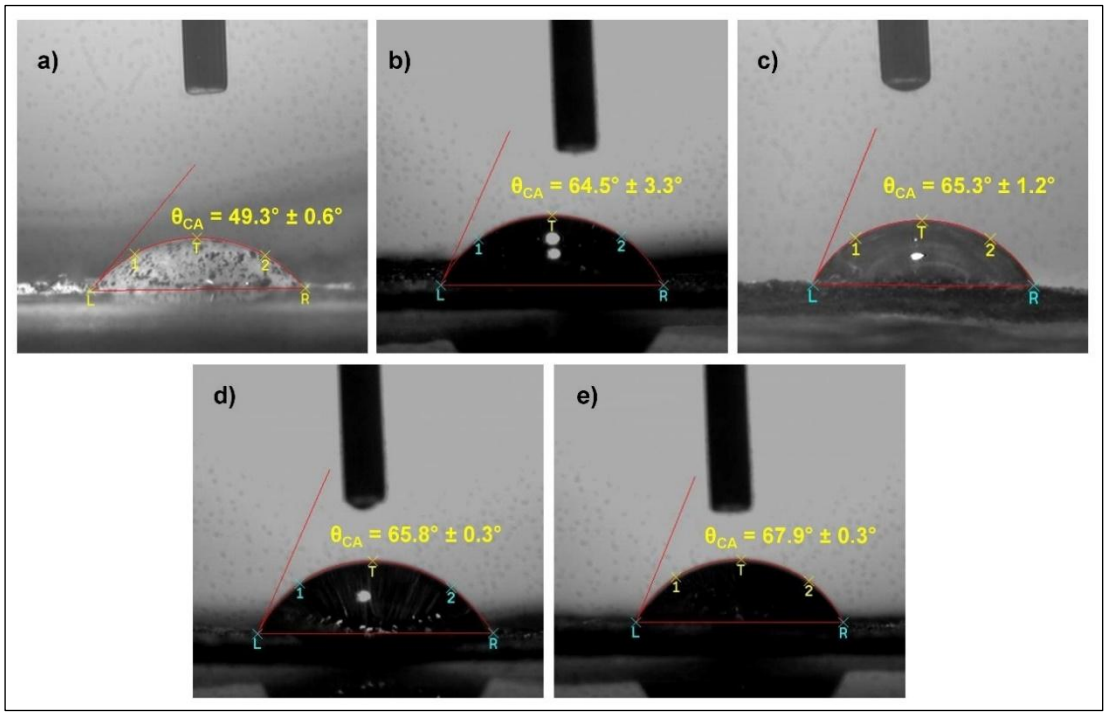

Figure 4.17 Water Contact Angle Measurements of the Prepared (a) S-PN-FP, (b) S-N/G-0.5-FP, (c) S-N/G-1.0-FP, (d) S-N/G-1.5-FP, and (e) S-N/G-2.0-FP

Table 4.5
Contact Angle Measurement Data of Samples S-PN, S-NG-0.5, S-NG-1.0, S-NG-1.5, and S-NG-2.0

Sample	WCA (°)	Surface Energy (mJ/m^2)
S-PN-FP	49.3° ± 0.6°	30.1 ± 0.1
S-NG-0.5-FP	64.5° ± 3.3°	26.0 ± 0.9
S-NG-1.0-FP	65.3° ± 1.2°	25.8 ± 0.3
S-NG-1.5-FP	65.8° ± 0.3°	25.7 ± 0.1
S-NG-2.0-FP	67.9° ± 0.3°	25.1 ± 0.1

For the S-NG-FP samples with varying Gr loadings, the θ_{CA} values were observed to be 64.5° ± 3.3°, 65.3° ± 1.2°, 65.8° ± 0.3°, and 67.9° ± 0.3° for S-NG-0.5-FP, S-NG-1.0-FP, S-NG-1.5-FP, and S-NG-2.0-FP, respectively. The corresponding surface energy values calculated using Equation (2.8), ranged from 25 to 26 mJ/m^2. These results indicate a slight increase in θ_{CA} with increasing Gr loading from 0.5 wt.% to 2.0 wt.%. This trend aligns with previous studies, which suggest that the observed increment is attributed to changes in surface morphology that influence wettability [293, 294]. However, the increase in θ_{CA} across the samples is not very noticeable. This suggests that the amount of Gr loading does not significantly influence the WCA, as the θ_{CA} values and surface energy remain relatively similar among the samples.

4.3.4 Molecular Vibrational Spectroscopy Analysis of NiO/Gr Composites

Raman spectroscopy was conducted to further investigate the defects and significant changes in the microstructures of the S-NG composites. The results, shown in Figure 4.18, indicate that the S-PN nanoparticles exhibit vibrational peaks at approximately 509 cm^{-1} and 1053 cm^{-1}, corresponding to the first-order longitudinal optical (LO) mode and second-order longitudinal optical (2LO) mode, respectively. The formation of the NiO phase in the samples was confirmed by the Raman vibrational bands of NiO, which appear at locations consistent with values reported in the literature [295]. In contrast, the Raman spectrum of the S-NG composites reveals three additional distinctive peaks, the G band at approximately 1571 cm^{-1}, the D band at approximately 1335 cm^{-1}, and the second-order overtone of the D vibration (2D) at approximately 2696 cm^{-1} [296]. The D band is associated with defects in the Gr structure, while the G band corresponds to the stretching vibrations of the in-plane sp^2-hybridized carbon atoms in Gr [288, 297].

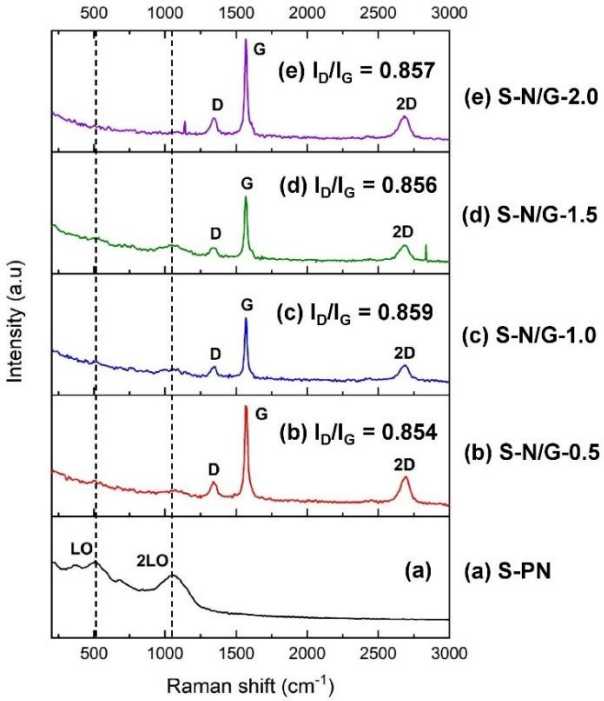

Figure 4.18 Raman Spectra of the S-PN and S-NG Composites Powder with Varying Gr Loading

As the Gr content increases from 0.5 wt.% to 2.0 wt.%, the intensity of the LO and 2LO peaks decreases significantly. This reduction is attributed to the lower concentration of NiO as the Gr content rises. The higher Gr content in the hybrid

samples likely weakens the NiO peaks as the laser beam cannot deeply penetrate the NiO layer. Furthermore, the shown D and G vibrational bands of the S-NG composites closely resemble those reported for pristine Gr, indicating that the Gr structure in the composites remains intact. This suggests that the NiO nanoparticles are successfully incorporated onto Gr sheets using the solution immersion method without disrupting the Gr structure.

The degree of graphitization in carbonaceous materials is often correlated with the I_D/I_G ratio. Low I_D/I_G values ($I_D/I_G \leq 1$) are a key characteristic indicating the pure Gr [298]. However, Gr sheets could lose their oxygen-containing functional groups during the reduction process, leading to the formation of defects in the Gr structure [299]. Based on the Raman spectrum, the calculated I_D/I_G ratio for each sample is less than 1, suggesting that Gr structure has low defects. Additionally, the Raman analysis of all S-NG composites samples shows the coexistence of NiO and Gr phonon modes, which successively confirms the successful formation of the composites.

4.3.5 Chemical Composition Analysis of NiO/Gr Composites

The chemical composition and oxidation state of the S-NG composites were further confirmed using XPS over a binding energy range of 0 to 1200 eV. Figure 4.19 (a) to (d) presents the XPS survey spectrum and high-resolution spectra of the Ni 2p, C 1s, and O 1s regions for the S-NG composites. As shown in Figure 4.19 (a), the composites primarily consist of C, O, and Ni. The high-resolution XPS spectrum of Ni 2p, displayed in Figure 4.19 (b), confirms the presence of NiO, as evidenced by the prominent peaks at 855.82 eV and 861.80 eV. Additionally, the Ni phase is represented by peaks at 854.15 eV and 858.03 eV. The high-resolution C 1s spectrum, shown in Figure 4.19 (c), reveals peaks corresponding to Gr in the form of non-oxygenated carbon bonds: C=C and C–C at 283.50 eV and 284.74 eV, respectively. Additionally, strong peaks at 285.99 eV and 285.47 eV correspond to carbonyl carbon (C=O) and oxygen-containing functional groups (C–O), respectively. The presence of highly conductive Gr in the composites may facilitate additional electron-transfer pathways and reduce electron-transfer distances, thereby enhancing conductivity [300].

Meanwhile, the high-resolution O 1s spectrum, presented in Figure 4.19 (d), exhibits deconvoluted peaks corresponding to the NiO phase at 528.34 eV, C=O at 529.95 eV, and C–O at 532.05 eV. The observed variation in oxidation states can be

attributed to the heterogeneous nature of the sample [301]. The high-resolution XPS results confirm the chemical composition and various oxidation states of the sample. These findings align well with the XRD data, confirming the presence of NiO and Gr in the synthesized composites.

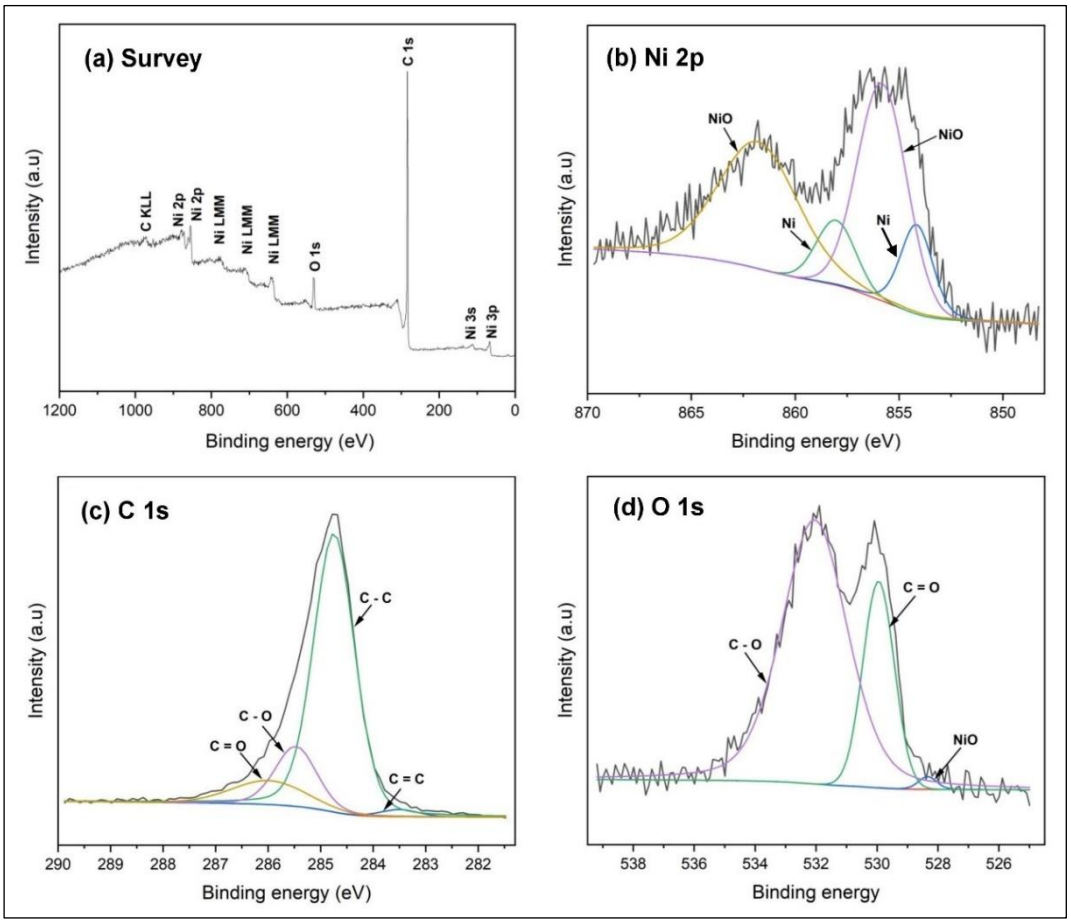

Figure 4.19 The XPS Spectra of the S-NG-1.0 Powder; (a) Full-Range Survey Spectra, High-Resolution Spectra of (b) Ni 2p Region, (c) C 1s Region, and (d) O 1s Region

4.3.6 Surface Area and Porosity Analysis of NiO/Gr Composites

BET analyses are used to further study the fibrous, porous structure of the synthesized material. The nitrogen (N_2) adsorption-desorption isotherm for S-PN and S-NG composites powder is shown in Figure 4.20. At a relative pressure P/P° between 0 and 1, the type IV isotherms with a noticeable hysteresis loop were observed [302, 303]. The early section of the isotherm generally shows monolayer-multilayer adsorption at low relative pressure, which than followed by capillary condensation and pore-filling [304]. The observed hysteresis loop's shape is related to pores formed by NiO nanoparticle aggregations, indicating that the sample is made of NiO-decorated

sheet-like Gr. According to the BJH method, which was used to determine the distribution of the average pore sizes, it indicates the presence of textural mesopores (2 – 50 nm) in the S-PN and S-NG composites samples with relatively uniform pore size distribution [17].

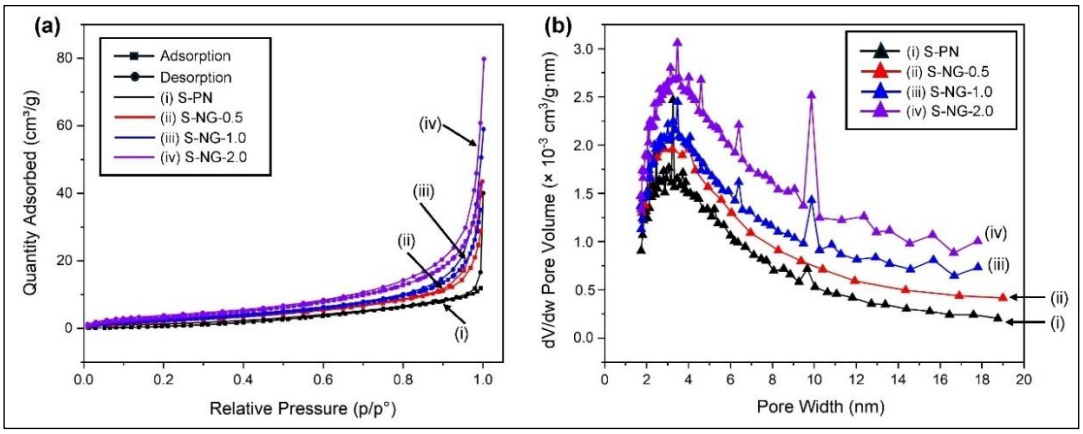

Figure 4.20 BET Isotherm Plot; (a) N_2 Adsorption Desorption of S-PN and S-NG Composites Powder with Varying Gr Loading, and (b) BJH Adsorption dv/dw Pore Volume of S-PN and S-NG Composites Powder with Varying Gr Loading, dv/dw refers to the Change Rate of Pore Volume with Pore Width

From the isotherm, it is confirmed that S-NG composites have larger BET surface area compared to the S-PN which supported by the estimations presented in Table 4.6. The calculated BET surface areas of S-PN were found to be 4.9 m^2/g and it increased as the Gr loading increasing. Generally, intrinsic Gr has a remarkably large surface area of up to 2600 m^2/g [305]. Due to its 2D sheet-like structure, increasing the amount of Gr in a composite enhances its surface area, thereby expanding the interlayer spacing where mesopores facilitate ion diffusion within the NG channels [306]. When more Gr is added, it may prevent complete aggregation by forming a more open, interconnected and porous network. An excessive amount of Gr can lead to wrinkles and defects that increase the total BET surface area, indicating greater surface roughness and resulting in a larger exposed surface area for adsorption.

Table 4.6
Comparison of the BJH Adsorption Average Pore Diameter and BET Surface Area of S-PN and S-N/G Composites Powder with Varying Gr Loading

Sample	BJH Adsorption average pore diameter (nm)	BET surface area (m^2/g)
S-PN	5.0	4.9
S-NG-0.5	5.4	8.9
S-NG-1.0	5.6	10.2
S-NG-2.0	5.7	13.5

4.3.7 Electrical Characterization of NiO/Gr Composites-based HGPG

The Hall effect, along with the van der Pauw method, was used to obtain additional information on the electrical characteristics of the prepared S-PN and S-NG composites on a cellulose-based substrate. The p-type conductivity of all samples was found to be comparable to that reported in other studies on NiO-based materials [307]. From the measurement findings, the carrier concentration varied from $(1.4 \pm 0.1) \times 10^{13}$ cm^{-3} to $(4.1 \pm 0.8) \times 10^{13}$ cm^{-3}, while the mobility of all samples ranged from $(1.1 \pm 0.1) \times 10^{2}$ $cm^2/V{\cdot}s$ to $(2.7 \pm 0.6) \times 10^{3}$ $cm^2/V{\cdot}s$, depending on the amount of Gr content. The Hall coefficient of the samples obtained from the measurement varied from $(1.6 \pm 0.1) \times 10^{5}$ cm^3/C to $(4.5 \pm 0.2) \times 10^{5}$ cm^3/C, as presented in Table 4.7. The results highlight the relationship between carrier concentration and resistivity, which ultimately affects conductivity [308].

Table 4.7
Hall Effect Measurement Data of S-PN and S-N/G Composites on Cellulose-Based Substrate with Varying Gr Loading

Sample	**Carrier Concentration (cm^{-3})**	**Hall Coefficient (cm^3/C)**	**Mobility ($cm^2/(V{\cdot}s)$)**	**Conductivity, σ (S/cm)**
S-PN-FP	$(3.2 \pm 0.2) \times 10^{13}$	$(2.0 \pm 0.1) \times 10^{5}$	$(1.1 \pm 0.1) \times 10^{2}$	$(0.6 \pm 0.1) \times 10^{-3}$
S-NG-0.5-FP	$(4.1 \pm 0.8) \times 10^{13}$	$(1.6 \pm 0.3) \times 10^{5}$	$(1.9 \pm 0.1) \times 10^{2}$	$(1.3 \pm 0.2) \times 10^{-3}$
S-NG-1.0-FP	$(3.0 \pm 0.2) \times 10^{13}$	$(2.1 \pm 0.2) \times 10^{5}$	$(2.7 \pm 0.6) \times 10^{3}$	$(1.3 \pm 0.2) \times 10^{-2}$
S-NG-1.5-FP	$(1.4 \pm 0.1) \times 10^{13}$	$(4.5 \pm 0.2) \times 10^{5}$	$(1.6 \pm 0.2) \times 10^{3}$	$(3.6 \pm 0.3) \times 10^{-3}$
S-NG-2.0-FP	$(3.9 \pm 0.1) \times 10^{13}$	$(1.6 \pm 0.1) \times 10^{5}$	$(6.5 \pm 0.4) \times 10^{2}$	$(4.0 \pm 0.1) \times 10^{-3}$

The Hall effect is also widely used as a method for accurately determining carrier mobility in semiconductor materials. By measuring the Hall coefficient and mobility, the electrical conductivity can be accurately estimated using Equation (3.6). From the calculations, S-NG-1.0-FP is estimated to have the highest conductivity value of $(1.3 \pm 0.2) \times 10^{-2}$ S/cm. The conductivity tends to increase as the Gr content increases from S-PN to S-NG-1.0. This observation aligns with a recent report by T. Rajyalakshmi et al. [309], in which they successfully developed conducting polyaniline and Gr composites using an in situ chemical oxidative polymerization method. According to their study, the conductivity of the prepared materials increased as the Gr content increased from 0 to 15 wt.%.

Gr is well known as a highly conductive material with extremely high carrier mobility [310-312]. The addition of Gr to NiO facilitates the movement of charge carriers and influences their mobility along the π-conjugated system of Gr, thereby

increasing electrical conductivity [313]. As more Gr layers are distributed throughout the matrix, the possibility of overlapping increases, further contributing to the increase in electrical conductivity. However, excessive Gr loading may lead to unstructured restacking, which could negatively affect the composite's electrical conductivity [314, 315]. This may explain the reduction in conductivity when the Gr loading exceeds 1.0 wt.%.

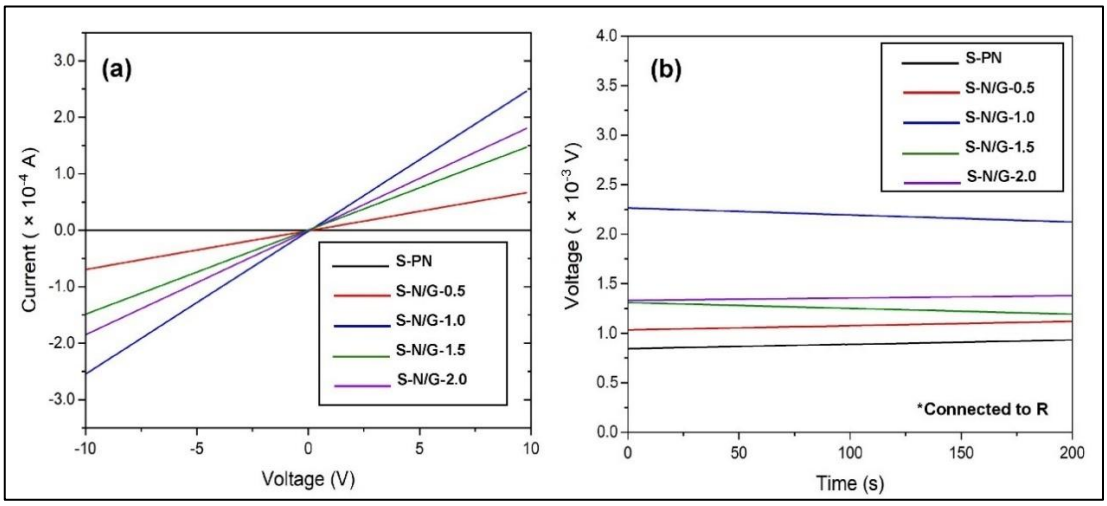

Figure 4.21 (a) The 2-Probe I-V Properties of S-PN and S-NG-FP with Varying Gr Loading. (b) The Plot of Voltage Versus Time Under Fixed RH of 75% with Zero Bias Applied for S-PN and S-NG-FP at Varying Gr Loading

Humidity-to-energy devices based on S-PN and S-NG composites, deposited on FP-based cellulose substrates with an adsorption area of 1.25 cm^2, were prepared to evaluate the devices' humidity response. Figure 4.21 (a) show the two-probe I-V properties of the devices, while Figure 4.21 (b) illustrates the voltage versus time at RT under 75% RH without an applied bias and connected to a 10 MΩ resistor. The results indicate that the S-NG-1.0 device produced the highest output voltage of (2.24 ± 0.03) × 10^{-3} V, a current density of (1.79 ± 0.02) × 10^{-10} A/cm^2, and an output power of (5.02 ± 0.13) × 10^{-13} W. The humidity energy conversion of the fabricated devices is presented in Table 4.8.

Table 4.8
The Humidity-To-Energy Performance of Fabricated S-PN-FP and S-NG-FP-Based HGPG Devices

Sample	RH (%)	R (MΩ)	Output voltage, V (V)	Current density, J (A/cm^2)	Power, P (W)
S-PN-FP	75	10	(8.89 ± 0.25) ×10^{-4}	(7.12 ± 0.20) ×10^{-11}	(7.92 ± 0.45) ×10^{-14}
S-NG-0.5-FP			(1.08 ± 0.03) ×10^{-3}	(8.80 ± 0.22) ×10^{-11}	(1.21 ± 0.06) ×10^{-13}
S-NG-1.0-FP			(2.24 ± 0.03) ×10^{-3}	(1.79 ± 0.02) ×10^{-10}	(5.02 ± 0.13) ×10^{-13}

S-NG-1.5-FP	$(1.25 \pm 0.03) \times 10^{-3}$	$(1.04 \pm 0.03) \times 10^{-10}$	$(1.69 \pm 0.09) \times 10^{-13}$
S-NG-2.0-FP	$(1.35 \pm 0.02) \times 10^{-3}$	$(1.12 \pm 0.01) \times 10^{-10}$	$(1.96 \pm 0.04) \times 10^{-13}$

Figure 4.22 (a) to (e) depict the current versus time under different RH levels ranging from 40% to 90%, without any applied bias and no connection to any resistor. According to the analysis, all devices exhibit excellent absorption (40% - 90% RH) (supplementary video (V2) in APPENDIX 3) and desorption (90% - 40% RH) (supplementary video (V3) in APPENDIX 4) during humidity fluctuations. A strong correlation exists between the electrical generation capacity of the device and moisture content, as evidenced by the output current increasing with RH and decreasing as RH decreases. This phenomenon supports the presence of an ion gradient and diffusion, which can be explained by the increase in ion concentration within a fixed amount of absorbed water as the RH rises [4, 316].

The results further reveal that as the RH level reached 90%, the S-NG-1.0 device exhibited the highest output current of 2.3 nA among the prepared devices, whereas the S-PN-FP-based device produced the lowest output current of 1.1 nA. This suggests that the varying amounts of Gr loading used in this study play a crucial role in humidity-to-energy applications, as they affect water molecule trapping and contribute to a significant output voltage [28]. The hygroscopic nature of NiO and Gr, along with the use of FP as a cellulose-based substrate, promotes ion mobility, generating currents and electric fields that enhance the efficiency of the humidity-to-energy devices [317-320].

To conduct a thorough investigation, the S-NG-1.0-FP-based HGPG device was tested at 75% RH under three different ambient temperatures (RT=25°C, 50°C, and 75°C) without a resistor connected, as illustrated in Figure 4.23 (a). The results clearly indicate that as the ambient temperature increases, less electrical energy is produced. The device exhibits its highest output voltage of $(5.19 \pm 0.05) \times 10^{-2}$ V at an ambient temperature of 25°C. This is attributed to the optimal balance between water molecule absorption and ion transport at this temperature. Additionally, this phenomenon can be explained by the decrease in RH as temperature rises, leading to a lower output voltage [316].

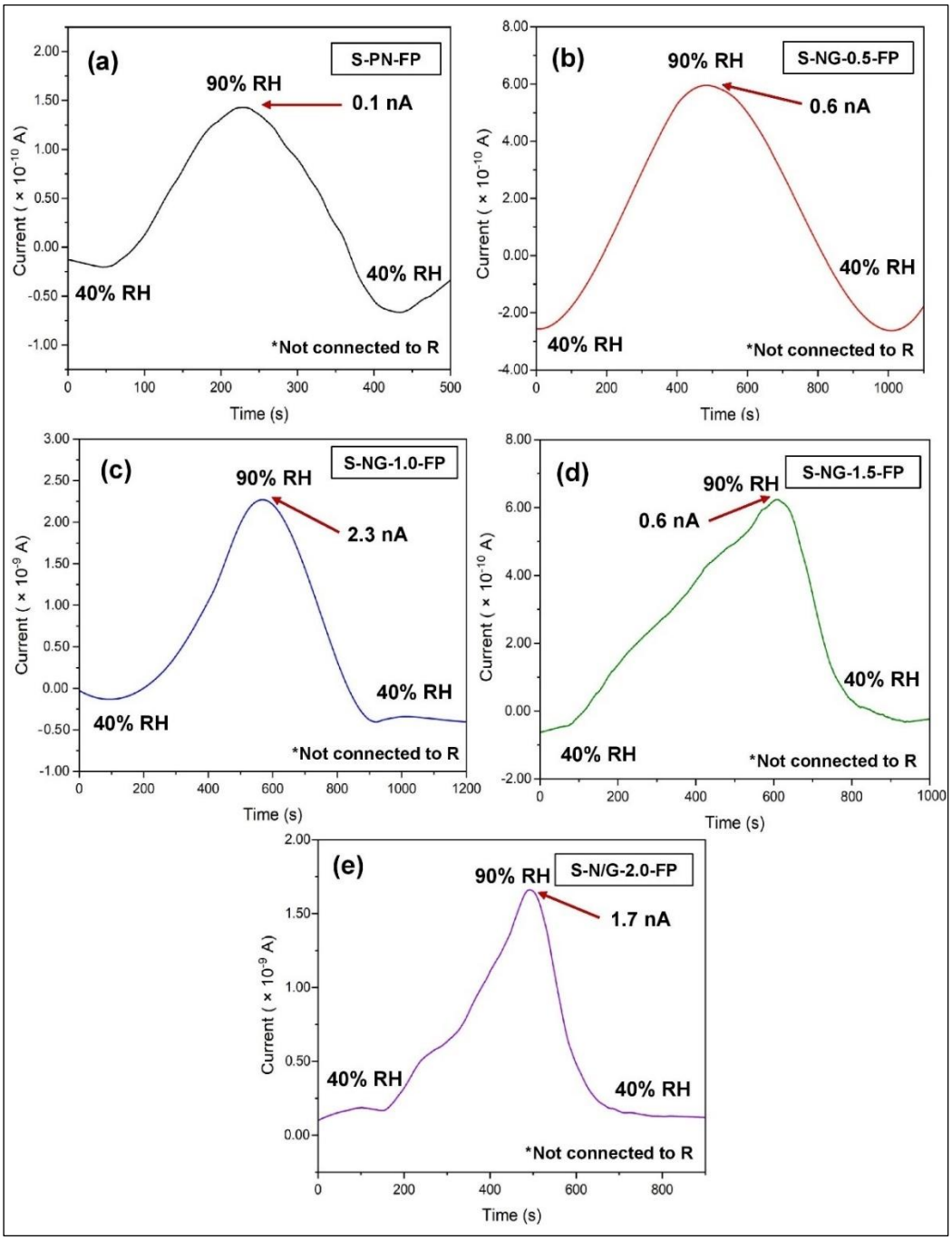

Figure 4.22 The Current Versus Time at Various RH Levels with Zero Bias Applied to The Samples: (a) S-PN-FP, (b) S-N/G-0.5-FP, (c) S-N/G-1.0-FP, (d) S-N/G-1.5-FP, and (e) S-N/G-2.0-FP

The long-term stability of the device is another essential parameter in evaluating the humidity conversion performance of the S-NG-1.0 composites. The humidity response of the S-NG-1.0-FP-based HGPG was evaluated approximately one year later at RT under 75% RH, and the resulting stability is shown in Figure 4.23 (b). The device was able to generate an output voltage even after more than 400 days, with an average output voltage of $(2.13 \pm 0.10) \times 10^{-3}$ V. This demonstrates that the S-NG-1.0-FP-based

HGPG exhibits reliable and commendable long-term stability in humidity response.

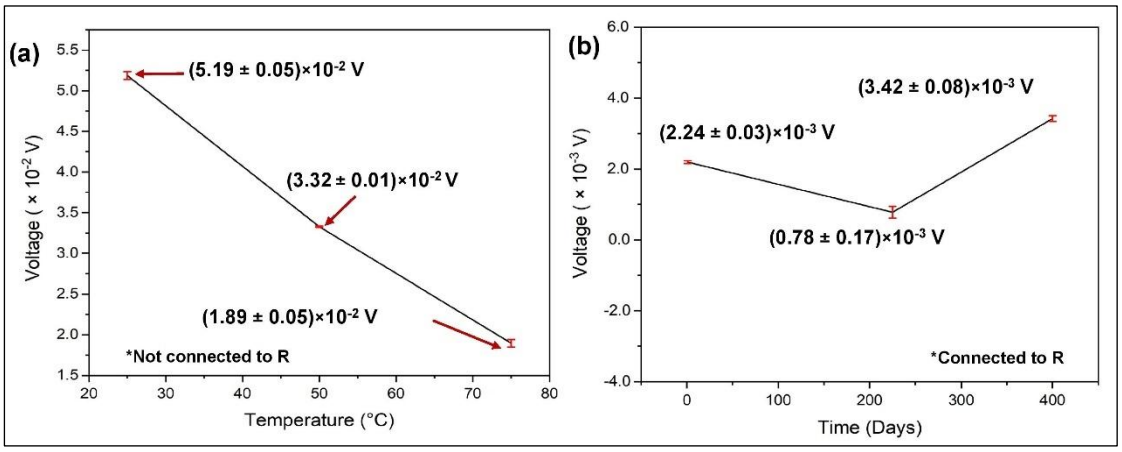

Figure 4.23 (a) Output Voltage Under RH of 75% For S-N/G-1.0-FP-Based HGPG Produced at Different Ambient Temperatures. (b) Plot of Output Voltage Measured at Different Days for the S-N/G-1.0-FP-Based HGPG Device at RT Under 75% RH

4.4 Conclusion

In conclusion, this study confirms the potential of S-NG composite as a promising material for harvesting energy from humidity. Through the non-sophisticated methods of sonicated solution immersion technique and the doctor-blade method, a humidity-to-electricity device was successfully developed using S-NG composite as the hygroscopic material on a cellulose substrate. All samples were analysed structurally, morphologically, chemically, and electrically using characterization techniques such as FESEM, EDX, HRTEM, XRD, WCA, Raman, XPS, BET, and Hall effect measurements. The results indicated relative consistency across various Gr loadings, demonstrating good dispersion of S-NG composites within the porous network of FP. As the Gr loading percentage increased, the S-NG composites particles became denser, forming a structure more firmly bonded to the fibrils. The XRD patterns vividly illustrated crystallized cubic NiO, which possesses highly crystalline and polycrystalline structures. The Debye-Scherrer formula was used to compute the D, showing a decrease in size with increasing Gr loading. The particle size derived from XRD analysis was further supported by HRTEM findings. Additionally, the results demonstrated that all samples exhibited hydrophilic properties. Raman spectroscopy confirmed the formation of the S-NG composites through the presence of D and G bands, which are associated with the carbon structure and were observed in all samples. XPS analysis further verified the presence of Ni, O, and C as the primary elements of

the S-NG composites. Based on Hall effect measurements, S-NG-1.0-FP was identified as the optimal Gr loading, exhibiting high conductivity and carrier mobility. The humidity-to-energy device based on the S-NG-1.0-FP sample demonstrated the highest humidity response, with an output voltage of $(2.24 \pm 0.03) \times 10^{-3}$ V, a current density of $(1.79 \pm 0.02) \times 10^{-10}$ A/cm^2, and an output power of $(5.02 \pm 0.13) \times 10^{-13}$ W, as summarized in Table 4.9. Furthermore, additional studies on the effect of ambient temperature revealed that the device achieved its maximum output voltage of $(5.19 \pm 0.05) \times 10^{-2}$ V at 25°C. Overall, these findings suggest that controlling the Gr loading element is crucial. These findings emphasize the feasibility and effectiveness of utilizing S-NG composite for humidity-based energy harvesting applications, which provides the opportunity for further progress in this field. However, as the power generated by the fabricated device remains low, further research should be undertaken to explore the development of materials that can enhance conductivity and electron mobility, thereby improving overall HGPG device performance.

Table 4.9
Humidity-To-Energy Performance of the Fabricated HGPG Devices Connected to a 10 MΩ Resistor Under 75% RH

Conditions	**Sample**	**Output voltage, V (V)**	**Current density, J (A/cm^2)**	**Power, P (W)**
Different Gr loading	S-PN-FP	$(8.89 \pm 0.25) \times 10^{-4}$	$(7.12 \pm 0.20) \times 10^{-11}$	$(7.92 \pm 0.45) \times 10^{-14}$
	U-NG-1.0-FP	$(0.14 \pm 0.01) \times 10^{-3}$	$(11.12 \pm 0.07) \times 10^{-12}$	$(1.93 \pm 0.12) \times 10^{-15}$
	S-NG-0.5-FP	$(1.08 \pm 0.03) \times 10^{-3}$	$(8.80 \pm 0.22) \times 10^{-11}$	$(1.21 \pm 0.06) \times 10^{-13}$
	S-NG-1.0-FP	$(2.24 \pm 0.03) \times 10^{-3}$	$(1.79 \pm 0.02) \times 10^{-10}$	$(5.02 \pm 0.13) \times 10^{-13}$
	S-NG-1.5-FP	$(1.25 \pm 0.03) \times 10^{-3}$	$(1.04 \pm 0.03) \times 10^{-10}$	$(1.69 \pm 0.09) \times 10^{-13}$
	S-NG-2.0-FP	$(1.35 \pm 0.02) \times 10^{-3}$	$(1.12 \pm 0.01) \times 10^{-10}$	$(1.96 \pm 0.04) \times 10^{-13}$

CHAPTER 5
SURFACE MODIFICATION THROUGH STEARIC ACID TREATMENT FOR HUMIDITY GRADIENT ENERGY HAVESTING APPLICATION

5.1 Introduction

As outlined in the working principle of humidity-to-energy conversion, the adsorption process constitutes a decisive stage in transducing ambient humidity into electrical energy. Materials exhibiting optimal hydrophilicity tend to demonstrate superior water adsorption kinetics, thereby enhancing the operational efficiency of humidity-driven energy harvesting devices [152, 321]. Nonetheless, achieving a balanced hydrophilic profile is critical: excessive hydrophilicity accelerates water uptake to the point of impeding recovery dynamics, whereas insufficient hydrophilicity slows adsorption rates, ultimately compromising device responsiveness [152]. To finely tune the adsorption–desorption equilibrium in the S-NG composites, this study employed surface modification via SA treatment at different parameters [153, 154], ensuring a controlled hydrophilic interface conducive to sustained and efficient humidity-to-electricity conversion.

5.2 Optimization Parameters for SA Treatment

To engineer an optimally tuned hydrophilic interface for the developed composite system, a systematic parametric investigation was undertaken, interrogating the synergistic influences of SA content, immersion temperature, and immersion duration on surface functionalization dynamics. These parameters critically govern the nucleation, growth, and molecular packing density of the SA-derived monolayer, thereby dictating surface free energy modulation, wettability characteristics, and the consequent charge-generation efficiency in humidity-to-electricity conversion. The SA functionalization regime encompassed controlled variations in precursor concentration (i.e., 1–4 wt.%), thermal immersion conditions (i.e., 30 °C, 60 °C, and 90 °C), and temporal exposure intervals (i.e., 2, 4, 6, and 8 h), as delineated in Sections 3.4.1 to 3.4.3. The ensuing analytical framework encompassed high-resolution hydrophilicity

quantification and comprehensive performance benchmarking of humidity-gradient power generation, enabling the precise correlation between interfacial chemistry and device-level energy harvesting efficacy.

5.2.1 Optimization at Various SA Concentration

Figure 5.1 presents the XRD diffraction profiles of samples subjected to varying SA loadings. Prominent reflections at 2θ ≈ 37.22°, 44.50°, and 62.49° are indexed to the ♣(1 1 1), ♣(2 0 0), and ♣(3 1 1) crystallographic planes of NiO (JCPDS No. 01-071-4750), respectively. Meanwhile, characteristic peaks at 26.52° and 54.62° correspond to the ★(0 0 2) and ★(0 0 4) planes of Gr (JCPDS No. 00-041-1487). In addition, the presence of SA is confirmed by the diffraction signal at 21.62°, attributable to the ♦(3 1 1) plane (JCPDS No. 00-038-1923). The magnified XRD spectra in Figure 5.1 reveal the emergence of SA-associated peaks corresponding to the ♦(3 1 1) plane, first appearing in S2%-NG-1.0, indicative of molecular interactions between the SA and the developed composite.

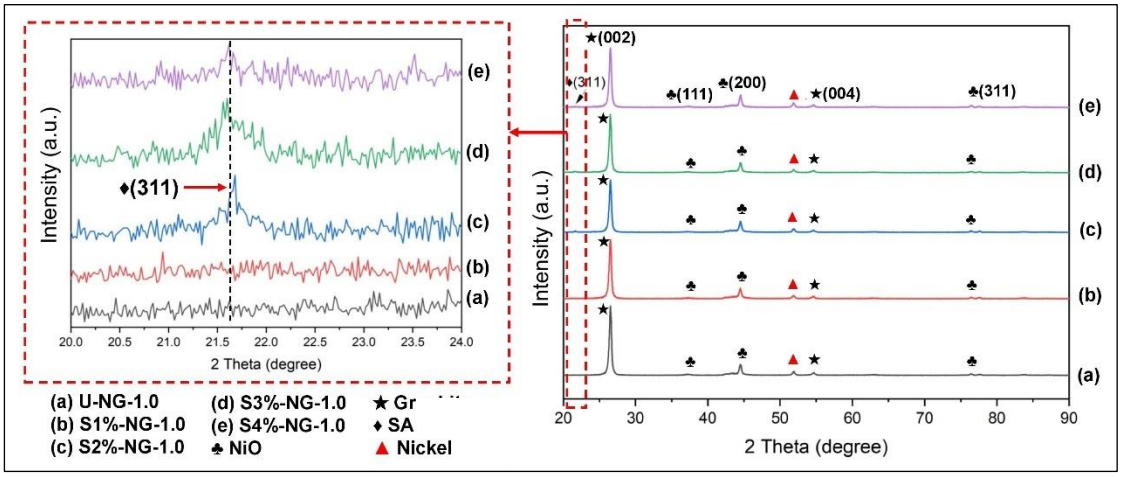

Figure 5.1 XRD Pattern for (a) U-NG-1.0, (b) S1%-NG-1.0 (c) S2%-NG-1.0 (d) S3%-NG-1.0 and (e) S4%-NG-1.0

Analysis of the XRD profiles revealed that the D of NiO, calculated from the ♣(1 1 1) plane orientation via the Debye–Scherrer formula (Equation (3.1)), exhibited a marked reduction from 8.5 nm to 6.4 nm upon SA functionalization, as detailed in Table 5.1. This reduction in D aligns with the observations of Patil et al. [322], who attributed such size suppression to the steric hindrance and lattice-growth inhibition

imparted by surface-passivating SA molecules. Intriguingly, progressive elevation of the SA content from 1 wt.% to 4 wt.% induced a pronounced crystallite coarsening, indicative of a transition in the surface–particle interaction regime whereby excess SA promotes nanoparticle agglomeration and facilitates crystallite enlargement through aggregation-mediated coalescence. Meanwhile, the interplanar spacing and unit cell volume exhibited nearly no significant changes, consistent with the nearly unchanged diffraction peak positions observed across all samples.

Table 5.1
The FWHM, 2θ, Interplanar Spacing, Unit Cell Volume, and Crystallite Size of NiO ♣(1 1 1) Plane for the Samples Treated with Different SA Content

Sample	FWHM, β (rad)	2θ (°)	Interplanar spacing, d (nm)	Unit Cell Volume, V (nm^3)	Crystallite size, D (nm)
U-NG-1.0	0.0173	37.02	0.242	0.074	8.5
S1%-NG-1.0	0.0229	37.26	0.241	0.073	6.4
S2%-NG-1.0	0.0174	37.28	0.241	0.073	8.4
S3%-NG-1.0	0.0166	37.26	0.241	0.073	8.8
S4%-NG-1.0	0.0142	37.34	0.241	0.073	10.3

The systematic investigation demonstrated that elevating the SA loading corresponding to progressively higher treatment concentrations, markedly enhanced the formation of a densely packed, well-ordered molecular overlayer on the S-NG-1.0 surface. This structural refinement translated into a monotonic increase in the θ_{CA} of S-NG-1.0-FP with rising SA content, as illustrated in Figure 5.2. The corresponding surface energy metrics, tabulated in Table 5.2, reveal the inverse correlation between θ_{CA} and surface energy: elevated surface energy, indicative of strong intermolecular attraction and facile interfacial bond formation, promotes rapid water spreading and thus lowers θ_{CA}, whereas diminished surface energy weakens intermolecular interactions, thereby increasing θ_{CA}.

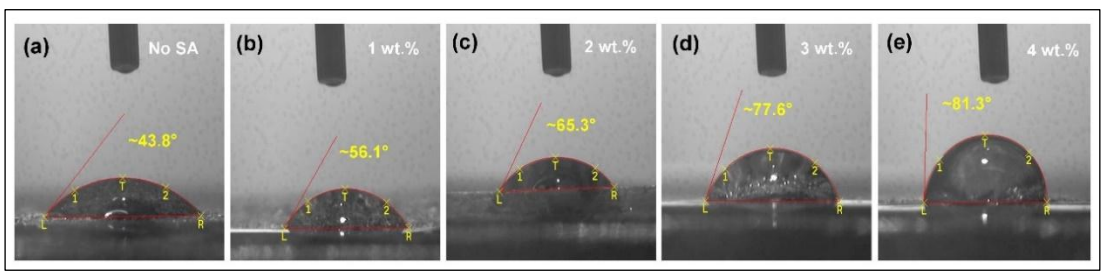

Figure 5.2 Water Contact Angle Measurements for (a) U-NG-1.0, (b) S1%-NG-1.0 (c) S2%-NG-1.0 (d) S3%-NG-1.0 and (e) S4%-NG-1.0

Table 5.2
Contact Angle Measurement Data of the Samples Treated with Different SA Content

Sample	Immersion Temperature (°C)	Immersion duration (hours)	WCA (°)	Surface Energy (mJ/m^2)
U-NG-1.0	60	6	43.8 ± 0.1	31.3 ± 0.1
S1%-NG-1.0			56.1 ± 0.3	28.4 ± 0.1
S2%-NG-1.0			65.3 ± 1.2	25.8 ± 0.3
S3%-NG-1.0			77.6 ± 0.8	22.1 ± 0.2
S4%-NG-1.0			81.3 ± 0.9	21.0 ± 0.3

There is a strong correlation between the sample's surface morphology and its wettability behaviour. Surface modification induced by SA treatment at higher concentrations enables more SA molecules to adhere to the sample surface, resulting in a denser and more uniformly distributed molecular layer. This contributes to a higher θ_{CA} and lower surface energy. Figure 5.3 (a) provides a clear illustration of the relationship between SA content and the θ_{CA}.

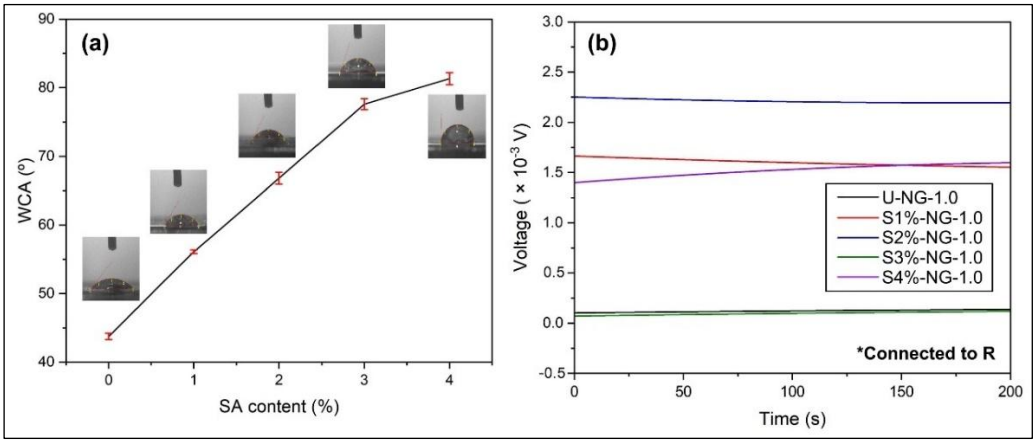

Figure 5.3 (a) Graph of Contact Angle Variation with The Different SA Content. (b) The Plots of Voltage Versus Time at A Fixed RH Of 75% with Zero Applied Bias for Cellulose-Based Devices using U-NG-1.0 and S-NG-1.0 Samples with Different SA Content

Figure 5.3 (b) shows the voltage versus time at RT and under 75% RH, recorded without an applied bias and with a 10 MΩ resistor connected. Table 5.3 summarizes the humidity-to-energy performance of the fabricated HGPG devices using S-NG-1.0-FP with varying SA content. The highest recorded output values were an output voltage of $(2.24 \pm 0.03) \times 10^{-3}$ V, a current density of $(1.79 \pm 0.02) \times 10^{-10}$ A/cm^2, and an output power of $(5.02 \pm 0.13) \times 10^{-13}$ W. These results indicate that the S-NG-1.0-FP

composite with 2 wt.% SA exhibited the most optimal characteristics for this application.

Table 5.3
The Humidity-To-Energy Performance of the Fabricated HGPG Device at Different SA Content Under Fixed SA Immersion Temperature Of 60°C and SA Immersion Duration of 6h

Sample	RH (%)	R (MΩ)	Output voltage, V (V)	Current density, J (A/cm^2)	Power, P (W)
U-NG-1.0	75	10	$(0.14 \pm 0.01) \times 10^{-3}$	$(11.12 \pm 0.07) \times 10^{-12}$	$(1.93 \pm 0.12) \times 10^{-15}$
S1%-NG-1.0			$(1.56 \pm 0.04) \times 10^{-3}$	$(1.25 \pm 0.03) \times 10^{-10}$	$(2.43 \pm 0.13) \times 10^{-13}$
S2%-NG-1.0			$(2.24 \pm 0.03) \times 10^{-3}$	$(1.79 \pm 0.02) \times 10^{-10}$	$(5.02 \pm 0.13) \times 10^{-13}$
S3%-NG-1.0			$(1.17 \pm 0.19) \times 10^{-4}$	$(9.36 \pm 1.52) \times 10^{-12}$	$(1.37 \pm 0.45) \times 10^{-15}$
S4%-NG-1.0			$(1.54 \pm 0.08) \times 10^{-3}$	$(1.23 \pm 0.06) \times 10^{-10}$	$(2.37 \pm 0.25) \times 10^{-13}$

5.2.2 Optimization at Different Immersion Temperature

Engineering a highly ordered molecular overlayer on the composite surface necessitates precise optimization of the SA synthesis temperature. Empirically, SA molecular assemblies exhibit accelerated nucleation kinetics, reduced defect density, and superior long-range ordering when processed above 25 °C [323]. In this work, SA functionalization was systematically performed at immersion temperatures of 30 °C, 60 °C, and 90 °C to elucidate the thermally induced ordering phenomena.

The corresponding XRD profiles, presented in Figure 5.4, reveal well-defined diffraction maxima at $2\theta \approx 37.24°$, 44.50°, and 62.49°, indexed to the ♣(1 1 1), ♣(2 0 0), and ♣(3 1 1) crystallographic planes of NiO (JCPDS No. 01-071-4750), respectively. Additionally, characteristic Gr diffraction signals are evident at 26.58° and 54.72°, corresponding to the ★(0 0 2) and ★(0 0 4) planes (JCPDS No. 00-041-1487), confirming the retention of Gr domains post-treatment. From the XRD profiles, a prominent diffraction signal at 21.62°, corresponding to the ♦(3 1 1) plane (JCPDS No. 00-038-1923), is distinctly observed for the S60-NG-1.0 sample, confirming the presence of crystalline SA. It is noteworthy that SA exhibits a melting range of approximately 69–70 °C. At 60 °C, SA exists in a semi-molten state, enabling enhanced molecular mobility that facilitates the formation of ordered crystalline domains, thereby producing distinct XRD signals [324]. At lower temperatures, the limited mobility of SA molecules suppresses crystalline ordering, resulting in extremely weak diffraction intensities, effectively rendering the SA peak absent. Conversely, at higher temperatures, SA becomes fully molten, and the elevated thermal energy disrupts the

molecular packing required for recrystallization, ultimately eliminating the corresponding SA peak from the XRD spectra.

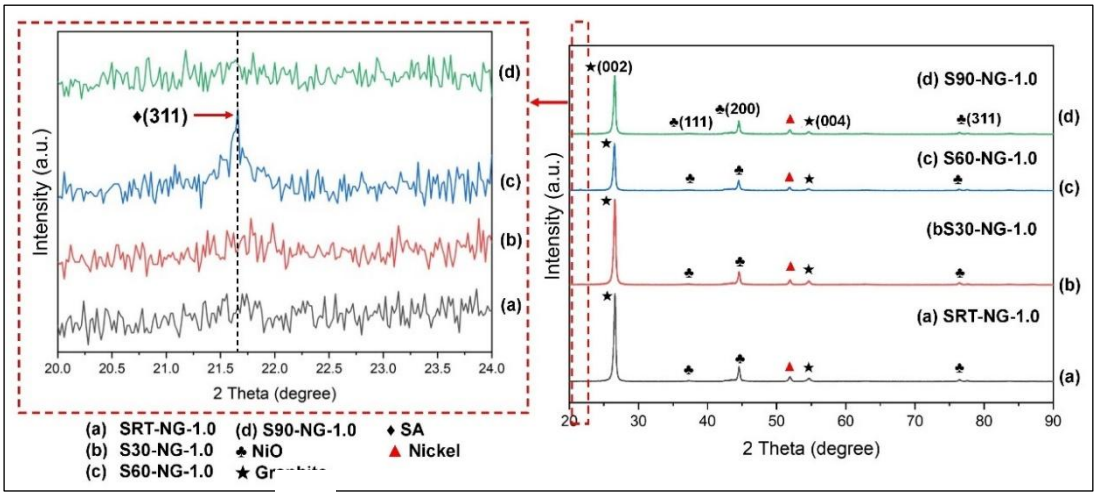

Figure 5.4 XRD Pattern for (a) SRT-NG-1.0, (b) S30-NG-1.0, (c) S60-NG-1.0 and (d) S90-NG-1.0

Table 5.4
The FWHM, 2θ, Interplanar Spacing, Unit Cell Volume, And Crystallite Size of NiO ♣(1 1 1) for the Samples Treated at Different SA Immersion Temperatures

Sample	FWHM, β (rad)	2θ (°)	Interplanar spacing, d (nm)	Unit Cell Volume, V (nm^3)	Crystallite size, D (nm)
SRT-NG-1.0	0.0221	37.30	0.241	0.073	6.6
S30-NG-1.0	0.0212	37.22	0.242	0.073	6.9
S60-NG-1.0	0.0174	37.28	0.241	0.073	8.4
S90-NG-1.0	0.0159	37.22	0.242	0.073	9.2

Furthermore, the D of the treated samples was derived from the ♣(1 1 1) diffraction peak of NiO using the Debye–Scherrer equation [Equation (3.1)]. The SA-RT sample exhibited a D of 6.6 nm, which increased marginally to 6.9 nm upon treatment at 30 °C. More substantial growth was observed at elevated immersion temperatures, with D reaching 8.4 nm at 60 °C and 9.2 nm at 90 °C. This temperature-dependent crystallite enlargement is consistent with the findings of Chao et al. [325], where increased thermal energy during functionalization promoted lattice reordering and grain coarsening.

From a device performance standpoint, moderate crystallite growth can enhance charge transport pathways by reducing grain boundary density, thereby lowering interfacial resistance and improving ionic mobility in humidity-to-electricity conversion. However, excessive crystallite coarsening as observed at 90 °C, may reduce the specific surface area and active adsorption sites, leading to diminished water uptake

capacity. Thus, the observed structural evolution underscores a critical trade-off: optimizing immersion temperature is essential to balance crystallite growth for efficient electron transport with the preservation of sufficient surface area for hygroscopic interactions, ultimately determining the overall energy harvesting efficiency of the HGPG device. Table 5.4 presents a summary of the structural evaluation derived from XRD analyses, detailing the FWHM, diffraction angle, interplanar spacing, unit cell volume, and crystallite size for the samples subjected to varying SA immersion temperatures.

Table 5.5 summarizes, and Figure 5.5 depicts, the progressive increase in θ_{CA} with rising immersion temperature is inversely correlated with surface energy, in agreement with theoretical predictions. Elevated temperatures accelerate the self-assembly kinetics of SA molecules, promoting the formation of a continuous, densely packed molecular layer on the composite interface and thereby attenuating hydrophilicity. Beyond 60 °C, the rate of θ_{CA} escalation becomes markedly pronounced, as observed in Figure 5.6 (a), indicative of a transition toward a strongly hydrophobic regime. This pronounced shift is plausibly attributed to thermally induced rearrangement and tighter packing of SA hydrocarbon chains, which minimizes polar group exposure and maximizes van der Waals interactions, thereby reducing the availability of active hydrophilic sites for water adsorption.

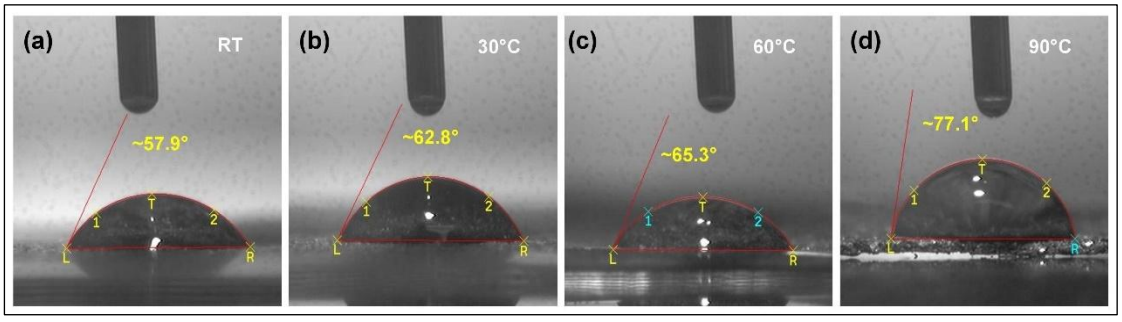

Figure 5.5 Water Contact Angle Measurements for (a) SRT-NG-1.0, (b) S30-NG-1.0, (c) S60-NG-1.0 and (d) S90-NG-1.0

Table 5.5
Contact Angle Measurement Data of the Samples Treated with Different Immersion Temperature

Sample	**SA content (wt.%)**	**Immersion duration (hours)**	**WCA (°)**	**Surface Energy (mJ/m^2)**
SRT-NG-1.0	2	6	57.9 ± 1.4	27.9 ± 0.4
S30-NG-1.0			62.8 ± 1.6	26.5 ± 0.5
S60-NG-1.0			65.3 ± 1.2	25.8 ± 0.3
S90-NG-1.0			77.1 ± 1.8	22.3 ± 0.6

To elucidate the influence of surface treatment temperature on humidity-to-electricity conversion kinetics, Figure 5.6 (b) presents the voltage–time profiles of S-NG-1.0-FP-based HGPG devices operated at ambient temperature under 75 % RH. The corresponding performance metrics, summarized in Table 5.6, reveal a clear dependence on thermal processing conditions. The optimum electro-hygroscopic response was achieved for the composite treated with SA at 60°C (S60-NG-1.0 sample), yielding a maximum output voltage of $(2.24 \pm 0.03) \times 10^{-3}$ V, a current density of $(1.79 \pm 0.02) \times 10^{-10}$ A/cm^2, and an output power of $(5.02 \pm 0.13) \times 10^{-13}$ W. This performance enhancement is attributed to the thermally induced ordering of the SA molecular layer, which optimizes the balance between hydrophilicity for rapid moisture adsorption and controlled desorption for efficient charge transport, thereby maximising the overall humidity-to-energy conversion efficiency.

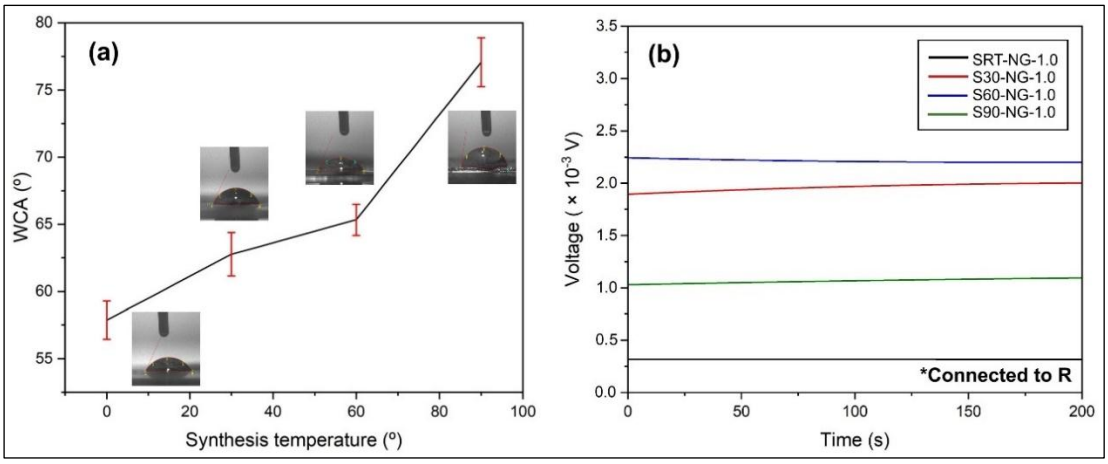

Figure 5.6 (a) Graph of Contact Angle Variation with the Different Immersion Temperature. (b) The Plots of Voltage Versus Time at a Fixed RH of 75% with Zero Applied Bias for HGPG Devices using S-N/G-1.0 Samples with Different Immersion Temperature

Table 5.6
The Humidity-To-Energy Performance of the Fabricated HGPG Device at Different SA Immersion Temperature Under Fixed SA Content of 2 Wt.% and Immersion Duration of 6h

Sample	**RH (%)**	**R (MΩ)**	**Output voltage, V (V)**	**Current density, J (A/cm^2)**	**Power, P (W)**
SRT-NG-1.0	75	10	$(3.12 \pm 0.02) \times 10^{-4}$	$(2.50 \pm 0.02) \times 10^{-11}$	$(9.73 \pm 0.13) \times 10^{-15}$
S30-NG-1.0			$(1.99 \pm 0.03) \times 10^{-3}$	$(1.59 \pm 0.02) \times 10^{-10}$	$(3.96 \pm 0.12) \times 10^{-13}$
S60-NG-1.0			$(2.24 \pm 0.03) \times 10^{-3}$	$(1.79 \pm 0.02) \times 10^{-10}$	$(5.02 \pm 0.13) \times 10^{-13}$
S90-NG-1.0			$(1.09 \pm 0.03) \times 10^{-3}$	$(8.72 \pm 2.24) \times 10^{-11}$	$(1.19 \pm 0.07) \times 10^{-13}$

5.2.3 Optimization at Different Immersion Time

Figure 5.7 presents the XRD diffraction profiles of S-NG-1.0 composites subjected to varying immersion durations during SA treatment. All samples exhibit nearly congruent diffraction signatures for NiO and Gr, indicating that the fundamental crystallographic framework and phase purity of both constituents remain largely unperturbed by SA functionalization. This suggests that the SA treatment exerts only a marginal influence on the intrinsic crystallization dynamics of NiO and Gr, thereby preserving their long-range structural order. Prominent diffractions at 37.24°, 44.50°, and 62.49° are indexed to the ♣(1 1 1), ♣(2 0 0), and ♣(3 1 1) crystallographic planes of cubic NiO (JCPDS No. 01-071-4750). For Gr, characteristic Bragg peaks appear at 26.58° and 54.72°, corresponding to the ★(0 0 2) and ★(0 0 4) planes (JCPDS No. 00-041-1487), respectively. Meanwhile, a distinct SA diffraction peak at ~21.62°, corresponding to the ♦(3 1 1) plane (JCPDS No. 00-038-1923), was detected for S6h-NG-1.0 and S8h-NG-1.0 as shown in magnified XRD pattern, signifying the incorporation of SA within the composite structure at immersion durations of 6 hours and beyond.

Notably, the diffraction signatures attributable to SA become increasingly accentuated with extended immersion, reaching maximal prominence at 8 h. This enhancement signifies a higher surface loading density of SA molecules, indicative of progressive molecular adsorption and consolidation on the composite surface over prolonged treatment durations. The D value revealed a progressive enlargement from 6.4 nm (SA-2 h) to 8.4 nm (SA-6 h), signifying that SA treatment facilitates NiO crystal growth along the Gr interface. However, extending the immersion to 8 h produced a reduction in D, as summarised in Table 5.7. This non-monotonic trend aligns with the observations of Ye et al. [326], wherein prolonged surface modification induces partial recrystallisation coupled with defect incorporation, culminating in lattice distortions and a concomitant deterioration of long-range crystalline order. The d for the NiO ♣ (1 1 1) plane remains remarkably consistent across all immersion durations, ranging from 0.241 to 0.242 nm. Such minimal variation indicates that the SA treatment does not induce appreciable lattice distortion, with any subtle shifts more likely attributable to minor strain relaxation or defect passivation at the surface rather than bulk structural changes. Similarly, the V is effectively invariant at approximately 0.073 nm^3 for all samples, except for a marginal increase to 0.074 nm^3 in S8h-NG-1.0. This slight

expansion could be associated with surface adsorption of SA molecules or relaxation of near-surface strain after prolonged immersion, subtly influencing the lattice parameter without compromising crystalline integrity.

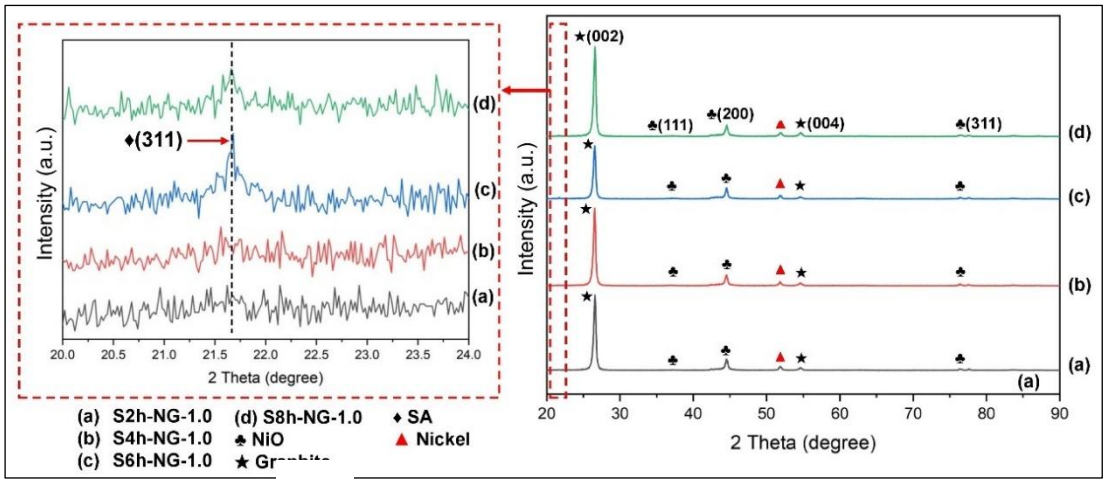

Figure 5.7 XRD Pattern for (a) S2h-NG-1.0, (b) S4h-NG-1.0, (c) S6h-NG-1.0 and (d) S8h-NG-1.0

Table 5.7
The FWHM, 2θ, Interplanar Spacing, Unit Cell Volume, and Crystallite Size of NiO ♣(1 1 1) for the Samples Treated with Different Immersion Duration

Sample	FWHM, β (rad)	2θ (°)	Interplanar spacing, d (nm)	Unit Cell Volume, V (nm^3)	Crystallite size, D (nm)
S2h-NG-1.0	0.0231	37.24	0.241	0.073	6.4
S4h-NG-1.0	0.0226	37.24	0.241	0.073	6.5
S6h-NG-1.0	0.0174	37.28	0.241	0.073	8.4
S8h-NG-1.0	0.0268	37.14	0.242	0.074	5.5

Water contact angle measurement results in Figure 5.8 were used to derive the surface energy via Equation (2.8) with the results summarized in Table 5.8. The sample subjected to an 8 h treatment exhibited the lowest surface energy across all tested durations, reflecting markedly diminished intermolecular attraction at the solid–liquid interface. This reduction is ascribed to the formation of a substantially thicker, more densely packed SA molecular overlayer, which impedes water ingress and consequently suppresses ion transport dynamics within the device architecture.

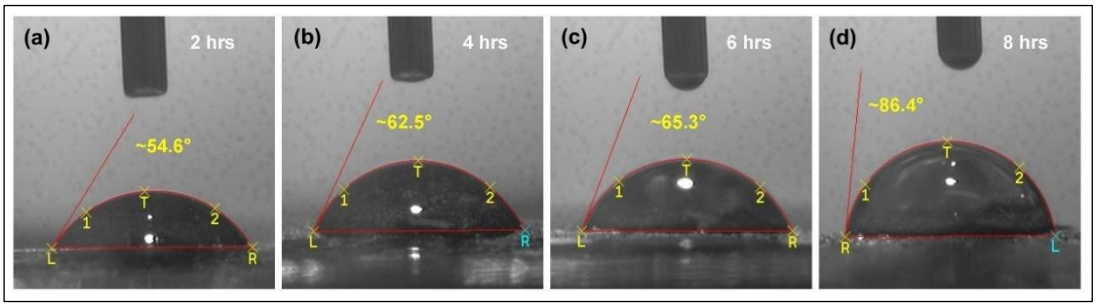

Figure 5.8 Water Contact Angle Measurements for (a) S2h-NG-1.0, (b) S4h-NG-1.0, (c) S6h-NG-1.0 and (d) S8h-NG-1.0

Table 5.8
Contact Angle Measurement Data of the Samples Treated with Different Immersion Duration

Sample	**SA content (wt.%)**	**Immersion Temperature (°C)**	**WCA (°)**	**Surface Energy (mJ/m^2)**
S2h-NG-1.0	2	60	54.6 ± 2.3	28.7 ± 0.6
S4h-NG-1.0			62.5 ± 1.5	26.6 ± 0.4
S6h-NG-1.0			65.3 ± 1.2	25.8 ± 0.3
S8h-NG-1.0			86.4 ± 1.9	19.4 ± 0.6

As illustrated in Figure 5.9 (a), the water θ_{CA} progressively increases with longer SA immersion durations, with a marked surge observed beyond the 6 h threshold. This change correlates with a gradual shift toward reduced surface energy and altered wettability characteristics. Figure 5.9 (b) presents the corresponding voltage–time profiles at RT and 75 % RH, recorded under open-circuit conditions with a 10 MΩ load resistor. The performance metrics, summarized in Table 5.9, clearly identify the 6 h treatment as the optimal condition, delivering an output voltage of $(2.24 \pm 0.03) \times 10^{-3}$ V, a current density of $(1.79 \pm 0.02) \times 10^{-10}$ A/cm^2, and an output power of $(5.02 \pm 0.13) \times 10^{-13}$ W. This optimum arises from a balanced SA molecular coverage that effectively tailors hydrophilicity while enhancing surface uniformity. At this coverage density, water adsorption–desorption dynamics are rapid enough to sustain efficient ion transport within the device, without the over-saturation effects observed at longer treatments. Such a fine-tuned surface state maximizes the interplay between hygroscopic water uptake and charge transport, thereby yielding superior humidity-to-electricity conversion efficiency [323].

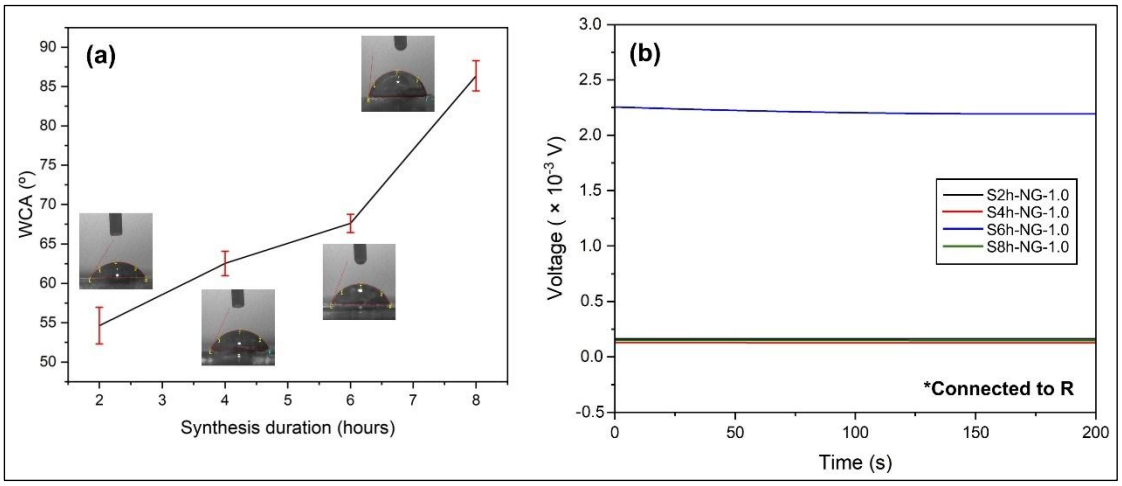

Figure 5.9 (a) Graph of Contact Angle Variation with the Different Immersion Duration. (b) The Plots of Voltage Versus Time at a Fixed RH of 75% with Zero Applied Bias for HGPG Devices using S-N/G-1.0 Samples with Different Immersion Duration

Table 5.9
The Humidity-To-Energy Performance of the Fabricated HGPG Device at Different SA Immersion Duration Under Fixed SA Content of 2 wt.% and Immersion Temperature of 60°C

Sample	RH (%)	R (MΩ)	Output voltage, V (V)	Current density, J (A/cm^2)	Power, P (W)
S2h-NG-1.0	75	10	$(1.65 \pm 0.01) \times 10^{-4}$	$(1.32 \pm 0.01) \times 10^{-11}$	$(2.72 \pm 0.03) \times 10^{-15}$
S4h-NG-1.0			$(1.27 \pm 0.01) \times 10^{-4}$	$(1.02 \pm 0.01) \times 10^{-11}$	$(1.61 \pm 0.03) \times 10^{-15}$
S6h-NG-1.0			$(2.24 \pm 0.03) \times 10^{-3}$	$(1.79 \pm 0.02) \times 10^{-10}$	$(5.02 \pm 0.13) \times 10^{-13}$
S8h-NG-1.0			$(1.43 \pm 0.01) \times 10^{-4}$	$(1.14 \pm 0.01) \times 10^{-11}$	$(2.04 \pm 0.03) \times 10^{-15}$

5.3 Conclusion

The present study systematically investigated the optimization of SA treatment to tailor the hydrophilicity of S-NG-1.0 composites for enhanced humidity-to-electricity conversion in HGPG devices. Through controlled variation of three critical parameters (SA concentration, SA immersion temperature, and SA treatment duration) the interplay between surface wettability, structural evolution, and energy-harvesting performance was elucidated. Results revealed that all SA-treated samples maintained inherent hydrophilic behaviour; however, the degree of hydrophilicity and surface energy was highly sensitive to treatment conditions. Excessive hydrophilicity accelerated water adsorption but hindered recovery dynamics, while insufficient hydrophilicity limited adsorption efficiency. As summarized in Table 5.10, optimal device performance was achieved with a 2 wt.% SA treatment at 60 °C for 6 h, yielding a contact angle of 65.3° ± 1.2° and a surface energy of 25.8 ± 0.3 mJ/m^2. Under these conditions, the molecular coverage was sufficiently uniform to enhance interfacial water adhesion and ion

transport, without imposing diffusion barriers. The optimized S-NG-1.0-FP device delivered an output voltage of $(2.24 \pm 0.03) \times 10^{-3}$ V, a current density of $(1.79 \pm 0.02) \times 10^{-10}$ A cm^{-2}, and an output power of $(5.02 \pm 0.13) \times 10^{-13}$ W at 75% RH under zero bias, representing a significant improvement over untreated composite. These findings establish a clear processing–structure–function relationship and demonstrate that fine-tuning SA surface functionalization is a decisive strategy for achieving balanced wettability and superior energy-harvesting performance in humidity-responsive devices.

Table 5.10
Humidity-To-Energy Performance of the Fabricated HGPG Devices Connected to a 10 MΩ Resistor under 75% RH

Conditions	**Sample**	**Output voltage, V (V)**	**Current density, J (A/cm^2)**	**Power, P (W)**
SA treatment with different SA content, treated at 60°C for 6 hours	U-NG-1.0	$(0.14 \pm 0.01) \times 10^{-3}$	$(11.12 \pm 0.07) \times 10^{-12}$	$(1.93 \pm 0.12) \times 10^{-15}$
	S1%-NG-1.0	$(1.56 \pm 0.04) \times 10^{-3}$	$(1.25 \pm 0.03) \times 10^{-10}$	$(2.43 \pm 0.13) \times 10^{-13}$
	S2%-NG-1.0	$(2.24 \pm 0.03) \times 10^{-3}$	$(1.79 \pm 0.02) \times 10^{-10}$	$(5.02 \pm 0.13) \times 10^{-13}$
	S3%-NG-1.0	$(1.17 \pm 0.19) \times 10^{-4}$	$(9.36 \pm 1.52) \times 10^{-12}$	$(1.37 \pm 0.45) \times 10^{-15}$
	S4%-NG-1.0	$(1.54 \pm 0.08) \times 10^{-3}$	$(1.23 \pm 0.06) \times 10^{-10}$	$(2.37 \pm 0.25) \times 10^{-13}$
SA treatment with 2 wt.% SA, treated for 6 hours at different immersion temperature	SRT-NG-1.0	$(3.12 \pm 0.02) \times 10^{-4}$	$(2.50 \pm 0.02) \times 10^{-11}$	$(9.73 \pm 0.13) \times 10^{-15}$
	S30-NG-1.0	$(1.99 \pm 0.03) \times 10^{-3}$	$(1.59 \pm 0.02) \times 10^{-10}$	$(3.96 \pm 0.12) \times 10^{-13}$
	S60-NG-1.0	$(2.24 \pm 0.03) \times 10^{-3}$	$(1.79 \pm 0.02) \times 10^{-10}$	$(5.02 \pm 0.13) \times 10^{-13}$
	S90-NG-1.0	$(1.09 \pm 0.03) \times 10^{-3}$	$(8.72 \pm 2.24) \times 10^{-11}$	$(1.19 \pm 0.07) \times 10^{-13}$
SA treatment with 2 wt.% SA, treated at 60°C for different immersion duration	S2h-NG-1.0	$(1.65 \pm 0.01) \times 10^{-4}$	$(1.32 \pm 0.01) \times 10^{-11}$	$(2.72 \pm 0.03) \times 10^{-15}$
	S4h-NG-1.0	$(1.27 \pm 0.01) \times 10^{-4}$	$(1.02 \pm 0.01) \times 10^{-11}$	$(1.61 \pm 0.03) \times 10^{-15}$
	S6h-NG-1.0	$(2.24 \pm 0.03) \times 10^{-3}$	$(1.79 \pm 0.02) \times 10^{-10}$	$(5.02 \pm 0.13) \times 10^{-13}$
	S8h-NG-1.0	$(1.43 \pm 0.01) \times 10^{-4}$	$(1.14 \pm 0.01) \times 10^{-11}$	$(2.04 \pm 0.03) \times 10^{-15}$

CHAPTER 6
FABRICATION AND PERFORMANCE ANALYSIS OF HUMIDITY GRADIENT ENERGY HARVESTING BASED ON HEMATITE/ NICKEL OXIDE/ GRAPHENE COMPOSITES AND HYDROGEL BASED CELLULOSE SUBSTRATE AS HYGROSCOPIC MATERIALS

6.1 Introduction

Metal oxides and Gr have emerged as pivotal functional materials for charge extraction and stability enhancement in energy devices owing to their band-level compatibility, cost-effectiveness, and environmental benignity [311, 312]. Gr, with its exceptional electron mobility and high surface conductivity, provides a highly conductive medium for ion transport, while transition-metal oxides, particularly NiO, offer complementary redox activity, excellent thermal and chemical stability, high theoretical specific capacity, low cost, and material abundance. The synergistic integration of NiO and Gr has therefore been extensively exploited in high-performance electrochemical systems, including batteries and supercapacitors [302, 312], as well as photovoltaic devices [311], where these composites consistently exhibit superior electrochemical behaviour [302, 312, 327].

Another promising candidate, iron oxide (hematite, α-Fe_2O_3), is widely recognised for its unique combination of optical, magnetic, and electrical functionalities, coupled with low cost and environmental sustainability [328, 329]. Hematite has been deployed in a wide range of applications, including photovoltaic cells [330], lithium-ion batteries [331, 332], supercapacitors [333, 334], and anticorrosion coatings[335]. As demonstrated by Mohamed et al. [330], hematite incorporation expands the active interfacial region, accelerates surface reaction kinetics, and enhances the material's hygroscopic capability, facilitating improved moisture adsorption and charge generation from ambient humidity. Furthermore, its ability to suppress electron–hole recombination prolongs charge carrier lifetimes, thereby increasing the efficiency of humidity-induced energy conversion [330].

In parallel, hydrogels have recently garnered considerable attention as next-generation functional matrices for HGPG due to their intrinsic hygroscopicity and unique ion-conduction behaviour [45, 336]. Hydrogels can absorb substantial amounts of atmospheric water, which acts as an electrolyte to promote ion mobility within the polymeric network [337]. By integrating hydrogels with functional fillers, advanced HGPG systems can be engineered to exploit humidity variations for direct electricity generation via ion migration across humidity gradients.

This chapter presented a comprehensive investigation into the synergistic incorporation of hematite, Co–Zn nanoceramic hydrogel, and recycled waste-derived components into HGPG architectures. Detailed structural, morphological, and functional analyses were performed, supported by comparative evaluations against established benchmarks. The integration of waste-derived materials provided a sustainable route for addressing global waste accumulation, positioning this strategy at the intersection of green energy harvesting and waste-to-energy valorisation.

6.2 Synthesis and Characterization of Hematite/NiO/Gr Composites on Cellulose-based Substrate for Humidity Gradient Energy Harvesting Application

Leveraging the gradient-configuration architecture of the humidity-to-energy device, the author successfully engineered S-HNG composite powders via a facile sonicated solution–immersion method, followed by deposition onto a cellulose-based substrate to yield the S-HNG-FP-based HGPG. This strategic material design integrates the synergistic functionalities of hematite, NiO, and Gr, enabling enhanced charge generation, transport, and retention under ambient humidity conditions. The detailed synthesis protocol for the S-HNG powder and device fabrication steps are provided in Sections 3.5 and 3.5.1. A comprehensive suite of characterisation techniques, including crystallographic analysis, nanoscale morphological evaluation, hydrophilicity profiling, and humidity-to-electricity conversion measurements was employed to systematically correlate the material's structural and surface properties with its electrical output. This integrated approach not only validates the S-HNG-FP composite as a high-performance hygroscopic medium but also establishes critical structure–property–function relationships for next-generation humidity-driven energy harvesting systems.

6.2.1 Structural Properties Analysis of Hematite/NiO/Gr Composites

The XRD patterns of prepared S-NG-1.0 and S-HNG powder are shown in Figure 6.1. Diffraction peaks at 2θ of 37.20° and 44.60° which corresponds to the ♣(1 1 1) and ♣(2 0 0) planes, signifying the formation of crystallized cubic NiO nanoparticles (JCPDS No. 01-071-4750). The XRD patterns clearly exhibit the planes of ★(0 0 2) and ★(0 0 4) at diffraction peak 26.60° and 54.66°, respectively, corresponding to crystallized hexagonal Gr (JCPDS No. 00-041-1487). The diffraction peaks at 35.82°, 43.50°, 57.54° and 63.14° were indexed to the ■(1 1 0), ■(2 0 2), ■ (1 2 2) and ■(2 1 4) planes, indicating the formation of crystallized trigonal hematite (JCPDS No. 00-033-0664). A small and negligible diffraction peak at 30.42°, marked by blue triangle symbol (▲) was indexed to the (2 2 0) plane, indicating the Fe_3O_4 also known as magnetite (JCPDS No. 01-073-9877). This peak arises from the incomplete transformation of iron precursor to hematite [338].

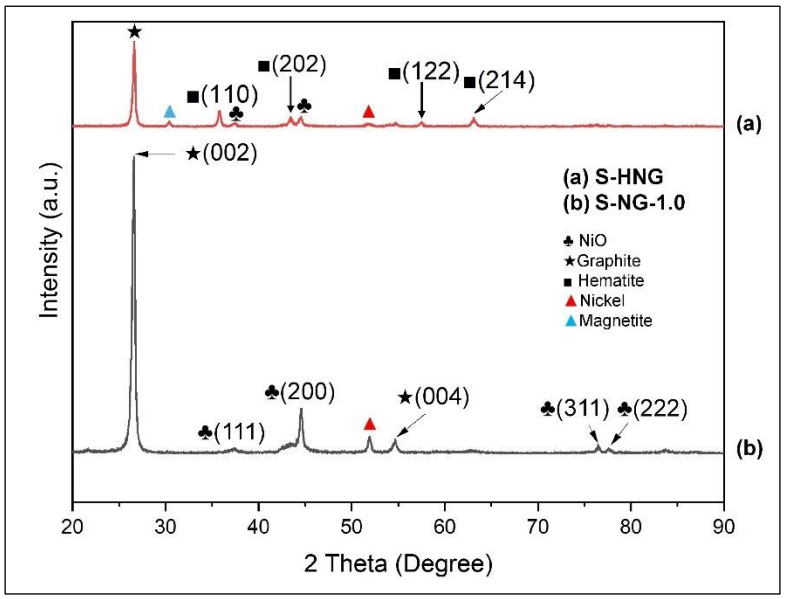

Figure 6.1 XRD Pattern of Synthesized S-NG-1.0 and S-HNG Composites

The estimated XRD parameters are summarized in Table 6.1. The results indicate that the presence of hematite significantly influences XRD characteristics. For the S-NG-1.0 composite, the D of NiO particles at the ♣(1 1 1) plane is calculated to be 7.93 ± 0.71 nm. This value increases substantially to 17.76 ± 0.57 nm in the S-HNG composite. The notable increase in NiO grain size suggests that the direct introduction of hematite promotes crystallite growth through co-crystallization and interfacial

interactions [339]. This enhancement is likely due to the heterogeneous nucleation and templating effects of hematite within the composite matrix, supporting the hypothesis that hematite functions as a structural scaffold facilitating NiO grain development [134]. Meanwhile, the interplanar spacing and unit cell volume remained nearly identical and essentially unchanged, respectively, with the average diffraction peak positions differing by only a negligible margin.

Table 6.1
The FWHM, 2θ, Interplanar Spacing, Unit Cell Volume and Crystallite Size of NiO ♣(1 1 1) for S-NG-1.0 and S-HNG

Sample	**FWHM, β (rad)**	**2θ (°)**	**Interplanar spacing, d (nm)**	**Unit Cell Volume, V (nm^3)**	**Crystallite size, D (nm)**
S-NG-1.0	0.0174	37.28	0.241	0.073	8.4
S-HNG	0.0084	37.22	0.242	0.073	17.4

6.2.2 Morphological and Elemental Analysis of Hematite/NiO/Gr Composites

The morphological and microstructural features of the synthesized S-HNG composites were elucidated via FESEM analysis. Figure 6.2 (a) and Figure 6.2 (b) depict the surface architectures of the S-NG-1.0 and S-HNG composites, respectively, with their corresponding high-magnification views shown in Figure 6.2 (c) and Figure 6.2 (d). The S-NG-1.0 composite exhibits densely agglomerated nanoparticles with an average diameter $Ø_{avg}$ of 45 ± 0.9 nm. In contrast, the S-HNG composite displays slightly coarser agglomerates ($Ø_{avg}$ = 57 ± 0.7 nm), indicative of hematite incorporation influencing the growth kinetics. Distinct Gr flakes, characterized by rippled and stratified surfaces likely originating from carbon lattice compression, are discernible in both samples. NiO and hematite nanoparticles are heterogeneously distributed across the Gr basal planes, generating a hierarchically porous and electrically conductive network [340]. The abundant edge sites and defect domains on the Gr substrate serve as preferential nucleation centres during synthesis, fostering the anchoring and redistribution of NiO and hematite crystallites to yield integrated heterostructures with enhanced interfacial contact.

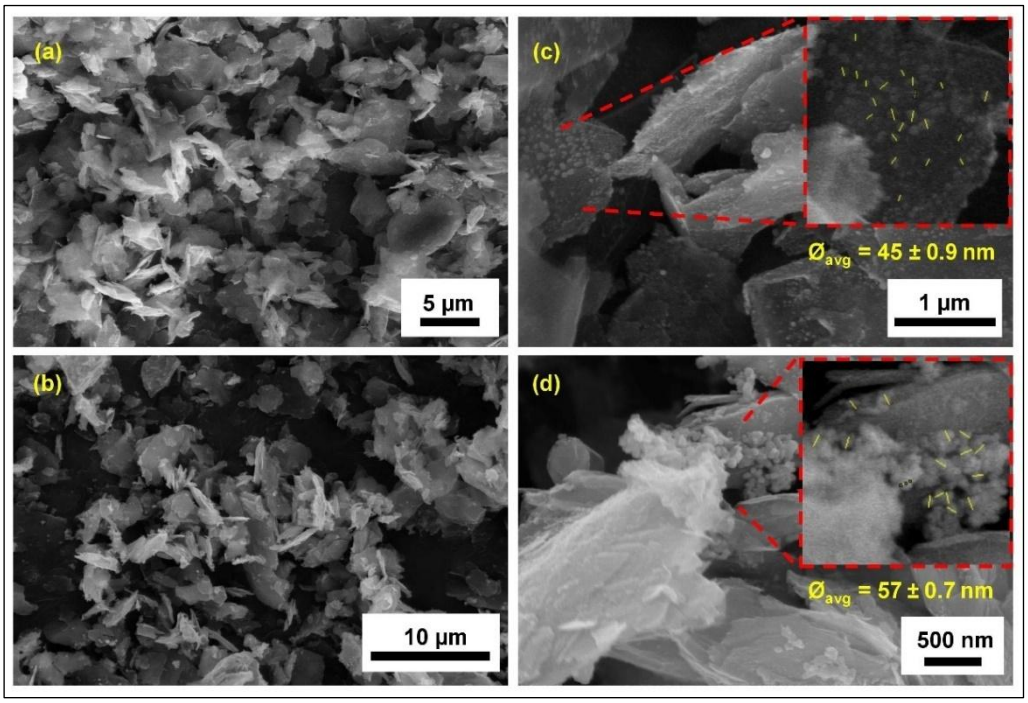

Figure 6.2 FESEM Images of Synthesized (a) S-NG-1.0 and (b) S-HNG Prepared using the Sonicated Solution Immersion Method, with (c) and (d) Showing Their Corresponding Magnified FESEM Images, respectively

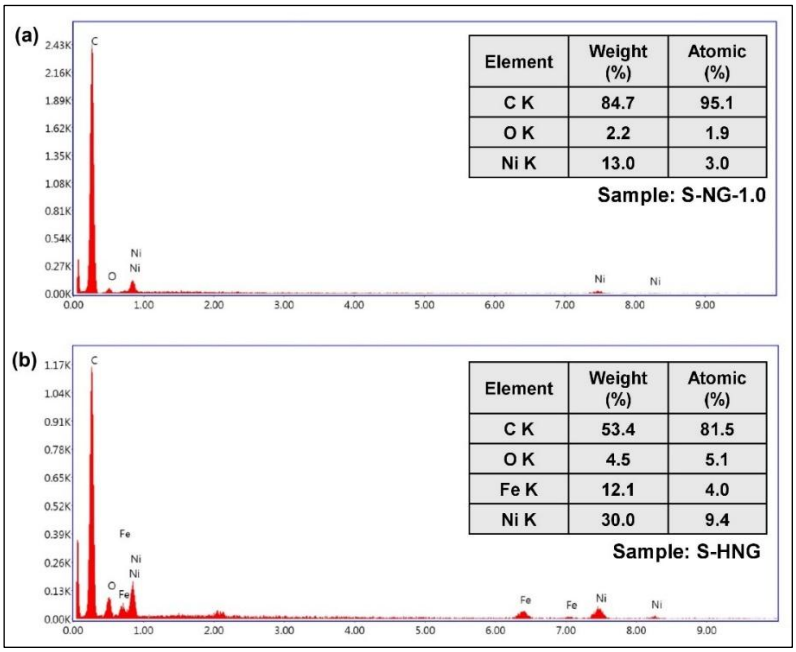

Figure 6.3 EDX Peaks with Analytic Elemental Composition of Synthesized (a) S-NG-1.0 and (b) S-HNG

The elemental composition of the S-NG-1.0 and S-HNG composites was analyzed using EDX spectroscopy. The EDX spectrum of the S-NG-1.0 composite, shown in Figure 6.3 (a), confirms the presence of C, Ni, and O. In contrast, the EDX

spectrum of the S-HNG composite in Figure 6.3 (b) shows an additional peak corresponding to iron (Fe), indicating the presence of hematite. The presence of C confirms the incorporation of Gr within the composites. As shown in Figure 6.3 (a) and Figure 6.3 [b (inset)], the C content in the S-NG-1.0 composite is higher than in the S-HNG composite, which is consistent with the XRD results. No other elements were detected in the EDX spectra, suggesting the purity of the synthesized composites.

6.2.3 Hydrophilicity Analysis of Hematite/NiO/Gr Composites

As established earlier, the hydrophilicity of the fabricated composites was quantified through θ_{CA} measurements, providing a direct metric for liquid spreading behaviour on the solid surface. The results, presented in Figure 6.4, confirm that both S-NG-1.0-FP and S-HNG-FP exhibit pronounced hydrophilic characteristics. The S-NG-1.0-FP sample demonstrated a θ_{CA} of 65.3° ± 1.2°, corresponding to a surface energy of 25.8 ± 0.3 mJ/m^2, calculated via Equation (2.8). In contrast, the S-HNG-FP exhibited a marginally lower θ_{CA} of 64.2° ± 3.6°, yielding a slightly elevated surface energy of 26.1 ± 1.0 mJ/m^2, as detailed in Table 6.2. These findings align with Shrimali et al. [341], who reported that hematite incorporation into NiO–Gr composites enhances water adsorption owing to the abundance of surface hydroxyl groups, thereby augmenting hydrophilic behaviour. This synergistic surface chemistry is expected to play a pivotal role in optimizing humidity-induced charge generation in HGPG systems.

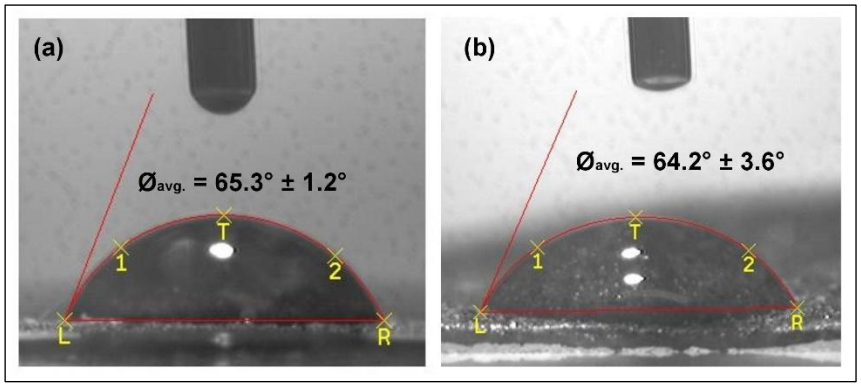

Figure 6.4 Water Contact Angle Measurement of Synthesized (a) S-NG-1.0-FP and (b) S-HNG-FP

Table 6.2 Contact Angle Measurement Data of Samples S-NG-1.0-FP and the S-HNG-FP

Sample	WCA (°)	Surface Energy (mJ/m^2)
S-NG-1.0-FP	65.3° ± 1.2°	25.8 ± 0.3
S-HNG-FP	64.2° ± 3.6°	26.1 ± 1.0

6.2.4 Surface Area and Porosity Analysis of Hematite/NiO/Gr Composites

Complementary BET and BJH analyses in Figure 6.5 further reveal that hematite incorporation markedly increases porosity and surface accessibility. The S-HNG composite exhibited a BET surface area of 12.3 m^2/g and a BJH average pore width of 29.2 nm, compared to 10.2 m^2/g and 5.6 nm, respectively, for S-NG-1.0 (Table 6.3). Such an expansion of specific surface area and mesoporous structure, attributed to the inherently porous morphology of hematite nanostructures, provides additional active sites for water adsorption and promotes more efficient ion migration [342]. The synergistic enhancement in hydrophilicity and porosity yields a dual benefit: improved electrolyte accessibility at the electrode interface and reduced ion transport resistance, both of which are critical for maximising humidity-to-electricity conversion efficiency. This integrated structure–property relationship firmly establishes S-HNG composites as a superior platform for high-performance HGPG devices.

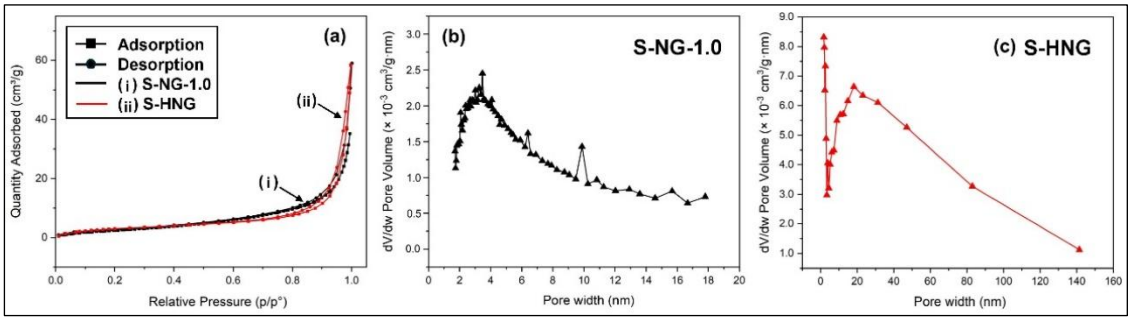

Figure 6.5 (a) BET Isotherm Plot of N_2 Adsorption Desorption Of S-NG-1.0 and S-HNG. BJH Adsorption dv/dw Pore Volume Of (b) S-NG-1.0 And (c) S-HN, dv/dw Refers to the Change Rate of Pore Volume with Pore Width

Table 6.3
Comparison of the BJH Adsorption Average Pore Diameter and BET Surface Area of S-NG-1.0 and the S-HNG Composites Powder

Sample	BJH Adsorption average pore diameter (nm)	BET surface area (m^2/g)
S-NG-1.0	5.6	10.2
S-HNG	29.2	12.3

6.2.5 Electrical Characterization Analysis of Hematite/NiO/Gr Composites

Given that humidity-to-energy conversion mechanisms often proceed via interfacial redox reactions, CV analysis was employed to elucidate the redox activity of the developed electrode materials. The CV profiles in Figure 6.6 reveal distinct electrochemical signatures for the two composites. The S-NG-1.0-FP sample exhibits a relatively broad voltammogram with moderate redox peak currents of approximately 5 × 10^{-5} A, indicative of limited faradaic activity. In stark contrast, the S-HNG-FP sample displays broader, more pronounced, and well-defined redox peaks, with peak currents nearly doubled to ~1 × 10^{-4} A. This enhancement reflects an increased density of electroactive sites and improved charge-transfer kinetics, attributable to the synergistic contribution of hematite and NiO nanoparticles interfaced with conductive Gr sheets. Both systems demonstrate pseudocapacitive behaviour, underscoring their ability to store charge through a combination of faradaic reactions and double-layer capacitance. The markedly superior redox response of the S-HNG-FP composite confirms that hematite incorporation not only enhance water adsorption and ion transport but also amplifies the interfacial redox dynamics essential for efficient humidity-to-electricity conversion.

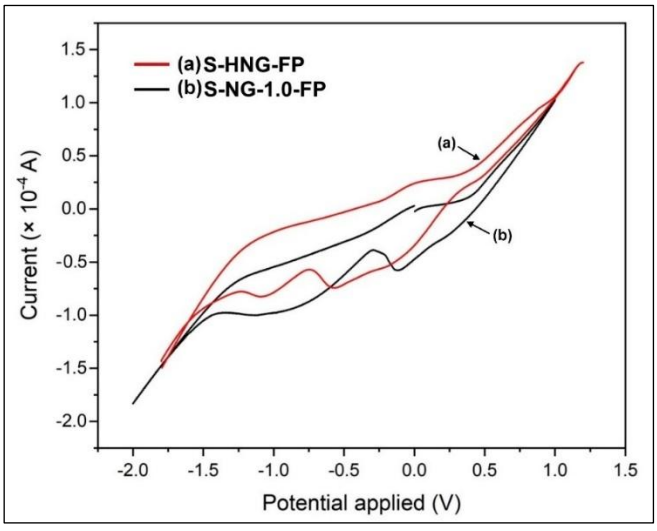

Figure 6.6 CV Analysis of the Prepared of S-NG-1.0-FP and S-HNG-FP

From the CV analysis, the S-HNG-FP electrode exhibited a markedly higher current magnitude compared to S-NG-1.0-FP, signifying an improved charge-storage capacity and superior electrochemical reactivity. This enhancement is attributed to the strategic incorporation of hematite, which introduces additional redox-active centres via

the Fe^{3+}/Fe^{2+} transition. These Fe-based sites operate in concert with the Ni^{2+}/Ni^{3+} redox couple, generating a complementary redox-active interface that simultaneously facilitates charge separation and accelerates ionic transport [134]. The CV profile of S-HNG-FP further revealed a distinct reduction feature near –1.0 V, characterised by sharper curvature and an enlarged hysteresis loop relative to S-NG-1.0-FP, hallmarks of intensified faradaic redox activity arising from the synergistic interplay between Fe and Ni oxides [133]. Mechanistically, this behaviour is consistent with reports by Banbela et al. [343], wherein the coupling of transition-metal oxide phases enlarges the electroactive surface area and mitigates charge-transfer resistance, thereby improving redox kinetics. In the S-HNG-FP sample, the hierarchical integration of NiO and hematite onto the Gr framework creates a highly conductive, porous, and electrochemically accessible architecture. This structural configuration maximizes electrolyte penetration, shortens ion-diffusion pathways, and sustains rapid electron shuttling, collectively enabling robust humidity-to-electricity transduction performance.

Hall effect measurements were conducted to investigate changes in electrical characteristics influenced by the introduction of hematite into the composite. Based on the findings, the carrier concentration decreased from $(3.0 \pm 0.2) \times 10^{13}$ cm^{-3} for S-NG-1.0-FP to $(0.5 \pm 0.1) \times 10^{13}$ cm^{-3} for S-HNG-FP. Similarly, the Hall mobility decreased from $(2.7 \pm 0.6) \times 10^{3}$ $cm^2/V{\cdot}s$ to $(2.3 \pm 0.1) \times 10^{3}$ $cm^2/V{\cdot}s$. The Hall coefficient was $(2.1 \pm 0.2) \times 10^{5}$ cm^3/C for S-NG-1.0-FP and $(13.9 \pm 0.3) \times 10^{5}$ cm^3/C for S-HNG-FP, as presented in Table 6.4. The electrical conductivity of the samples, calculated using Equation (3.6), showed that S-HNG-FP had a lower conductivity of $(1.7 \pm 0.1) \times 10^{-3}$ S/cm compared to S-NG-1.0-FP with a conductivity of $(1.3 \pm 0.2) \times 10^{-2}$ S/cm. This reduction is primarily attributed to the properties of hematite, which has a wide bandgap, resulting in low intrinsic electrical conductivity [344]. The addition of hematite introduces additional resistance in the composite, as electrons within hematite require higher energy to move and to overcome potential barriers. In other words, hematite particles disrupt the continuous conductive network formed by Gr, thereby lowering the Hall-measured conductivity.

Table 6.4
Hall Effect Measurement Data of S-Ng-1.0 and the S-Hng Composites on Cellulose-Based Substrate

Sample	Carrier Concentration (cm^{-3})	Hall Coefficient (cm^3/C)	Mobility ($cm^2/(V \cdot s)$)	Conductivity, σ (S/cm)
S-NG-1.0-FP	$(3.0 \pm 0.2) \times 10^{13}$	$(2.1 \pm 0.2) \times 10^{5}$	$(2.7 \pm 0.6) \times 10^{3}$	$(1.3 \pm 0.2) \times 10^{-2}$
S-HNG-FP	$(0.5 \pm 0.1) \times 10^{13}$	$(13.9 \pm 0.3) \times 10^{5}$	$(2.3 \pm 0.1) \times 10^{3}$	$(1.7 \pm 0.1) \times 10^{-3}$

Humidity-response measurements were performed on both S-NG-1.0-FP and S-HNG-FP to assess their operational efficacy in HGPG configurations. The voltage–time profiles recorded at a fixed RH of 75% with an adsorption area of 1.25 cm² are shown in Figure 6.7, while the performance metrics are summarized in Table 6.5. The S-NG-1.0-FP-based HGPG yielded an output voltage of $(2.24 \pm 0.03) \times 10^{-3}$ V, whereas the S-HNG-FP-based device exhibited a marginally superior output of $(3.01 \pm 0.23) \times 10^{-3}$ V. This performance gain highlights the strategic advantage of hematite incorporation, which serve as a multifunctional charge-transport mediator under humid conditions and is a critical determinant in amplifying the device's electrical output [124]. Mechanistically, this improvement is ascribed to the presence of larger crystallites in the hematite-containing composite, which mitigate grain boundary resistance and thereby facilitate more efficient ion migration, as corroborated by FESEM analyses.

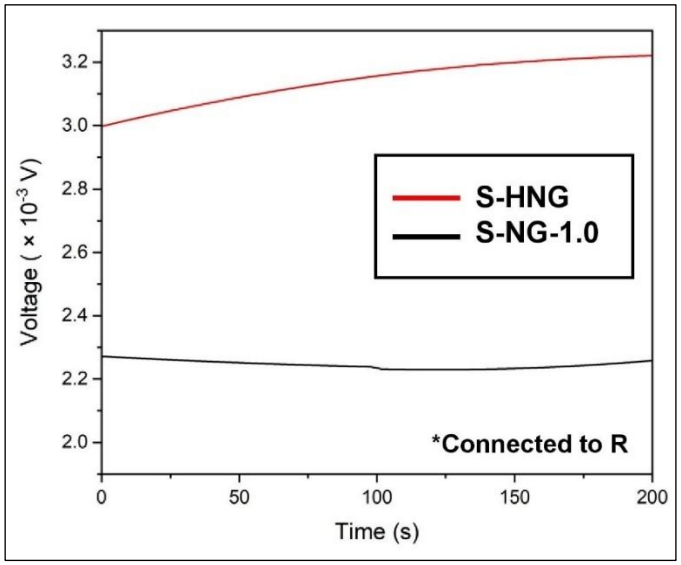

Figure 6.7 The Voltage Versus Time at a fixed RH of 75% with Zero Bias Applied for S-NG-1.0-FP-based and S-HNG-1.0-FP-based HGPGs

Table 6.5
The Humidity-To-Energy Performance of Fabricated S-NG-1.0-FP and the S-HNG-FP-based HGPG devices

Sample	RH (%)	R (MΩ)	Output voltage, V (V)	Current density, J (A/cm^2)	Power, P (W)
S-NG-1.0-FP	75	10	$(2.24 \pm 0.03) \times 10^{-3}$	$(1.79 \pm 0.02) \times 10^{-10}$	$(5.02 \pm 0.13) \times 10^{-13}$
S-HNG-FP	75	10	$(3.01 \pm 0.23) \times 10^{-3}$	$(2.41 \pm 0.02) \times 10^{-10}$	$(9.06 \pm 0.07) \times 10^{-13}$

In accordance with the established humidity-to-electricity conversion mechanism, which predominantly involves surface-mediated redox processes, the inclusion of hematite introduces an additional Fe^{3+}/Fe^{2+} redox couple that synergistically complements the Ni^{2+}/Ni^{3+} redox activity of NiO [345]. This dual redox functionality enhances charge separation dynamics, increases the density of electrochemically active sites, and accelerates ionic transport across the composite–electrolyte interface, ultimately enabling more efficient transduction of ambient humidity into usable electrical energy.

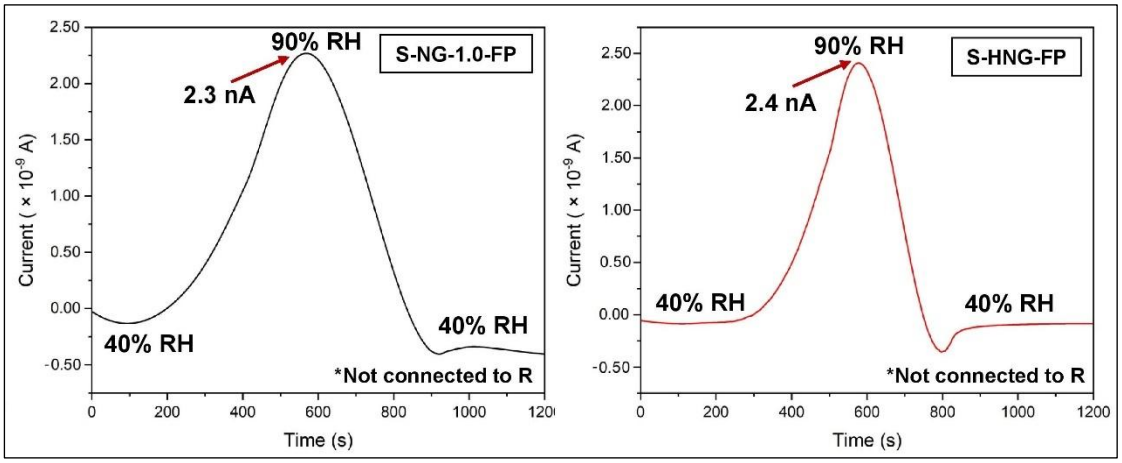

Figure 6.8 The Current Versus Time at Various RH Levels with Zero Bias Applied For (b) S-NG-1.0-FP-Based HGPG and (c) S-HNG-FP-Based HGPG

The current–time transients across varying RH levels, as depicted in Figure 6.8, reveal that both devices exhibit robust and reversible humidity responsiveness. During the adsorption phase, a stable baseline current was sustained at 40% RH, followed by a progressive augmentation in current magnitude as the RH increased to 90%. Notably, at peak humidity, the S-HNG-FP–based HGPG delivered a marginally higher steady-state current of 2.4 nA compared to the 2.3 nA attained by its S-NG-1.0-FP counterpart. Upon transitioning into the desorption regime, wherein RH was sequentially reduced from 90% to 40%, both systems demonstrated a commensurate decline in current

output, underscoring their excellent reversibility and dynamic equilibrium response under cyclic humidity variations.

6.3 Synthesis and Characterization of Hematite/NiO/Gr Composites on Cellulose-based Substrate for Humidity Gradient Energy Harvesting Application at Different Immersion Growth Temperature

The gradient architecture of the hygroscopic material induces directional charge-carrier diffusion, thereby generating an electric potential between the electrodes and initiating current flow. For humidity-to-energy conversion, sustaining this mechanism is critical to ensure continuous transduction of ambient moisture into electrical power. Achieving such stability requires synthesis process optimization aimed at tailoring material modifications, particularly those that enhance surface physicochemical properties. Among these parameters, synthesis temperature plays a decisive role, directly influencing surface morphology, defect chemistry, and interfacial interactions, thereby dictating the overall device performance. In this study, the S-HNG composites were subjected to controlled surface modification under varying synthesis temperatures to evaluate their efficacy as high-performance hygroscopic materials.

6.3.1 Structural Properties Analysis of Hematite/NiO/Gr Composites

XRD patterns of prepared S-HNG powder are shown in Figure 6.9. Diffraction peaks at 37.3° and 44.44°which corresponds to the ♣(1 1 1) and ♣(2 0 0) planes, signifying the formation of crystallized cubic NiO nanoparticles (JCPDS No. 01-071-4750). The XRD patterns clearly exhibit the planes of ★(0 0 2) and ★(0 0 4) at diffraction peak 26.52° and 54.66°, respectively, corresponding to crystallized hexagonal graphite (JCPDS 00-041-1487). The diffraction peaks at 35.68°, 43.44°, 57.38° and 63.04° were indexed to the ■(1 1 0), ■(2 0 2), ■(1 2 2) and ■(2 1 4) planes, indicating the formation of crystallized trigonal hematite (JCPDS No. 00-033-0664).

From XRD results, the D of hematite, NiO and Gr nanostructures were calculated from ●(1 1 0), ♣(1 1 1) and ★(0 0 2) peak, respectively, by using Debye-Scherrer equation [Equation (3.1)]. The estimation of XRD parameters is presented in Table 6.6. As expected, the findings indicate that the synthesis temperature significantly influences XRD properties. At a temperature used in synthesis of 75°C, the D of

hematite particles at the ●(1 1 0) plane is calculated as 23.50 ± 0.78 nm. It slightly increases to 24.29 ± 1.21 nm and 24.42 ± 1.25nm, at higher temperatures of synthesis of 85°C and 95°C, respectively. Similarly, the D of NiO particles at the ♣(1 1 1) plane is estimated to increase from 17.54 ± 2.15 nm to 18.17 ± 1.00 nm as the synthesis temperature rises. These findings align with several reports that have investigated the hematite and NiO structure [232, 346-348]. It is anticipated that higher synthesis temperatures accelerate the reaction rate, resulting in a faster crystallite grain formation process, which in turn, leads to larger D [347]. Additionally, as observed in the XRD spectra, the intensity of the Gr peak ★(0 0 2) decreases from 24.33 ± 0.29 nm to 23.25 ± 0.31 nm with increasing synthesis temperature, consistent with a prior report [349].

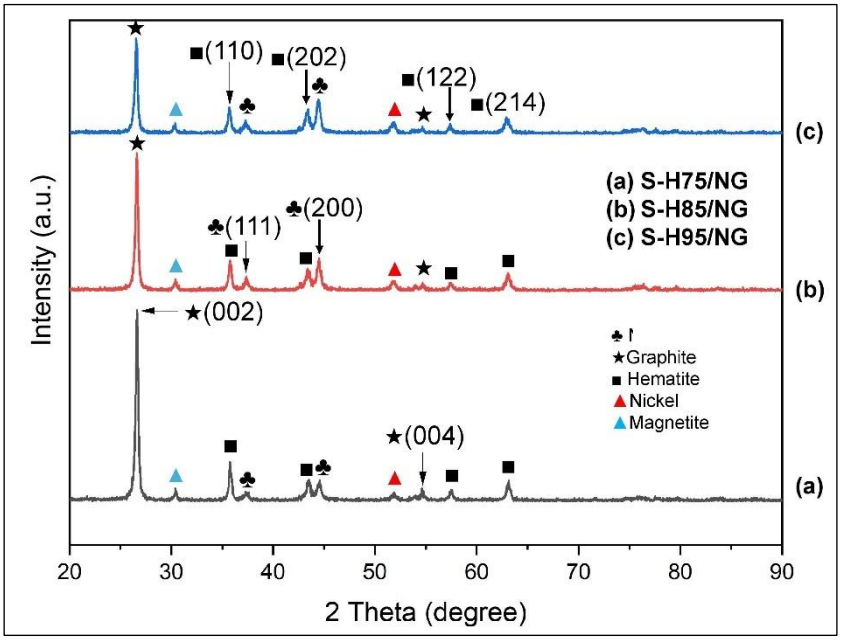

Figure 6.9 XRD Pattern of S-HNG at Synthesis Temperature of 75°C, 85°C and 95°C

Table 6.6
The FWHM and Crystallite Size of Hematite ■(1 1 0), NiO ♣(1 1 1) and Gr ★(0 0 2) Calculated using the Debye-Scherrer Formula

Sample	■ (1 1 0)		♣ (1 1 1)		★ (0 0 2)	
	FWHM, β (rad.)	**Crystallite size, D (nm)**	**FWHM, β (rad.)**	**Crystallite size, D (nm)**	**FWHM, β (rad.)**	**Crystallite size, D (nm)**
75°C	$(6.21\pm0.21)\times10^{-3}$	23.50 ± 0.78	$(8.43\pm1.03)\times10^{-3}$	17.54 ± 2.15	$(5.86\pm0.07)\times10^{-3}$	24.33 ± 0.29
85°C	$(6.01\pm0.30)\times10^{-3}$	24.29 ± 1.21	$(8.35\pm0.67)\times10^{-3}$	17.62 ± 1.39	$(5.90\pm0.04)\times10^{-3}$	24.19 ± 0.16
95°C	$(5.98\pm0.30)\times10^{-3}$	24.42 ± 1.25	$(8.08\pm0.44)\times10^{-3}$	18.17 ± 1.00	$(6.13\pm0.08)\times10^{-3}$	23.25 ± 0.31

6.3.2 Morphological and Elemental Analysis of Hematite/NiO/Gr Composites

FESEM analysis revealed loosely agglomerated nanoparticles randomly distributed across the S-HNG composite surface, with an $Ø_{avg}$ ranging from 44 to 97 nm [Figure 6.10 (a-f)]. As reported in the literature, precise control over particle dimensions at the nanoscale is pivotal for advancing high-efficiency humidity-driven energy harvesting systems, as reduced particle size enhances specific surface area and facilitates superior electronic coupling, thereby improving energy conversion efficiency and charge-transport dynamics [53, 350].

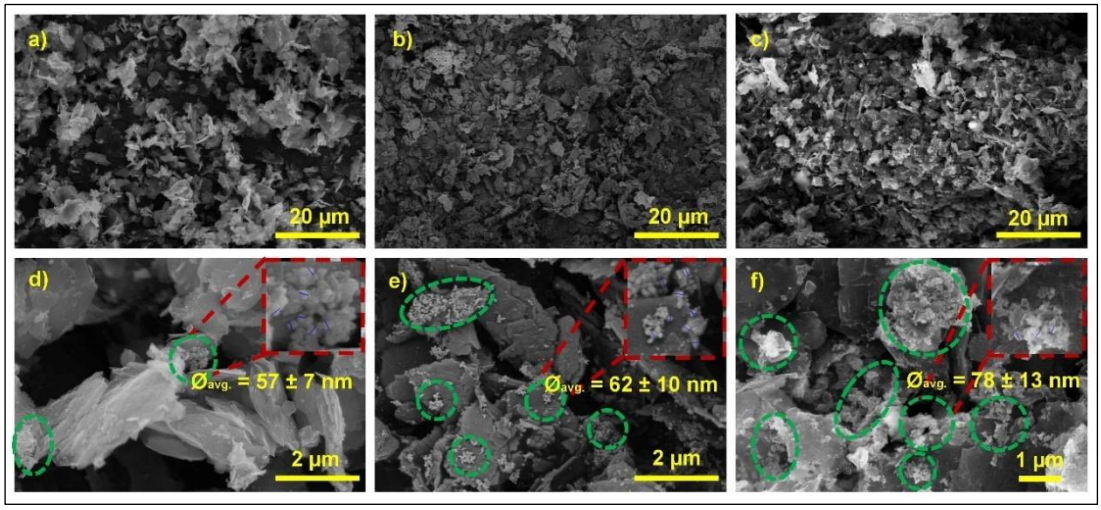

Figure 6.10 FESEM Images of Synthesized S-HNG Prepared via the Sonicated Solution Immersion Method at Synthesis Temperatures of (a) and (d) 75°C, (b) and (e) 85°C, (c) and (f) 95°C, respectively. The Green Dashed Line Indicates Regions of Nanoparticle Agglomeration

At a synthesis temperature of 75 °C, the nanoparticles exhibit moderate agglomeration with an $Ø_{avg}$ of 57 ± 7 nm, indicating that this temperature provides sufficient thermal energy to promote the nucleation and growth of NiO and hematite on the Gr flakes. Increasing the synthesis temperature to 85 °C results in a higher particle yield and a moderate increase in size ($Ø_{avg} \approx 62 \pm 10$ nm). At 95 °C, extensive nanoparticle formation is observed, accompanied by more pronounced agglomeration and an $Ø_{avg}$ of 78 ± 13 nm, which still within the nanoscale regime but with greater clustering due to intensified particle growth kinetics.

Figure 6.11 (a) presents the FESEM micrograph of the S-H95/NG-FP surface, revealing a uniform and well-integrated dispersion of HNG composites intricately embedded within the microchannels of the cellulose-based FP substrate. The topography exhibits pronounced surface roughness and an interconnected porous network—morphological attributes that are highly conducive to enhanced water-vapour adsorption and subsequent ion transport. A magnified view in Figure 6.11 (b) further elucidates the presence of densely agglomerated HNG domains, firmly anchored onto the FP fibrillar matrix and uniformly distributed along the inter-fibril regions, thereby ensuring robust interfacial contact and optimal active surface exposure for humidity-to-electricity conversion.

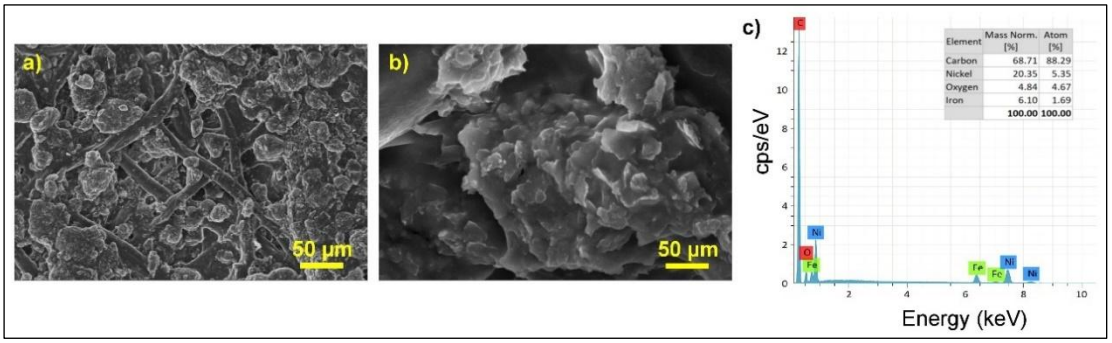

Figure 6.11 (a) FESEM Image of S-H95/NG-FP, (b) Magnified FESEM Image of S-H95/NG-FP, and (c) EDX Spectrum with Elemental Composition Analysis of S-H95/NG-FP

Figure 6.11 (c) presents the EDX spectrum of S-H95/NG-FP, clearly confirming the presence of C, Ni, O, and Fe, thereby validating the successful deposition of HNG composites onto the FP substrate. Complementary EDX elemental mapping, shown in Figure 6.12 (a–f), reveals the spatial distribution of these constituent elements across the sample. In the mapping, C, Ni, O, and Fe are visualized in purple, green, red, and light blue, respectively. An additional Au peak is observed, originating from the gold coating applied to the sample to mitigate surface charging effects during high-resolution imaging. Collectively, these results substantiate not only the incorporation but also the uniform dispersion of all targeted elements within the composite matrix, highlighting the structural coherence and compositional homogeneity of the synthesized material.

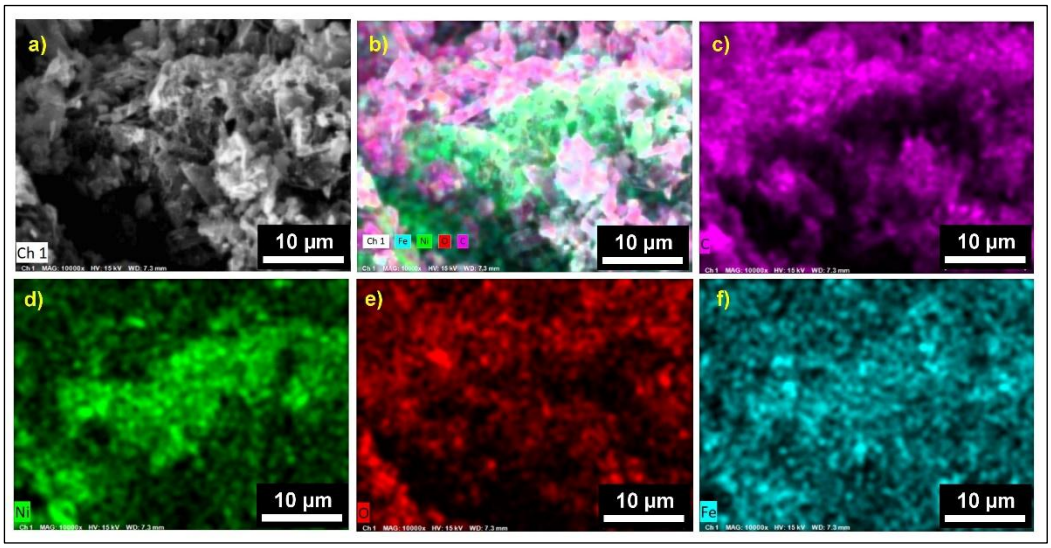

Figure 6.12 (a) EDX Colour Mapping: (b) Overall Mapping, (c) C, (d) Ni, (e) O and (f) Fe in the S-H95/NG-FP

In this study, the maximum synthesis temperature was constrained to 95 °C due to equipment limitations. The results clearly demonstrate that synthesis temperature exerts a profound influence on nanoparticle aggregation dynamics. Elevated thermal energy modulates interparticle forces by diminishing electrostatic repulsive barriers, thereby enabling van der Waals attractions to dominate and driving extensive agglomeration [232, 351]. While a moderate degree of agglomeration can be advantageous by increasing surface roughness and thereby facilitating greater water molecule adsorption [352-354], excessive clustering of particles severely reduces the accessible specific surface area for effective hygroscopic interactions [21]. Literature reports further corroborate that excessively high synthesis temperatures induce severe nanoparticle coalescence, which impairs humidity-to-electricity conversion efficiency by restricting moisture diffusion pathways and limiting active surface–moisture interactions [355-357]. These findings highlight the criticality of engineering optimal nanoparticle dispersion to maximize accessible surface area and facilitate efficient water molecule capture for enhanced energy conversion.

The HRTEM images displayed in Figure 6.13 (a) shows that S-H95/NG contains aggregated nanoparticles of irregular size and spherical shape with hematite and NiO nanoparticles anchor to Gr. The HRTEM image shown in Figure 6.13 (b) reveals clear crystal lattice fringes with a lattice spacing of 0.310 nm, corresponding to the (0 0 2) crystal plane of the Gr phase. Meanwhile, lattice spacings of 0.257 nm, 0.241 nm, and 0.204 nm have been identified based on the HRTEM image which align with the

calculated spacings of the (1 1 0) plane of hematite, the (1 1 1) plane of NiO, and the (1 1 1) plane of Ni, respectively. From the histogram of particle sizes S-H95/NG presented in Figure 6.13 (c), it is evident that most HNG nanoparticles range in size from 48 to 75 nm, with an average size of 59 ± 7 nm. The particle size provided by the HRTEM analysis is in agreement to the information obtained from XRD analysis.

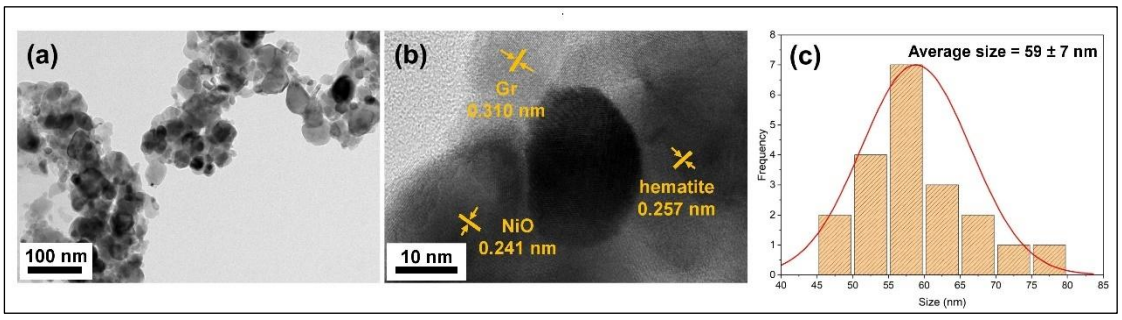

Figure 6.13 TEM Images of the S-H95/NG: (a) Low Magnification and (b) High Magnification. (c) Histograms of The Particle Size Distribution of The S-HNG

6.3.3 Hydrophilicity Analysis of Hematite/NiO/Gr Composites

The WCA results presented in Figure 6.14 confirm that all samples exhibit hydrophilic characteristics. Notably, as the synthesis temperature increases from 75 °C to 95 °C, the θ_{CA} decreases progressively. Specifically, S-H75/NG-FP records a θ_{CA} of 64.2° ± 3.6° with a surface energy of 26.0 ± 1.0 mJ/m², while S-H85/NG-FP exhibits a θ_{CA} of 63.2° ± 0.5° with a surface energy of 26.4 ± 0.1 mJ/m². The lowest θ_{CA} of 62.6° ± 0.1°, corresponding to a surface energy of 26.6 ± 0.1 mJ/m², is observed for S-H95/NG-FP, as summarized in Table 6.7. This progressive decrease in θ_{CA} is attributed to enhanced hydrophilicity induced by increased surface roughness [358]. As corroborated by FESEM observations, higher synthesis temperatures promote greater nanoparticle agglomeration, thereby increasing surface roughness and generating additional porous spaces [232, 359], which collectively contribute to the reduced θ_{CA}.

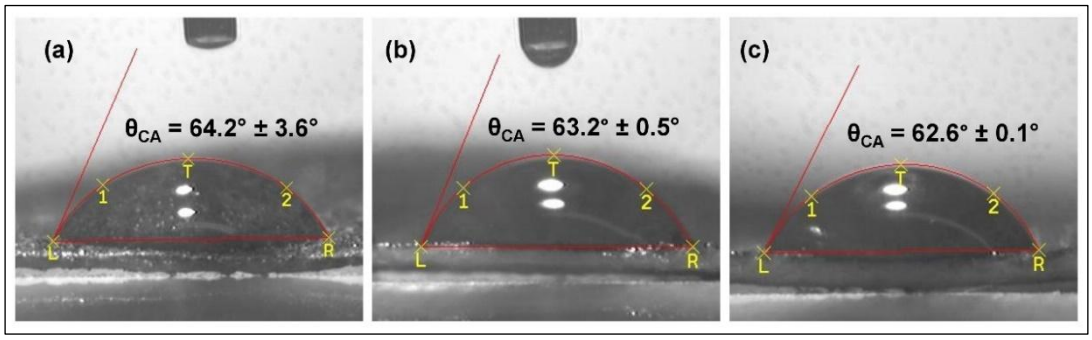

Figure 6.14 Water Contact Angle Measurement of S-HNG Composites on Cellulose-Based Substrate with Different Synthesis Temperature (a) 75°C (b) 85°C and (c) 95°C

Table 6.7
Contact angle measurement data of samples S-H75/NG-FP, S-H85/NG-FP and S-H95/NG-FP

Sample	WCA (°)	Surface Energy (mJ/m^2)
S-H75/NG-FP	64.2° ± 3.6°	26.1 ± 1.0
S-H85/NG-FP	63.2° ± 0.5°	26.4 ± 0.1
S-H95/NG-FP	62.6° ± 0.1°	26.6 ± 0.1

6.3.4 Chemical Composition Analysis of Hematite/NiO/Gr Composites

The chemical composition and oxidation states of the S-H95/NG composites were further investigated using XPS over a binding energy range of 0 to 1200 eV. Figure 6.15(a) to (d) presents the XPS survey spectrum and the high-resolution spectra of the Ni 2p, C 1s, and Fe 2p regions for the S-H95/NG composites. As shown in Figure 6.15 (a), the composite primarily consists of C, Ni, and Fe. The high-resolution Ni 2p spectrum in Figure 6.15 (b) confirms the presence of NiO, indicated by prominent peaks at 856.38 eV and 862.01 eV. Metallic Ni is also detected, with corresponding peaks at 854.78 eV and 860.61 eV. Figure 6.15 (c) displays the high-resolution C 1s spectrum, which reveals peaks associated with Gr, particularly non-oxygenated carbon bonds such as C=C and C–C at 284.08 eV and 284.74 eV, respectively. Additional peaks at 285.41 eV and 286.02 eV correspond to oxygen-containing functional groups, namely C–O and carbonyl carbon (C=O), respectively.

Additionally, the Fe 2p spectrum in Figure 6.15 (d) exhibits peaks corresponding to the hematite phase at 713.97 eV, as well as a minor peak at 725.53 eV attributed to magnetite [360, 361]. Peaks at 710.11 eV and 723.98 eV are assigned to Fe, while peaks at 711.89 eV and 724.78 eV are attributed to FeO. Meanwhile, the high-resolution O 1s spectrum, presented in Figure 6.15 (e), exhibits peaks corresponding to the NiO phase at 530.38 eV, C=O at 532.10 eV, C–O at 533.54 eV, FeO at 531.08 eV

and hematite at 529.45 eV [301]. Overall, the high-resolution XPS results confirm the chemical composition of the sample, aligning well with the XRD data and verifying the presence of hematite, NiO, and Gr in the synthesized composites.

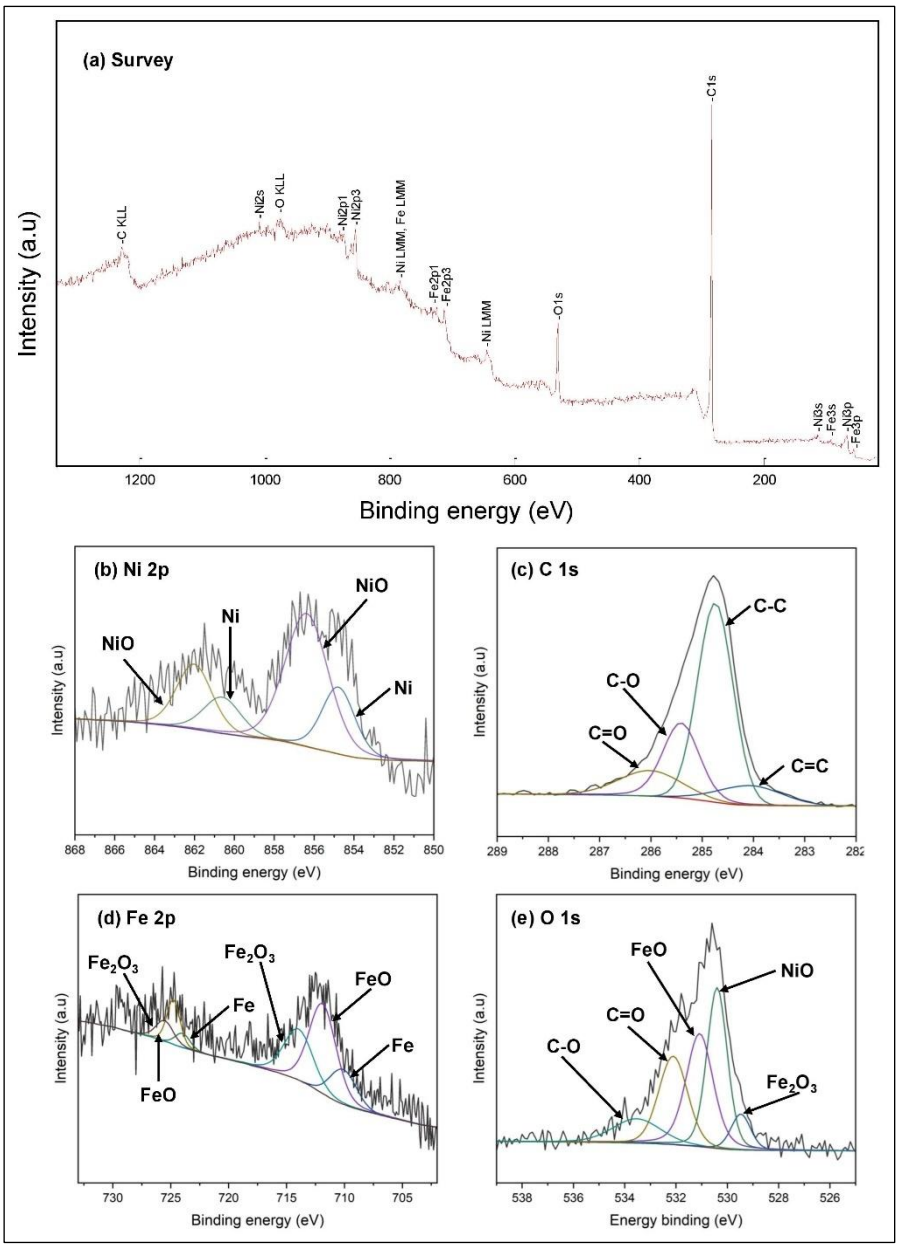

Figure 6.15 The XPS Spectra of the S-H95/NG Powder; (a) Full-Range Survey Spectra, High-Resolution Spectra of (b) Ni 2p Region, (c) C 1s Region, (d) Fe 2p Region and (e) O 1s Region

6.3.5 Surface Area and Porosity Analysis of Hematite/NiO/Gr Composites

BET analysis revealed a progressive decrease in both specific surface area and BJH average pore width of the S-HNG composites with increasing synthesis

temperature. As presented in Table 6.8, S-H75/NG exhibited the highest BET surface area (12.3 m^2/g), which marginally declined to 12.0 m^2/g for S-H85/NG and dropped sharply to 2.3 m^2/g for S-H95/NG. A similar trend was observed for the BJH average pore width, decreasing from 29.2 nm (S-H75/NG) to 26.8 nm (S-H85/NG) and further to 25.9 nm (S-H95/NG). Comparable trends in surface area reduction with increased synthesis temperature have been reported in previous studies [362, 363]. This decline is plausibly attributed to temperature-induced aggregation of hematite and NiO nanoparticles on Gr surfaces, leading to partial pore filling and blockage, which in turn limits the number of accessible mesopores for N_2 adsorption during BET measurements.

Table 6.8
Comparison of the BJH Adsorption Average Pore Diameter and BET Surface Area of S-H75/NG, S-H85/NG and S-H95/NG Composites Powder

Sample	BJH Adsorption average pore diameter (nm)	BET surface area (m^2/g)
S-H75/NG	29.2	12.3
S-H85/NG	26.8	12.0
S-H95/NG	25.9	2.3

6.3.6 Electrical Characterization Analysis of Hematite/NiO/Gr Composites

Hall effect measurements were conducted to investigate the electrical characteristics of S-HNG synthesized at different temperatures. Based on the findings, the carrier concentration increased from $(0.45 \pm 0.1) \times 10^{13}\ cm^{-3}$ to $(0.63 \pm 0.3) \times 10^{13}\ cm^{-3}$ as the synthesis temperature increased. Similarly, the Hall mobility increased with rising synthesis temperature, from $(2.3 \pm 0.1) \times 10^{3}\ cm^2/V{\cdot}s$ to $(2.6 \pm 1.3) \times 10^{4}\ cm^2/V{\cdot}s$. Meanwhile, the Hall coefficient decreased from $(13.9 \pm 0.3) \times 10^{5}\ cm^3/C$ for S-H75/NG-1.0-FP to $(10.7 \pm 0.5) \times 10^{5}\ cm^3/C$ and $(10.0 \pm 0.4) \times 10^{5}\ cm^3/C$ for S-H85/NG-FP and S-H95/NG-FP, respectively.

The electrical conductivity of the samples calculated using Equation (3.6), showed that S-H95/NG-FP exhibited the highest conductivity among the samples, with a value of $(2.6 \pm 1.3) \times 10^{-2}$ S/cm, as presented in Table 6.9. These results indicate that synthesis temperature plays a significant role in enhancing the Hall-measured conductivity. The enhanced conductivity observed for S-H95/NG-FP based on Hall effect measurements, indicates lower resistivity within the developed material. This leads to higher carrier mobility, which in turn results in increased conductivity. This improvement is attributed to the greater thermal energy during synthesis, which promotes the formation of larger crystal domains and improved crystallinity, in

alignment with the XRD results obtained [134]. In addition, according to Wang et al. [364], microstructures with optimized surface area and conductive pathways can form at the ideal synthesis temperature. This contributes to enhanced electron diffusion within the Gr matrix, thereby facilitating higher conductivity.

Table 6.9
Hall Effect Measurement Data of S-H75/NG, S-H85/NG and S-H95/NG Composites on Cellulose-Based Substrate

Sample	**Carrier Concentration (cm^{-3})**	**Hall Coefficient (cm^3/C)**	**Mobility ($cm^2/(V·s)$)**	**Conductivity, σ (S/cm)**
S-H75/NG-FP	$(0.45 \pm 0.1) \times 10^{13}$	$(13.9 \pm 0.3) \times 10^5$	$(2.3 \pm 0.1) \times 10^3$	$(1.7 \pm 0.1) \times 10^{-3}$
S-H85/NG-FP	$(0.58 \pm 0.2) \times 10^{13}$	$(10.7 \pm 0.5) \times 10^5$	$(3.3 \pm 0.2) \times 10^3$	$(3.1 \pm 0.1) \times 10^{-3}$
S-H95/NG-FP	$(0.63 \pm 0.1) \times 10^{13}$	$(10.0 \pm 0.4) \times 10^5$	$(2.6 \pm 1.3) \times 10^4$	$(2.6 \pm 1.3) \times 10^{-2}$

On the other hand, other measurements were conducted at specific RH levels to evaluate the samples' response to humidity and their operational effectiveness. HGPG devices with a humidity absorption area of 1.25 cm^2 were fabricated using S-HNG composites synthesized at range of temperatures, 75°C, 85°C and 95°C. The voltage versus time at a fixed RH of 75% is shown in Figure 6.16 (a), and Table 6.10 highlights the samples' performance in harvesting humidity into electricity. The results indicate that S-H95/NG-FP-based HGPG exhibited the best performance, with an output voltage of $(3.87 \pm 0.06) \times 10^{-3}$V. In comparison, S-H75/NG-FP-based HGPG and S-H85/NG-FP-based HGPG generated voltages output of $(3.01 \pm 0.23) \times 10^{-3}$V and $(3.45 \pm 0.22) \times 10^{-3}$V, respectively. These results highlight the critical role of synthesis temperature in dictating overall electrical conversion efficiency. The observed performance enhancement is intrinsically linked to temperature-induced modulation of surface hydrophilicity. As previously discussed, S-H95/NG-FP exhibits superior hydrophilic characteristics relative to S-H75/NG-FP and S-H85/NG-FP, enabling more effective adsorption and retention of water molecules. This enhanced water-trapping capability facilitates increased ion mobility and redox activity within the composite, culminating in a marked improvement in output voltage [152].

Table 6.10
The Humidity-To-Energy Performance of Fabricated S-H75/NG-FP, S-H85/NG-FP and S-H95/NG-FP-Based HGPG Devices

Sample	**RH (%)**	**R (MΩ)**	**Output voltage, V (V)**	**Current density, J (A/cm^2)**	**Power, P (W)**
S-H75/NG-FP	75	10	$(3.01 \pm 0.23) \times 10^{-3}$	$(2.41 \pm 0.02) \times 10^{-10}$	$(9.06 \pm 0.07) \times 10^{-13}$
S-H85/NG-FP			$(3.45 \pm 0.22) \times 10^{-3}$	$(2.76 \pm 0.18) \times 10^{-10}$	$(1.19 \pm 0.15) \times 10^{-12}$
S-H95/NG-FP			$(3.87 \pm 0.06) \times 10^{-3}$	$(3.09 \pm 0.05) \times 10^{-10}$	$(1.50 \pm 0.05) \times 10^{-12}$

Figure 6.16 (b) shows the current versus time at varying RH levels. From the graph, all samples demonstrated a good response to humidity changes. They maintained a steady electrical signal at 40% RH and increased steadily as it reached 90% RH during the adsorption process. At 90% RH, S-H95/NG-FP-based HGPG produced the highest current of 3.3 nA, compared to S-H75/NG-FP-based HGPG and S-H85/NG-FP-based HGPG, which generated slightly lower currents of 2.4 nA and 2.7 nA, respectively. During the desorption process, as RH decreased from 90% to 40%, all samples showed a drop in current.

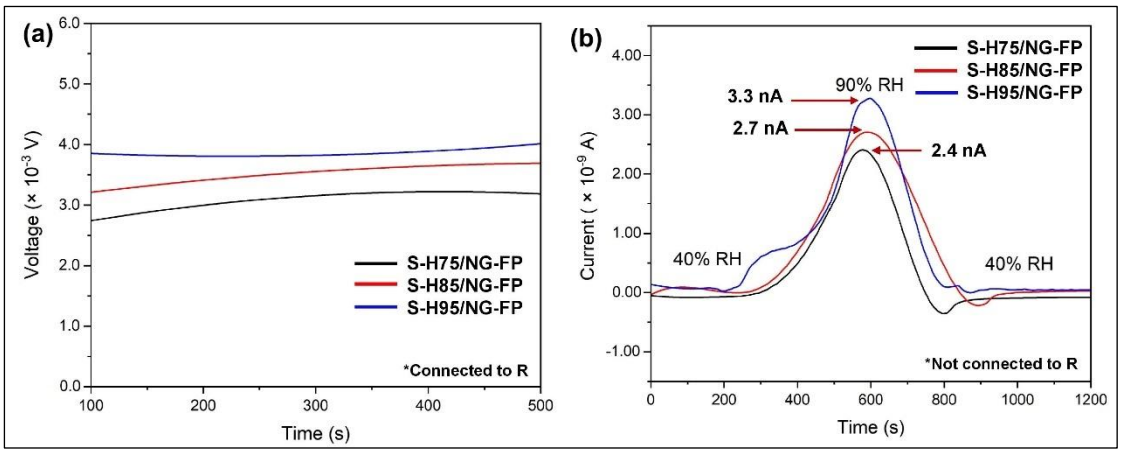

Figure 6.16 (a) The Voltage Versus Time at a Fixed RH Of 75% with Zero Bias Applied to Fabricated S-H75/NG-FP, S-H85/NG-FP and S-H95/NG-FP-Based HGPG. (b) The Current Versus Time at Various RH Levels with Zero Bias Applied to Fabricated S-H75/NG-FP, S-H85/NG-FP and S-H95/NG-FP-Based HGPG

Due to equipment limitations, the maximum immersion bath temperature attainable in this study was 95 °C, which consequently served as the highest synthesis temperature investigated. Literature reports indicate that, particularly in humidity-driven energy harvesting applications, synthesis temperatures exceeding 95 °C can markedly influence nanoparticle attributes such as size, shape, and crystallinity, thereby potentially enhancing device performance [365, 366]. Nonetheless, the optimal synthesis temperature is highly dependent on the material system, synthesis route, and intended application [32, 367-370]. For instance, a study on Ni-MOFs for supercapacitor electrodes reported that synthesis at 80 °C yielded materials with larger specific surface areas and superior electrochemical performance [371]. Conversely, work on bismuth antimony telluride ($Bi_{0.5}Sb_{1.5}Te_3$) thin films revealed that powders

synthesized at 150 °C achieved optimal thermoelectric and semiconducting characteristics [372].

Based on this research, higher synthesis temperatures enhanced the hydrophilic nature of the sample by increasing nanoparticle aggregation, surface roughness, and porosity, which collectively reduced the θ_{CA} and improved humidity responsiveness. Overall, this work highlights the importance of synthesis temperature in tuning material properties such as morphology, hydrophilicity, and crystallinity to maximize the efficiency of humidity-to-energy conversion.

6.4 Enhanced Humidity Gradient Energy Harvesting with Hematite/NiO/Gr Composites on Hydrogel/FP for Humidity Gradient Energy Harvesting Application

The integration of cellulose with hydrogel offers a substantial advancement in realizing gradient configurations for next-generation HGPG devices. In this study, S-H95/NG composite powder was synthesized via a straightforward sonicated solution immersion method, as outlined in Section 3.5, and subsequently deposited onto a Co–Zn-based nanoceramic hydrogel–cellulose substrate. The substrate was prepared using a sol–gel process, while the fabrication of the HGPG device incorporating the S-HNG composite on the Co–Zn-based nanoceramic hydrogel film is described in Section 3.5.2. Comprehensive evaluations, including structural characterization, morphological analysis, hydrophilicity assessment, and electrical performance measurements, were undertaken to determine the suitability of the prepared sample for HGPG applications.

6.4.1 Structural Properties Analysis of Hematite/NiO/Gr-Hydrogel/FP

The XRD patterns of prepared S-HNG-hydrogel/FP are shown in Figure 6.17. Diffraction peaks at 37.72° and 44.04° which corresponds to the ♣(1 1 1) and ♣(2 0 0) planes, signifying the formation of crystallized cubic NiO nanoparticles (JCPDS No. 01-071-4750). The XRD patterns clearly exhibit the planes of ★(0 0 2) at diffraction peak 26.02° corresponding to crystallized hexagonal graphite (JCPDS No. 00-041-1487). The diffraction peaks at 35.24°, 43.44° and 64.20° were indexed to the ■(1 1 0), ■(2 0 2) and ■(2 1 4) planes, indicating the formation of crystallized trigonal hematite (JCPDS No. 00-33-0664).

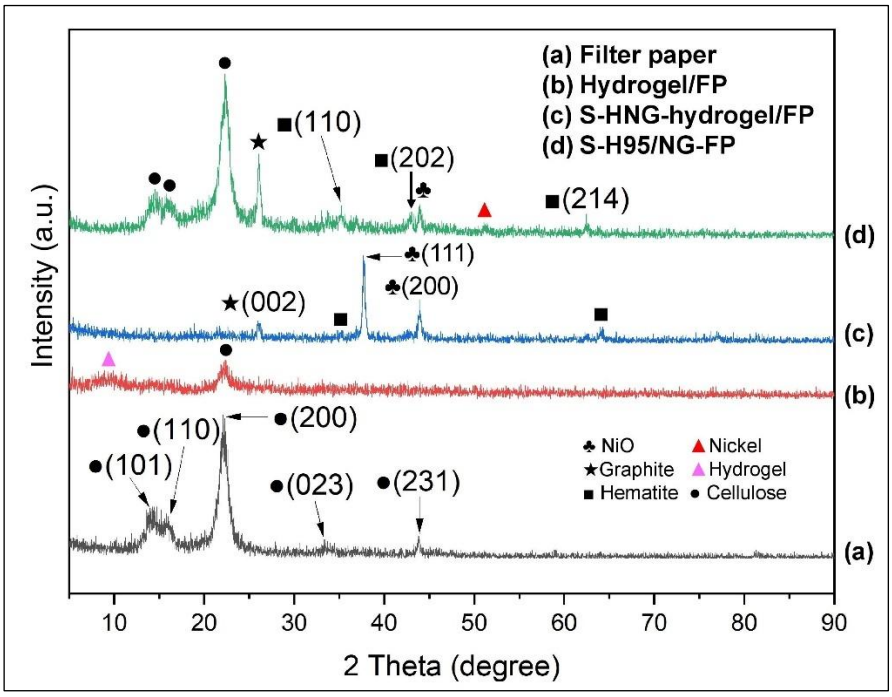

Figure 6.17 XRD Pattern of (a) FP, (b) Hydrogel/FP, (c) S-HNG-hydrogel/FP and (d) S-H95/NG-FP

Additionally, the XRD patterns clearly exhibit the planes of ●(1 0 1), ● (1 1 0), ● (2 0 0), ● (0 2 3) and ● (2 3 1) at diffraction peak 13.98°, 15.84°, 22.14°, 33.34° and 43.74°, respectively, corresponding to crystalline phase with monoclinic structure of cellulose (JCPDS No. 00-056-1718) [286, 287]. The hydrogel component on the Co-Zn hydrogel-cellulose substrate is most likely represented by the broad peak, marked by the pink triangle symbol (▲) in the XRD pattern around 9.30° indexing to the ♦(0 0 3) plane [373, 374]. The peak that was observed aligns with the hydrogel network's structural ordering. This indicates semi-crystalline in the hydrogel matrix or ordered regions within the polymer network, which are typical of cellulose-based hydrogels [375, 376].

Based on the XRD results, the D of the Gr nanostructures was calculated from the ★(0 0 2) peak using Equation (3.1). The estimated XRD parameters are summarized in Table 6.11. It was found that S-H95/NG-FP exhibits a D value of 20.14 ± 0.49 nm, which is larger than that of S-HNG-hydrogel/FP with a D of 18.45 ± 0.20 nm. This suggests that the hydrogel film disrupts the stacking of Gr layers, resulting in a diminished intensity of the Gr peak in the XRD pattern [377, 378]. According to Das et al. [379], sharp Ni and NiO peaks accompanied by a weak Gr peak indicate that NiO/Ni particles cover and interfere with the ordered stacking of Gr sheets in the composite.

The interplanar spacing and unit cell volume exhibited consistency, with only negligible deviations in their mean diffraction peak positions.

Table 6.11
The FWHM, 2θ, Interplanar Spacing, Unit Cell Volume and Crystallite Size of Gr ★(0 0 2) for S-H95/NG-FP and S-HNG-hydrogel/FP

Sample	**FWHM, β (rad)**	**2θ (°)**	**Interplanar spacing, d (nm)**	**Unit Cell Volume, V (nm^3)**	**Crystallite size, D (nm)**
S-H95/NG-FP	$(7.07\pm0.17) \times 10^{-3}$	26.12	$0.34 \pm (7.26 \times 10^{-4})$	$0.32 \pm (2.03 \times 10^{-3})$	20.14 ± 0.49
S-HNG-hydrogel/FP	$(7.72\pm0.08) \times 10^{-3}$	25.99	$0.34 \pm (1.83 \times 10^{-4})$	$0.32 \pm (5.17 \times 10^{-4})$	18.45 ± 0.20

6.4.2 Morphological and Elemental Analysis of Hematite/NiO/Gr-Hydrogel/FP

Figure 6.18 (a) shows the FESEM image of the cross-section of the prepared S-HNG-hydrogel/FP. The image reveals that the sample has an approximate thickness of 240 μm. Meanwhile, Figure 6.18 (b) displays the top-view FESEM image of the sample, which exhibits a porous and heterogeneous surface morphology. Bubble-like formations are visible on the surface, likely resulting from phase separation or air entrapment during the gelation or drying process of the hydrogel. These spherical features which vary in size, appear to enhance the porous structure of the surface. Nanochannels formed between the HNG composites are evident in the FESEM images shown in Figure 6.18 (c) and (d), which display both porosity and an interconnected network within the material, forming heteromorphic nanochannels with a wide range of nanoscale widths.

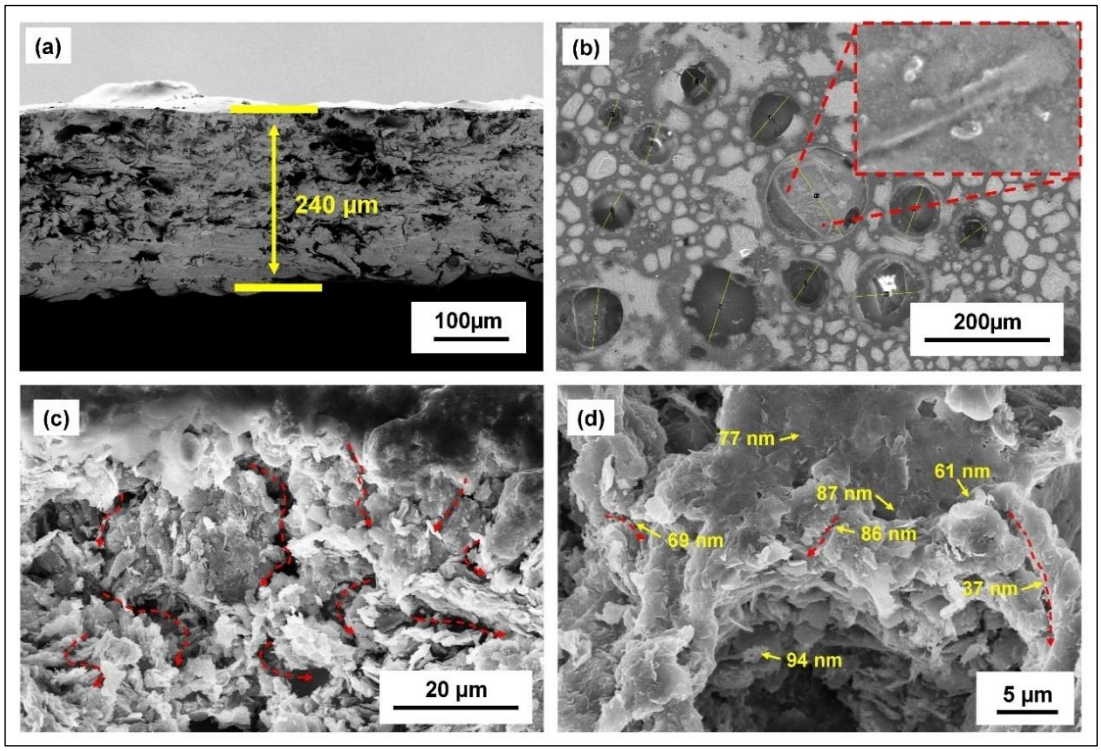

Figure 6.18 FESEM Images of the Prepared S-HNG-Hydrogel/FP: (a) Thickness of S-HNG-Hydrogel/FP, (b) Top-View Image, (c) Cross-Sectional Image, and (d) Magnified Cross-Sectional Image. The Red Dashed Arrow Indicates the Interconnected Porosity within the S-HNG-Hydrogel/FP

The cellulose fibers are visible through the pores, suggesting that the hydrogel network forms and spreads throughout the cellulose base. This observation is supported by the EDX results of the cross-sectional sample shown in Figure 6.19, which confirm the presence of C, Ni, O, and Fe from the HNG composite, as well as C, Co, and Zn from the Co-Zn-based nanoceramic hydrogel-cellulose substrate. The Co and Zn elements are uniformly distributed throughout the sample, while Ni and Fe are predominantly concentrated at the surface due to the top-side deposition of the HNG composite. The extra peaks observed in the EDX spectrum are attributed to the Pt coating, which was applied to reduce charging effects during FESEM and EDX imaging. The interconnected pores, exposed cellulose fibers, and bubble-like structures contribute to an increased surface area, which is advantageous for ion mobility and water absorption which are key factors in enhancing the performance of HGPG devices.

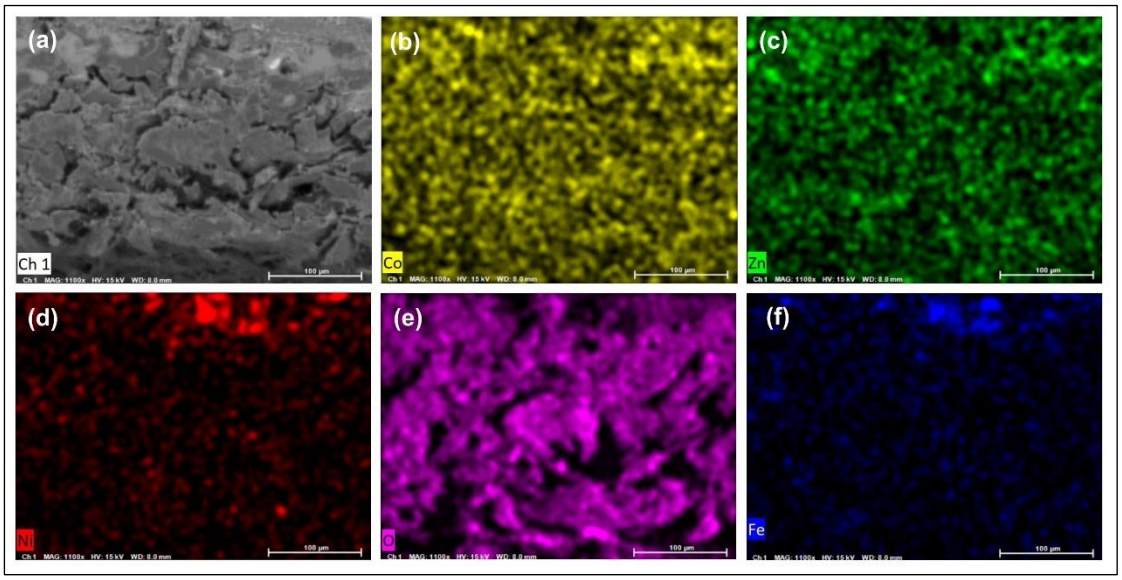

Figure 6.19 (a) EDX Colour Mapping: (b) Co, (c) Zn, (d) Ni, (e) O and (f) Fe in the S-HNG-hydrogel/FP

The HRTEM images of the prepared S-HNG-hydrogel/FP, containing aggregated nanoparticles of irregular sizes and spherical shapes, are shown in Figure 6.20 (a). The HRTEM image in Figure 6.20 (b) reveals clear lattice fringes with spacings of 0.238 nm, corresponding to the (1 1 1) planes of the NiO phase of the Ni phase, respectively. Meanwhile, lattice fringes with spacings of 0.253 nm and 0.304 nm are observed, corresponding to the (1 1 0) plane of the hematite phase and the (2 0 0) plane of the Gr phase, respectively. These observations confirm that hematite/NiO nanoparticles are anchored onto the Gr surface, with some degree of nanoparticle overlap. The particle size distribution, shown in the histogram in Figure 6.20 (c), indicates that the nanoparticles range from 46 to 69 nm, with an average size of 55 ± 5 nm. The particle size determined from HRTEM analysis is consistent with the values obtained from XRD measurements.

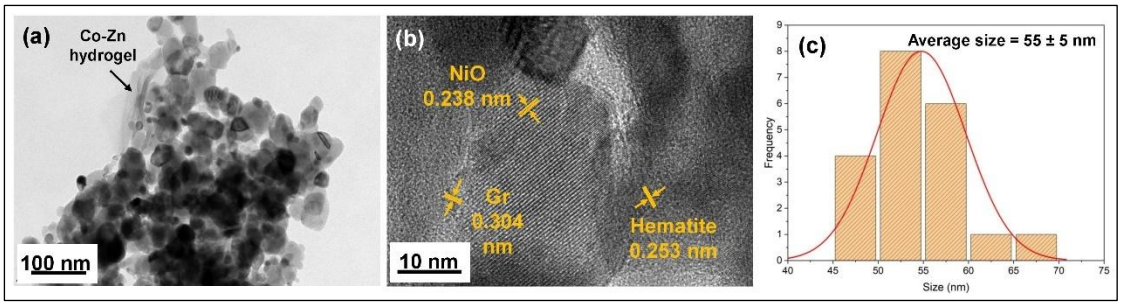

Figure 6.20 TEM Images of the S-HNG-hydrogel/FP: (a) Low Magnification and (b) High Magnification. (c) Histograms of the Particle Size Distribution of the S-HNG-hydrogel/FP

6.4.3 Hydrophilicity Analysis of Hematite/NiO/Gr-Hydrogel/FP

Figure 6.21 shows that the prepared S-HNG-hydrogel/FP exhibits strong hydrophilic properties, with a θ_{CA} of $44.6° \pm 0.4°$, corresponding to a higher surface energy of 31.2 ± 0.1 mJ/m^2. In comparison, S-H95/NG-FP shows slightly higher θ_{CA} of $62.6° \pm 0.1°$, with a surface energy of 26.6 ± 0.1 mJ/m^2, as summarized in Table 6.12. The enhanced hydrophilicity observed in the hydrogel-integrated sample is attributed to the Co-Zn hydrogel network, which forms through metal-ligand interactions and sol-gel transition, improving both water interaction and gelation behaviour.

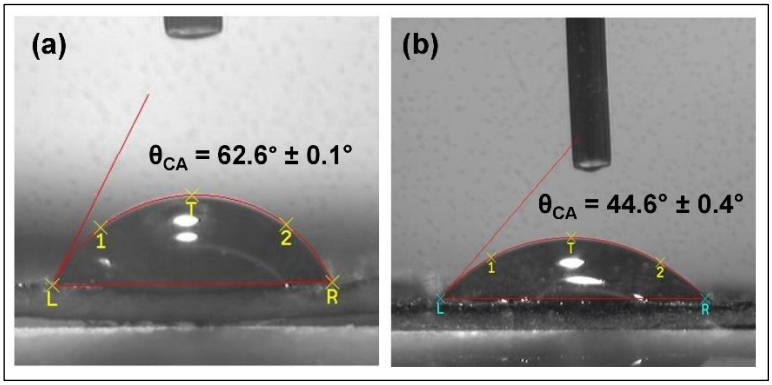

Figure 6.21 Water Contact Angle Measurement of S-HNG-hydrogel/FP

Table 6.12
Contact Angle Measurement Data of samples S-H95/NG-FP and S-HNG-hydrogel/FP

Sample	WCA (°)	Surface Energy (mJ/m^2)
S-H95/NG-FP	$62.6° \pm 0.1°$	26.6 ± 0.1
S-HNG-hydrogel/FP	$44.6° \pm 0.4°$	31.2 ± 0.1

As illustrated in Figure 6.22, the synthesized Co-Zn hydrogel was dropped onto a microscope glass slide. When heated in a furnace (Protherm) at 90 °C for 3 minutes, the hydrogel visibly shrank and dried. In contrast, exposure to a high-humidity environment (90% RH for 10 minutes) caused the hydrogel to expand significantly, indicating its strong affinity for water absorption from the surrounding environment. The integration of the hydrogel into the composite structure enhances hydrophilicity and moisture interaction, attributed to its abundance of hydroxyl (-OH) and amine (-NH_2) groups [380]. These functional groups contribute to the observed low contact angle, high surface energy, and improved moisture adhesion, making the material suitable for HGPG applications [381].

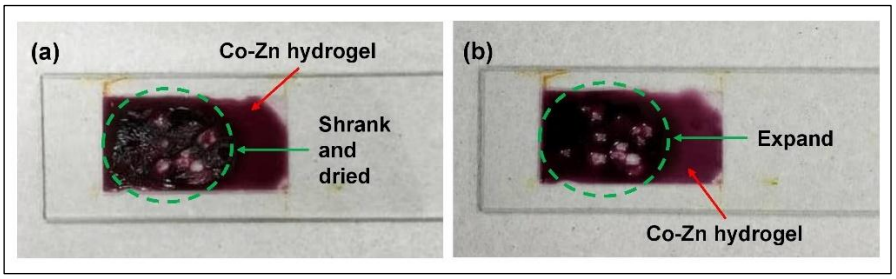

Figure 6.22 Co-Zn Hydrogel on a Microscope Glass Slide: (a) After Heating at 90 °C for 3 minutes, Showing Visible Shrinkage and Drying, and (b) After Exposure to a High-Humidity Environment (90% RH) for 10 Minutes, Showing Visible Expansion

6.4.4 Surface Area and Porosity Analysis of Hematite/NiO/Gr-Hydrogel/FP

Based on BET analysis, it was discovered that the BET surface area and BJH average pore width of S-HNG-hydrogel/FP were lower than those of the sample of S-H95/NG-FP. This is due to the pores and surface features of the cellulose substrate have been covered by the hydrogel layer. The hydrogel has a tendency to form a dense network that fills in the gaps between fibers result in smooth surface topography during gelation and drying. Thus, the hydrogel-coated sample has lower surface area and smaller average pore Ø due to fewer accessible pores for N_2 adsorption during BET measurement.

BET measurements were used to determine the Density Functional Theory (DFT) pore characteristics of the samples. For the S-H95/NG-FP sample, the analysis revealed the presence of micropores (< 2 nm) with a micropore volume of 5.8×10^{-3} m^3/g. In contrast, the S-HNG–hydrogel/FP sample exhibited no detectable microporosity, as the hydrogel layer likely blocked the micropores, rendering them inaccessible for N_2 adsorption analysis. Notably, as summarized in Table 6.13, the S-HNG–hydrogel/FP sample displayed a pore volume of approximately 4.1×10^{-2} m^3/g and a total surface area in pores larger than 2 nm of 28.9 m^2/g, both of which are higher than those of the S-H95/NG-FP sample. These results indicate that the hydrogel introduces additional mesoporous structures into the composite. Such mesoporosity is beneficial for enhancing moisture adsorption and facilitating ion transport, both of which are essential for high-performance HGPG applications.

Table 6.13
Comparison of BET Surface Area and DFT Pore Size Distribution between S-H95/NG-FP and S-HNG-hydrogel/FP

Sample	BJH Adsorption average pore diameter (nm)	BET surface area (m^2/g)	Volume in Pores < 2 nm ($\times 10^{-3}$ m^3/g)	Total Volume in Pores <= 100 nm ($\times 10^{-2}$ m^3/g)	Total Area in Pores >= 2 nm (m^2/g)
S-H95/NG-FP	8.5	68.4	5.8	2.0	21.6
S-HNG-hydrogel/FP	3.9	56.5	0.0	4.1	28.9

6.4.5 Electrical Characterization Analysis of Hematite/NiO/Gr-Hydrogel/FP

Measurements were conducted on S-H95/NG-FP and S-HNG hydrogel/FP to assess their humidity responsiveness and operational performance in HGPG applications. Figure 6.23 (a) presents the current–time response at various RH levels. Both samples exhibited a clear and stable response to humidity variations, maintaining a consistent electrical signal at 40% RH during the adsorption phase, which progressively increased as the RH rose to 90%. At 90% RH, the S-H95/NG-FP-based HGPG produced a current of 3.3 nA, whereas the S-HNG hydrogel/FP-based HGPG achieved a substantially higher current of 13.0 nA. This pronounced enhancement is attributed to the hydrogel layer, which provides a highly hygroscopic and ion-conductive network that facilitates rapid water uptake and efficient ion transport across the device. During the desorption phase, as the RH decreased from 90% to 40%, both devices displayed a corresponding decline in current output, demonstrating their reversible and stable humidity response characteristics.

The voltage–time profiles at a fixed RH of 75% are shown in Figure 6.23 (b), with the corresponding performance metrics summarized in Table 6.14. The S-H95/NG-FP-based HGPG delivered an output voltage of $(3.87 \pm 0.06) \times 10^{-3}$ V, a current density of $(3.09 \pm 0.05) \times 10^{-10}$ A/cm^2, and an output power of $(1.50 \pm 0.05) \times 10^{-12}$ W. In contrast, the S-HNG hydrogel/FP-based HGPG achieved a markedly higher output voltage of $(11.50 \pm 0.20) \times 10^{-3}$ V, a current density of $(9.23 \pm 0.16) \times 10^{-10}$ A/cm^2, and an output power of $(13.23 \pm 0.23) \times 10^{-12}$ W. This substantial enhancement in performance is attributed to the hydrogel's exceptional hygroscopicity and interconnected three-dimensional porous network, which enable greater water uptake, serve as a reservoir for active material, and facilitate enhanced ion dissociation. Moreover, as supported by the BET analysis discussed earlier, hydrogel integration

optimizes the microstructural architecture and overall porosity, thereby reducing diffusion resistance by allowing water molecules to readily permeate the structure under high-humidity conditions [113]. In addition, the hydrogel's capacity to promote ion mobility strengthens the development of a moisture gradient, further boosting voltage generation [382].

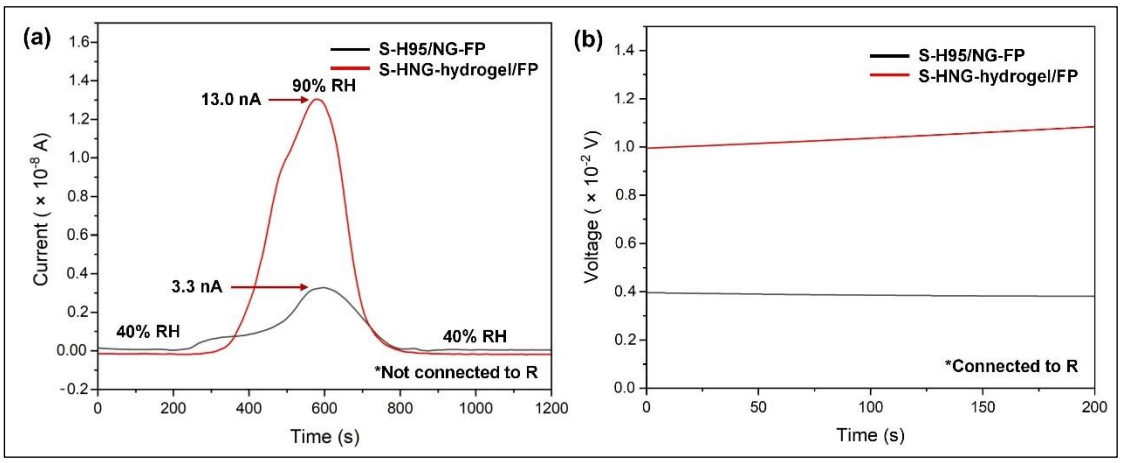

Figure 6.23 (a) The Current Versus Time at Various RH Levels with Zero Bias Applied to Fabricated S-H95/NG-FP and S-HNG-Hydrogel/FP-Based HGPG. (b) the Voltage Versus Time at a Fixed RH of 75% with Zero Bias Applied to Fabricated S-H95/NG-FP and S-HNG-Hydrogel/FP-Based HGPG

Table 6.14
The Humidity-To-Energy Performance of Fabricated S-H95/NG-FP and S-HNG-Hydrogel/FP-Based HGPG Devices

Sample	RH (%)	R (MΩ)	Output voltage, V (V)	Current density, J (A/cm^2)	Power, P (W)
S-H95/NG-FP	75	10	$(3.87 \pm 0.06) \times 10^{-3}$	$(3.09 \pm 0.05) \times 10^{-10}$	$(1.50 \pm 0.05) \times 10^{-12}$
S-HNG-hydrogel/FP			$(11.50 \pm 0.20) \times 10^{-3}$	$(9.23 \pm 0.16) \times 10^{-10}$	$(13.23 \pm 0.23) \times 10^{-12}$

6.4.6 Working mechanism of Hematite/NiO/Gr Composites on Hydrogel/FP for Humidity Gradient Energy Harvesting Application

The working mechanism of the developed HGPG device is illustrated in Figure 6.4 highlighting the voltage generation phenomena during humidity conversion. Cellulose paper, specifically FP, was used as the substrate in the HGPG device. A material property gradient is introduced when the S-HNG composites layer is deposited on the FP substrate, due to differences in surface energy, conductivity, and hygroscopicity between the composites and the cellulose. This gradient facilitates directed ion migration, enabling charge separation and the generation of electricity

[383-385]. The fibrous, porous architecture of cellulose paper is well known for forming spontaneous, randomized capillary channels [386]. Meanwhile, the interface between NiO and Gr incorporated with hematite, gives rise to heteromorphic nanochannels, which differ in shape, conductivity, and surface properties. As illustrated in Figure 6.4 (a), a network of continuous, heteromorphic nanochannels is formed by the aligned nanopores in hematite/NiO and Gr. These nanochannels are essential for promoting directional water molecule migration, facilitating ion transport, and generating internal potential differences crucial for power generation [387, 388].

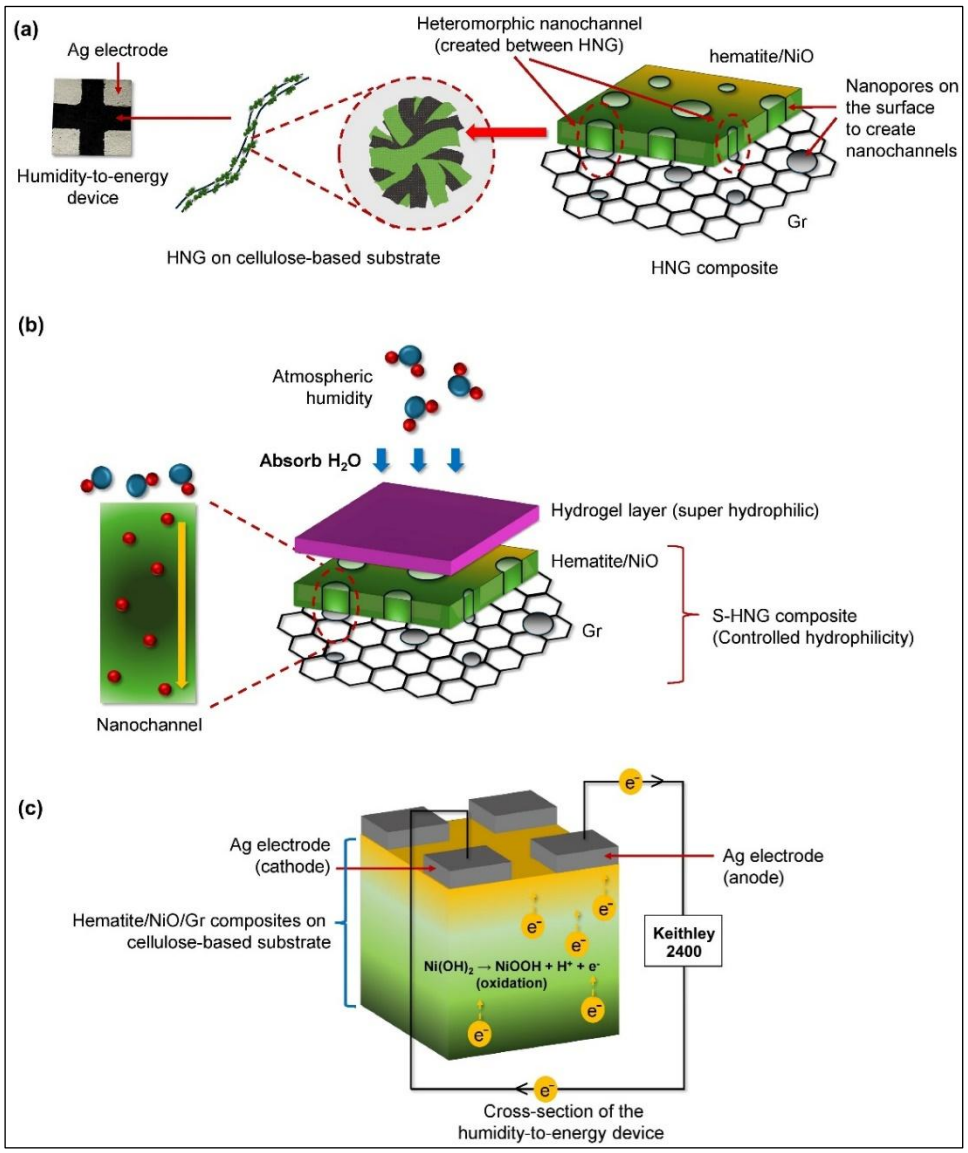

Figure 6.24 Operation Mechanism of the Constructed Humidity-To-Energy Device, Illustrating the Voltage Generation during Humidity Conversion: (a) Formation of Heteromorphic Nanochannels Between Synthesized HNG, (b) Nanochannels Facilitate Continuous Charge Separation and Maintain Ionic Current, (c) Surface Reactions During Humidity Conversion that Enable Electricity Generation via the Developed Hygroscopic Materials

A HGPG device incorporating S-HNG-hydrogel/FP is equipped with Ag metal contacts positioned at its edges. The Co-Zn hydrogel functions as a highly porous and hydrophilic layer that efficiently captures water molecules from ambient air, enabling continuous hydration driven by the concentration gradient at the composite-hydrogel interface. The presence of Co^{2+} and Zn^{2+} ions in the hydrogel reduces the energy barrier for water diffusion. This enhancement is attributed to electrostatic interactions between the divalent metal ions and water molecules, which promote sustained proton and hydroxide mobility [389]. The absorbed water molecules undergo partial dissociation into H^+ and OH^- ions due to ionization effects [390]. While OH^- ions may be trapped or neutralized at the surface, H^+ ions continue to migrate through a network of interconnected heteromorphic nanochannels formed by the aligned nanopores within the HNG composite layer. These nanochannels are critical for facilitating directional proton flow, supporting ion transport, and contributing to the development of internal potential differences necessary for power generation [387, 388].

Simultaneously, electrocatalytic surface redox reactions occur spontaneously and serve as the primary power source. As water molecules reach the composite layer, they trigger and participate in redox reactions. In this phase, H^+ ions facilitate the oxidation of $Ni(OH)_2$ to NiOOH, releasing electrons and additional protons, while Fe^{3+} in hematite is reduced to Fe^{2+} by accepting electrons [391, 392]. Following these reactions, the released H^+ ions continue migrating through the nanochannels within the composite. Sustained proton transport helps maintain the redox cycle and supports continuous charge separation. The electrons generated from oxidation are conducted through the highly conductive Gr layer toward the Ag electrode, generating a measurable voltage and current. Several reported studies on humidity-based energy harvesting have involved surface redox reactions, confirming that humidity can trigger electrochemical processes for power generation, consistent with the findings of this study [393-396].

Figure 6.24 (b) illustrates how the system functions as a self-sustained moisture-gradient material for humidity conversion. Humidity distribution across the device is typically non-uniform [397]. Asymmetry in the material, such as that introduced by the heteromorphic nanochannels, along with factors like device orientation, may cause one side to absorb slightly more moisture than the other. This leads to a significant potential gradient across the hydrogel and composite structure. Consequently, the device's output voltage and current are measured across the two metal contacts. The roles of the Ag

electrodes as anode or cathode depend on the local humidity conditions and the direction of internal ion flow [398]. Typically, the anode is the electrode at which oxidation occurs, and electrons are released into the external circuit, while the cathode is where electrons are received, facilitating reduction reactions and electron collection.

6.5 Innovative Humidity Gradient Energy Harvesting Using Hematite/NiO/Gr Composites on Hydrogel/RP for Humidity Gradient Energy Harvesting Application

The integration of RP with hydrogel represents a noteworthy advancement toward achieving a gradient configuration in HGPG devices, while simultaneously aligning with the waste-to-energy concept for long-term sustainable energy solutions. In this study, HNG composite powder was synthesized via a straightforward sonicated solution immersion method, as outlined in Section 3.5. The synthesized composite was subsequently deposited onto a Co-Zn-based nanoceramic hydrogel–RP substrate. The preparation of the RP substrate integrated with hydrogel, employing the sol–gel method, along with the fabrication of the HGPG device incorporating the S-HNG composite on the Co-Zn-based nanoceramic hydrogel film, are detailed in Section 3.5.3. The potential of the developed sample for HGPG applications was systematically evaluated through comprehensive analyses, including structural characterization, morphological examination, hydrophilicity assessment, and electrical performance testing.

6.5.1 Structural Properties Analysis of Hematite/NiO/Gr-Hydrogel/RP

The XRD patterns of prepared S-HNG-hydrogel/RP are shown in Figure 6.25. Diffraction peaks at 37.70°, 43.90° and 62.70° which corresponds to the ♣(1 1 1), ♣(2 0 0) and ♣(2 2 0) planes, signifying the formation of crystallized cubic NiO nanoparticles (JCPDS No. 01-071-4750). The XRD patterns clearly exhibit the planes of ★(0 0 2) at diffraction peak 26.28° corresponding to crystallized hexagonal graphite (JCPDS No. 00-056-0160). The diffraction peaks at 35.40°, 43.12° and 64.02° were indexed to the ■(1 1 0), ■(2 0 2) and ■(2 1 4) planes, indicating the formation of crystallized trigonal hematite (JCPDS No. 00-033-0664). Additionally, the XRD patterns clearly exhibit the planes of ●(1 0 1), ●(1 1 0), ●(1 1 1), ●(2 0 0), ●(0 2 3) and ●(2 3 1) at diffraction peak 14.04°, 15.80°, 19.12°, 22.30°, 33.44° and 43.84°,

respectively, corresponding to crystalline phase with monoclinic structure of cellulose (JCPDS No. 00-056-1718) [286, 287]. A sharp diffraction peak at 29.06°, marked by a brown triangle symbol (▲), was indexed to the (1 0 4) plane, indicating the presence of trigonal $CaCO_3$, an additive derived from the RP (JCPDS No. 00-005-0586) [399].

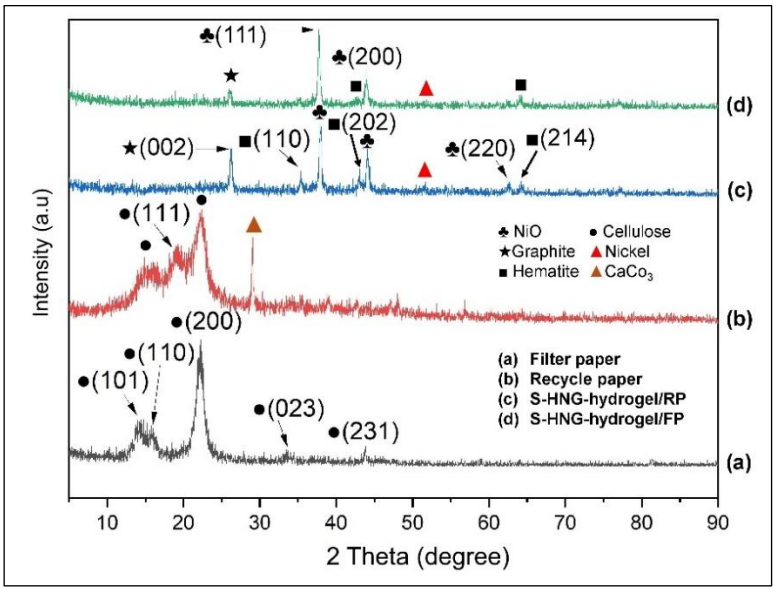

Figure 6.25 XRD Pattern of (a) FP, (b) RP, (c) S-HNG-hydrogel/RP and (d) S-HNG-hydrogel/FP

Table 6.15
The FWHM, 2θ, Interplanar Spacing, Unit Cell Volume and Crystallite Size of NiO ♣(1 1 1) for S-HNG-hydrogel/FP and S-HNG-hydrogel/RP

Sample	FWHM, β (rad)	2θ (°)	Interplanar spacing, d (nm)	Unit Cell Volume, V (nm^3)	Crystallite size, D (nm)
S-HNG-hydrogel/RP	$(6.35 \pm 0.05) \times 10^{-3}$	37.94	$0.24 \pm (5.11 \times 10^{-4})$	$0.07 \pm (4.48 \times 10^{-4})$	23.12 ± 0.18
S-HNG-hydrogel/FP	$(6.24 \pm 0.04) \times 10^{-3}$	37.75	$0.24 \pm (4.30 \times 10^{-4})$	$0.07 \pm (3.81 \times 10^{-4})$	23.49 ± 0.16

From the result analysis, it is observed that the XRD pattern of hydrogel/RP is similar to hydrogel/FP with some extra peaks indicating the RP may consist of additives such as inks and fillers (i.e., $CaCo_3$) [400]. On the other hand, the S-HNG-hydrogel/RP sample shows a more prominent Gr peak, indicating that the addition of RP significantly enhances the visibility of the Gr peak while reducing the crystallinity of NiO, as presented in Table 6.15. According to Damnalı et al. [401], RP typically contains higher levels of chemical variability which improve crystallite alignment and, thus, increase the intensity of the XRD signal for carbon-based phases. However, the D of NiO calculated from the ♣(1 1 1) peak using Equation (3.1) shows only a very slight increase, indicating that the D values for both samples are relatively similar and not significantly

affected. In addition, the interplanar spacing and unit cell volume were effectively identical, with their average diffraction peak positions differing by only a marginal amount.

6.5.2 Morphological and Elemental Analysis of Hematite/NiO/Gr-Hydrogel/RP

Figure 6.26 (a) presents the FESEM cross-sectional image of the S-HNG-hydrogel/RP sample, revealing an overall thickness of approximately 474 μm. The cross-sectional view in Figure 6.26 (b) highlights a well-developed network structure characterized by pronounced porosity and high interconnectivity within the material. The top-view FESEM image in Figure 6.26 (c) shows a porous surface morphology populated with spherical features of varying dimensions, with an average size of 58.2 ± 16.5 μm. A magnified view in Figure 6.26 (d) further reveals that these pores form interconnected pathways, which are advantageous for moisture penetration and ion transport.

The hydrogel network is observed to penetrate and distribute uniformly throughout the cellulose matrix, as evidenced by the EDX cross-sectional analysis shown in Figure 6.27. The EDX spectrum confirms the presence of C, Ni, O, and Fe from the S-HNG composite, together with C, Co, and Zn originating from the Co-Zn-based nanoceramic hydrogel-cellulose substrate. Calcium (Ca) peaks were also detected, validating that the additive in the RP is Ca, consistent with the XRD results and in agreement with previous reports [402, 403]. Extra peaks in the spectrum correspond to the thin Au coating applied to reduce surface charging during FESEM and EDX characterization. The comparable porous structure and elemental composition observed for composites on both hydrogel/RP and hydrogel/FP substrates indicate that RP-based HGPG devices can perform on par with those fabricated using commercial FP, making RP a promising low-cost and sustainable alternative for humidity-driven energy harvesting applications.

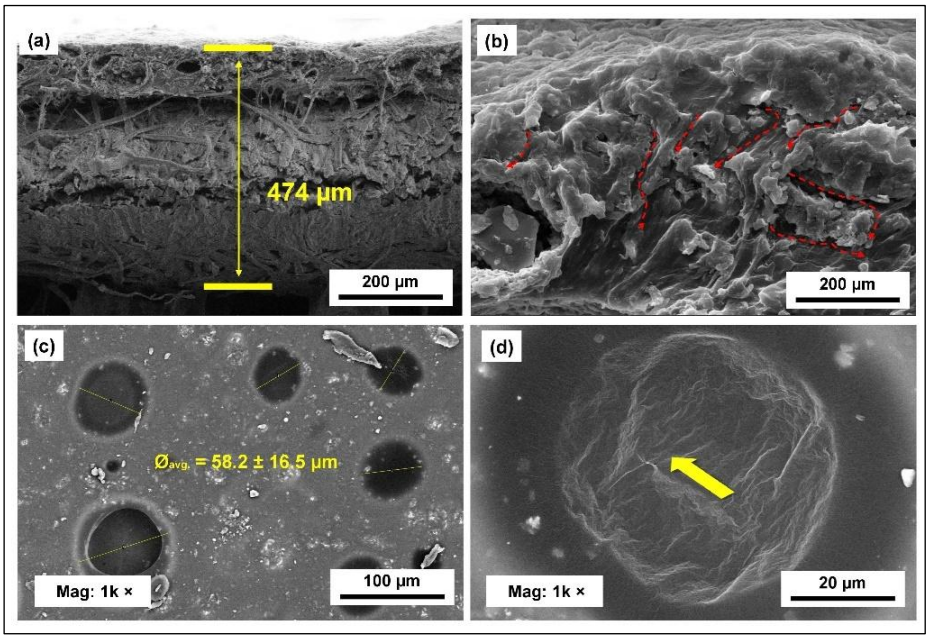

Figure 6.26 FESEM Images of the Prepared S-HNG-Hydrogel/RP: (a) Thickness of S-HNG-Hydrogel/RP, (b) Magnified Cross-Sectional Image, (c) Top-View Image, and (d) Magnified Top-View Image Showing a Clear View of The Pores. The Red Dashed Arrow Indicates the Interconnected Porosity within the S-HNG-Hydrogel/RP

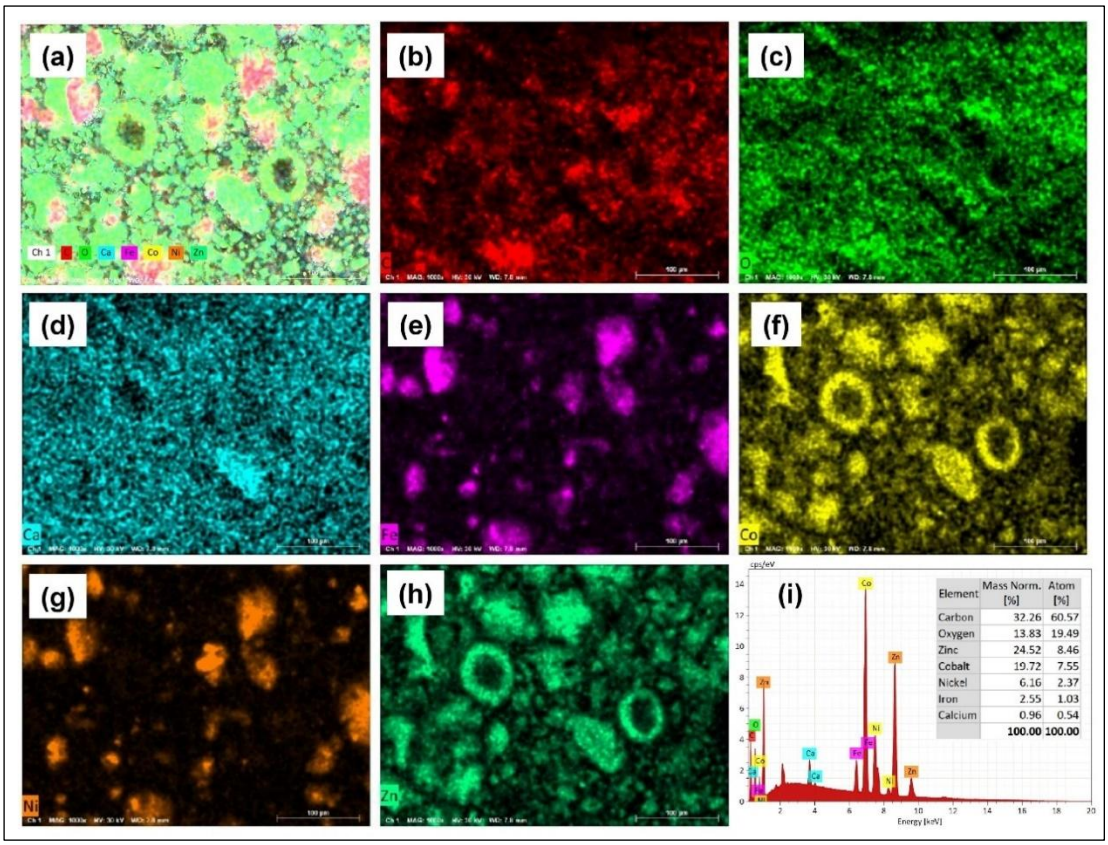

Figure 6.27 (a) EDX Colour Mapping: (b) C, (c) O, (d) Ca, (e) Fe, (f) Co, (g) Ni and (h) Zn in the S-HNG-hydrogel/RP

6.5.3 Hydrophilicity Analysis of Hematite/NiO/Gr-Hydrogel/RP

The WCA measurements were carried out to evaluate the hydrophilic properties of S-HNG-hydrogel/RP and to compare them with those of S-HNG-hydrogel/FP. Based on the results shown in Figure 6.28, S-HNG-hydrogel/RP exhibited a slightly higher θ_{CA} of $56.4° \pm 0.3°$, with an estimated surface energy of 28.3 ± 0.1 mJ/m^2, calculated using Equation (2.8). However, as presented in Table 6.16, S-HNG-hydrogel/FP demonstrated stronger hydrophilic properties, with a lower θ_{CA} of $44.6° \pm 0.4°$ and a surface energy of 31.2 ± 0.1 mJ/m^2.

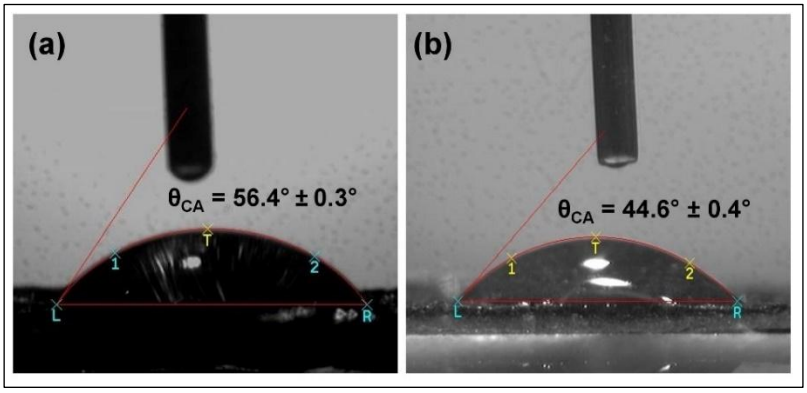

Figure 6.28 Water Contact Angle Measurement of (a) S-HNG-hydrogel/RP and (b) S-HNG-hydrogel/FP

Table 6.16
Contact Angle Measurement Data of Samples S-HNG-hydrogel/FP and S-HNG-hydrogel/RP

Sample	WCA (°)	Surface Energy (mJ/m^2)
S-HNG-hydrogel/RP	$56.4° \pm 0.3°$	28.3 ± 0.1
S-HNG-hydrogel/FP	$44.6° \pm 0.4°$	31.2 ± 0.1

As previously discussed, the higher θ_{CA} observed for the RP sample is likely due to the presence of additives that hinder water interaction. According to Cherkas et al. [399], additives such as Ca, as detected in the EDX analysis, can affect the porosity of paper, thereby influencing its hydrophilicity. Nevertheless, the sample still exhibits hydrophilic behaviour, attributed to the presence of the Co-Zn hydrogel network, which facilitates water attraction.

6.5.4 Surface Area and Porosity Analysis of Hematite/NiO/Gr-Hydrogel/RP

Based on BET analysis, the S-HNG-hydrogel/RP exhibited a significantly lower surface area of 0.3 m^2/g compared to 56.5 m^2/g for the S-HNG-hydrogel/FP, as shown in Table 6.17. This substantial reduction is likely attributable to the presence of wastepaper additives such as ink, coatings, and lignin, which can coat fiber surfaces or obstruct pore spaces, thereby limiting N_2 adsorption during BET measurements [404]. Additionally, RP fibers are generally shorter and more fragmented than FP fibers, resulting in irregular and poorly interconnected pore networks that further decrease the accessible surface area [405]. DFT pore size distribution analysis revealed that the S-HNG-hydrogel/RP sample contained pores larger than 2 nm, with a total pore area of 7.9×10^{-2} m^2/g. In contrast, the S-HNG-hydrogel/FP substrate exhibited a markedly higher total pore area of 28.9 m^2/g. These results indicate that the S-HNG-hydrogel/FP possesses a more developed mesoporous architecture, which can facilitate more efficient water molecule and ion transport within the HGPG system.

Table 6.17
Comparison of BET Surface Area and DFT Pore Size Distribution between S-HNG-hydrogel/FP and S-HNG-hydrogel/RP

Sample	BET surface area (m^2/g)	Total Area in Pores >= 2 nm (m^2/g)
S-HNG-hydrogel/RP	0.3	7.9×10^{-2}
S-HNG-hydrogel/FP	56.5	28.9

6.5.5 Electrical Characterization Analysis of Hematite/NiO/Gr-Hydrogel/RP

Measurements were performed on the S-HNG-hydrogel/RP to assess its humidity response and operational performance in HGPG devices. The voltage–time profiles at a fixed RH of 75% are shown in Figure 6.29 (a), with the corresponding electrical output data summarized in Table 6.18. The HGPG device incorporating the S-HNG-hydrogel/RP substrate generated an output voltage of $(2.30 \pm 0.01) \times 10^{-3}$ V, which is markedly higher than that of the pure RP substrate without composite or hydrogel integration, yielding only $(0.75 \pm 0.01) \times 10^{-3}$ V. In comparison, the S-HNG-hydrogel/FP-based HGPG achieved a substantially higher output voltage of $(11.50 \pm 0.20) \times 10^{-3}$ V. This performance gap is attributed to the superior material properties of the FP-based device, as discussed earlier. Specifically, the S-HNG-hydrogel/FP exhibits a greater surface area and larger total pore volume than its RP-based counterpart, enabling more efficient adsorption and retention of water molecules—an essential

factor for effective humidity-to-energy conversion in HGPG systems [345]. This interpretation is further supported by the WCA measurements, which revealed stronger hydrophilicity in the S-HNG-hydrogel/FP compared to the S-HNG-hydrogel/RP.

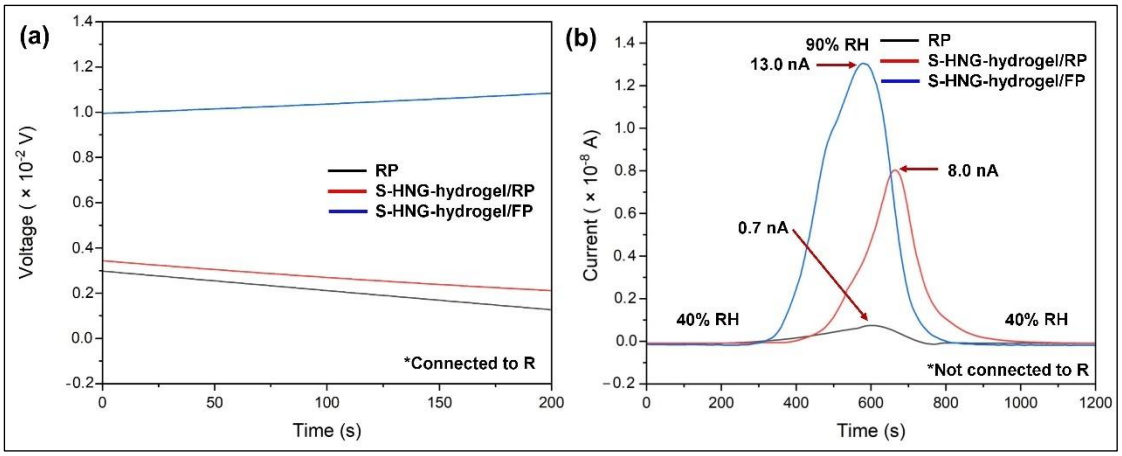

Figure 6.29 (a) The Voltage Versus Time at a Fixed RH of 75% with Zero Bias Applied to Fabricated S-HNG-Hydrogel/RP and S-HNG-Hydrogel/FP-Based HGPG. (b) The Current Versus Time at Various RH Levels with Zero Bias Applied to Fabricated S-HNG-Hydrogel/RP and S-HNG-Hydrogel/FP-Based HGPG

Table 6.18
The Humidity-To-Energy Performance of Fabricated S-HNG-hydrogel/FP and S-HNG-hydrogel/RP-based HGPG devices

Sample	**RH (%)**	**R (MΩ)**	**Output voltage, V (V)**	**Current density, J (A/cm^2)**	**Power, P (W)**
Pure RP	75	10	$(0.75 \pm 0.01) \times 10^{-3}$	$(6.00 \pm 0.08) \times 10^{-11}$	$(5.63 \pm 0.15) \times 10^{-14}$
S-HNG-hydrogel/RP			$(2.30 \pm 0.01) \times 10^{-3}$	$(1.84 \pm 0.01) \times 10^{-10}$	$(5.29 \pm 0.05) \times 10^{-13}$
S-HNG-hydrogel/FP			$(11.50 \pm 0.20) \times 10^{-3}$	$(9.23 \pm 0.16) \times 10^{-10}$	$(13.23 \pm 0.23) \times 10^{-12}$

The current-time response at different RH levels is shown in Figure 6.29 (b). The graph demonstrates that the S-HNG-hydrogel/RP-based HGPG device responded effectively to changes in humidity. During the adsorption process, it maintained a stable electrical signal at 40% RH, which gradually increased as the RH rose to 90%. At 90% RH, the S-HNG-hydrogel/RP-based HGPG produced a current of 8.0 nA, while the S-HNG-hydrogel/FP-based HGPG generated a higher current of 13.0 nA. During the desorption process, as RH decreased from 90% to 40%, both samples exhibited a corresponding decrease in current, confirming that both devices responded well to humidity changes. Nevertheless, the S-HNG-hydrogel/RP-based HGPG is still considered a viable and eco-friendly alternative for HGPG applications, contributing to the advancement of sustainable, waste-to-energy harvesting technologies.

To further evaluate its performance, the S-HNG-hydrogel/RP-based HGPG device was subjected to a simulated mouth-blowing test to assess its response to rapid humidity fluctuations. As shown in Figure 6.30 and the supplementary video (V4) in APPENDIX 5, the device exhibited a pronounced and immediate electrical response to sudden airflow. This behaviour underscores its high sensitivity to transient humidity changes and its ability to effectively convert moisture into electrical energy, thereby demonstrating strong potential for powering low-power electronic devices.

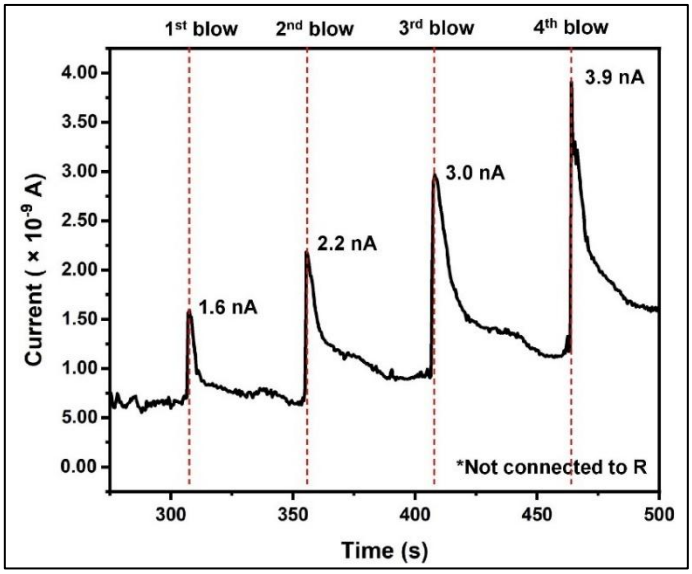

Figure 6.30 Humidity Response of S-HNG-hydrogel/RP-based HGPG to Humidity Changes Under Blowing Conditions

6.6 Conclusion

This investigation substantively propels the frontier of humidity-to-energy transduction by executing a deliberate optimization of both compositional architecture and synthetic protocol. A bespoke hygroscopic nanocomposite, architecture from S-HNG and integrated with a Co–Zn-based hydrogel on a cellulose scaffold, was meticulously engineered to surmount persistent bottlenecks in achieving stable, high-efficiency energy conversion. The resultant composite manifests exceptional hygroscopic uptake kinetics and superior humidity-to-electricity conversion efficacy, stemming from its hierarchically tailored morphology, maximized specific surface area, and optimized surface hydrophilicity. Through deployment of a cost-effective, low-temperature sonicated solution-immersion materials synthesis, the fabricated HGPG demonstrated exemplary operational endurance, acute responsiveness to relative

humidity fluctuations, and intrinsic adaptability to dynamic environmental stimuli. The strategic inclusion of hematite nanophases and Co–Zn-based hydrogel proved pivotal in modulating interfacial charge dynamics, expediting ionic flux, and fortifying charge separation processes which collectively culminating in an enhanced power conversion trajectory. As summarized in Table 6.19, the optimally configured HGPG attained peak performance metrics of $(11.5 \pm 2.1) \times 10^{-5}$ V, $(9.23 \pm 0.16) \times 10^{-10}$ A/cm^2 in current density, and $(13.23 \pm 0.23) \times 10^{-12}$ W under 75% RH, underscoring the synergistic efficacy of the composite–hydrogel framework. Extending the paradigm of sustainable material integration, this study further validates the incorporation of waste-derived RP substrates as a viable platform for HGPG fabrication. The S-HNG/Co–Zn-hydrogel/RP configuration yielded an output voltage of $(2.30 \pm 0.01) \times 10^{-3}$ V, substantiating its potential as an eco-conscious, economically scalable alternative. While scope remains for further refinement, these findings consolidate the technological promise of such architectures as next-generation, environmentally benign power generation modules for autonomous systems operating in humidity-rich milieus.

Table 6.19
Humidity-To-Energy Performance of the Fabricated HGPG Devices Connected to a 10 MΩ Resistor under 75% RH

Conditions	**Sample**	**Output voltage, V (V)**	**Current density, J (A/cm^2)**	**Power, P (W)**
Introduction of hematite in NG	S-NG-1.0-FP	$(2.24 \pm 0.03) \times 10^{-3}$	$(1.79 \pm 0.02) \times 10^{-10}$	$(5.02 \pm 0.13) \times 10^{-13}$
	S-HNG-FP	$(3.01 \pm 0.23) \times 10^{-3}$	$(2.41 \pm 0.02) \times 10^{-10}$	$(9.06 \pm 0.07) \times 10^{-13}$
Different synthesis temperature	S-H75/NG-FP	$(3.01 \pm 0.23) \times 10^{-3}$	$(2.41 \pm 0.02) \times 10^{-10}$	$(9.06 \pm 0.07) \times 10^{-13}$
	S-H85/NG-FP	$(3.45 \pm 0.22) \times 10^{-3}$	$(2.76 \pm 0.18) \times 10^{-10}$	$(1.19 \pm 0.15) \times 10^{-12}$
	S-H95/NG-FP	$(3.87 \pm 0.06) \times 10^{-3}$	$(3.09 \pm 0.05) \times 10^{-10}$	$(1.50 \pm 0.05) \times 10^{-12}$
Integration with hydrogel and RP	S-HNG-hydrogel/FP	$(11.50 \pm 0.20) \times 10^{-3}$	$(9.23 \pm 0.16) \times 10^{-10}$	$(13.23 \pm 0.23) \times 10^{-12}$
	Pure RP	$(0.75 \pm 0.01) \times 10^{-3}$	$(6.00 \pm 0.08) \times 10^{-11}$	$(5.63 \pm 0.15) \times 10^{-14}$
	S-HNG-hydrogel/RP	$(2.30 \pm 0.01) \times 10^{-3}$	$(1.84 \pm 0.01) \times 10^{-10}$	$(5.29 \pm 0.05) \times 10^{-13}$

CHAPTER 7
HEMATITE/ NICKEL OXIDE/ GRAPHENE ON HYDROGEL-BASED CELLULOSE SUBSTRATE FOR PIEZOELECTRIC NANOGENERATOR AND HYBRID DEVICES APPLICATIONS

7.1 Introduction

Besides humidity, the immediate environment offers a diverse range of energy sources that can be harvested, including mechanical energy [171]. Mechanical sources are commonly acknowledged as widely available and abundant forms of energy. Various forms of natural vibration and motion are prevalent in our environment, such as vibration waves, mechanical impacts, gusts of wind, vehicular transportation, and bodily movements [406]. Mechanical energy can originate from sources like respiration, blood circulation, heart impulses, and even the smallest respiratory movements [176]. Several methods exist for converting mechanical energy into electrical energy. Among these are electromagnetic induction, piezoelectric generation, and electrostatic storage. Piezoelectric energy harvesting systems have shown considerable promise as a feasible technique for providing an alternative to conventional electrical energy sources. Of the various effects used for energy scavenging, piezoelectricity has emerged as the most promising. Compared to electromagnetic and electrostatic methods, piezoelectric energy conversion offers superior efficiency and greater adaptability for use in portable electronic devices [407]. To date, the development of PENGs has increased significantly, indicating major growth in the field and suggesting strong potential for continued advancement in the coming years [408].

NiO and Gr have been widely utilized in PENGs due to their properties that are suitable for converting mechanical energy into electricity [409-411]. NiO has been reported to exhibit high dielectric properties, which enhance the local electric field within PENG materials, thereby aiding charge polarization [412]. Meanwhile, Gr is well known for its high electrical conductivity, which facilitates rapid charge transfer and collection. This reduces internal resistance and consequently boosts the output current of the PENG [413]. Hematite has also been frequently reported as an effective nanofiller in PENGs, contributing to improved piezoelectric output [414]. However, to the best of

our knowledge, no studies have directly combined hematite, NiO, and Gr in a single PENG application in the recent literature. HNG composite is expected to provide synergistic effects, complementing each component's functionality as a novel piezoelectric material.

In this chapter, a comprehensive study is presented on the development of a novel piezoelectric material based on a S-HNG composite. This includes the integration of a Co-Zn nanoceramic hydrogel and the utilization of waste materials in the PENG architecture. The study also introduces a newly discovered hybrid energy harvesting device comprising of HGPG and PENG (HGPG-PENG), capable of generating electricity from two renewable sources (i.e, humidity and mechanical movement). Detailed discussions and relevant comparisons have been provided throughout the chapter to support the development and performance of the HGPG-PENG, highlighting its dual-functionality as a clean energy harvesting device.

7.2 Synthesis and Characterization of Hematite/NiO/Gr Composites on Hydrogel-based Cellulose Substrate for Piezoelectric Nanogenerator Applications

In this study, the S-HNG composite was synthesized using a sonicated solution immersion process and implemented in the PENG device, as detailed in Sections 3.6. Comprehensive analyses were conducted to evaluate the potential of the S-HNG-hydrogel/FP and S-HNG-hydrogel/RP for PENG applications, as well as their performance in the hybrid HGPG-PENG system.

7.2.1 Piezoelectric Coefficient Analysis

The d_{33} measurement was conducted to confirm the suitability of the developed S-HNG-hydrogel films for PENG applications. The measured d_{33} values were 12.36 ± 0.21 pC/N for the S-HNG-hydrogel/FP and 12.00 ± 0.20 pC/N for the S-HNG-hydrogel/RP. Interestingly, the samples exhibited measurable d_{33} values without any electrical poling. According to Huang et al. [415], the presence of NiO within the piezoelectric material induces spontaneous polarization, as NiO has the ability to initiate dipole alignment even without a poling process. Gr has also been reported to enhance the d_{33} of piezoelectric materials without the need for high-field poling [416]. This finding is supported by the performance of the S-HNG-hydrogel/FP-based PENG,

which demonstrates its ability to generate electrical energy from applied mechanical force.

7.2.2 PENG and HGPG–PENG Hybrid Devices Performance Analysis

To evaluate the output performance, a custom-built tapping solenoid applying a 2 N force at 10 Hz was used. As shown in Figure 7.1, the S-HNG-hydrogel/FP-based PENG generated an average peak-to-peak voltage (V_{PP}) of 12.0 ± 0.2 V, while the S-HNG-hydrogel/RP-based PENG produced a comparable average V_{PP} of 4.5 ± 0.2 V. The measurements were conducted at RT without any external resistor or applied bias, to demonstrate the intrinsic capability of the fabricated PENG devices to convert mechanical energy into electrical energy.

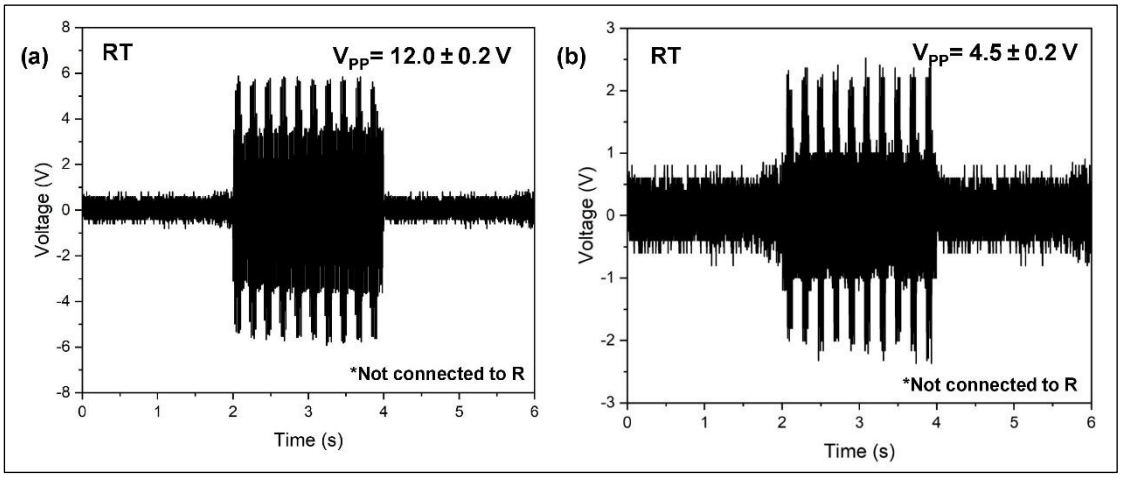

Figure 7.1 Output V_{PP} of (a) S-HNG-hydrogel/FP and (b) S-HNG-hydrogel/RP-based PENG under Solenoid Tapping with a Force of 2 N Force at 10 Hz

To assess the operational durability and effectiveness of the devices, the stability of the S-HNG-hydrogel/FP-based PENG was examined. As shown in Figure 7.2, the device was subjected to 5000 cycles over 100 seconds, and its output voltage remained relatively stable, with minor fluctuations likely due to the coil winding tolerance of the push-pull solenoid. Figure 7.3 compares the performances of both the FP- and RP-based PENGs under various forces, including single-finger tapping, two-finger tapping, and full-hand tapping. Results show that the V_{PP} values varied accordingly, depending on the magnitude of the applied force, as summarized in Table 7.1. A demonstration of the

S-HNG-hydrogel/RP-based PENG under full-hand tapping is shown in Supplementary Video (V5) in APPENDIX 6.

Table 7.1
The V_{PP} and P_d of S-HNG-hydrogel/FP-based and RP-based HGPG-PENG Devices under Various Tapping Forces

Sample	Active area (cm^2)	R (MΩ)	Tapping force	Peak-to-peak voltage, V_{PP} (V)	Power density, P_d (W/cm^2)
S-HNG-hydrogel/FP	0.25	10	1 finger	4.6 ± 0.4	$(8.4 \pm 0.6) \times 10^{-6}$
			2 fingers	5.0 ± 0.4	$(1.0 \pm 0.1) \times 10^{-5}$
			Full hand	6.3 ± 0.6	$(1.6 \pm 0.2) \times 10^{-5}$
S-HNG-hydrogel/RP	0.25	10	1 finger	4.0 ± 0.2	$(6.5 \pm 0.4) \times 10^{-6}$
			2 fingers	5.3 ± 0.2	$(1.1 \pm 0.1) \times 10^{-5}$
			Full hand	6.8 ± 0.7	$(1.9 \pm 0.2) \times 10^{-5}$

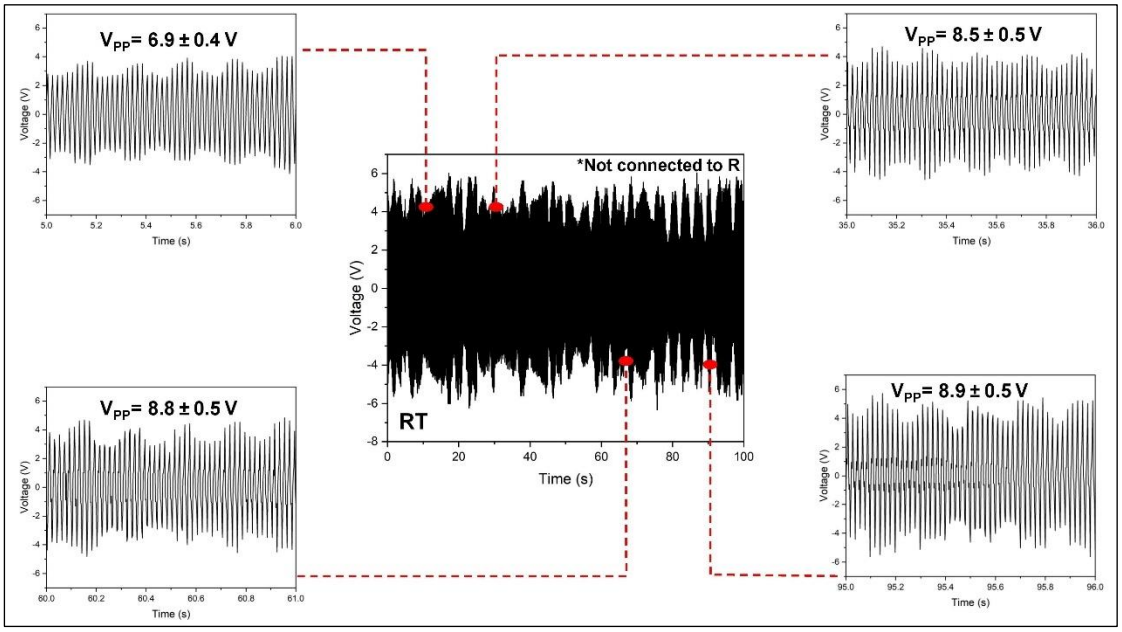

Figure 7.2 S-HNG-hydrogel/FP-based PENG Stability under ~100 s

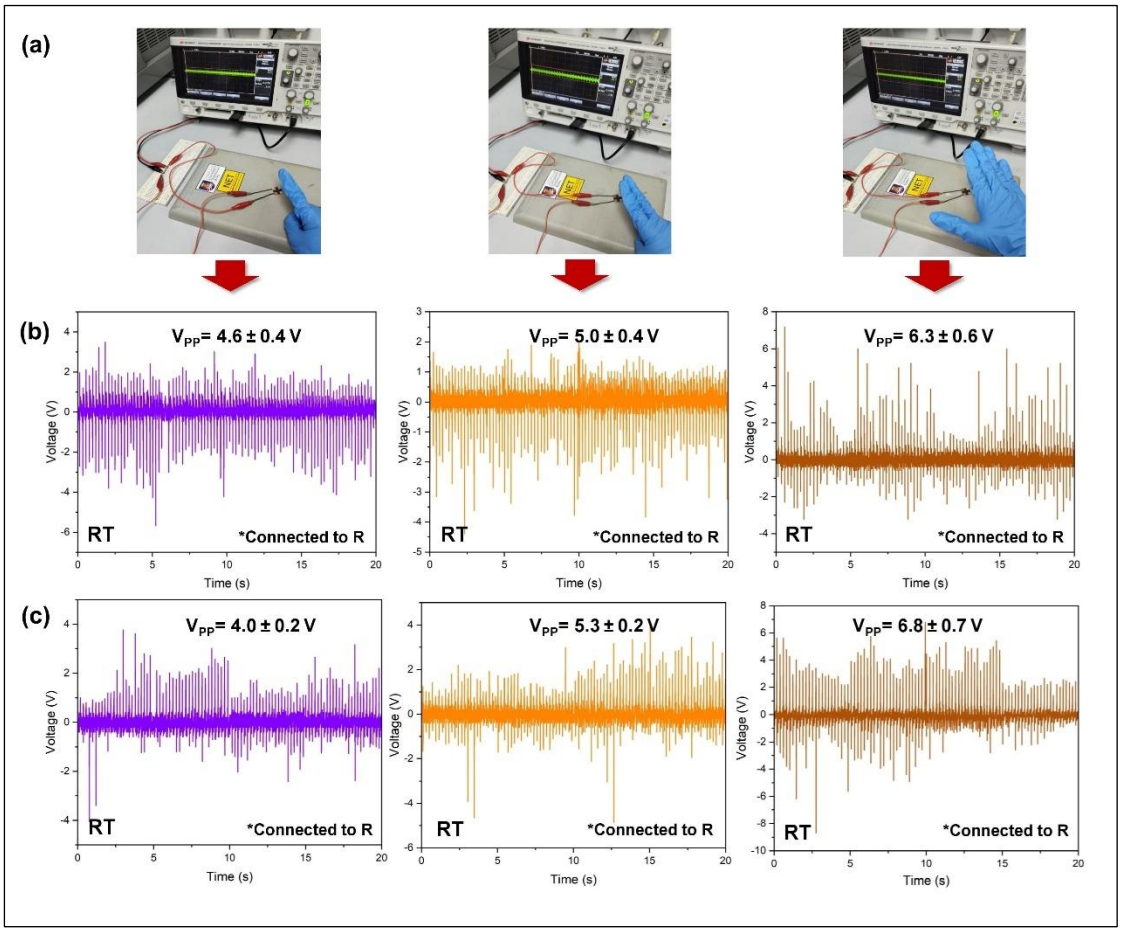

Figure 7.3 (a) Image of the Fabricated PENG during Testing under Various Applied Forces. Output V_{PP} of (b) S-HNG-hydrogel/FP-based PENG and (c) S-HNG-hydrogel/RP-based PENG under Different Applied Forces: Single-Finger Tapping (Purple), Two-Finger Tapping (Orange), and Full-Hand Tapping (Brown)

The PENG produced an alternating current (AC) output, necessitating conversion to direct current (DC) for practical device operation. A full-wave diode bridge rectifier was employed to achieve AC–DC conversion, with an LED selected as a visual load to validate the device's real-world applicability. The rectified output was stored in a 1 μF capacitor, and the charging dynamics were monitored using a digital multimeter. Under a 2 N solenoid-driven tapping force, the S-HNG–hydrogel/FP-based PENG charged the capacitor to approximately 2.1 V within 2 min, subsequently powering the LED, as shown in Figure 7.4. Under identical conditions, the S-HNG–hydrogel/RP-based PENG achieved a terminal voltage of ~1.2 V, also successfully illuminating the LED (Figure 7.5; Supplementary Video (V6), APPENDIX 7). These results confirm the feasibility of the developed PENG architectures for direct integration into low-power electronic systems.

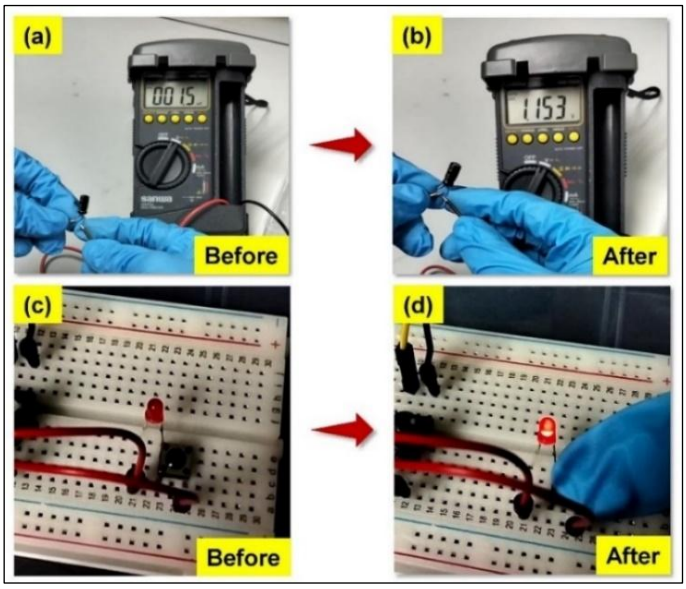

Figure 7.4 (a) Before and (b) After Measuring the Voltage Across a Capacitor using the S-HNG-hydrogel/FP-based PENG. (c) Before and (d) After Applying Solenoid Tapping to the S-HNG-hydrogel/FP-Based PENG, Successfully Lighting Up a Red LED

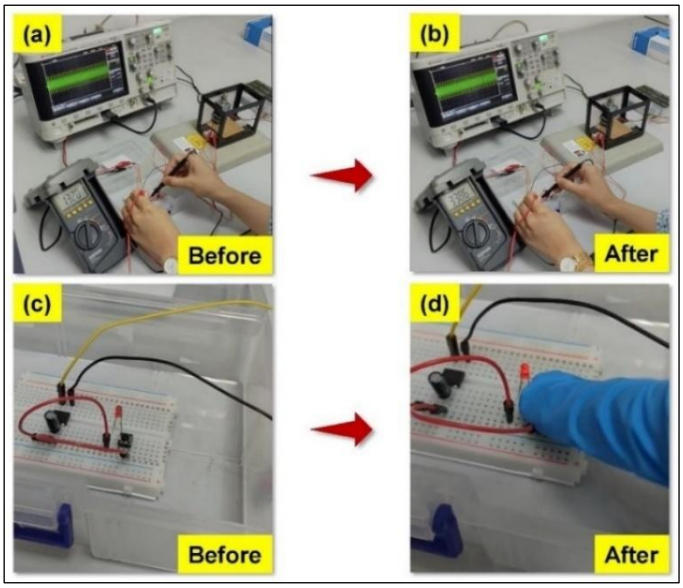

Figure 7.5 (a) Before and (b) After Measuring the Voltage Across a Capacitor using The S-HNG-Hydrogel/RP-Based PENG. (c) Before and (d) After Applying Solenoid Tapping to the S-HNG-Hydrogel/RP-Based PENG, Successfully Lighting Up a Red LED

The PENG developed in this study adopts a planar electrode architecture as shown in Figure 7.6 (a), in which the electrode gap and the intervening piezoelectric material define the active energy conversion region. In the unstrained state, the S-HNG–hydrogel/FP-based PENG remains electrically neutral, with no measurable current.

Upon application of mechanical pressure directly to the metal electrode, the device undergoes in-plane compression, perturbing the internal charge equilibrium and inducing piezoelectric polarization as illustrated in Figure 7.6 (b). Unlike conventional sandwich-type PENGs, where the electric field is oriented through the thickness, this configuration generates an electric field parallel to the device surface. Releasing the applied force reverses the polarization direction, producing a current of opposite polarity as the electric dipoles relax to their initial alignment. The corresponding output voltage profile under repeated pressing–releasing cycles, along with a magnified view of a single cycle, is shown in Figure 7.6 (c).

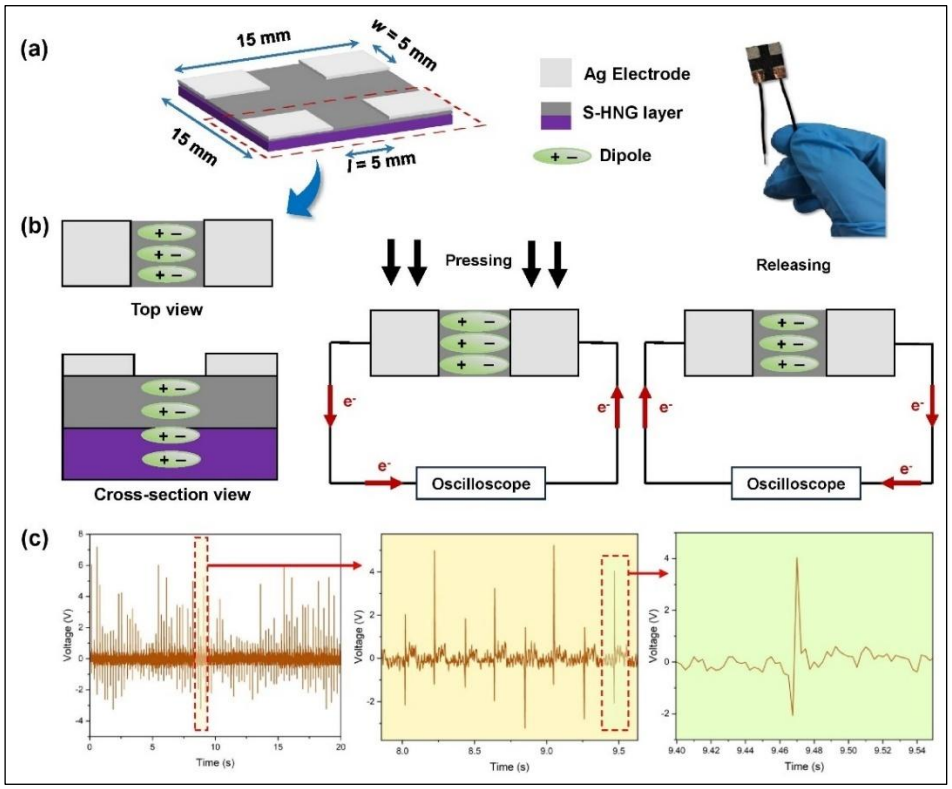

Figure 7.6 (a) Basic Structure of the S-HNG-Hydrogel/FP-Based PENG with a Planar Electrode Configuration and the Actual Image of Fabricated S-HNG-Hydrogel/FP-Based PENG. (b) Schematic Illustration of the Working Mechanism of the Developed S-HNG-Hydrogel/FP-Based PENG During One Cycle. (c) Output Voltage of the S-HNG-Hydrogel/FP-Based PENG with a Corresponding Zoomed-In View of a Single Voltage Cycle

To evaluate the functionality of the S-HNG-hydrogel/FP and RP materials in a hybrid HGPG-PENG system, the devices were tested under varying RH levels using the same tapping solenoid (2 N at 10 Hz), as described in detail in Section 3.8.3.5. As shown

in Figure 7.7, the generated voltage increased with higher RH, indicating that humidity enhances the mechanical-to-electrical energy conversion performance. Table 7.2 summarizes the performance of both the S-HNG-hydrogel/FP-based and RP-based HGPG-PENG devices.

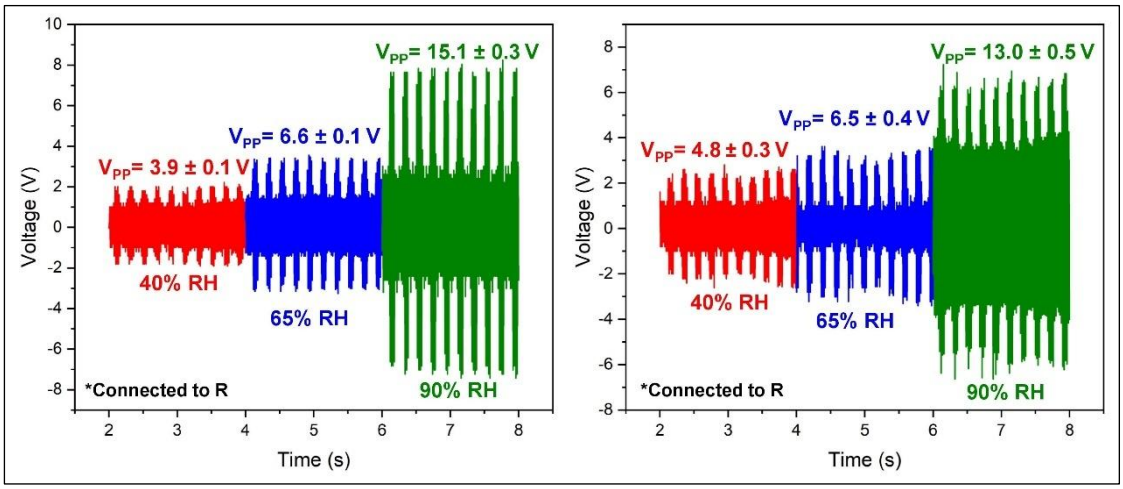

Figure 7.7 Output V_{PP} of (a) S-HNG-hydrogel/FP and (b) S-HNG-hydrogel/RP-based HGPG-PENG under Solenoid Tapping with a Force of 2 N Force at 10 Hz Measured at Different Humidity Levels: 40% RH (red), 65% RH (Blue), and 90% RH (Green)

Table 7.2
The V_{PP} and P_d of S-HNG-hydrogel/FP-based and RP-Based HGPG-PENG Devices under Different RH Level

Sample	**Active area (cm^2)**	**R (MΩ)**	**RH (%)**	**Peak-to-peak voltage, V_{PP} (V)**	**Power density, P_d (W/cm^2)**
S-HNG-hydrogel/FP	0.25	10	40	3.9 ± 0.1	$(0.6 \pm 0.1) \times 10^{-5}$
			65	6.6 ± 0.1	$(1.7 \pm 0.1) \times 10^{-5}$
			90	15.1 ± 0.3	$(9.1 \pm 0.4) \times 10^{-5}$
S-HNG-hydrogel/RP	0.25	10	40	4.8 ± 0.3	$(0.9 \pm 0.1) \times 10^{-5}$
			65	6.5 ± 0.4	$(1.7 \pm 0.2) \times 10^{-5}$
			90	13.0 ± 0.5	$(6.5 \pm 0.5) \times 10^{-5}$

For comprehensive evaluation, the HGPG–PENG hybrid devices were examined under 75% RH using a tapping solenoid (2 N at 10 Hz), with the results presented in Figure 7.8. Since the oscilloscope output displays the PENG waveform in AC form, it was converted to its DC equivalent using Equation (3.8). As summarized in Table 7.3, mechanical excitation from the HGPG-PENG generated markedly higher voltages compared to the HGPG alone. This enhancement arises from the engineered material's capacity to promote synergistic coupling between humidity-induced ionic dynamics and piezoelectric charge generation, thereby accelerating ion mobility and enabling more efficient charge transport.

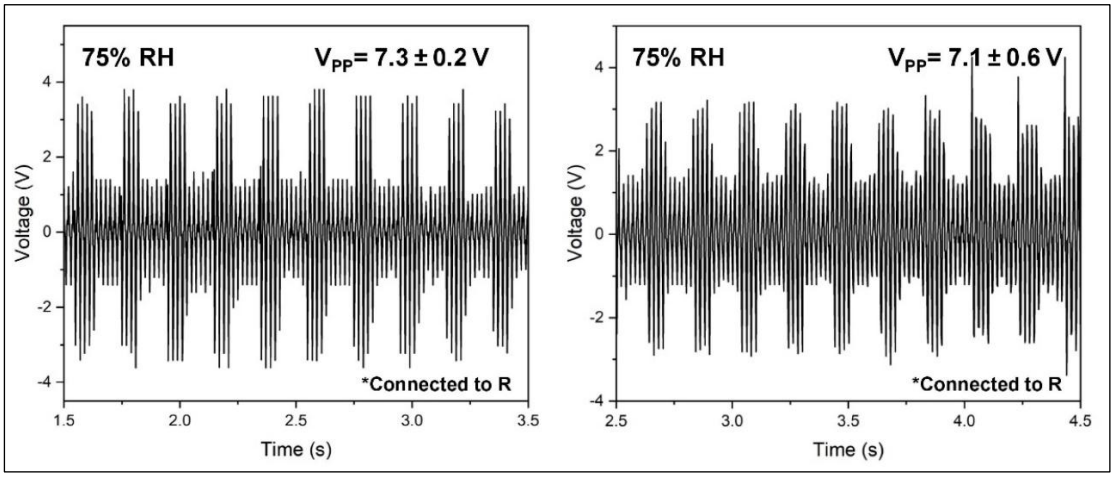

Figure 7.8 Output V_{PP} of (a) S-HNG-hydrogel/FP and (b) S-HNG-hydrogel/RP-based HGPG-PENG under Solenoid Tapping with a Force of 2 N Force at 10 Hz at 75% RH

Table 7.3
Performance Comparison of S-HNG-Hydrogel/FP-Based HGPG, RP-Based HGPG, and HGPG-PENG Hybrid Devices Evaluated under 75% RH

Sample	**R (MΩ)**	**RH (%)**	**$V_{PP,\ HGPG\text{-}PENG}$ (V)**	**$V_{RMS,\ HGPG\text{-}PENG}$ (V)**	**V_{HGPG} (V)**
S-HNG-hydrogel/FP	10	75	7.3 ± 0.2	2.6 ± 0.1	$(11.50 \pm 0.20) \times 10^{-3}$
S-HNG-hydrogel/RP			7.1 ± 0.6	2.5 ± 0.2	$(2.30 \pm 0.01) \times 10^{-3}$

While the RP-based device produced slightly lower V_{PP} than the FP-based device, it still exhibited comparable performance and contributed significantly to the development of an innovative and sustainable energy harvesting system. Furthermore, the RP-based HGPG-PENG device demonstrated impressive long-term stability, maintaining consistent electrical output after 200 days, as shown in Figure 7.9.

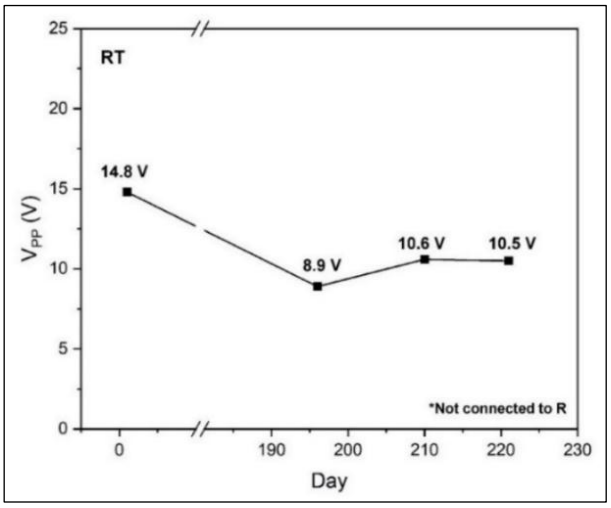

Figure 7.9 Plot of Output V_{PP} Measured at Different Days for the S-HNG-Hydrogel/RP-Based HGPG-PENG Device at RT

7.3 Conclusion

This study establishes S-HNG–hydrogel/FP as a novel piezoelectric material engineered through a simple, scalable, and cost-effective synthesis–fabrication route. Without the need for additional electrical poling, the material achieved a notable piezoelectric charge coefficient (d_{33}) of 12.36 ± 0.21 pC/N. When integrated into a PENG architecture, the S-HNG–hydrogel/FP device delivered an average V_{PP} of 12.0 ± 0.2 V under a 2 N, 10 Hz actuation from a custom-built tapping solenoid, and consistently generated measurable electrical signals under diverse mechanical stimuli, including single-finger, dual-finger, and full-hand tapping. Incorporation of RP as a sustainable substrate further validated the versatility of the design. The S-HNG–hydrogel/RP-based PENG exhibited performance comparable to its FP counterpart, successfully charging a capacitor via a diode bridge rectifier and powering an LED. The device demonstrated exceptional operational stability, maintaining continuous signal generation over extended durations exceeding 200 days. Crucially, both FP- and RP-based devices exhibited dual-mode energy harvesting capability within integrated HGPG–PENG systems, enabling concurrent conversion of ambient humidity gradients and mechanical inputs into electrical energy using a single, multifunctional material platform. These findings not only underscore the technological viability of HNG-based composites for hybrid energy harvesting but also pave the way for eco-conscious, self-powered systems that leverage sustainable substrates and multimodal energy transduction mechanisms.

CHAPTER 8
CONCLUSION AND FUTURE DEVELOPMENT

8.1 Conclusion

The first objective was successfully accomplished through a rigorous structural, morphological, wettability, and performance assessment of actinomorphic-structured NG composites functionalized via SA treatment. HGPGs were fabricated using SA–functionalized NG (S-NG) composites on FP substrates with Gr loadings systematically varied between 0.5 and 2.0 wt%, enabling precise correlation of composition with device performance. XRD pattern confirmed the coexistence of crystalline NiO and Gr phases, while FESEM images revealed that S-NG composites displayed graphene flakes decorated with NiO nanoparticles, forming electro-conductive, porous heterostructures intimately integrated within the cellulose fibril network of FP. WCA measurements indicated predominantly hydrophilic behaviour, with contact angles rising slightly from 64.5° ± 3.3° to 67.9° ± 0.3° as Gr loading increased. The introduction of heteromorphic nanochannels, fabricated via the sonicated solution-immersion method, imparted well-defined crystallinity, hierarchical surface topology, and tuneable hydrophilicity conducive to rapid adsorption–desorption dynamics. Among all compositions, the 1.0 wt% Gr composite (S-NG-1.0) exhibited the highest electrical conductivity, $(1.3 \pm 0.2) \times 10^{-2}$ S/cm, and delivered superior humidity-to-electricity conversion, achieving an output voltage of $(2.24 \pm 0.03) \times 10^{-3}$ V, a current density of $(1.79 \pm 0.02) \times 10^{-10}$ A/cm^2, and an output power of $(5.02 \pm 0.13) \times 10^{-13}$ W.

The second objective has been successfully achieved through a comprehensive optimization of S-NG composites on cellulose-based FP substrates, correlating structural characteristics, surface morphology, wettability, chemical composition, and HGPG performance. Systematic variation of SA concentration, immersion temperature, and immersion duration revealed that device performance is highly sensitive to surface functionalization conditions, with balanced hydrophilicity being critical for efficient humidity-to-electricity conversion. The optimal parameters of 2 wt.% SA content, 60 °C immersion temperature, and 6 h immersion duration, produced a uniformly packed molecular overlayer that enhanced interfacial water adhesion and ion transport while avoiding over-saturation effects. Under these conditions, the optimized S-NG-1.0-FP

device achieved a contact angle of 65.3° ± 1.2°, a surface energy of 25.8 ± 0.3 mJ/m^2, and superior performance metrics, including an output voltage of an output voltage of (2.24 ± 0.03) × 10^{-3} V, a current density of (1.79 ± 0.02) × 10^{-10} A cm^{-2}, and an output power of (5.02 ± 0.13) × 10^{-13} W at 75% RH. These findings clearly establish the processing–structure–function relationship and confirm SA surface functionalization as a strategy for achieving high-performance, humidity-responsive HGPG devices.

Incorporation of hematite into the NG composite was found to induce distinct modifications in surface morphology, crystallographic arrangement, and chemical composition, while markedly enhancing HGPG performance, thereby fulfilling the third objective of elucidating the structure–property–performance relationships underpinning hematite integration in advanced humidity to energy conversion materials. The hematite-modified NG composite, functionalized with SA, was comprehensively characterized to elucidate its structure–property–performance relationships. Although the intrinsically wide bandgap of hematite contributed to a reduced Hall conductivity of (1.7 ± 0.1) × 10^{-3} S cm^{-1}, the S-HNG–FP-based HGPG device exhibited superior humidity-to-electricity conversion, delivering an output voltage of (3.01 ± 0.23) × 10^{-3} V, a current density of (2.41 ± 0.02) × 10^{-10} A cm^{-2}, and an output power of (9.06 ± 0.07) × 10^{-13} W. CV analysis further confirmed enhanced redox activity of S-HNG-FP relative to S-NG-FP, underscoring the pivotal role of hematite in boosting device performance. To counteract the reduced Hall conductivity, synthesis temperatures to prepare S-HNG composites were systematically varied (75 °C, 85 °C, and 95 °C). As anticipated, higher synthesis temperatures improved conductivity, with the maximum value of (2.6 ± 1.3) × 10^{-2} S cm^{-1} achieved at 95 °C. The FESEM image analysis revealed increased particle agglomeration at elevated temperatures, resulting in higher surface roughness and improved hydrophilicity, as evidenced by reduced θ_{CA}. However, BET analysis indicated that excessive agglomeration diminished accessible pore volume and surface area. Despite this trade-off, the S-HNG-FP sample synthesized at 95 °C demonstrated the best HGPG performance, achieving an output power of (1.50 ± 0.05) × 10^{-12} W.

The fourth objective of this study was achieved by demonstrating that integrating HNG composites with Co–Zn-based nanoceramic hydrogel films, synthesized via the sol–gel method and deposited on both FP and RP cellulose-based substrates, significantly enhanced humidity-to-energy conversion performance, confirming the effectiveness of this architecture for high-efficiency, sustainable HGPG

devices. The integration of Co-Zn-based nanoceramic hydrogel into the HNG composite was successfully explored. The hydrogel was synthesized via sol-gel method, and FP substrates were immersed to create hydrogel/FP, onto which the S-HNG layer was deposited (S-HNG-hydrogel/FP). XRD and EDX analyses confirmed the presence of Co-Zn elements and successful hydrogel formation. FESEM images showed a porous structure, and WCA measurements indicated enhanced hydrophilicity. BET analysis further revealed the development of an additional porosity network, beneficial for ion transport and moisture absorption. The S-HNG-hydrogel/FP-based HGPG achieved significantly enhanced performance, with an output voltage of $(11.50 \pm 0.20) \times 10^{-3}$ V, current density of $(9.23 \pm 0.16) \times 10^{-10}$ A/cm^2, and output power of $(13.23 \pm 0.23) \times 10^{-12}$ W. This study also embraced sustainability through innovation, aligning with circular economy principles by integrating RP into device fabrication. RP which prepared via a home-based method, was used to replace FP in the device, resulting in the S-HNG-hydrogel/RP-based HGPG. This device demonstrated comparable performance to its FP-based HGPG, achieving $(2.30 \pm 0.01) \times 10^{-3}$ V, $(1.84 \pm 0.01) \times 10^{-10}$ A/cm^2, and $(5.29 \pm 0.05) \times 10^{-13}$ W.

The fifth objective has been successfully achieved through the comprehensive characterization of the HNG composite integrated with Co–Zn-based nanoceramic hydrogel films, confirming its exceptional multifunctional performance in both PENG and hybrid HGPG–PENG configurations. The engineered composite exhibited a high piezoelectric coefficient, robust voltage output, and excellent humidity-to-electricity conversion efficiency, underpinned by its optimized material's properties. The integration of S-HNG-hydrogel/FP and S-HNG-hydrogel/RP into PENG devices yielded promising piezoelectric coefficients of 12.36 ± 0.21 pC/N and 12.00 ± 0.20 pC/N, respectively. The S-HNG-hydrogel/FP-based PENG generated an average V_{PP} of 12.0 ± 0.2 V, while the RP-based counterpart achieved a comparable average V_{PP} of 4.5 ± 0.2 V. Both configurations successfully charged capacitors and powered LEDs under a 2 N solenoid tap, demonstrating practical applicability. Furthermore, the dual-mode HGPG–PENG systems showcased stable and synergistic energy harvesting from both mechanical and moisture sources, highlighting the versatility of the composite–hydrogel integration as a scalable, cost-effective, and sustainable platform for next-generation self-powered electronics. The hybrid device based on S-HNG-hydrogel/FP achieved a V_{PP} of 15.1 ± 0.3 V and a power density of $(9.1 \pm 0.4) \times 10^{-}$

^{5} W/cm^2, while the S-HNG-hydrogel/RP-based device attained a V_{PP} of 13.0 ± 0.5 V and a power density of (6.5 ± 0.5) × 10^{-5} W/cm^2 under 90%RH.

Table 8.1 presents the humidity to energy conversion performance of HGPG devices across the various parameters investigated in this study, while Table 8.2 details the output characteristics of the hybrid HGPG- PENG configurations. Collectively, these findings demonstrate that the strategic integration of structural engineering, precise surface chemistry modulation, and sustainable substrate design delivers a powerful synergistic effect, establishing an effective pathway toward high efficiency, multifunctional energy harvesters.

Table 8.1
Humidity-To-Energy Performance of the Fabricated HGPG Devices Connected to a 10 MΩ Resistor under 75% RH

Conditions	**Sample**	**Output voltage, V (V)**	**Current density, J (A/cm^2)**	**Power, P (W)**
Different Gr loading	S-PN-FP	(8.89 ± 0.25) ×10^{-4}	(7.12 ± 0.20) ×10^{-11}	(7.92 ± 0.45) ×10^{-14}
	U-NG-1.0-FP	(0.14 ± 0.01) × 10^{-3}	(11.12 ± 0.07) × 10^{-12}	(1.93 ± 0.12) × 10^{-15}
	S-NG-0.5-FP	(1.08 ± 0.03) ×10^{-3}	(8.80 ± 0.22) ×10^{-11}	(1.21 ± 0.06) ×10^{-13}
	S-NG-1.0-FP	(2.24 ± 0.03) ×10^{-3}	(1.79 ± 0.02) ×10^{-10}	(5.02 ± 0.13) ×10^{-13}
	S-NG-1.5-FP	(1.25 ± 0.03) ×10^{-3}	(1.04 ± 0.03) ×10^{-10}	(1.69 ± 0.09) ×10^{-13}
	S-NG-2.0-FP	(1.35 ± 0.02) ×10^{-3}	(1.12 ± 0.01) ×10^{-10}	(1.96 ± 0.04) ×10^{-13}
SA treatment with different SA content, treated at 60°C for 6 hours	U-NG-1.0	(0.14 ± 0.01) × 10^{-3}	(11.12 ± 0.07) × 10^{-12}	(1.93 ± 0.12) × 10^{-15}
	S1%-NG-1.0	(1.56 ± 0.04) ×10^{-3}	(1.25 ± 0.03) ×10^{-10}	(2.43 ± 0.13) ×10^{-13}
	S2%-NG-1.0	(2.24 ± 0.03) ×10^{-3}	(1.79 ± 0.02) ×10^{-10}	(5.02 ± 0.13) ×10^{-13}
	S3%-NG-1.0	(1.17 ± 0.19) ×10^{-4}	(9.36 ± 1.52) ×10^{-12}	(1.37 ± 0.45) ×10^{-15}
	S4%-NG-1.0	(1.54 ± 0.08) ×10^{-3}	(1.23 ± 0.06) ×10^{-10}	(2.37 ± 0.25) ×10^{-13}
SA treatment with 2 wt.% SA, treated for 6 hours at different immersion temperature	SRT-NG-1.0	(3.12 ± 0.02) ×10^{-4}	(2.50 ± 0.02) ×10^{-11}	(9.73 ± 0.13) ×10^{-15}
	S30-NG-1.0	(1.99 ± 0.03) ×10^{-3}	(1.59 ± 0.02) ×10^{-10}	(3.96 ± 0.12) ×10^{-13}
	S60-NG-1.0	(2.24 ± 0.03) ×10^{-3}	(1.79 ± 0.02) ×10^{-10}	(5.02 ± 0.13) ×10^{-13}
	S90-NG-1.0	(1.09 ± 0.03) ×10^{-3}	(8.72 ± 2.24) ×10^{-11}	(1.19 ± 0.07) ×10^{-13}
SA treatment with 2 wt.% SA, treated at 60°C for different immersion duration	S2h-NG-1.0	(1.65 ± 0.01) ×10^{-4}	(1.32 ± 0.01) ×10^{-11}	(2.72 ± 0.03) ×10^{-15}
	S4h-NG-1.0	(1.27 ± 0.01) ×10^{-4}	(1.02 ± 0.01) ×10^{-11}	(1.61 ± 0.03) ×10^{-15}
	S6h-NG-1.0	(2.24 ± 0.03) ×10^{-3}	(1.79 ± 0.02) ×10^{-10}	(5.02 ± 0.13) ×10^{-13}
	S8h-NG-1.0	(1.43 ± 0.01) ×10^{-4}	(1.14 ± 0.01) ×10^{-11}	(2.04 ± 0.03) ×10^{-15}
Introduction of hematite in NG	S-NG-1.0-FP	(2.24 ± 0.03) × 10^{-3}	(1.79 ± 0.02) × 10^{-10}	(5.02 ± 0.13) ×10^{-13}
	S-HNG-FP	(3.01 ± 0.23) ×10^{-3}	(2.41 ± 0.02) × 10^{-10}	(9.06 ± 0.07) ×10^{-13}
Different synthesis temperature	S-H75/NG-FP	(3.01 ± 0.23) ×10^{-3}	(2.41 ± 0.02) × 10^{-10}	(9.06 ± 0.07) ×10^{-13}
	S-H85/NG-FP	(3.45 ± 0.22) × 10^{-3}	(2.76 ± 0.18) ×10^{-10}	(1.19 ± 0.15) ×10^{-12}
	S-H95/NG-FP	(3.87 ± 0.06) × 10^{-3}	(3.09 ± 0.05) × 10^{-10}	(1.50 ± 0.05) ×10^{-12}
Integration with hydrogel and RP	S-HNG-hydrogel/FP	(11.50 ± 0.20) × 10^{-3}	(9.23 ± 0.16) ×10^{-10}	(13.23 ± 0.23)×10^{-12}
	Pure RP	(0.75 ± 0.01) × 10^{-3}	(6.00 ± 0.08) ×10^{-11}	(5.63 ± 0.15) × 10^{-14}
	S-HNG-hydrogel/RP	(2.30 ± 0.01) × 10^{-3}	(1.84 ± 0.01) × 10^{-10}	(5.29 ± 0.05) × 10^{-13}

Table 8.2
Performance of HGPG-PENG Devices under Tapping Solenoid (2 N at 10 Hz) at Different RH Levels

Condition	**Sample**	**RH (%)**	**Peak-to-peak voltage, V_{PP} (V)**	**Power density, P_d (W/cm^2)**
Different type of substrate	S-HNG-hydrogel/FP	40	3.9 ± 0.1	(0.6 ± 0.1) × 10^{-5}
		65	6.6 ± 0.1	(1.7 ± 0.1) × 10^{-5}

	90	15.1 ± 0.3	$(9.1 \pm 0.4) \times 10^{-5}$
S-HNG-hydrogel/RP	40	4.8 ± 0.3	$(0.9 \pm 0.1) \times 10^{-5}$
	65	6.5 ± 0.4	$(1.7 \pm 0.2) \times 10^{-5}$
	90	13.0 ± 0.5	$(6.5 \pm 0.5) \times 10^{-5}$

This study represents a pioneering advancement in the development of both hygroscopic materials for HGPG and piezoelectric materials for PENG. By utilizing the previously unexplored S-HNG integrated with Co-Zn-based nanoceramic hydrogel on FP substrates, this research provides new insights into the potential of these materials to enhance electricity generation from both humidity and mechanical energy sources. Furthermore, the incorporation of RP into energy harvesting devices highlights significant environmental and economic advantages, reinforcing the feasibility of sustainable energy technologies. This work aligns closely with several United Nations SDGs, particularly SDG 7 – Affordable and Clean Energy, SDG 9 – Industry, Innovation, and Infrastructure, and SDG 12 – Responsible Consumption and Production. The developed energy-harvesting materials and devices (i.e., HGPG, PENG, and the hybrid HGPG-PENG) are noteworthy not only for their RE generation capabilities but also for their contribution to environmentally friendly innovation and effective waste management.

8.2 Future Development

The fabricated S-HNG hydrogel/FP and S-HNG hydrogel/RP devices exhibit substantial promise as multifunctional hygroscopic and piezoelectric components for self-powered energy harvesting systems. While this work marks significant progress in advancing HGPG and PENG materials, further systematic studies are warranted to maximize energy harvesting efficiency and electrical output. One promising strategy involves incorporating ZnO fillers into the S-HNG composite. Owing to its diverse nanostructures, excellent structural and chemical stability, and high humidity sensitivity, ZnO has been extensively employed in nanogenerator architectures [417-419] and is poised to further elevate HGPG performance. Incorporation of ZnO, potentially through tailored doping strategies, could yield superior charge generation and transport characteristics. Beyond compositional engineering, process parameters such as immersion time during synthesis and annealing duration merit careful optimization, as prior reports confirm their pivotal role in modulating crystallinity, morphology, particle size, porosity, and surface chemistry [420, 421]. Such structural

refinements directly influence the charge generation efficiency of HGPGs in humidity-to-electricity conversion and PENGs in mechanical-to-electricity transduction, offering clear avenues for performance enhancement.

REFERENCES

[1] Q. Hassan *et al.*, "A review of hybrid renewable energy systems: Solar and wind-powered solutions: Challenges, opportunities, and policy implications," *Results in Engineering,* vol. 20, p. 101621, 2023/12/01/ 2023, doi: https://doi.org/10.1016/j.rineng.2023.101621.

[2] N. S. Mohamed Mustakim *et al.*, "Review of recent advances in piezoelectric material for nanogenerator application: preparation methods, material selection, performance, applications, and future outlook," *Journal of Materials Science,* vol. 59, no. 41, pp. 19380-19423, 2024/11/01 2024, doi: 10.1007/s10853-024-10293-4.

[3] D. Kamaruzaman *et al.*, "Polystyrene Waste-ZnO nanocomposite film for energy harvesting via hydrophobic triboelectric nanogenerator: Transforming waste into energy," *Materials Today Sustainability,* vol. 26, p. 100726, 2024/06/01/ 2024, doi: https://doi.org/10.1016/j.mtsust.2024.100726.

[4] F. Zhao *et al.*, "Direct Power Generation from a Graphene Oxide Film under Moisture," *Adv Mater,* vol. 27, no. 29, pp. 4351-7, Aug 5 2015, doi: 10.1002/adma.201501867.

[5] R. K. R *et al.*, "A Review on Vibration Based Piezoelectric Energy Harvesters," *SAHYADRI International Journals of Research,* vol. 3, no. 1, pp. 47-56, 06/05 2017. [Online]. Available: https://sijr.sahyadri.edu.in/Articles/Volume%203/Issue%201/6.pdf.

[6] S. Sapkal *et al.*, "A review of piezoelectric materials for nanogenerator applications," *Journal of Materials Science: Materials in Electronics,* vol. 33, no. 36, pp. 26633-26677, 2022/12/01 2022, doi: 10.1007/s10854-022-09339-7.

[7] W. Lv *et al.*, "DNA-dispersed graphene/NiO hybrid materials for highly sensitive non-enzymatic glucose sensor," *Electrochimica Acta,* vol. 73, pp. 129-135, 2012/07/01/ 2012, doi: https://doi.org/10.1016/j.electacta.2011.11.089.

[8] R. B. Chrisma *et al.*, "A review on the electrochemical behavior of graphene–transition metal oxide nanocomposites for energy storage applications," *Journal of Materials Science,* vol. 58, no. 14, pp. 6124-6150, 2023/04/01 2023, doi: 10.1007/s10853-023-08386-7.

[9] Z.-X. Liu *et al.*, "A Bioinspired Gradient Design Strategy for Cellulose-Based Electromagnetic Wave Absorbing Structural Materials," *Nano Letters,* vol. 24,

no. 3, pp. 881-889, 2024/01/24 2024, doi: 10.1021/acs.nanolett.3c03989.

[10] M. Ma *et al.*, "Cellulose nanofiber/MXene/FeCo composites with gradient structure for highly absorbed electromagnetic interference shielding," *Chemical Engineering Journal*, vol. 452, p. 139471, 2023/01/15/ 2023, doi: https://doi.org/10.1016/j.cej.2022.139471.

[11] Z. Ling *et al.*, "Gradient variations of cellulose supramolecular structures in moso bamboo culm: from nano- to microhorizons," *Wood Science and Technology*, vol. 57, no. 2, pp. 359-373, 2023/03/01 2023, doi: 10.1007/s00226-023-01455-9.

[12] P. S. Jadhav *et al.*, "Composition Gradient Cellulose–Aerogel Nanocomposites Regulating Thermal Insulation," *Small Science*, vol. 3, no. 10, p. 2300042, 2023, doi: https://doi.org/10.1002/smsc.202300042.

[13] W. Zheng *et al.*, "3D cellulose scaffold with gradient pore structure controlled by hydrogen bond competition: Super-strength and multifunctional oil/water separation," *Carbohydrate Polymers*, vol. 344, p. 122544, 2024/11/15/ 2024, doi: https://doi.org/10.1016/j.carbpol.2024.122544.

[14] A. Etale *et al.*, "Cellulose: A Review of Water Interactions, Applications in Composites, and Water Treatment," *Chemical Reviews*, vol. 123, no. 5, pp. 2016-2048, 2023/03/08 2023, doi: 10.1021/acs.chemrev.2c00477.

[15] B.-Y. Zhao *et al.*, "Adsorption/desorption performance of cellulose membrane for Pb(ii)," *Green Processing and Synthesis*, vol. 12, no. 1, 2023, doi: doi:10.1515/gps-2023-0014.

[16] L. Chen *et al.*, "Nanocellulose-based functional materials for advanced energy and sensor applications," *Nano Research*, vol. 15, no. 8, pp. 7432-7452, 2022/08/01 2022, doi: 10.1007/s12274-022-4374-7.

[17] H. Sahin *et al.*, "A Study on Physical and Chemical Properties of Cellulose Paper Immersed in Various Solvent Mixtures," *International journal of molecular sciences*, vol. 9, pp. 78-88, 02/01 2008, doi: 10.3390/ijms9010078.

[18] B. Solahuddin *et al.*, "Effect of Shredded Waste Paper on Properties of Concrete," *IOP Conference Series: Earth and Environmental Science*, vol. 682, p. 012006, 02/01 2021, doi: 10.1088/1755-1315/682/1/012006.

[19] B. T. Amena *et al.*, "Influence of Physical–Mechanical Strength and Water Absorption Capacity on Sawdust–Waste Paper–Recycled Plastic Hybrid Composite for Ceiling Tile Application," *Journal of Composites Science*, vol. 8,

no. 5, doi: 10.3390/jcs8050176.

[20] D. Bjelić *et al.*, " “Waste to energy” as a driver towards a sustainable and circular energy future for the Balkan countries," *Energy, Sustainability and Society*, vol. 14, no. 1, p. 3, 2024/01/02 2024, doi: 10.1186/s13705-023-00435-y.

[21] X. Liu *et al.*, "Power generation from ambient humidity using protein nanowires," *Nature*, vol. 578, no. 7796, pp. 550-554, 2020/02/01 2020, doi: 10.1038/s41586-020-2010-9.

[22] Guoping Ren *et al.*, "A facile and sustainable hygroelectric generator using whole-cell Geobacter Sulfurreducens," *Nano Energy*, vol. 89, p. 106361, 2021, doi: 10.1016/j.nanoen.2021.106361.

[23] F. Z. Jiangli Xue, Chuangang Hu, Yang Zhao, Hongxia Luo, Liming Dai, Liangti Qu, "Vapor-Activated Power Generation on Conductive Polymer," *Adv. Funct. Mater.*, 2016, doi: 10.1002/adfm.201604188.

[24] Y. H. Huhu Cheng, Fei Zhao, Ce Yang, Panpan Zhang, Lan Jiang, Gaoquan Shi§ *et al.*, "Spontaneous power source in ambient air of a well-directionally reduced graphene oxide bulk," *The Royal Society of Chemistry*, 2018 July 17 2018, doi: https://doi.org/10.1039/C8EE01502C.

[25] Jixiang Gui *et al.*, "Hybrid solar evaporation system for water and electricity co-generation: Comprehensive utilization of solar and water energy," *Nano Energy*, vol. 107, p. 108155, 2023, doi: 10.1016/j.nanoen.2022.108155.

[26] Y. L. Fei Zhao, Huhu Cheng, Lan Jiang, and Liangti Qu, "Highly efficient moisture-enabled electricity generation from graphene
oxide frameworks," *The Royal Society of Chemistry*, 2016, doi: 10.1039/C5EE03701H.

[27] C. P. Teng *et al.*, "Advances in Cellulose-Based Composites for Energy Applications " (in eng), *Materials*, vol. 16, no. 10, May 20 2023, doi: 10.3390/ma16103856.

[28] A. S. R. A. Subki *et al.*, "Effects of varying the amount of reduced graphene oxide loading on the humidity sensing performance of zinc oxide/reduced graphene oxide nanocomposites on cellulose filter paper," *Journal of Alloys and Compounds*, vol. 926, p. 166728, 2022, doi: https://doi.org/10.1016/j.jallcom.2022.166728.

[29] A. Nik Nur Amiera *et al.*, "Extraction and Characterisation of Cellulose Nanocrystals Structures from Waste Office Paper," *Journal of Advanced*

Research in Fluid Mechanics and Thermal Sciences, vol. 61, no. 2, pp. 202-211, 03/28 2024. [Online]. Available: https://semarakilmu.com.my/journals/index.php/fluid_mechanics_thermal_sciences/article/view/3508.

[30] D. M. de Oliveira *et al.*, "Waste Paper as a Valuable Resource: An Overview of Recent Trends in the Polymeric Composites Field," *Polymers*, vol. 15, no. 2, doi: 10.3390/polym15020426.

[31] Z. Ma *et al.*, "Material Flow Patterns of the Global Waste Paper Trade and Potential Impacts of China's Import Ban," *Environmental Science & Technology,* vol. 55, no. 13, pp. 8492-8501, 2021/07/06 2021, doi: 10.1021/acs.est.1c00642.

[32] P. Duan *et al.*, "Moisture-based green energy harvesting over 600 hours via photocatalysis-enhanced hydrovoltaic effect," *Nature Communications,* vol. 16, no. 1, p. 239, 2025/01/02 2025, doi: 10.1038/s41467-024-55516-z.

[33] N. S. Mohamed Mustakim *et al.*, "Quantum dots processed by SILAR for solar cell applications," *Solar Energy,* vol. 163, pp. 256-270, 2018 March 18 2018, doi: https://doi.org/10.1016/j.solener.2018.02.003.

[34] N. S. Mustakim *et al.*, "Effect of silver sulphide (Ag2S) layer towards the performance of copper indium sulphide (CuInS2) quantum dots sensitised solar cell," *International Journal of Nanotechnology,* vol. 17, no. 11-12, pp. 795-806, 2020 Jan 1 2020, doi: https://doi.org/10.1504/IJNT.2020.112383.

[35] S. K. G. Kumaravel, Mohammed Mahmood Hamed Al Shekaili, Qais Hamed Saif Abdullah AL Othmani, "A Solar Photovoltaic Performance Monitoring and Statistical Forecasting Model Using a Multi-Layer Feed-Forward Neural Network and Artificial Intelligence," *Baghdad Science Journal,* vol. 21, no. 5(SI), p. 1868, 2024 May 25 2024, doi: https://doi.org/10.21123/bsj.2024.10736.

[36] M. H. Mamat *et al.*, "Triboelectric Nanogenerator Based on Tin Doped Zinc Oxide and Polyvinyl Alcohol Composite Thin Film for Energy Harvesting Applications," *Journal of Advanced Research in Applied Mechanics,* vol. 126, no. 1, pp. 165-177, 2024 Oct 30 2024, doi: https://doi.org/10.37934/aram.126.1.165177.

[37] S. J. Malode *et al.*, "Recent advances and viability in biofuel production," *Energy Conversion and Management: X,* vol. 10, p. 100070, 2021 June 1 2021,

doi: https://doi.org/10.1016/j.ecmx.2020.100070.

[38] J. Joshiba Ganesan *et al.*, "Low-carbon biofuels from macroalgae towards a sustainable circular bioeconomy and green future," *Biomass and Bioenergy,* vol. 190, p. 107389, 2024 Nov 1 2024, doi: https://doi.org/10.1016/j.biombioe.2024.107389.

[39] H. Yan *et al.*, "A review of humidity gradient-based power generator: Devices, materials and mechanisms," *Nano Energy,* vol. 101, p. 107591, 2022/10/01/ 2022, doi: https://doi.org/10.1016/j.nanoen.2022.107591.

[40] Y. Zhang *et al.*, "Sustainable power generation for at least one month from ambient humidity using unique nanofluidic diode," *Nature Communications,* vol. 13, no. 1, p. 3484, 2022/06/16 2022, doi: 10.1038/s41467-022-31067-z.

[41] Y. Zhang *et al.*, "Digestion of Ambient Humidity for Energy Generation," *Joule,* vol. 4, no. 12, pp. 2532-2536, 2020/12/16/ 2020, doi: https://doi.org/10.1016/j.joule.2020.10.003.

[42] M. Ma *et al.*, "Bio-Inspired Polymer Composite Actuator and Generator Driven by Water Gradients," *Science,* vol. 339, no. 6116, pp. 186-189, 2013 Jan 11 2013, doi: https://doi.org/10.1126/science.1230262.

[43] X. Chen *et al.*, "Bacillus spores as building blocks for stimuli-responsive materials and nanogenerators," *Nature Nanotechnology,* vol. 9, no. 2, pp. 137-141, 2014/02/01 2014, doi: 10.1038/nnano.2013.290.

[44] K. Zhao *et al.*, "Humidity-Tolerant Moisture-Driven Energy Generator with MXene Aerogel–Organohydrogel Bilayer," *ACS Nano,* vol. 17, no. 6, pp. 5472-5485, 2023/03/28 2023, doi: 10.1021/acsnano.2c10747.

[45] F. Cao *et al.*, "Efficient energy harvesting: High power wearable humidity generators with PAM-LiCl/CMC structure," *Nano Energy,* vol. 134, p. 110590, 2025/02/01/ 2025, doi: https://doi.org/10.1016/j.nanoen.2024.110590.

[46] H. Li *et al.*, "Achieving efficient multifunctional platform utilizing sugarcane for water-electricity cogeneration and dyes reduction," *Chemical Engineering Journal,* vol. 505, p. 159258, 2025/02/01/ 2025, doi: https://doi.org/10.1016/j.cej.2025.159258.

[47] N. S. Renzhi Ma, Liang Xue, Jingwen Sun, Wenyao Zhang, Wenqing Zhang, *et al.*, "Atomic-scale engineering of cation vacancies in two-dimensional unilamellar metal oxide nanosheets for electricity generation from water evaporation," vol. 110, p. 108348, 2023, doi: 10.1016/j.nanoen.2023.108348.

[48] X. C. Wanglin Zhang, Jiamin Zhao, Xinyue Wang, Xiuzhen Li, Tao Liu, Bin Luo, *et al.*, "Cellulose template-based triboelectric nanogenerators for self-powered sensing at high humidity," *Nano Energy*, vol. 108, p. 108196, 2023, doi: 10.1016/j.nanoen.2023.108196.

[49] B. Seo *et al.*, "Humidity-thermoelectric bimodal energy harvester for sustainable power generation," *Nano Energy*, vol. 107, 2023, doi: 10.1016/j.nanoen.2022.108120.

[50] Q. Lyu *et al.*, "Moist-Induced Electricity Generation by Electrospun Cellulose Acetate Membranes with Optimized Porous Structures," *ACS Applied Materials & Interfaces*, vol. 12, no. 51, pp. 57373-57381, 2020/12/23 2020, doi: 10.1021/acsami.0c17931.

[51] Y. Long *et al.*, "Moisture-induced autonomous surface potential oscillations for energy harvesting," *Nat Commun*, vol. 12, no. 1, p. 5287, Sep 6 2021, doi: 10.1038/s41467-021-25554-y.

[52] Y. Komazaki *et al.*, "Energy harvesting by ambient humidity variation with continuous milliampere current output and energy storage," *Sustainable Energy & Fuels*, vol. 5, no. 14, pp. 3570-3577, 2021, doi: 10.1039/D1SE00562F.

[53] S. Daripa *et al.*, "Efficient Moisture-Induced Energy Harvesting from Water-Soluble Conjugated Block Copolymer-Functionalized Reduced Graphene Oxide," *ACS Omega*, vol. 6, no. 11, pp. 7257-7265, 2021/03/23 2021, doi: 10.1021/acsomega.0c03717.

[54] M. X. Daozhi Shen, Guisheng Zou, Lei Liu, Walter W. Duley, Y. Norman Zhou, "Self-Powered Wearable Electronics Based on Moisture Enabled Electricity Generation," *Adv Mater*, vol. 30, no. 18, p. e1705925, 2018, doi: https://doi.org/10.1002/adma.201705925.

[55] P. Vijaya Kumar *et al.*, "Synthesis and characterization of NiO nanoparticles by chemical as well as green routes and their comparisons with respect to cytotoxic effect and toxicity studies in microbial and MCF-7 cancer cell models," *SN Applied Sciences*, vol. 1, no. 9, p. 1083, 2019/08/24 2019, doi: 10.1007/s42452-019-1113-0.

[56] M. N. Yahya *et al.*, "Modified locally derived graphene nanoplatelets for enhanced rheological, filtration and lubricity characteristics of water-based drilling fluids," *Arabian Journal of Chemistry*, vol. 16, no. 12, p. 105305, 2023/12/01/ 2023, doi: https://doi.org/10.1016/j.arabjc.2023.105305.

[57] M. Z. Musa *et al.*, "Fabrication and structural properties of flower-like TiO2 nanorod array films grown on glass substrate without FTO layer," *Materials Letters*, vol. 273, p. 127902, 2020/08/15/ 2020, doi: https://doi.org/10.1016/j.matlet.2020.127902.

[58] N. Parimon *et al.*, "Annealing temperature dependency of structural, optical and electrical characteristics of manganese-doped nickel oxide nanosheet array films for humidity sensing applications," *Nanomaterials and Nanotechnology*, vol. 11, p. 1847980420982788, 2021/01/01 2021, doi: 10.1177/1847980420982788.

[59] H. Parangusan *et al.*, "Humidity sensor based on poly(lactic acid)/PANI–ZnO composite electrospun fibers," *RSC Advances*, 10.1039/D1RA02842A vol. 11, no. 46, pp. 28735-28743, 2021, doi: 10.1039/D1RA02842A.

[60] M. H. Mamat *et al.*, "Synthesis, structural and optical properties of mesostructured, X-doped NiO (x = Zn, Sn, Fe) nanoflake network films," *Materials Research Bulletin*, vol. 127, p. 110860, 2020/07/01/ 2020, doi: https://doi.org/10.1016/j.materresbull.2020.110860.

[61] V. S. Kumbhar *et al.*, "Mesoporous design of ultrathin NiO nanosheet-coated vertically aligned hexagonal CoS nanoplate core–shell array for flexible all-solid-state supercapacitors," *Journal of Alloys and Compounds*, vol. 863, p. 158064, 2021/05/15/ 2021, doi: https://doi.org/10.1016/j.jallcom.2020.158064.

[62] S. Chen *et al.*, "High Performance Flexible Lithium-Ion Battery Electrodes: Ion Exchange Assisted Fabrication of Carbon Coated Nickel Oxide Nanosheet Arrays on Carbon Cloth," *Advanced Functional Materials*, https://doi.org/10.1002/adfm.202101199 vol. 31, no. 24, p. 2101199, 2021/06/01 2021, doi: https://doi.org/10.1002/adfm.202101199.

[63] M. R. Younis *et al.*, "Recent Advances on Graphene Quantum Dots for Bioimaging Applications," (in English), *Frontiers in Chemistry*, Review vol. 8, 2020-June-03 2020, doi: 10.3389/fchem.2020.00424.

[64] Z. Lin *et al.*, "Two-dimensional amorphous NiO as a plasmonic photocatalyst for solar H(2) evolution," (in eng), *Nat Commun*, vol. 9, no. 1, p. 4036, Oct 2 2018, doi: 10.1038/s41467-018-06456-y.

[65] L. Gu *et al.*, "Enhancing the current density of a piezoelectric nanogenerator using a three-dimensional intercalation electrode," *Nature Communications*, vol. 11, no. 1, p. 1030, 2020/02/25 2020, doi: 10.1038/s41467-020-14846-4.

[66] Z. Wang *et al.*, "Hydrogel Electrolytes for Flexible Aqueous Energy Storage

Devices," *Advanced Functional Materials,* https://doi.org/10.1002/adfm.201804560 vol. 28, no. 48, p. 1804560, 2018/11/01 2018, doi: https://doi.org/10.1002/adfm.201804560.

[67] H. Yan *et al.*, "Development and mechanism investigation of TiO2/Co hydrogel microgenerator utilizing humidity gradient," *Energy Conversion and Management,* vol. 291, 2023, doi: 10.1016/j.enconman.2023.117256.

[68] X. Zhang *et al.*, "A flexible and high voltage symmetric supercapacitor based on hybrid configuration of cobalt hexacyanoferrate/reduced graphene oxide hydrogels," *Chemical Engineering Journal,* vol. 335, pp. 321-329, 2018, doi: 10.1016/j.cej.2017.10.158.

[69] X. Meng *et al.*, "Cobalt Sulfide/Graphene Composite Hydrogel as Electrode for High-Performance Pseudocapacitors," *Sci Rep,* vol. 6, p. 21717, Feb 16 2016, doi: 10.1038/srep21717.

[70] Y. Xu *et al.*, "Deep ultraviolet hydrogel based on 2D cobalt-doped titanate," *Light Sci Appl,* vol. 12, no. 1, p. 1, Jan 1 2023, doi: 10.1038/s41377-022-00991-6.

[71] Y. Meng *et al.*, "Self-assembled copper/cobalt-containing polypyrrole hydrogels for highly efficient ORR electrocatalysts," *Journal of Molecular Liquids,* vol. 298, 2020, doi: 10.1016/j.molliq.2019.112010.

[72] Q. Yi *et al.*, "Peroxymonosulfate activation by three-dimensional cobalt hydroxide/graphene oxide hydrogel for wastewater treatment through an automated process," *Chemical Engineering Journal,* vol. 400, 2020, doi: 10.1016/j.cej.2020.125965.

[73] X. Meng *et al.*, "Graphene-based cobalt sulfide composite hydrogel with enhanced electrochemical properties for supercapacitors," *New Journal of Chemistry,* vol. 40, no. 3, pp. 2843-2849, 2016, doi: 10.1039/c5nj03423j.

[74] S. Farzaneh *et al.*, "Fabrication and characterization of cobalt ferrite magnetic hydrogel combined with static magnetic field as a potential bio-composite for bone tissue engineering," *Journal of Drug Delivery Science and Technology,* vol. 64, 2021, doi: 10.1016/j.jddst.2021.102525.

[75] P. N. Dave *et al.*, "Drug release and thermal properties of magnetic cobalt ferrite (CoFe(2)O(4)) nanocomposite hydrogels based on poly(acrylic acid-g-N-isopropyl acrylamide) grafted onto gum ghatti," *Int J Biol Macromol,* vol. 224, pp. 358-369, Jan 1 2023, doi: 10.1016/j.ijbiomac.2022.10.129.

[76] S. Khongkla *et al.*, "A composite zinc oxide and magnetic molecularly imprinted polymer hydrogel adsorbent for the extraction of sulfonamides in milk," *Microchemical Journal,* vol. 191, 2023, doi: 10.1016/j.microc.2023.108865.

[77] R. Monfared-Hajishirkiaee *et al.*, "Multifunctional chitosan/carbon dots/sodium alginate/zinc oxide double-layer sponge hydrogel with high antibacterial, mechanical and hemostatic properties," *OpenNano,* vol. 12, 2023, doi: 10.1016/j.onano.2023.100162.

[78] Y. Pang *et al.*, "Self-adhesive frost-resistant conductive hydrogel electrolytes based on TA@WSCA-Zn autocatalytic system for flexible and foldable solid-state capacitors," *Chemical Engineering Journal,* vol. 469, 2023, doi: 10.1016/j.cej.2023.143943.

[79] J. Yu *et al.*, "UV-light-driven synthesis of Ag-Zn nanoparticles encased in hydrogels for H2S sensing," *Food Packaging and Shelf Life,* vol. 39, 2023, doi: 10.1016/j.fpsl.2023.101151.

[80] H. Sun *et al.*, "Zinc alginate hydrogels with embedded RL-QN15 peptide-loaded hollow polydopamine nanoparticles for diabetic wound healing therapy," *Materials & Design,* vol. 222, 2022, doi: 10.1016/j.matdes.2022.111085.

[81] H. Cheng *et al.*, "Zinc insulin hexamer loaded alginate zinc hydrogel: Preparation, characterization and in vivo hypoglycemic ability," *Eur J Pharm Biopharm,* vol. 179, pp. 173-181, Oct 2022, doi: 10.1016/j.ejpb.2022.08.016.

[82] X. Ai *et al.*, "Zinc polyacrylamide hydrogel electrolyte for quasi-solid-state electrochromic devices with low-temperature tolerance," *Cell Reports Physical Science,* vol. 3, no. 11, 2022, doi: 10.1016/j.xcrp.2022.101148.

[83] P. A. Vinosha *et al.*, "Review on recent advances of zinc substituted cobalt ferrite nanoparticles: Synthesis characterization and diverse applications," *Ceramics International,* vol. 47, no. 8, pp. 10512-10535, 2021, doi: 10.1016/j.ceramint.2020.12.289.

[84] T. Tatarchuk *et al.*, "Eco-friendly synthesis of cobalt-zinc ferrites using quince extract for adsorption and catalytic applications: An approach towards environmental remediation," *Chemosphere,* vol. 294, p. 133565, May 2022, doi: 10.1016/j.chemosphere.2022.133565.

[85] C. Mang *et al.*, "Electromagnetic wave absorption properties of cobalt-zinc ferrite nanoparticles doped with rare earth elements," *Journal of Rare Earths,* vol. 39, no. 11, pp. 1415-1426, 2021, doi: 10.1016/j.jre.2020.08.011.

[86] R. Shu *et al.*, "Facile synthesis of cobalt-zinc ferrite microspheres decorated nitrogen-doped multi-walled carbon nanotubes hybrid composites with excellent microwave absorption in the X-band," *Composites Science and Technology*, vol. 184, 2019, doi: 10.1016/j.compscitech.2019.107839.

[87] T. Tatarchuk *et al.*, "Green synthesis, structure, cations distribution and bonding characteristics of superparamagnetic cobalt-zinc ferrites nanoparticles for Pb(II) adsorption and magnetic hyperthermia applications," *Journal of Molecular Liquids*, vol. 328, 2021, doi: 10.1016/j.molliq.2021.115375.

[88] T. T. Nguyen *et al.*, "Hierarchical 3D Oxygenated Cobalt Vanadium Selenide Nanosheets as Advanced Electrode for Flexible Zinc-Cobalt and Zinc-Air Batteries," *Small*, vol. 16, no. 48, p. e2004661, Dec 2020, doi: 10.1002/smll.202004661.

[89] M. Shahi *et al.*, "Hybrid supercapacitors constructed from double-shelled cobalt-zinc sulfide/copper oxide nanoarrays and ferrous sulfide/graphene oxide nanostructures," *J Colloid Interface Sci*, vol. 585, pp. 750-763, Mar 2021, doi: 10.1016/j.jcis.2020.10.055.

[90] Z. Lu *et al.*, "An Isolated Zinc–Cobalt Atomic Pair for Highly Active and Durable Oxygen Reduction," *Angewandte Chemie International Edition*, vol. 58, no. 9, pp. 2622-2626, 2019, doi: 10.1002/anie.201810175.

[91] H. Zhang *et al.*, "Surface oxygen vacancy inducing peroxymonosulfate activation through electron donation of pollutants over cobalt-zinc ferrite for water purification," *Applied Catalysis B: Environmental*, vol. 270, 2020, doi: 10.1016/j.apcatb.2020.118874.

[92] H. Mahajan *et al.*, "Synthesis and investigation of structural, morphological, and magnetic properties of the manganese doped cobalt-zinc spinel ferrite," *Journal of Alloys and Compounds*, vol. 896, 2022, doi: 10.1016/j.jallcom.2021.162966.

[93] X. Wei *et al.*, "Yolk-shell-structured zinc-cobalt binary metal sulfide @ N-doped carbon for enhanced lithium-ion storage," *Nano Energy*, vol. 64, 2019, doi: 10.1016/j.nanoen.2019.103899.

[94] C. Chen *et al.*, "Nanoscale Ion Regulation in Wood-Based Structures and Their Device Applications," *Advanced Materials*, vol. 33, no. 28, p. 2002890, 2021, doi: https://doi.org/10.1002/adma.202002890.

[95] P. C. Ani *et al.*, "Cellulose from waste materials for electrochemical energy storage applications: A review," *Applied Surface Science Advances*, vol. 11, p.

100298, 2022/10/01/ 2022, doi: https://doi.org/10.1016/j.apsadv.2022.100298.

[96] R. Li *et al.*, "The Application of Cellulose Nanofibrils in Energy Systems," *Batteries*, vol. 9, no. 8, doi: 10.3390/batteries9080399.

[97] C. P. Teng *et al.*, "Advances in Cellulose-Based Composites for Energy Applications," *Materials*, vol. 16, no. 10, doi: 10.3390/ma16103856.

[98] N. A. N. M. N. Azman *et al.*, "Cellulose Morphologies for Energy Applications," in *Regenerated Cellulose and Composites: Morphology-Property Relationship*, M. Shabbir Ed. Singapore: Springer Nature Singapore, 2023, pp. 197-221.

[99] W. Ge *et al.*, "Cellulose nanocrystal composite films for contactless moisture-electric conversion," *RSC Advances*, 10.1039/D4RA08459D vol. 15, no. 4, pp. 2651-2656, 2025, doi: 10.1039/D4RA08459D.

[100] D. Thakur *et al.*, "Heterogeneous bilayer system of cellulose nanofibers for a moisture-enabled electric generator," *Cellulose*, vol. 32, no. 5, pp. 3285-3298, 2025/03/01 2025, doi: 10.1007/s10570-025-06441-x.

[101] P. Wang *et al.*, "Enhanced output performance in paper-based piezoelectric nanogenerators via polarization-engineered Schottky barrier contacts," *Journal of Materials Chemistry C*, 10.1039/D5TC01203A vol. 13, no. 23, pp. 11938-11949, 2025, doi: 10.1039/D5TC01203A.

[102] S. Lu *et al.*, "Flexible cellulose-based hybrid nanogenerators for self-powered wearable bio-monitoring applications," *Journal of Colloid and Interface Science*, vol. 685, pp. 1087-1098, 2025/05/01/ 2025, doi: https://doi.org/10.1016/j.jcis.2025.01.190.

[103] M. Cao *et al.*, "All-Cellulose Nanofiber-Based Sustainable Triboelectric Nanogenerators for Enhanced Energy Harvesting," *Polymers*, vol. 16, no. 13, p. 1784, 2024. [Online]. Available: https://www.mdpi.com/2073-4360/16/13/1784.

[104] J. González *et al.*, "Advanced Cellulose–Nanocarbon Composite Films for High-Performance Triboelectric and Piezoelectric Nanogenerators," *Nanomaterials*, vol. 13, no. 7, p. 1206, 2023. [Online]. Available: https://www.mdpi.com/2079-4991/13/7/1206.

[105] K. Maity *et al.*, "Cellulose Nanocrystal-Based All-3D-Printed Pyro-Piezoelectric Nanogenerator for Hybrid Energy Harvesting and Self-Powered Cardiorespiratory Monitoring toward the Human–Machine Interface," *ACS*

Applied Materials & Interfaces, vol. 15, no. 11, pp. 13956-13970, 2023/03/22 2023, doi: 10.1021/acsami.2c21680.

[106] Z. Li *et al.*, "Asymmetrically Patterned Cellulose Nanofibers/Graphene Oxide Composite Film for Humidity Sensing and Moist-Induced Electricity Generation," *ACS Applied Materials & Interfaces,* vol. 12, no. 49, pp. 55205-55214, 2020/12/09 2020, doi: 10.1021/acsami.0c17970.

[107] S. Nie *et al.*, "Chemically Functionalized Cellulose Nanofibrils for Improving Triboelectric Charge Density of a Triboelectric Nanogenerator," *ACS Sustainable Chemistry & Engineering,* vol. 8, no. 50, pp. 18678-18685, 2020/12/21 2020, doi: 10.1021/acssuschemeng.0c07531.

[108] N. Wang *et al.*, "Dual-electric-polarity augmented cyanoethyl cellulose-based triboelectric nanogenerator with ultra-high triboelectric charge density and enhanced electrical output property at high humidity," *Nano Energy,* vol. 103, p. 107748, 2022/12/01/ 2022, doi: https://doi.org/10.1016/j.nanoen.2022.107748.

[109] Y. Tan *et al.*, "Porous nanocomposites by cotton-derived carbon/NiO with high performance for lithium-ion storage," *Journal of Alloys and Compounds,* vol. 874, p. 159788, 2021/09/05/ 2021, doi: https://doi.org/10.1016/j.jallcom.2021.159788.

[110] J. Wu *et al.*, "Organic solar cells based on cellulose nanopaper from agroforestry residues with an efficiency of over 16% and effectively wide-angle light capturing," *Journal of Materials Chemistry A,* 10.1039/C9TA14039E vol. 8, no. 11, pp. 5442-5448, 2020, doi: 10.1039/C9TA14039E.

[111] T. Su *et al.*, "MXene/cellulose nanofiber-foam based high performance degradable piezoresistive sensor with greatly expanded interlayer distances," *Nano Energy,* vol. 87, p. 106151, 2021/09/01/ 2021, doi: https://doi.org/10.1016/j.nanoen.2021.106151.

[112] Q. Xu *et al.*, "Nanocellulose Building Block for the Construction of Hygroscopic Aerogels," *Accounts of Materials Research,* vol. 5, no. 7, pp. 846-856, 2024/07/26 2024, doi: 10.1021/accountsmr.4c00085.

[113] Y. Du *et al.*, "Moisture Harvesting by the Structure Regulation of Hygroscopic Hydrogel for Energy and Water Sustainability," *Advanced Electronic Materials,* vol. n/a, no. n/a, p. 2400802, doi: https://doi.org/10.1002/aelm.202400802.

[114] L. Zhu *et al.*, "Hygroscopic and moisture-stable cellulose nanofiber aerogel for

effective and repeatable moisture-enabled electricity generation," *Chemical Engineering Journal*, vol. 511, p. 162246, 2025/05/01/ 2025, doi: https://doi.org/10.1016/j.cej.2025.162246.

[115] A. Ghaffarkhah *et al.*, "Ambient-Dried MOF/Cellulose-Based Aerogels for Atmospheric Water Harvesting and Sustainable Water Management in Agriculture," *Advanced Functional Materials*, vol. n/a, no. n/a, p. 2506427, doi: https://doi.org/10.1002/adfm.202506427.

[116] Z. Sun *et al.*, "Emerging design principles, materials, and applications for moisture-enabled electric generation," *eScience*, vol. 2, no. 1, pp. 32-46, 2022/01/01/ 2022, doi: https://doi.org/10.1016/j.esci.2021.12.009.

[117] Y. Yu *et al.*, "Thermoresponsive Aerogel Enabling Ultrafast Adsorption-Release Cycles for Atmospheric Harvesting," *ACS Applied Materials & Interfaces*, vol. 17, no. 22, pp. 32906-32913, 2025/06/04 2025, doi: 10.1021/acsami.5c05485.

[118] Z. Yao *et al.*, "Innovative Hygroscopic Material for Humidity Regulation: Diatomaceous Earth Composite Porous Ceramic," *Crystals*, vol. 15, no. 2, p. 158, 2025. [Online]. Available: https://www.mdpi.com/2073-4352/15/2/158.

[119] S. N. Abd Elwadood *et al.*, "A Super-Hygroscopic Solar-Regenerated Alginate-Based Composite for Atmospheric Water Harvesting," *Small*, vol. 20, no. 37, p. 2400420, 2024, doi: https://doi.org/10.1002/smll.202400420.

[120] G. Graeber *et al.*, "Extreme Water Uptake of Hygroscopic Hydrogels through Maximized Swelling-Induced Salt Loading," *Advanced Materials*, vol. 36, no. 12, p. 2211783, 2024, doi: https://doi.org/10.1002/adma.202211783.

[121] S.-Y. Yuan *et al.*, "Unlocking the potential of hematite photoanodes in acidic electrolytes: Boosting performance with ultra-small IrOx nanoparticles for efficient water splitting," *EcoEnergy*, vol. 2, no. 2, pp. 322-335, 2024, doi: https://doi.org/10.1002/ece2.41.

[122] A. Chnani *et al.*, "Ultrathin Hematite-Hercynite Films for Future Unassisted Solar Water Splitting," *Advanced Materials Technologies*, vol. 8, no. 22, p. 2300655, 2023, doi: https://doi.org/10.1002/admt.202300655.

[123] L. Bhattacharya *et al.*, "Theoretical insights into metal-doped nanostructured hematite catalyst supported by graphene underlayer for photoelectrochemical water splitting applications," *Discover Catalysis*, vol. 2, no. 1, p. 7, 2025/05/15 2025, doi: 10.1007/s44344-025-00011-w.

[124] W. Zou *et al.*, "Humidity-Sensing Performance of TiO2/RGO and α-Fe2O3/RGO Composites," *Sensors*, vol. 25, no. 3, p. 691, 2025. [Online]. Available: https://www.mdpi.com/1424-8220/25/3/691.

[125] W. R. Wan Ahmad *et al.*, "Impact of annealing temperature to the performance of hematite-based humidity sensor," *Indonesian Journal of Electrical Engineering and Computer Science*, vol. 13, pp. 1079-1086, 03/01 2019, doi: 10.11591/ijeecs.v13.i3.pp1079-1086.

[126] E. M. Ahmed *et al.*, "Thermal stability, mechanical strength, and ionic conductivity of hematite nanoparticle/CS nanocomposites," *Polymers and Polymer Composites*, vol. 33, p. 09673911251327811, 2025, doi: 10.1177/09673911251327811.

[127] S. P. Kok *et al.*, "Effect of Hygroscopic and Electronic Materials, Challenges, and Sensing Requirements in Humidity-Controlled Industry," *Journal of Electronic Materials*, 2025/07/05 2025, doi: 10.1007/s11664-025-12140-x.

[128] A. Wei *et al.*, "Triboelectric Nanogenerator Driven Self-Powered Photoelectrochemical Water Splitting Based on Hematite Photoanodes," *ACS Nano*, vol. 12, no. 8, pp. 8625-8632, 2018/08/28 2018, doi: 10.1021/acsnano.8b04363.

[129] I. Corrales-Mendoza *et al.*, "Porous Hematite Photocatalytic Structures on Freestanding CuO-Sb2O5-SnO2 Ceramics for Solar-Driven Water Splitting and Flow-Through Water Purification," *Journal of Electronic Materials*, vol. 54, no. 1, pp. 556-567, 2025/01/01 2025, doi: 10.1007/s11664-024-11603-x.

[130] G. Dong *et al.*, "Enhancing photoelectrochemical performance and stability of Ti-doped hematite photoanode via pentanuclear Co-based MOF modification," (in English), *Frontiers in Chemistry*, Original Research vol. Volume 12 - 2024, 2024-August-30 2024, doi: 10.3389/fchem.2024.1454524.

[131] C. Xu *et al.*, "Inducing hollow and porous hematite nanorod photoanodes by rare earth and transition metal doping for enhanced solar water splitting," *Journal of Materials Chemistry A*, 10.1039/D4TA01258E vol. 12, no. 20, pp. 11831-11840, 2024, doi: 10.1039/D4TA01258E.

[132] J. Park *et al.*, "Sn-Controlled Co-Doped Hematite for Efficient Solar-Assisted Chargeable Zn–Air Batteries," *ACS Applied Materials & Interfaces*, vol. 13, no. 46, pp. 54906-54915, 2021/11/24 2021, doi: 10.1021/acsami.1c13872.

[133] S. A. Kadam *et al.*, "Microporous α-Fe2O3@NiO Heterostructures Synthesized for Enhanced Supercapacitor Performance," *ChemistrySelect,* vol. 9, no. 14, p. e202302376, 2024, doi: https://doi.org/10.1002/slct.202302376.

[134] G. Mummoorthi *et al.*, "Synthesis and Characterization of Ternary α-Fe2O3/NiO/rGO Composite for High-Performance Supercapacitors," *ACS Omega,* vol. 7, no. 31, pp. 27390-27399, 2022/08/09 2022, doi: 10.1021/acsomega.2c02418.

[135] S. Zarghami *et al.*, "Superhydrophilic and underwater superoleophobic membranes - A review of synthesis methods," *Progress in Polymer Science,* vol. 98, p. 101166, 2019/11/01/ 2019, doi: https://doi.org/10.1016/j.progpolymsci.2019.101166.

[136] J. Ren *et al.*, "A novel TiO2@stearic acid/chitosan coating with reversible wettability for controllable oil/water and emulsions separation," *Carbohydrate Polymers,* vol. 232, p. 115807, 2020/03/15/ 2020, doi: https://doi.org/10.1016/j.carbpol.2019.115807.

[137] M. A. Mehmood *et al.*, "Modification in Surface Properties of Bismuth after Thermal Plasma Treatment," *Journal of Materials Engineering and Performance,* vol. 34, no. 3, pp. 1944-1958, 2025/02/01 2025, doi: 10.1007/s11665-024-09214-y.

[138] Q. Shu *et al.*, "Atmospheric pressure argon plasma: an effective method to improve the hydrophilicity of the cellulose in paper," *Cellulose,* vol. 30, no. 18, pp. 11767-11782, 2023/12/01 2023, doi: 10.1007/s10570-023-05596-9.

[139] P. Chytrosz-Wrobel *et al.*, "Effect of oxygen plasma-treatment on surface functional groups, wettability, and nanotopography features of medically relevant polymers with various crystallinities," *Applied Surface Science Advances,* vol. 18, p. 100497, 2023/12/01/ 2023, doi: https://doi.org/10.1016/j.apsadv.2023.100497.

[140] T. Kawano *et al.*, "Surface Modification of a Regenerated Cellulose Film Using Low-Pressure Plasma Treatment with Various Reactive Gases," *ACS Omega,* vol. 7, no. 48, pp. 44085-44092, 2022/12/06 2022, doi: 10.1021/acsomega.2c05499.

[141] A. Hadžić *et al.*, "Superbiphilic Laser-Microengineered Surfaces with A Self-Assembled Monolayer Coating for Exceptional Boiling Performance,"

Advanced Functional Materials, vol. 34, no. 10, p. 2310662, 2024, doi: https://doi.org/10.1002/adfm.202310662.

[142] R. Ariza *et al.*, "Multiscale ultrafast laser texturing of marble for reduced surface wetting," *Applied Surface Science,* vol. 577, p. 151850, 2022/03/01/ 2022, doi: https://doi.org/10.1016/j.apsusc.2021.151850.

[143] M. Barili *et al.*, "A Hybrid Approach to Surface Engineering Based on Laser Texturing and Coating," *Journal of Manufacturing and Materials Processing,* vol. 7, no. 2, p. 59, 2023. [Online]. Available: https://www.mdpi.com/2504-4494/7/2/59.

[144] J. Liu *et al.*, "Adjusting the stability of plasma treated superhydrophobic surfaces by different modifications or microstructures," *RSC Advances,* 10.1039/C6RA14005J vol. 6, no. 83, pp. 79437-79447, 2016, doi: 10.1039/C6RA14005J.

[145] Y. Huang *et al.*, "Effect of stearic acid and sodium stearate on hydrophobicity of nano calcium carbonate and mechanism of water vapor adsorption," *Scientific Reports,* vol. 15, no. 1, p. 364, 2025/01/02 2025, doi: 10.1038/s41598-024-82802-z.

[146] J. Yang *et al.*, "Study on the Hydrophobic Modification Mechanism of Stearic Acid on the Surface of Coal Gasification Fly Ash," *Molecules,* vol. 29, no. 17, p. 4071, 2024. [Online]. Available: https://www.mdpi.com/1420-3049/29/17/4071.

[147] M. Qu *et al.*, "Stearic Acid-Enhanced Triboelectric Nanogenerators with High Waterproof, Output Performance, and Wear Resistance for Efficient Harvesting of Mechanical Energy and Self-Powered Sensing for Human Motion Monitoring," *ACS Applied Electronic Materials,* vol. 6, no. 3, pp. 1651-1665, 2024/03/26 2024, doi: 10.1021/acsaelm.3c01580.

[148] G.-J. Chen *et al.*, "The Microstructures and Characteristics of NiO Films: Effects of Substrate Temperature," *Micromachines,* vol. 13, no. 11, p. 1940, 2022. [Online]. Available: https://www.mdpi.com/2072-666X/13/11/1940.

[149] M. Narwal *et al.*, "Surface Modification of NiO-Al2O3 Nanocomposites using Stearic Acid as a Modifier and their Applications in Self-cleaning and Removal of Dyes," *ChemistrySelect,* vol. 9, no. 11, p. e202304675, 2024, doi: https://doi.org/10.1002/slct.202304675.

[150] J.-j. Ruan *et al.*, "Superhydrophobic synergistic antibacterial ZrO2-based

surfaces with tertiary hierarchical structures fabricated by femtosecond laser texturing and surface modification," *Journal of Alloys and Compounds,* vol. 1002, p. 175331, 2024/10/15/ 2024, doi: https://doi.org/10.1016/j.jallcom.2024.175331.

[151] Z. Zhao *et al.,* "Improving the hydrophobicity, dimensional stability and mold resistance of bamboo by paraffin/microcrystalline wax/stearic acid modification," *Construction and Building Materials,* vol. 414, p. 134902, 2024/02/02/ 2024, doi: https://doi.org/10.1016/j.conbuildmat.2024.134902.

[152] X. Li *et al.,* "Self-Powered Carbon Ink/Filter Paper Flexible Humidity Sensor Based on Moisture-Induced Voltage Generation," *Langmuir,* vol. 38, no. 27, pp. 8232-8240, 2022/07/12 2022, doi: 10.1021/acs.langmuir.2c00566.

[153] R. S. Sabry *et al.,* "A systematic study to evaluate effects of stearic acid on superhydrophobicity and photocatalytic properties of Ag-doped ZnO nanostructures," *Journal of Materials Science: Materials in Electronics,* vol. 31, no. 16, pp. 13382-13391, 2020, doi: 10.1007/s10854-020-03893-8.

[154] A. Patti *et al.,* "The universal usefulness of stearic acid as surface modifier: applications to the polymer formulations and composite processing," *Journal of Industrial and Engineering Chemistry,* vol. 96, pp. 1-33, 2021, doi: 10.1016/j.jiec.2021.01.024.

[155] T. Azam *et al.,* "Biomimetic highly hydrophobic stearic acid functionalized MOF sponge for efficient oil/water separation," *Materials Research Express,* vol. 8, no. 1, p. 015019, 2021/01/20 2021, doi: 10.1088/2053-1591/abd822.

[156] M. Yu *et al.,* "ZnO nanoparticles coated and stearic acid modified superhydrophobic chitosan film for self-cleaning and oil–water separation," *International Journal of Biological Macromolecules,* vol. 231, p. 123293, 2023/03/15/ 2023, doi: https://doi.org/10.1016/j.ijbiomac.2023.123293.

[157] F. Kunc *et al.,* "Physical Characterization and Cellular Toxicity Studies of Commercial NiO Nanoparticles," *Nanomaterials,* vol. 12, no. 11, p. 1822, 2022. [Online]. Available: https://www.mdpi.com/2079-4991/12/11/1822.

[158] Z. Bai *et al.,* "Fabrication of superhydrophobic reduced-graphene oxide/nickel coating with mechanical durability, self-cleaning and anticorrosion performance," *Nano Materials Science,* vol. 2, no. 2, pp. 151-158, 2020/06/01/ 2020, doi: https://doi.org/10.1016/j.nanoms.2019.05.001.

[159] M. Narwal *et al.,* "Surface Modification of NiO Nanoparticles Using Stearic

Acid and Their Application as Adsorbent," in *Proceedings of the 3rd International Conference on Advances in Materials Processing: Challenges and Opportunities*, Singapore, A. Tewari *et al.*, Eds., 2023// 2023: Springer Nature Singapore, pp. 3-8.

[160] M. E. Mohamed *et al.*, "Fabrication of eco-friendly graphene-based superhydrophobic coating on steel substrate and its corrosion resistance, chemical and mechanical stability," *Scientific Reports*, vol. 12, no. 1, p. 10530, 2022/06/22 2022, doi: 10.1038/s41598-022-14353-0.

[161] S. Shen *et al.*, "Triboelectric polymer with excellent enhanced electrical output performance over a wide temperature range," *Nano Energy*, vol. 110, p. 108347, 2023/06/01/ 2023, doi: https://doi.org/10.1016/j.nanoen.2023.108347.

[162] Y. Zhao *et al.*, "Extreme environment-resistant high performance triboelectric nanogenerator for energy harvesting and self-powered positioning system," *Nano Today*, vol. 61, p. 102616, 2025/04/01/ 2025, doi: https://doi.org/10.1016/j.nantod.2024.102616.

[163] H. Zhang *et al.*, "Stearic Acid Reinforced Triboelectric Nanogenerator with High Output Performance and Anti-wear Characteristics for Self-powered Anticorrosion System," *Chemistry Letters*, vol. 50, no. 5, pp. 844-848, 2021, doi: 10.1246/cl.210019.

[164] W. Zhang *et al.*, "Wearable and self-powered sensors made by triboelectric nanogenerators assembled from antibacterial bromobutyl rubber," *Nano Energy*, vol. 82, p. 105769, 2021/04/01/ 2021, doi: https://doi.org/10.1016/j.nanoen.2021.105769.

[165] F. Wang *et al.*, "High performance piezoelectric nanogenerator with silver nanowires embedded in polymer matrix for mechanical energy harvesting," *Ceramics International*, vol. 47, no. 24, pp. 35096-35104, 2021/12/15/ 2021, doi: https://doi.org/10.1016/j.ceramint.2021.09.052.

[166] Y. Zhang *et al.*, "Performance Enhancement of Flexible Piezoelectric Nanogenerator via Doping and Rational 3D Structure Design For Self-Powered Mechanosensational System," *Advanced Functional Materials*, vol. 29, no. 42, p. 1904259, 2019, doi: https://doi.org/10.1002/adfm.201904259.

[167] D. Damjanovic, "Piezoelectricity," pp. 300-309, 2005. [Online]. Available: https://scholar.google.com/scholar?cluster=20891855824584341O&hl=en&oi=scholarr.

[168] S. Mishra *et al.*, "Advances in Piezoelectric Polymer Composites for Energy Harvesting Applications: A Systematic Review," *Macromolecular Materials and Engineering,* vol. 304, no. 1, p. 1800463, 2019, doi: https://doi.org/10.1002/mame.201800463.

[169] Y. Zhang *et al.*, "Progress in lead-free piezoelectric nanofiller materials and related composite nanogenerator devices," *Nanoscale Advances,* 10.1039/C9NA00809H vol. 2, no. 8, pp. 3131-3149, 2020, doi: 10.1039/C9NA00809H.

[170] I. Chopra, "Review of State of Art of Smart Structures and Integrated Systems," *AIAA Journal,* vol. 40, no. 11, pp. 2145-2187, 2002, doi: 10.2514/2.1561.

[171] D. Hu *et al.*, "Strategies to achieve high performance piezoelectric nanogenerators," *Nano Energy,* vol. 55, pp. 288-304, 2019/01/01/ 2019, doi: https://doi.org/10.1016/j.nanoen.2018.10.053.

[172] S. Xu *et al.*, "Self-powered nanowire devices," *Nature Nanotechnology,* vol. 5, no. 5, pp. 366-373, 2010/05/01 2010, doi: 10.1038/nnano.2010.46.

[173] L. Jin *et al.*, "Polarization-free high-crystallization β-PVDF piezoelectric nanogenerator toward self-powered 3D acceleration sensor," *Nano Energy,* vol. 50, pp. 632-638, 2018/08/01/ 2018, doi: https://doi.org/10.1016/j.nanoen.2018.05.068.

[174] E. J. Ko *et al.*, "Synthesis and characterization of nanofiber-type hydrophobic organic materials as electrodes for improved performance of PVDF-based piezoelectric nanogenerators," *Nano Energy,* vol. 58, pp. 11-22, 2019/04/01/ 2019, doi: https://doi.org/10.1016/j.nanoen.2019.01.022.

[175] H. Khan *et al.*, "Liquid metal-based synthesis of high performance monolayer SnS piezoelectric nanogenerators," *Nature Communications,* vol. 11, no. 1, p. 3449, 2020/07/10 2020, doi: 10.1038/s41467-020-17296-0.

[176] Z. Hanani *et al.*, "Lead-free nanocomposite piezoelectric nanogenerator film for biomechanical energy harvesting," *Nano Energy,* vol. 81, p. 105661, 2021/03/01/ 2021, doi: https://doi.org/10.1016/j.nanoen.2020.105661.

[177] D. Zhang *et al.*, "Flexible self-powered high-performance ammonia sensor based on Au-decorated MoSe2 nanoflowers driven by single layer MoS2-flake piezoelectric nanogenerator," *Nano Energy,* vol. 65, p. 103974, 2019/11/01/ 2019, doi: https://doi.org/10.1016/j.nanoen.2019.103974.

[178] L. Zhang *et al.*, "Enhanced performance of piezoelectric nanogenerator based

on aligned nanofibers and three-dimensional interdigital electrodes," *Nano Energy,* vol. 65, p. 103924, 2019/11/01/ 2019, doi: https://doi.org/10.1016/j.nanoen.2019.103924.

[179] J. Li *et al.*, "Enhanced piezoelectric output of the PVDF-TrFE/ZnO flexible piezoelectric nanogenerator by surface modification," *Applied Surface Science,* vol. 463, pp. 626-634, 2019/01/01/ 2019, doi: https://doi.org/10.1016/j.apsusc.2018.08.266.

[180] S. A. Han *et al.*, "Point-Defect-Passivated MoS2 Nanosheet-Based High Performance Piezoelectric Nanogenerator," *Advanced Materials,* vol. 30, no. 21, p. 1800342, 2018, doi: https://doi.org/10.1002/adma.201800342.

[181] S. Badatya *et al.*, "Transparent flexible graphene quantum dot-(PVDF-HFP) piezoelectric nanogenerator," *Materials Letters,* vol. 290, p. 129493, 2021/05/01/ 2021, doi: https://doi.org/10.1016/j.matlet.2021.129493.

[182] P. Li *et al.*, "A self-powered 2D-material sensor unit driven by a SnSe piezoelectric nanogenerator," *Journal of Materials Chemistry A,* 10.1039/D0TA10457D vol. 9, no. 8, pp. 4716-4723, 2021, doi: 10.1039/D0TA10457D.

[183] X. Wang *et al.*, "Bionic Single-Electrode Electronic Skin Unit Based on Piezoelectric Nanogenerator," *ACS Nano,* vol. 12, no. 8, pp. 8588-8596, 2018/08/28 2018, doi: 10.1021/acsnano.8b04244.

[184] J. Sun *et al.*, "Sustainable and Biodegradable Wood Sponge Piezoelectric Nanogenerator for Sensing and Energy Harvesting Applications," *ACS Nano,* vol. 14, no. 11, pp. 14665-14674, 2020/11/24 2020, doi: 10.1021/acsnano.0c05493.

[185] X. Yang *et al.*, "A flexible piezoelectric-triboelectric hybrid nanogenerator in one structure with dual doping enhancement effects," *Current Applied Physics,* vol. 32, pp. 50-58, 2021/12/01/ 2021, doi: https://doi.org/10.1016/j.cap.2021.09.003.

[186] A. N. Filippin *et al.*, "3D core-multishell piezoelectric nanogenerators," *Nano Energy,* vol. 58, pp. 476-483, 2019/04/01/ 2019, doi: https://doi.org/10.1016/j.nanoen.2019.01.047.

[187] J. Miao *et al.*, "Piezoelectric materials and their applications in the microfluidic drive technology," *IOP Conference Series: Materials Science and Engineering,* vol. 490, no. 2, p. 022042, 2019/04/01 2019, doi: 10.1088/1757-

899X/490/2/022042.

[188] Y. Su *et al.*, "Reduction of precious metal ions in aqueous solutions by contact-electro-catalysis," *Nature Communications*, vol. 15, no. 1, p. 4196, 2024/05/17 2024, doi: 10.1038/s41467-024-48407-w.

[189] S. Park *et al.*, "Energy harvesting efficiency of piezoelectric polymer film with graphene and metal electrodes," *Scientific Reports*, vol. 7, no. 1, p. 17290, 2017/12/11 2017, doi: 10.1038/s41598-017-17791-3.

[190] N. D. Kulkarni *et al.*, "Development of highly flexible PVDF-TiO2 nanocomposites for piezoelectric nanogenerator applications," *Materials Research Bulletin*, vol. 157, p. 112039, 2023/01/01/ 2023, doi: https://doi.org/10.1016/j.materresbull.2022.112039.

[191] Y. Li *et al.*, "Piezoelectric Nanogenerator Based on Electrospinning PVDF/Cellulose Acetate Composite Membranes for Energy Harvesting," *Materials*, vol. 15, no. 19, p. 7026, 2022. [Online]. Available: https://www.mdpi.com/1996-1944/15/19/7026.

[192] S. Liu *et al.*, "Transfer-Free PZT Thin Films for Flexible Nanogenerators Derived from a Single-Step Modified Sol–Gel Process on 2D Mica," *ACS Applied Materials & Interfaces*, vol. 12, no. 49, pp. 54991-54999, 2020/12/09 2020, doi: 10.1021/acsami.0c16973.

[193] W.-S. Jung *et al.*, "High Output Piezo/Triboelectric Hybrid Generator," *Scientific Reports*, vol. 5, no. 1, p. 9309, 2015/03/20 2015, doi: 10.1038/srep09309.

[194] B. S. Athira *et al.*, "High-Performance Flexible Piezoelectric Nanogenerator Based on Electrospun PVDF-BaTiO3 Nanofibers for Self-Powered Vibration Sensing Applications," *ACS Applied Materials & Interfaces*, vol. 14, no. 39, pp. 44239-44250, 2022/10/05 2022, doi: 10.1021/acsami.2c07911.

[195] N. Mufti *et al.*, "Enhanced piezoelectric nanogenerator performance with AZO/NiO heterojunction," *Materials Science for Energy Technologies*, vol. 6, pp. 81-88, 2023/01/01/ 2023, doi: https://doi.org/10.1016/j.mset.2022.11.009.

[196] L. Lu *et al.*, "Flexible PVDF based piezoelectric nanogenerators," *Nano Energy*, vol. 78, p. 105251, 2020/12/01/ 2020, doi: https://doi.org/10.1016/j.nanoen.2020.105251.

[197] H. Su *et al.*, "Enhanced energy harvesting ability of polydimethylsiloxane-BaTiO3-based flexible piezoelectric nanogenerator for tactile imitation

application," *Nano Energy,* vol. 83, p. 105809, 2021/05/01/ 2021, doi: https://doi.org/10.1016/j.nanoen.2021.105809.

[198] W. Deng *et al.*, "Piezoelectric nanogenerators for personalized healthcare," *Chemical Society Reviews,* 10.1039/D1CS00858G vol. 51, no. 9, pp. 3380-3435, 2022, doi: 10.1039/D1CS00858G.

[199] Y. Zhang *et al.*, "Self-powered pacemaker based on all-in-one flexible piezoelectric nanogenerator," *Nano Energy,* vol. 99, p. 107420, 2022/08/01/ 2022, doi: https://doi.org/10.1016/j.nanoen.2022.107420.

[200] J. Kim *et al.*, "Discovery of Cellulose as a Smart Material. Volume 39, Number 12, June 13, 2006, pp 4202−4206," *Macromolecules,* vol. 39, no. 16, pp. 5583-5583, 2006/08/01 2006, doi: 10.1021/ma0614489.

[201] S. Rezania *et al.*, "Review on Waste-to-Energy Approaches toward a Circular Economy in Developed and Developing Countries," *Processes,* vol. 11, no. 9, p. 2566doi: 10.3390/pr11092566.

[202] C. Senarathna *et al.*, "Paper Recycling for a Sustainable Future: Global Trends," *Journal of Research technology & Engineering,* vol. 3, pp. 169-186, 07/13 2023. [Online]. Available: https://www.jrte.org/2023/07/13/paper-recycling-for-a-sustainable-future-global-trends/.

[203] N. Vukovic *et al.*, "Waste-to-Energy Generation: Complex Efficiency Analysis of Modern Technologies," *Sustainability,* vol. 14, no. 21, p. 13814, 2022. [Online]. Available: https://www.mdpi.com/2071-1050/14/21/13814.

[204] D. Nurmalasari *et al.*, "Utilization of Waste Paper Through Recycling and Entrepreneurial Spirit Development," *International Journal of Service Science, Management, Engineering, and Technology,* vol. 1, no. 2, pp. 1-3, 04/29 2022. [Online]. Available: https://ejournalisse.com/index.php/isse/article/view/7.

[205] "United Nations Environment Programme and International Solid Waste Association, Global Waste Management Outlook 2024 - Beyond an age of waste: Turning Rubbish into a Resource," 2024. [Online]. Available: https://wedocs.unep.org/20.500.11822/44939.

[206] Y. A. Hajam *et al.*, "Environmental waste management strategies and vermi transformation for sustainable development," *Environmental Challenges,* vol. 13, p. 100747, 2023/12/01/ 2023, doi: https://doi.org/10.1016/j.envc.2023.100747.

[207] P. R. R. Vipul S. Agarkar, Dyanesh Sankulwar , Prof. Aamir Sayed, "Case Study

on Paper Recycling," *International Journal for Innovative Research in Science & Technology*|, vol. 2, no. 11, 2016.

[208] M. Agrawal *et al.*, "Waste Paper Collection for Recycling: Overview and their Reuse Potential," 07/10 2021.

[209] S. C. Patil *et al.*, "Current and emerging waste-to-energy technologies: A comparative study with multi-criteria decision analysis," *Smart Energy*, vol. 16, p. 100157, 2024/11/01/ 2024, doi: https://doi.org/10.1016/j.segy.2024.100157.

[210] P. Lisbona *et al.*, "Waste to energy: Trends and perspectives," *Chemical Engineering Journal Advances*, vol. 14, p. 100494, 2023/05/15/ 2023, doi: https://doi.org/10.1016/j.ceja.2023.100494.

[211] Y. H. Lee *et al.*, "Significant enhancement of the output voltage of piezoelectric/triboelectric hybrid nanogenerators based on MAPbBr3 single crystals embedded into a porous PVDF matrix," *Nano Energy*, vol. 102, p. 107676, 2022/11/01/ 2022, doi: https://doi.org/10.1016/j.nanoen.2022.107676.

[212] J.-H. Zhang *et al.*, "Coupling Enhanced Performance of Triboelectric–Piezoelectric Hybrid Nanogenerator Based on Nanoporous Film of Poly(vinylidene fluoride)/BaTiO3 Composite Electrospun Fibers," *ACS Materials Letters*, vol. 4, no. 5, pp. 847-852, 2022/05/02 2022, doi: 10.1021/acsmaterialslett.1c00819.

[213] H. M. Mousa *et al.*, "A hybrid triboelectric and piezoelectric nanogenerator with α-Al2O3 NPs/Doku and PVDF/SWCNTs nanofibers," *Colloids and Surfaces A: Physicochemical and Engineering Aspects*, vol. 656, p. 130403, 2023/01/05/ 2023, doi: https://doi.org/10.1016/j.colsurfa.2022.130403.

[214] A. Nawaz *et al.*, "ZnFe2O4 nanocomposite films for electromagnetic-triboelectric-piezoelectric effect-based hybrid multimodal nanogenerator," *Chemical Engineering Journal*, vol. 454, p. 140262, 2023/02/15/ 2023, doi: https://doi.org/10.1016/j.cej.2022.140262.

[215] V. Singh *et al.*, "MoS2-PVDF/PDMS based flexible hybrid piezo-triboelectric nanogenerator for harvesting mechanical energy," *Journal of Alloys and Compounds*, vol. 941, p. 168850, 2023/04/25/ 2023, doi: https://doi.org/10.1016/j.jallcom.2023.168850.

[216] B. Toroń *et al.*, "A new hybrid piezo/triboelectric SbSeI nanogenerator," *Energy*, vol. 238, p. 122048, 2022/01/01/ 2022, doi: https://doi.org/10.1016/j.energy.2021.122048.

[217] K.-J. I. Egbe *et al.*, "Piezoelectric-triboelectric-electromagnetic Hybrid Rotational Energy Harvesters (H-REH)," *International Journal of Mechanical Sciences,* vol. 235, p. 107722, 2022/12/01/ 2022, doi: https://doi.org/10.1016/j.ijmecsci.2022.107722.

[218] J. Wang *et al.*, "A hybrid sensor for motor tics recognition based on piezoelectric and triboelectric design and fabrication," *Sensors and Actuators A: Physical,* vol. 342, p. 113622, 2022/08/01/ 2022, doi: https://doi.org/10.1016/j.sna.2022.113622.

[219] X. Kang *et al.*, "Flexible wearable hybrid nanogenerator to harvest solar energy and human kinetic energy," *Nano Energy,* vol. 103, p. 107808, 2022/12/01/ 2022, doi: https://doi.org/10.1016/j.nanoen.2022.107808.

[220] R. Ahmed *et al.*, "Development of a Tree-Shaped Hybrid Nanogenerator Using Flexible Sheets of Photovoltaic and Piezoelectric Films," *Energies,* vol. 12, no. 2, p. 229, 2019. [Online]. Available: https://www.mdpi.com/1996-1073/12/2/229.

[221] C. Song *et al.*, "A self-supported structure hybrid triboelectric/piezoelectric nanogenerator for bio-mechanical energy harvesting and pressure sensing," *Microelectronic Engineering,* vol. 256, p. 111723, 2022/02/15/ 2022, doi: https://doi.org/10.1016/j.mee.2022.111723.

[222] X. García-Casas *et al.*, "Plasma engineering of microstructured piezo – Triboelectric hybrid nanogenerators for wide bandwidth vibration energy harvesting," *Nano Energy,* vol. 91, p. 106673, 2022/01/01/ 2022, doi: https://doi.org/10.1016/j.nanoen.2021.106673.

[223] S. Banerjee *et al.*, "A lead-free flexible piezoelectric-triboelectric hybrid nanogenerator composed of uniquely designed PVDF/KNN-ZS nanofibrous web," *Energy,* vol. 244, p. 123102, 2022/04/01/ 2022, doi: https://doi.org/10.1016/j.energy.2022.123102.

[224] Z. Yu *et al.*, "Integrated piezo-tribo hybrid acoustic-driven nanogenerator based on porous MWCNTs/PVDF-TrFE aerogel bulk with embedded PDMS tympanum structure for broadband sound energy harvesting," *Nano Energy,* vol. 97, p. 107205, 2022/06/15/ 2022, doi: https://doi.org/10.1016/j.nanoen.2022.107205.

[225] J. Jo *et al.*, "Hybrid nanogenerator for self-powered object recognition," *Journal of Science: Advanced Materials and Devices,* vol. 9, no. 2, p. 100693,

2024/06/01/ 2024, doi: https://doi.org/10.1016/j.jsamd.2024.100693.

[226] Z. Gao *et al.*, "Hybrid electromagnetic and moisture energy harvesting enabled by ionic diode films," *Nature Communications,* vol. 16, no. 1, p. 312, 2025/01/02 2025, doi: 10.1038/s41467-024-55030-2.

[227] G. Ren *et al.*, "All-Biobased Hydrovoltaic-Photovoltaic Electricity Generators for All-Weather Energy Harvesting," *Research,* vol. 2022, 2022, doi: doi:10.34133/2022/9873203.

[228] L. Yang *et al.*, "A Hybrid Artificial Photocatalysis System Splits Atmospheric Water for Simultaneous Dehumidification and Power Generation," *Advanced Materials,* vol. 31, no. 51, p. 1902963, 2019, doi: https://doi.org/10.1002/adma.201902963.

[229] L. Yang *et al.*, "Energy Harvesting from Atmospheric Humidity by a Hydrogel-Integrated Ferroelectric-Semiconductor System," *Joule,* vol. 4, no. 1, pp. 176-188, 2020, doi: 10.1016/j.joule.2019.10.008.

[230] D. K. Nandakumar *et al.*, "A solar cell that breathes in moisture for energy generation," *Nano Energy,* vol. 68, p. 104263, 2020/02/01/ 2020, doi: https://doi.org/10.1016/j.nanoen.2019.104263.

[231] S. Nasir *et al.*, "Potential valorization of by-product materials from oil palm: A review of alternative and sustainable carbon sources for carbon-based nanomaterials synthesis," *BioResources*, 2019.

[232] M. A. J. Kouhbanani *et al.*, "The inhibitory role of synthesized Nickel oxide nanoparticles against Hep-G2, MCF-7, and HT-29 cell lines: the inhibitory role of NiO NPs against Hep-G2, MCF-7, and HT-29 cell lines," *Green Chemistry Letters and Reviews,* vol. 14, no. 3, pp. 444-454, 2021 July 3 2021, doi: https://doi.org/10.1080/17518253.2021.1939435.

[233] P. Y. Kang Liu, Song Li, Jia Li, Tianpeng Ding, Guobin Xue, Qian Chen, Guang Feng, Jun Zhou, "Induced Potential in Porous Carbon Films through Water Vapor Absorption," *Angew Chem Int Ed Engl,* vol. 55, no. 28, pp. 8003-7, 2016, doi: 10.1002/anie.201602708.

[234] V. Chopra *et al.*, "18 - Thermoluminescent study of borates for dosimetric applications," in *Phosphor Handbook*, V. B. Pawade *et al.* Eds.: Woodhead Publishing, 2023, pp. 393-415.

[235] N. Kumar *et al.*, "1 - Metal oxide–assisted heterostructures: At a glance," in *Metal Oxide-Based Heterostructures*, N. Kumar *et al.* Eds.: Elsevier, 2023, pp.

3-42.

[236] S. P. Kumar *et al.*, "3 - Characterization of flexible ceramics," in *Advanced Flexible Ceramics*, R. K. Gupta *et al.* Eds.: Elsevier, 2023, pp. 25-43.

[237] D. Titus *et al.*, "Chapter 12 - Nanoparticle characterization techniques," in *Green Synthesis, Characterization and Applications of Nanoparticles*, A. K. Shukla *et al.* Eds.: Elsevier, 2019, pp. 303-319.

[238] S. Agrawal, "6 - Spectroscopy techniques for rare-earth-activated phosphors," in *Rare-Earth-Activated Phosphors*, V. Dubey *et al.* Eds.: Elsevier, 2022, pp. 147-175.

[239] D. Kalita *et al.*, "3 - Fluoropolymer nanocomposites: introduction, fundamental properties, and high-performance applications," in *Advanced Fluoropolymer Nanocomposites*, K. Deshmukh *et al.* Eds.: Woodhead Publishing, 2023, pp. 79-120.

[240] N. Li *et al.*, "Guidelines for Raman spectroscopy and imaging techniques in food safety analysis," *Food Safety and Health*, vol. 2, no. 2, pp. 221-237, 2024, doi: https://doi.org/10.1002/fsh3.12040.

[241] L. Wu *et al.*, "A review on current progress of Raman-based techniques in food safety: From normal Raman spectroscopy to SESORS," *Food Research International*, vol. 169, p. 112944, 2023/07/01/ 2023, doi: https://doi.org/10.1016/j.foodres.2023.112944.

[242] Z. Hajizadeh *et al.*, "3 - Identification and analytical methods," in *Heterogeneous Micro and Nanoscale Composites for the Catalysis of Organic Reactions*, A. Maleki Ed.: Elsevier, 2022, pp. 33-51.

[243] Z. P. Tshabalala *et al.*, "Chapter 5 - Tools and techniques for characterization and evaluation of nanosensors," in *Nanosensors for Smart Cities*, B. Han *et al.* Eds.: Elsevier, 2020, pp. 85-110.

[244] V. Pradeep Kumar *et al.*, "Band-gap dependence of two-photon absorption mechanism in NiO nanoparticles synthesized at different calcination temperatures," *Optical Materials*, vol. 142, p. 114063, 2023/08/01/ 2023, doi: https://doi.org/10.1016/j.optmat.2023.114063.

[245] T. W. Napporn *et al.*, "Chapter 8 - Characterization Methods for Components and Materials," in *Fuel Cells and Hydrogen*, V. Hacker *et al.* Eds.: Elsevier, 2018, pp. 155-173.

[246] K. Mattsson *et al.*, "Chapter 13 - Nanoplastics in aquatic environments—

Sources, sampling techniques, and identification methods," in *Microplastic Contamination in Aquatic Environments (Second Edition)*, E. Y. Zeng Ed.: Elsevier, 2024, pp. 381-397.

[247] Y. Gong *et al.*, "Application of fourier transform infrared (FTIR) spectroscopy in sample preparation: Material characterization and mechanism investigation," *Advances in Sample Preparation,* vol. 11, p. 100122, 2024/08/01/ 2024, doi: https://doi.org/10.1016/j.sampre.2024.100122.

[248] A. Kumari *et al.*, "Application of Fourier Transform-Infrared Spectroscopy as a Tool for Early Cancer Detection," *American Journal of Biomedical Sciences,* pp. 139-148, 07/01 2018, doi: 10.5099/aj180300139.

[249] M. M. Baig *et al.*, "The complementary advanced characterization and electrochemical techniques for electrode materials for supercapacitors," *Journal of Energy Storage,* vol. 44, p. 103370, 2021/12/01/ 2021, doi: https://doi.org/10.1016/j.est.2021.103370.

[250] T. Virtanen *et al.*, "Analysis of membrane fouling by Brunauer-Emmett-Teller nitrogen adsorption/desorption technique," *Scientific Reports,* vol. 10, no. 1, p. 3427, 2020/02/25 2020, doi: 10.1038/s41598-020-59994-1.

[251] S.-Y. Peng *et al.*, "Hydrothermal synthesis of hydroxyapatite nanocrystals from calcium-rich limestone sludge waste: Preparation, characterization, and application for Pb2+ adsorption in aqueous solution," *Inorganic Chemistry Communications,* vol. 160, p. 111943, 2024/02/01/ 2024, doi: https://doi.org/10.1016/j.inoche.2023.111943.

[252] D. S. Macedo *et al.*, "More Accurate Measurement of Return Peak Current in Cyclic Voltammetry Using Diffusional Baseline Fitting," *Analytical Chemistry,* vol. 96, no. 4, pp. 1530-1537, 2024/01/30 2024, doi: 10.1021/acs.analchem.3c04181.

[253] H. Yamada *et al.*, "Cyclic Voltammetry Part 1: Fundamentals," *Electrochemistry,* vol. 90, no. 10, pp. 102005-102005, 2022, doi: 10.5796/electrochemistry.22-66082.

[254] K. Wijeratne, "Conducting Polymer Electrodes for Thermogalvanic Cells," 2018.

[255] M. G. B. Patel *et al.*, "Investigate the Origin of the Hall Effect," *Journal of Nanoscience, Nanoengineering &*

Applications, vol. 11, pp. 8-16, 07/26 2021, doi: 10.37591/JoNSNEA.

[256] D. Collomb *et al.*, "Frontiers of graphene-based Hall-effect sensors," *Journal of Physics: Condensed Matter,* vol. 33, no. 24, p. 243002, 2021/05/18 2021, doi: 10.1088/1361-648X/abf7e2.

[257] B. I. Oladapo *et al.*, "Enhancing tissue regeneration with self-healing elastic piezoelectricity for sustainable implants," *Nano Energy,* vol. 120, p. 109092, 2024/02/01/ 2024, doi: https://doi.org/10.1016/j.nanoen.2023.109092.

[258] K. L. Montero *et al.*, "Effect of Electrode Structure on the Performance of Fully Printed Piezoelectric Energy Harvesters," *IEEE Journal on Flexible Electronics,* vol. 1, no. 1, pp. 24-31, 2022, doi: 10.1109/JFLEX.2022.3156050.

[259] Z. Zhou *et al.*, "Lead-free, high-current output piezoelectric nanogenerators using three-dimensional interdigitated electrodes," *Chemical Engineering Journal,* vol. 442, p. 136241, 2022/08/15/ 2022, doi: https://doi.org/10.1016/j.cej.2022.136241.

[260] M. J. M. Pelgrom, "Electrical Theory," in *Analog-to-Digital Conversion,* M. J. M. Pelgrom Ed. Cham: Springer International Publishing, 2022, pp. 49-110.

[261] M. Gasulla *et al.*, "Power Gain from Energy Harvesting Sources at High MPPT Sampling Rates," *Sensors,* vol. 23, no. 9, p. 4388, 2023. [Online]. Available: https://www.mdpi.com/1424-8220/23/9/4388.

[262] Y. H. P. Ha Yong Lee, and Kyung Hyun Ko, "Correlation between Surface Morphology and Hydrophilic," *Langmuir,* vol. 16, pp. 7289-7293, 2000, doi: 10.1021/la9915567.

[263] S. F. Jin Tan, Zhuhua Zhang, Jun Yin, Luxian Li, Xiang Wang, Wanlin Guo, "Self-sustained electricity generator driven by the compatible integration of ambient moisture adsorption and evaporation," *Nat Commun,* vol. 13, no. 1, p. 3643, Jun 25 2022, doi: 10.1038/s41467-022-31221-7.

[264] J. Xu *et al.*, "Sustainable moisture energy," *Nature Reviews Materials,* 2024, doi: 10.1038/s41578-023-00643-0.

[265] S. Sagadevan *et al.*, "Eco-friendly green approach of nickel oxide nanoparticles for biomedical applications," *Open Chemistry,* vol. 21, no. 1, 2023, doi: 10.1515/chem-2023-0141.

[266] H. Yan *et al.*, "A review of humidity gradient-based power generator: Devices, materials and mechanisms," *Nano Energy,* vol. 101, 2022, doi: 10.1016/j.nanoen.2022.107591.

[267] M. Yang *et al.*, "Acetone sensors with high stability to humidity changes based

on Ru-doped NiO flower-like microspheres," *Sensors and Actuators B: Chemical,* vol. 313, p. 127965, 2020 Jun 15 2020, doi: https://doi.org/10.1016/j.snb.2020.127965.

[268] C. Zhu *et al.*, "Graphene oxide humidity sensor with laser-induced graphene porous electrodes," *Sensors and Actuators B: Chemical,* vol. 325, p. 128790, 2020 Dec 15 2020, doi: https://doi.org/10.1016/j.snb.2020.128790.

[269] W. R. W. Ahmad *et al.*, "The Effect of Ultrasonic Irradiation to Hematite Nanorod Arrays Properties for Humidity Sensor Applications," *19th IEEE International Colloquium on Signal Processing & Its Applications (CSPA),* pp. 144-149, 2023 March 3 2023, doi: https://doi.org/10.1109/CSPA57446.2023.10087704.

[270] M. U. Khan *et al.*, "All printed full range humidity sensor based on Fe2O3," *Sensors and Actuators A: Physical,* vol. 311, p. 112072, 2020 Aug 15 2020, doi: https://doi.org/10.1016/j.sna.2020.112072.

[271] F. Deng *et al.*, "Hygroscopic Porous Polymer for Sorption-Based Atmospheric Water Harvesting," *Advanced Science,* vol. 9, no. 33, p. 2204724, 2022 Oct 1 2022, doi: https://doi.org/10.1002/advs.202204724.

[272] S.-C. Shi *et al.*, "Hydrophobicity and Macroscale Tribology Behavior of Stearic Acid/Hydroxypropyl Methylcellulose Dual-Layer Composite," *Materials,* vol. 14, no. 24, p. 7707, 2021. [Online]. Available: https://www.mdpi.com/1996-1944/14/24/7707.

[273] S. D. Khairnar *et al.*, "Facile synthesis of nickel oxide nanoparticles for the degradation of Methylene blue and Rhodamine B dye: a comparative study," *Journal of Taibah University for Science,* vol. 13, no. 1, pp. 1108-1118, 2019, doi: 10.1080/16583655.2019.1686248.

[274] M. A. Arfaoui *et al.*, "Preparation of a hydrophobic recycled jute-based nonwoven using a titanium dioxide/stearic acid coating," *The Journal of The Textile Institute,* vol. 110, no. 1, pp. 16-25, 2019/01/02 2019, doi: 10.1080/00405000.2018.1455313.

[275] T. Batakliev *et al.*, "Effects of Graphene Nanoplatelets and Multiwall Carbon Nanotubes on the Structure and Mechanical Properties of Poly(lactic acid) Composites: A Comparative Study," *Applied Sciences,* vol. 9, no. 3, p. 469, 2019. [Online]. Available: https://www.mdpi.com/2076-3417/9/3/469.

[276] A. Riveiro *et al.*, "Laser Surface Texturing of Polymers for Biomedical

Applications," (in English), *Frontiers in Physics,* Review vol. 6, 2018-February-27 2018, doi: 10.3389/fphy.2018.00016.

[277] R. Bayati *et al.*, "Modification of properties of yttria stabilized zirconia epitaxial thin films by excimer laser annealing," (in eng), *ACS Appl Mater Interfaces,* vol. 6, no. 24, pp. 22316-25, Dec 24 2014, doi: 10.1021/am506298y.

[278] H. E. Rizk *et al.*, "Preparation and Characterization of Pyramids/Particles NiO/SnO2 Composite for Sorption and Separation of Molybdenum and Zirconium Ions from Some Synthetic Fission Products," *Journal of Inorganic and Organometallic Polymers and Materials,* 2024/09/25 2024, doi: 10.1007/s10904-024-03370-3.

[279] G. Escobar Cano *et al.*, "Sol‑Gel-Process-Based Molten-Flux Synthesis of Plate-like La2NiO4+ δ Particles," *Crystals*, vol. 12, no. 10, 2022, doi: 10.3390/cryst12101346.

[280] M. Wardani *et al.*, "Synthesis of NiO nanoparticles via green route using Ageratum conyzoides L. leaf extract and their catalytic activity," *IOP Conference Series: Materials Science and Engineering,* vol. 509, no. 1, p. 012077, 2019/04/01 2019, doi: 10.1088/1757-899X/509/1/012077.

[281] U. T. Nakate *et al.*, "Ultra thin NiO nanosheets for high performance hydrogen gas sensor device," *Applied Surface Science*, vol. 506, p. 144971, 2020/03/15/ 2020, doi: https://doi.org/10.1016/j.apsusc.2019.144971.

[282] M. Zubair *et al.*, "The effects of 5 MeV carbon ion irradiation on micro-fine grain graphite," *Radiation Physics and Chemistry,* vol. 166, p. 108512, 2020/01/01/ 2020, doi: https://doi.org/10.1016/j.radphyschem.2019.108512.

[283] Y. Wang *et al.*, "Mechanochemical conversion of graphite to highly Cross-linked alkynyl carbon material as excellent mercury (II) sorbent," *Chemical Engineering Journal,* vol. 415, p. 129009, 2021/07/01/ 2021, doi: https://doi.org/10.1016/j.cej.2021.129009.

[284] A. Kiran *et al.*, "Green synthesis of NiO and NiO@graphene oxide nanomaterials using Elettaria cardamomum leaves: Structural and electrochemical studies," *Heliyon,* vol. 10, no. 20, 2024, doi: 10.1016/j.heliyon.2024.e38613.

[285] P. Van Tuan *et al.*, "In-situ hydrothermal fabrication and photocatalytic behavior of ZnO/reduced graphene oxide nanocomposites with varying

graphene oxide concentrations," *Materials Science in Semiconductor Processing*, vol. 115, p. 105114, 2020/08/15/ 2020, doi: https://doi.org/10.1016/j.mssp.2020.105114.

[286] L. Wannasen *et al.*, "Enhancing electrochemical properties of bacterial cellulose-derived carbon nanofibers through physical CO2 activation," *Materials Science for Energy Technologies*, vol. 8, pp. 13-23, 2025/01/01/ 2025, doi: https://doi.org/10.1016/j.mset.2024.07.005.

[287] M. M. Rahman *et al.*, "Production of cellulose nanocrystals from the waste banana (M. oranta) tree rachis fiber as a reinforcement to fabricate useful bionanocomposite," *Carbohydrate Polymer Technologies and Applications*, vol. 8, p. 100607, 2024/12/01/ 2024, doi: https://doi.org/10.1016/j.carpta.2024.100607.

[288] H. Koyakutty *et al.*, "Defect rich Ni/NiO-graphene heterostructures with oxygen bridges for enhanced electrocatalytic glucose oxidation towards selective sensing," *Materials Chemistry and Physics*, vol. 309, p. 128330, 2023/11/01/ 2023, doi: https://doi.org/10.1016/j.matchemphys.2023.128330.

[289] R. Verma *et al.*, "Reduced graphene Oxide/NiO based nano-composites for the efficient removal of alizarin dye, indigo dye and reduction of nitro aromatic compounds," *Heliyon*, vol. 9, no. 6, 2023, doi: 10.1016/j.heliyon.2023.e17162.

[290] B. Pricilla *et al.*, "GO/NiO nanocomposite: Chemosensor for L-Leucine and a potential antibacterial agent," *Materials Today: Proceedings*, vol. 47, 12/30 2020, doi: 10.1016/j.matpr.2020.11.466.

[291] A. Sankar *et al.*, "NiO nanoparticles/graphene nanocomposite as high-performance pseudocapacitor electrodes: Design and implementation," *Diamond and Related Materials*, vol. 122, p. 108804, 2022/02/01/ 2022, doi: https://doi.org/10.1016/j.diamond.2021.108804.

[292] Komal *et al.*, "Amelioration of adsorptive efficacy by synergistic assemblage of functionalized graphene oxide with esterified cellulose nanofibers for mitigation of pharmaceutical waste," *Journal of Hazardous Materials*, vol. 424, p. 127541, 2022/02/15/ 2022, doi: https://doi.org/10.1016/j.jhazmat.2021.127541.

[293] S. Y. Misyura *et al.*, "The effect of textured surface on graphene wettability and droplet evaporation," *Journal of Materials Science*, vol. 57, no. 3, pp. 1850-1862, 2022/01/01 2022, doi: 10.1007/s10853-021-06853-7.

[294] R. Moradi *et al.*, "Preparation and Characterization of Polyvinylidene

Fluoride/Graphene Superhydrophobic Fibrous Films," *Polymers,* vol. 7, no. 8, pp. 1444-1463, 2015. [Online]. Available: https://www.mdpi.com/2073-4360/7/8/1444.

[295] R. Verma *et al.*, "Reduced graphene Oxide/NiO based nano-composites for the efficient removal of alizarin dye, indigo dye and reduction of nitro aromatic compounds," *Heliyon,* vol. 9, no. 6, p. e17162, 2023/06/01/ 2023, doi: https://doi.org/10.1016/j.heliyon.2023.e17162.

[296] X. Gao *et al.*, "Interfacial structure and strengthening mechanisms of NiO-coated graphene reinforced aluminum matrix composites," *Journal of Materials Research and Technology,* 2025/01/15/ 2025, doi: https://doi.org/10.1016/j.jmrt.2024.12.102.

[297] S. Bachankar *et al.*, "Enhanced Supercapacitive Charge Storage in a Nickel Oxide-Graphene Oxide Composite: Synergistic Effect," *Korean Journal of Materials Research,* vol. 34, no. 12, pp. 609-619, 12 2024, doi: 10.3740/MRSK.2024.34.12.609.

[298] F. Sultanov *et al.*, "Enhancing lithium-sulfur battery performance with biomass-derived graphene-like porous carbon and NiO nanoparticles composites," *Journal of Power Sources,* vol. 593, p. 233959, 2024/02/15/ 2024, doi: https://doi.org/10.1016/j.jpowsour.2023.233959.

[299] P. C. Maity *et al.*, "A two-dimensional hybrid of NiO nanowalls and reduced graphene oxide for superior field emission," *Diamond and Related Materials,* vol. 139, p. 110339, 2023/11/01/ 2023, doi: https://doi.org/10.1016/j.diamond.2023.110339.

[300] W. Huang *et al.*, "3D NiO hollow sphere/reduced graphene oxide composite for high-performance glucose biosensor," *Scientific Reports,* vol. 7, no. 1, p. 5220, 2017/07/12 2017, doi: 10.1038/s41598-017-05528-1.

[301] G. Manibalan *et al.*, "Synthesis of heterogeneous NiO nanoparticles for high-performance electrochemical supercapacitor application," *Journal of Materials Science: Materials in Electronics,* vol. 32, no. 5, pp. 5945-5954, 2021/03/01 2021, doi: 10.1007/s10854-021-05315-9.

[302] M. K. Singh *et al.*, "Effective assembling of nickel oxide-reduced graphene oxide heterostructures for ultrahigh capacity supercapattery," *Journal of Power Sources,* vol. 595, p. 234060, 2024 March 1 2024, doi: https://doi.org/10.1016/j.jpowsour.2024.234060.

[303] R. Wu *et al.*, "Preparation and electrochemical properties of carboxylated graphene-supported NiO nanosheets for supercapacitors," *Journal of Electroanalytical Chemistry,* vol. 952, p. 117986, 2024/01/01/ 2024, doi: https://doi.org/10.1016/j.jelechem.2023.117986.

[304] A. P. Naik *et al.*, "Facile synthesis of fibrous, mesoporous Ni1 − xO nanosponge supported on Ni foam for enhanced pseudocapacitor applications," *Journal of Materials Science,* vol. 55, no. 26, pp. 12232-12248, 2020/09/01 2020, doi: 10.1007/s10853-020-04884-0.

[305] Ş. Taşdemir *et al.*, "Surface Area of Graphene Governs Its Neurotoxicity," *ACS Biomaterials Science & Engineering,* vol. 9, no. 6, pp. 3297-3305, 2023/06/12 2023, doi: 10.1021/acsbiomaterials.3c00104.

[306] N. A. Elessawy *et al.*, "Development and evaluation of cost-effective and green Bi-functional nickel oxide decorated graphene electrocatalysts for alkaline fuel cells," *Results in Engineering,* vol. 17, p. 100871, 2023/03/01/ 2023, doi: https://doi.org/10.1016/j.rineng.2022.100871.

[307] P. Tippo *et al.*, "Investigation of NiO film by sparking method under a magnetic field and NiO/ZnO heterojunction," *Materials Research Express,* vol. 7, no. 5, p. 056403, 2020/05/11 2020, doi: 10.1088/2053-1591/ab8df6.

[308] X.-Y. Zhang *et al.*, "Modulation of the conductive behavior of NiO thin film deposited by HiPIMS through varying the O2 flow ratio," *Ceramics International,* vol. 48, no. 23, Part A, pp. 34668-34677, 2022/12/01/ 2022, doi: https://doi.org/10.1016/j.ceramint.2022.08.054.

[309] T. Rajyalakshmi *et al.*, "Synthesis, characterization and Hall-effect studies of highly conductive polyaniline/graphene nanocomposites," *SN Applied Sciences,* vol. 2, no. 4, p. 530, 2020/03/02 2020, doi: 10.1007/s42452-020-2349-4.

[310] N. Shah *et al.*, "Highly stable integration of graphene Hall sensors on a microfluidic platform for magnetic sensing in whole blood," *Microsystems & Nanoengineering,* vol. 9, no. 1, p. 71, 2023/05/31 2023, doi: 10.1038/s41378-023-00530-2.

[311] T. Mahmoudi *et al.*, "Highly stable perovskite solar cells based on perovskite/NiO-graphene composites and NiO interface with 25.9 mA/cm2 photocurrent density and 20.8% efficiency," *Nano Energy,* vol. 79, p. 105452, 2021/01/01/ 2021, doi: https://doi.org/10.1016/j.nanoen.2020.105452.

[312] E. S. Agudosi *et al.*, "Fabrication of 3D binder-free graphene NiO electrode for

highly stable supercapattery," *Scientific Reports,* vol. 10, no. 1, p. 11214, 2020/07/08 2020, doi: 10.1038/s41598-020-68067-2.

[313] Y. Liu *et al.*, "Nickel Oxide/Graphene Composites: Synthesis and Applications," *Chemistry – A European Journal,* vol. 25, no. 9, pp. 2141-2160, 2019, doi: https://doi.org/10.1002/chem.201803982.

[314] Y. Wang *et al.*, "Enhanced electrical and mechanical properties of graphene/copper composite through reduced graphene oxide-assisted coating," *Journal of Materials Research and Technology,* vol. 33, pp. 8121-8131, 2024/11/01/ 2024, doi: https://doi.org/10.1016/j.jmrt.2024.11.162.

[315] Ö. Güler *et al.*, "A short review on mechanical properties of graphene reinforced metal matrix composites," *Journal of Materials Research and Technology,* vol. 9, no. 3, pp. 6808-6833, 2020/05/01/ 2020, doi: https://doi.org/10.1016/j.jmrt.2020.01.077.

[316] D. Shen *et al.*, "Self-Powered Wearable Electronics Based on Moisture Enabled Electricity Generation," *Advanced Materials,* vol. 30, no. 18, p. 1705925, 2018/05/01 2018, doi: https://doi.org/10.1002/adma.201705925.

[317] D. Tripathi *et al.*, "Highly Sensitive Humidity Sensor Based on Freestanding Graphene Oxide Sheets for Respiration and Moisture Detection," *Journal of Electronic Materials,* vol. 52, no. 4, pp. 2396-2408, 2023/04/01 2023, doi: 10.1007/s11664-022-10186-9.

[318] Afsana *et al.*, "Low-Cost Flexible Graphene Oxide Humidity Sensor Fabricated Using Inkjet Printing and Aerosol Deposition," *Journal of The Electrochemical Society,* vol. 171, no. 7, p. 077513, 2024/07/19 2024, doi: 10.1149/1945-7111/ad6038.

[319] S. I. Jung *et al.*, "Graphene oxide decorated multi-frequency surface acoustic wave humidity sensor for hygienic applications," *Scientific Reports,* vol. 13, no. 1, p. 6838, 2023/04/26 2023, doi: 10.1038/s41598-023-34099-7.

[320] E. Ouda *et al.*, "Flexible humidity sensor based on light-scribed graphene oxide," *Journal of Materials Science: Materials in Electronics,* vol. 33, no. 23, pp. 18241-18251, 2022/08/01 2022, doi: 10.1007/s10854-022-08681-0.

[321] H. Zhao *et al.*, "Effect of oxygen functional groups on competitive adsorption of benzene and water on carbon materials: Density functional theory study," *Science of The Total Environment,* vol. 863, p. 160772, 2023/03/10/ 2023, doi: https://doi.org/10.1016/j.scitotenv.2022.160772.

[322] S. Patil *et al.*, "Characterization of NiO–Al 2 O 3 composite and its conductivity in biogas for solid oxide fuel cell," *Materials Science-Poland,* vol. 34, 05/15 2016, doi: 10.1515/msp-2016-0045.

[323] C. A. Thennakoon *et al.*, "Factors Affecting the Hydrophobic Property of Stearic Acid Self-Assembled on the TiO2 Substrate," *ACS Omega,* vol. 7, no. 51, pp. 48184-48191, 2022/12/27 2022, doi: 10.1021/acsomega.2c06217.

[324] S. Ishak *et al.*, "Microencapsulation of stearic acid with SiO2 shell as phase change material for potential energy storage," *Scientific Reports,* vol. 10, no. 1, p. 15023, 2020/09/14 2020, doi: 10.1038/s41598-020-71940-9.

[325] Y. Chao *et al.*, "Effect of Organic Modification Temperature on the Microstructure of Nanoscale Titania," *Journal of Inorganic Materials,* vol. 24, no. 3, pp. 438-442, 2009, doi: 10.3724/sp.j.1077.2009.00438.

[326] S. Ye *et al.*, "The effect of sonication treatment of graphene oxide on the mechanical properties of the assembled films," *RSC Advances,* 10.1039/C6RA03996K vol. 6, no. 46, pp. 39681-39687, 2016, doi: 10.1039/C6RA03996K.

[327] A. Kiran *et al.*, "Green synthesis of NiO and NiO@graphene oxide nanomaterials using Elettaria cardamomum leaves: Structural and electrochemical studies," *Heliyon,* vol. 10, no. 20, p. e38613, 2024 Oct 30 2024, doi: https://doi.org/10.1016/j.heliyon.2024.e38613.

[328] Z. S. Hoda Sharouf, "Synthesizing and Using Iron Oxide Nanoparticles as Nanocomposite in Cotton Fabrics Nanofinishing," *Baghdad Science Journal,* vol. 21, no. 1, p. 0072, 2024 Jan 1 2024, doi: https://doi.org/10.21123/bsj.2023.7743.

[329] P. G. Struchalin *et al.*, "Solar steam generation enabled by iron oxide nanoparticles: Prototype experiments and theoretical model," *International Journal of Heat and Mass Transfer,* vol. 158, p. 119987, 2020 Sept 1 2020, doi: https://doi.org/10.1016/j.ijheatmasstransfer.2020.119987.

[330] F. Mohamed *et al.*, "Synthesis and characterization of biogenic iron oxides of different nanomorphologies from pomegranate peels for efficient solar hydrogen production," *Journal of Materials Research and Technology,* vol. 9, no. 3, pp. 4255-4271, 2020 May 1 2020, doi: https://doi.org/10.1016/j.jmrt.2020.02.052.

[331] Q. Wu *et al.*, "Fe3O4 anodes for lithium batteries: Production techniques and

general applications," *Comptes Rendus Chimie,* vol. 22, no. 1, pp. 96-102, 2019 Jan 1 2019, doi: https://doi.org/10.1016/j.crci.2018.09.016.

[332] W. Zhu *et al.*, "Improved performance in lithium ion battery of CNT-Fe3O4@graphene induced by three-dimensional structured construction," *Colloids and Surfaces A: Physicochemical and Engineering Aspects,* vol. 612, p. 126014, 2021 March 5 2021, doi: https://doi.org/10.1016/j.colsurfa.2020.126014.

[333] T. Feng *et al.*, "Engineering iron-rich nanomaterials for supercapacitors," *Chemical Engineering Journal,* vol. 473, p. 145045, 2023 Oct 1 2023, doi: https://doi.org/10.1016/j.cej.2023.145045.

[334] T. Kim *et al.*, "Iron oxide supercapacitor of high volumetric energy and power density using binder-free supersonic spraying and self-healing rGO," *Ceramics International,* vol. 48, no. 10, pp. 13684-13694, 2022 May 15 2022, doi: https://doi.org/10.1016/j.ceramint.2022.01.250.

[335] K. A. S. Ayat Monther Alqudsi, "Effect of Graphene and Fe3O4 on the Protection Efficiency of Polyeugenol Conducted Coating for Stainless Steel 316L in NaCl solution," *Baghdad Science Journal,* vol. 21, no. 11, pp. 3428-3437, 2024 Nov 1 2024, doi: https://doi.org/10.21123/bsj.2024.8876.

[336] H. Yan *et al.*, "Unlocking the potential of hydrogel-electrode electrical double layer for high-performance moisture-enabled electric generators," *Device,* vol. 3, no. 2, p. 100568, 2025/02/21/ 2025, doi: https://doi.org/10.1016/j.device.2024.100568.

[337] Z. Li *et al.*, "Recent advances in polysaccharide-based hydrogels for synthesis and applications," *Aggregate,* vol. 2, no. 2, p. e21, 2021, doi: https://doi.org/10.1002/agt2.21.

[338] H.-J. Ahn *et al.*, "Magnetite-Free Sn-Doped Hematite Nanoflake Layers for Enhanced Photoelectrochemical Water Splitting," *ChemElectroChem,* vol. 9, no. 11, p. e202200066, 2022, doi: https://doi.org/10.1002/celc.202200066.

[339] Z. Alhashem *et al.*, "Structural and Magnetic Properties Study of Fe2O3/NiO/Ni2FeO4 Nanocomposites," *Crystals,* vol. 11, no. 6, p. 613, 2021. [Online]. Available: https://www.mdpi.com/2073-4352/11/6/613.

[340] A. A. Khaleed *et al.*, "Gas sensing study of hydrothermal reflux synthesized NiO/graphene foam electrode for CO sensing," *Journal of Materials Science,* vol. 52, no. 4, pp. 2035-2044, 2017/02/01 2017, doi: 10.1007/s10853-016-0491-

6.

[341] K. Shrimali *et al.*, "The surface state of hematite and its wetting characteristics," *Journal of Colloid and Interface Science,* vol. 477, pp. 16-24, 2016/09/01/ 2016, doi: https://doi.org/10.1016/j.jcis.2016.05.030.

[342] N. Manikandan *et al.*, "Electrochemical capacitance performance of high surface area, porous hematite (α -Fe2O3) nanorods," *Journal of Materials Science: Materials in Electronics,* vol. 33, no. 9, pp. 7109-7118, 2022/03/01 2022, doi: 10.1007/s10854-022-07893-8.

[343] H. M. Banbela *et al.*, "Preparation, Characterization, and Electrochemical Performance of the Hematite/Oxidized Multi-Walled Carbon Nanotubes Nanocomposite," *Molecules,* vol. 27, no. 9, p. 2708, 2022. [Online]. Available: https://www.mdpi.com/1420-3049/27/9/2708.

[344] K. Movlaee *et al.*, "Iron-Based Nanomaterials/Graphene Composites for Advanced Electrochemical Sensors," *Nanomaterials,* vol. 7, no. 12, p. 406, 2017. [Online]. Available: https://www.mdpi.com/2079-4991/7/12/406.

[345] M. Zhang *et al.*, "Three-Dimensional Core-Branch α -Fe2O3@NiO/Carbon Cloth Heterostructured Electrodes for Flexible Supercapacitors," (in English), *Frontiers in Chemistry,* Original Research vol. Volume 7 - 2019, 2020-January-08 2020, doi: 10.3389/fchem.2019.00887.

[346] M. Rincón Joya *et al.*, "Evaluation of Photocatalytic Activity in Water Pollutants and Cytotoxic Response of α -Fe2O3 Nanoparticles," *ACS Omega,* vol. 4, no. 17, pp. 17477-17486, 2019 Oct 22 2019, doi: http://doi.org/10.1021/acsomega.9b02251.

[347] U. Utari *et al.*, "Effect of Synthesis Temperature on Structural and Magnetic Properties in Hematite (α -Fe2O3) Nanoparticles Produced by Co-Precipitation Method," *Defect and Diffusion Forum,* vol. 417, pp. 219-225, 2022 Jun 28 2022, doi: https://doi.org/10.4028/p-e8v51k.

[348] D. H. Taffa *et al.*, "Influence of Annealing Temperature on the OER Activity of NiO(111) Nanosheets Prepared via Microwave and Solvothermal Synthesis Approaches," *ACS Applied Materials & Interfaces,* vol. 16, no. 45, pp. 62142-62154, 2024 Nov 13 2024, doi: https://doi.org/10.1021/acsami.4c14277.

[349] R. Al-Gaashani *et al.*, "Effects of preparation temperature on production of graphene oxide by novel chemical processing," *Ceramics International,* vol. 47,

2021 April 1 2020, doi: https://doi.org/10.1016/j.ceramint.2020.12.159.

[350] J. Zhang *et al.*, "Enhancing the Humidity Resistance of Triboelectric Nanogenerators: A Review," *Small*, vol. 20, no. 36, p. 2401846, 2024, doi: https://doi.org/10.1002/smll.202401846.

[351] E. Castagnotto *et al.*, "Characterization of the Caput Mortuum purple hematite pigment and synthesis of a modern analogue," *Dyes and Pigments*, vol. 185, p. 108881, 2021 Feb 1 2021, doi: https://doi.org/10.1016/j.dyepig.2020.108881.

[352] M. Saeed-Ul-Hassan *et al.*, "A comparative study of moisture adsorption on GO, MOF-5, and GO/MOF-5 composite for applications in atmospheric water harvesting," *Nanoscale Advances*, 10.1039/D4NA00150H vol. 6, no. 14, pp. 3668-3679, 2024, doi: 10.1039/D4NA00150H.

[353] H. Yu *et al.*, "Characterization and optimization of pore structure and water adsorption capacity in pinecone-derived activated carbon by steam activation," *Powder Technology*, vol. 431, p. 119084, 2024/01/01/ 2024, doi: https://doi.org/10.1016/j.powtec.2023.119084.

[354] H. Gong *et al.*, "Study on the influence of the agglomeration effect of composite nanoparticles on the photothermal properties of nanofluids," *Solar Energy*, vol. 270, p. 112406, 2024/03/01/ 2024, doi: https://doi.org/10.1016/j.solener.2024.112406.

[355] T. Hu *et al.*, "A Review on Recent Progress in Preparation of Medium-Temperature Solar-Thermal Nanofluids with Stable Dispersion," (in eng), *Nanomaterials (Basel)*, vol. 13, no. 8, Apr 18 2023, doi: 10.3390/nano13081399.

[356] Y. Ma *et al.*, "Synergistic Role of Temperature and Salinity in Aggregation of Nonionic Surfactant-Coated Silica Nanoparticles," *Langmuir*, vol. 39, no. 16, pp. 5917-5928, 2023/04/25 2023, doi: 10.1021/acs.langmuir.3c00432.

[357] X. Chen *et al.*, "Co/N co-doped flower-like carbon-based phase change materials toward solar energy harvesting," *Aggregate*, vol. 5, no. 1, p. e413, 2024, doi: https://doi.org/10.1002/agt2.413.

[358] Y. Cheng *et al.*, "Rapid and Persistent Suction Condensation on Hydrophilic Surfaces for High-Efficiency Water Collection," *Nano Letters*, vol. 21, no. 17, pp. 7411-7418, 2021 Sept 8 2021, doi: https://doi.org/10.1021/acs.nanolett.1c01928.

[359] P. Zhang *et al.*, "Effect of particle surface roughness on the flowability and

spreadability of Haynes 230 powder during laser powder bed fusion process," *Journal of Materials Research and Technology,* vol. 26, pp. 4444-4454, 2023 Sept 1 2023, doi: https://doi.org/10.1016/j.jmrt.2023.08.173.

[360] J. S. Justus *et al.*, "Judging phase purity of hematite (α -Fe2O3) nanoparticles through structural and magnetic studies," *Materials Research Express,* vol. 8, no. 5, p. 055005, 2021/05/19 2021, doi: 10.1088/2053-1591/abff09.

[361] M. Li *et al.*, "XPS Investigation of Magnetization Reduction Behavior and Kinetics of Oolitic Hematite in Gas-Based Roasting," *Minerals*, vol. 14, no. 5, p. 462, 2024. [Online]. Available: https://www.mdpi.com/2075-163X/14/5/462.

[362] G. Chen *et al.*, "Effect of calcination temperatures on the electrochemical performances of nickel oxide/reduction graphene oxide (NiO/RGO) composites synthesized by hydrothermal method," *Journal of Physics and Chemistry of Solids,* vol. 98, pp. 209-219, 2016/11/01/ 2016, doi: https://doi.org/10.1016/j.jpcs.2016.07.003.

[363] M. Sethi *et al.*, "A porous graphene–NiFe2O4 nanocomposite with high electrochemical performance and high cycling stability for energy storage applications††Electronic supplementary information (ESI) available. See DOI: 10.1039/d0na00440e," *Nanoscale Advances,* vol. 2, no. 9, pp. 4229-4241, 2020/09/16/ 2020, doi: https://doi.org/10.1039/d0na00440e.

[364] K. Wang *et al.*, "Effect of Hydrothermal Method Temperature on the Spherical Flowerlike Nanostructures NiCo(OH)4-NiO," *Nanomaterials,* vol. 12, no. 13, p. 2276, 2022. [Online]. Available: https://www.mdpi.com/2079-4991/12/13/2276.

[365] S. Kumar *et al.*, "Improved humidity sensitivity and possible energy harvesters in lithium modified potassium niobium tantalate oxide," *Materials Chemistry and Physics,* vol. 288, p. 126384, 2022/09/01/ 2022, doi: https://doi.org/10.1016/j.matchemphys.2022.126384.

[366] C. Ou *et al.*, "Template-Assisted Hydrothermal Growth of Aligned Zinc Oxide Nanowires for Piezoelectric Energy Harvesting Applications," *ACS Applied Materials & Interfaces,* vol. 8, no. 22, pp. 13678-13683, 2016/06/08 2016, doi: 10.1021/acsami.6b04041.

[367] F. E. B. Anang *et al.*, "Thermo-Convective Solution Growth of Vertically Aligned Zinc Oxide Nanowire Arrays for Piezoelectric Energy Harvesting," *Micromachines,* vol. 15, no. 10, p. 1179, 2024. [Online]. Available:

https://www.mdpi.com/2072-666X/15/10/1179.

[368] S. Mohan *et al.*, "Hydrothermal synthesis and characterization of Zinc Oxide nanoparticles of various shapes under different reaction conditions," *Nano Express*, vol. 1, no. 3, p. 030028, 2020/11/30 2020, doi: 10.1088/2632-959X/abc813.

[369] M. Khan *et al.*, "Effect of hydrothermal reaction temperature on MoO3 nanostructure properties for enhanced electrochemical performance as an electrode material in supercapacitors," *Ceramics International*, vol. 50, no. 19, Part A, pp. 34943-34955, 2024/10/01/ 2024, doi: https://doi.org/10.1016/j.ceramint.2024.06.303.

[370] L. Zeng *et al.*, "Tuning crystal structure of MnO2 during different hydrothermal synthesis temperature and its electrochemical performance as cathode material for zinc ion battery," *Vacuum*, vol. 192, p. 110398, 2021/10/01/ 2021, doi: https://doi.org/10.1016/j.vacuum.2021.110398.

[371] W. Shen *et al.*, "Effect of Solvothermal Temperature on Morphology and Supercapacitor Performance of Ni-MOF," *Molecules*, vol. 27, no. 23, p. 8226, 2022. [Online]. Available: https://www.mdpi.com/1420-3049/27/23/8226.

[372] H. Mansouri *et al.*, "Effect of Hydrothermal Synthesis Temperature on the Microstructural and Thermoelectric Characteristics of Thermally Deposited Bi0.5Sb1.5Te3 Thin Films," *Journal of Electronic Materials*, 11/21 2021, doi: 10.1007/s11664-021-09332-6.

[373] J. Pu *et al.*, "Nickel–cobalt hydroxide nanosheets arrays on Ni foam for pseudocapacitor applications," *Journal of Power Sources*, vol. 250, pp. 250-256, 2014/03/15/ 2014, doi: https://doi.org/10.1016/j.jpowsour.2013.10.108.

[374] H. Jiang *et al.*, "Cobalt–Nickel Layered Double Hydroxides on Electrospun MXene for Superior Asymmetric Supercapacitor Electrodes," *ACS Omega*, vol. 8, no. 51, pp. 49017-49026, 2023/12/26 2023, doi: 10.1021/acsomega.3c06674.

[375] M. Fahad *et al.*, "Investigation of Thermal Gel Formation of Methylcellulose in Glycols Using DSC and XRD," *Gels*, vol. 7, no. 4, p. 205, 2021. [Online]. Available: https://www.mdpi.com/2310-2861/7/4/205.

[376] Y. Dong *et al.*, "Preparation and characterization of enzymatically cross-linked gelatin/cellulose nanocrystal composite hydrogels," *RSC Advances*, 10.1039/D1RA00965F vol. 11, no. 18, pp. 10794-10803, 2021, doi: 10.1039/D1RA00965F.

[377] H. Guo *et al.*, "Preparation of Graphene Oxide-Based Hydrogels as Efficient Dye Adsorbents for Wastewater Treatment," *Nanoscale Research Letters,* vol. 10, no. 1, p. 272, 2015/06/27 2015, doi: 10.1186/s11671-015-0931-2.

[378] S. Omidi *et al.*, "Eco-friendly synthesis of graphene–chitosan composite hydrogel as efficient adsorbent for Congo red," *RSC Advances,* 10.1039/C8RA00510A vol. 8, no. 22, pp. 12179-12189, 2018, doi: 10.1039/C8RA00510A.

[379] H. T. Das *et al.*, "Performance of Solid-state Hybrid Energy-storage Device using Reduced Graphene-oxide Anchored Sol-gel Derived Ni/NiO Nanocomposite," *Scientific Reports,* vol. 7, no. 1, p. 15342, 2017/11/10 2017, doi: 10.1038/s41598-017-15444-z.

[380] M. N. Alam *et al.*, "Sustainable Production of Cellulose-Based Hydrogels with Superb Absorbing Potential in Physiological Saline," *ACS Omega,* vol. 4, no. 5, pp. 9419-9426, 2019/05/31 2019, doi: 10.1021/acsomega.9b00651.

[381] M. Xi *et al.*, "Cobalt-Ion Superhygroscopic Hydrogels Serve as Chip Heat Sinks Achieving a 5 °C Temperature Reduction via Evaporative Cooling," *Small Methods,* vol. 8, no. 12, p. 2301753, 2024, doi: https://doi.org/10.1002/smtd.202301753.

[382] F. Ni *et al.*, "Hygroscopic polymer gels toward atmospheric moisture exploitations for energy management and freshwater generation," *Matter,* vol. 5, no. 9, pp. 2624-2658, 2022, doi: 10.1016/j.matt.2022.06.010.

[383] W. Cheng *et al.*, "Ion Concentration Gradient Induced Efficient Ion Migration in Hydrogen-Bonded Organic Frameworks for High-Performance, Self-Powered Humidity Sensing," *Small,* vol. 21, no. 18, p. 2412497, 2025, doi: https://doi.org/10.1002/smll.202412497.

[384] C. Dong *et al.*, "Synergetic enhancement of moisture-electric generation through interfacial evaporation and active electrode," *Desalination,* vol. 593, p. 118210, 2025/01/05/ 2025, doi: https://doi.org/10.1016/j.desal.2024.118210.

[385] X. Wei *et al.*, "Design of Moisture-Enabled Electric Generators Utilizing sp- and sp2-Hybridized Two-Dimensional Carbon Materials: A Minireview and Perspectives," *Energy & Fuels,* vol. 38, no. 21, pp. 20242-20257, 2024/11/07 2024, doi: 10.1021/acs.energyfuels.4c03934.

[386] W. Zhu *et al.*, "Fibrous cellulose nanoarchitectonics on N-doped Carbon-based Metal-Free catalytic nanofilter for highly efficient advanced oxidation process,"

Chemical Engineering Journal, vol. 460, p. 141593, 2023/03/15/ 2023, doi: https://doi.org/10.1016/j.cej.2023.141593.

[387] Q. Wang *et al.*, "Nanochannel-Based Ion Transport and Its Application in Osmotic Energy Conversion: A Critical Review," *Advanced Physics Research*, vol. 2, no. 9, p. 2300016, 2023, doi: https://doi.org/10.1002/apxr.202300016.

[388] W. Chen *et al.*, "Polymer-based membranes for promoting osmotic energy conversion," *Giant*, vol. 10, p. 100094, 2022/06/01/ 2022, doi: https://doi.org/10.1016/j.giant.2022.100094.

[389] Z. Du *et al.*, "Proton-conducting hydrogel electrolytes with tight contact to binder-free MXene electrodes for high-performance thermally chargeable supercapacitor," *Carbon Energy*, vol. 6, no. 11, p. e562, 2024, doi: https://doi.org/10.1002/cey2.562.

[390] C. Guo *et al.*, "Radiative cooling assisted self-sustaining and highly efficient moisture energy harvesting," *Nature Communications*, vol. 15, no. 1, p. 6100, 2024/07/19 2024, doi: 10.1038/s41467-024-50396-9.

[391] A. S. M. Ismail *et al.*, "Detection of Spontaneous FeOOH Formation at the Hematite/Ni(Fe)OOH Interface During Photoelectrochemical Water Splitting by Operando X-ray Absorption Spectroscopy," *ACS Catalysis*, vol. 11, no. 19, pp. 12324-12335, 2021/10/01 2021, doi: 10.1021/acscatal.1c02566.

[392] G. Wartner *et al.*, "Insights into the electronic structure of Fe–Ni thin-film catalysts during the oxygen evolution reaction using operando resonant photoelectron spectroscopy," *Journal of Materials Chemistry A*, 10.1039/D2TA08961K vol. 11, no. 15, pp. 8066-8080, 2023, doi: 10.1039/D2TA08961K.

[393] H. Zhong *et al.*, "Asymmetric self-powered cellulose-based aerogel for moisture-electricity generation and humidity sensing," *Chemical Engineering Journal*, vol. 486, p. 150203, 2024/04/15/ 2024, doi: https://doi.org/10.1016/j.cej.2024.150203.

[394] S. Li *et al.*, "Humidity-sensitive chemoelectric flexible sensors based on metal-air redox reaction for health management," *Nature Communications*, vol. 13, no. 1, p. 5416, 2022/09/15 2022, doi: 10.1038/s41467-022-33133-y.

[395] X. Yang *et al.*, "Harvesting clean energy from moisture," *Device*, vol. 1, no. 1, p. 100016, 2023/07/21/ 2023, doi: https://doi.org/10.1016/j.device.2023.100016.

[396] D. Gao *et al.*, "Fast Self-Charging Flexible Device Based on Metal–Air Redox Reaction under Normal Humidity," *Energy Technology*, vol. 12, no. 4, p. 2301014, 2024, doi: https://doi.org/10.1002/ente.202301014.

[397] W. Qian *et al.*, "Estimating indoor air temperature and humidity distributions by data assimilation with finite observations: Validation using an actual residential room," *Building and Environment*, vol. 269, p. 112495, 2025/02/01/ 2025, doi: https://doi.org/10.1016/j.buildenv.2024.112495.

[398] C. Liu *et al.*, "Understanding electrochemical potentials of cathode materials in rechargeable batteries," *Materials Today*, vol. 19, no. 2, pp. 109-123, 2016/03/01/ 2016, doi: https://doi.org/10.1016/j.mattod.2015.10.009.

[399] O. Cherkas *et al.*, "X-ray absorption and diffraction analysis for determination of the amount of calcium carbonate and porosity in paper sheets," *Cellulose*, vol. 23, no. 5, pp. 2831-2840, 2016/10/01 2016, doi: 10.1007/s10570-016-1001-3.

[400] C. Delgado-Orti *et al.*, "Development of PLA–Waste Paper Biocomposites with High Cellulose Content," *Polymers*, vol. 16, no. 14, p. 2000, 2024. [Online]. Available: https://www.mdpi.com/2073-4360/16/14/2000.

[401] O. F. Damnalı *et al.*, "Synergistic impact of graphene and carbon nanotubes on waste paper for hybrid nanocomposite substrates," *Cellulose*, vol. 26, no. 6, pp. 3935-3954, 2019/04/01 2019, doi: 10.1007/s10570-019-02339-7.

[402] M. L. Hassan *et al.*, "Utilization of paper sludge in preparation of high-purity calcium formate," *Biomass Conversion and Biorefinery*, vol. 15, no. 3, pp. 4565-4578, 2025/02/01 2025, doi: 10.1007/s13399-023-05216-3.

[403] S. Manandhar *et al.*, "Recycling Waste Paper for Further Implementation: XRD, FTIR, SEM, and EDS Studies," *Journal of Oleo Science*, vol. 71, no. 4, pp. 619-626, 2022, doi: 10.5650/jos.ess21396.

[404] M. R. Ghalhari *et al.*, "Cellulose-based hydrogel beads derived from wastepapers: application for organic dye adsorption," *Cellulose*, vol. 30, no. 15, pp. 9669-9691, 2023/10/01 2023, doi: 10.1007/s10570-023-05467-3.

[405] T. Pinthong *et al.*, "Development of Natural Active Agent-Containing Porous Hydrogel Sheets with High Water Content for Wound Dressings," *Gels*, vol. 9, no. 6, p. 459, 2023. [Online]. Available: https://www.mdpi.com/2310-2861/9/6/459.

[406] D. Zhou *et al.*, "A piezoelectric nanogenerator promotes highly stretchable and self-chargeable supercapacitors," *Materials Horizons*, 10.1039/D0MH00610F

vol. 7, no. 8, pp. 2158-2167, 2020, doi: 10.1039/D0MH00610F.

[407] H. Liang *et al.*, "A review on vibration-based piezoelectric energy harvesting from the aspect of compliant mechanisms," *Sensors and Actuators A: Physical*, vol. 331, p. 112743, 2021/11/01/ 2021, doi: https://doi.org/10.1016/j.sna.2021.112743.

[408] S. M. AlTowireb *et al.*, "Core-Shell structures for the enhancement of energy harvesting in piezoelectric Nanogenerators: A review," *Sustainable Energy Technologies and Assessments*, vol. 55, p. 102982, 2023/02/01/ 2023, doi: https://doi.org/10.1016/j.seta.2022.102982.

[409] B. Amrutha *et al.*, "Enhancing piezoelectric effect of PVDF electrospun fiber through NiO nanoparticles for wearable applications," *Heliyon*, vol. 10, no. 7, 2024, doi: 10.1016/j.heliyon.2024.e29192.

[410] L. Kou *et al.*, "Enhanced Piezoelectric Nanogenerator Based on Tridoped Graphene and Ti3CNTx MXene Quasi-3D Heterostructure," *Industrial & Engineering Chemistry Research*, vol. 63, no. 36, pp. 15853-15868, 2024/09/11 2024, doi: 10.1021/acs.iecr.4c00987.

[411] S. P. Adıgüzel *et al.*, "High Performance Piezoelectric Nanogenerators Based on Polyvinylidene Fluoride-Graphene Nanoribbon Composite Thin Films," *Macromolecular Rapid Communications*, vol. 45, no. 19, p. 2400360, 2024, doi: https://doi.org/10.1002/marc.202400360.

[412] A. Mondal *et al.*, "Enhanced Piezoelectric Performance in Nickel Oxide Nanoparticle-Embedded Flexible PVDF Film," *Journal of Electronic Materials*, vol. 53, no. 11, pp. 6933-6944, 2024/11/01 2024, doi: 10.1007/s11664-024-11363-8.

[413] M. Salama *et al.*, "Boosting piezoelectric properties of PVDF nanofibers via embedded graphene oxide nanosheets," *Scientific Reports*, vol. 14, no. 1, p. 16484, 2024/07/17 2024, doi: 10.1038/s41598-024-66258-9.

[414] S. Ghosh *et al.*, "Water flow and finger-tapping mediated piezoelectric energy generation using a natural hematite-based flexible PVDF-HFP membrane," *Journal of Materials Chemistry C*, 10.1039/D3TC01920A vol. 11, no. 39, pp. 13418-13428, 2023, doi: 10.1039/D3TC01920A.

[415] M. Huang *et al.*, "Oppositely Charged Interfacial Janus Nanoparticles Induce the Formation of Highly Ferroelectric Poling-Free PVDF Films for Piezoelectric Energy Generation," *ACS Applied Nano Materials*, vol. 7, no. 11, pp. 12734-

12744, 2024/06/14 2024, doi: 10.1021/acsanm.4c01263.

[416] I. O. Pariy *et al.*, "Piezoelectric Response in Hybrid Micropillar Arrays of Poly(Vinylidene Fluoride) and Reduced Graphene Oxide," *Polymers*, vol. 11, no. 6, p. 1065, 2019. [Online]. Available: https://www.mdpi.com/2073-4360/11/6/1065.

[417] M. U. K. Sadaf *et al.*, "Neodymium doped zinc oxide based advanced flexible piezoelectric energy harvester and self-powered biomotion sensor," *Nano Trends*, vol. 8, p. 100063, 2024/12/01/ 2024, doi: https://doi.org/10.1016/j.nwnano.2024.100063.

[418] H. M. Venkatesan *et al.*, "High-performance triboelectric nanogenerators based on Ag-doped ZnO loaded electrospun PVDF nanofiber mats for energy harvesting and healthcare monitoring," *Scientific Reports*, vol. 15, no. 1, p. 3347, 2025/01/27 2025, doi: 10.1038/s41598-025-87148-8.

[419] M. A. Mustaffa *et al.*, "Towards a Highly Efficient ZnO Based Nanogenerator," *Micromachines*, vol. 13, no. 12, p. 2200, 2022. [Online]. Available: https://www.mdpi.com/2072-666X/13/12/2200.

[420] F. Nasirpouri *et al.*, "Microstructure, ion adsorption and magnetic behavior of mesoporous γ -Fe2O3 ferrite nanoparticles," *RSC Advances*, 10.1039/D3RA01663C vol. 13, no. 36, pp. 25140-25158, 2023, doi: 10.1039/D3RA01663C.

[421] A. Jomekian *et al.*, "Synthesis of ultra-porous zeolitic imidazolate Framework-300 under different synthesis conditions for sorption of CO2," *Journal of Solid State Chemistry*, vol. 335, p. 124700, 2024/07/01/ 2024, doi: https://doi.org/10.1016/j.jssc.2024.124700.

APPENDICES

APPENDIX 1

Supplementary Video (V1)

Process of Making Recycled Paper Using a Home-based Method

https://youtu.be/wImE7uaIRmM

Go to Top

APPENDIX 2

NiO (JCPDS No. 01-071-4750) for XRD analysis

PDF Card No.: 01-071-4750 Quality:I

Sub-File Name:	Inorganic, Mineral, Alloy&Metal, Common Phase, Forensic, ICSD Pattern
Formula:	Ni O
Name:	Bunsenite, syn — I/Ic (RIR)= 4.76
Crystal System:	Cubic — Space Group: Fm-3m(225) — Dmeas:
Cell Parameters:	a= 4.2000 b= 4.2000 c= 4.2000
	Alpha= 90.000 Beta= 90.000 Gamma= 90.000
	Volume= 74.088 Z= 4
Reference:	Davey, W.P., Hoffmann, E.O. Phys. Rev.15(1920)333.
Radiation:	CuKa1 Wavelength= 1.54060
2Theta range:	37.04 - 144.72
Database comments:	ANX: AX. Analysis: Ni1 O1. Formula from original source: Ni O. ICSD Collection Code: 53930. Minor Warning: No e.s.d reported/abstracted on the cell dimension. No R factors reported/abstracted. Wyckoff Sequence: b a. Unit Cell Data Source: Powder Diffraction.

Relative Intensity

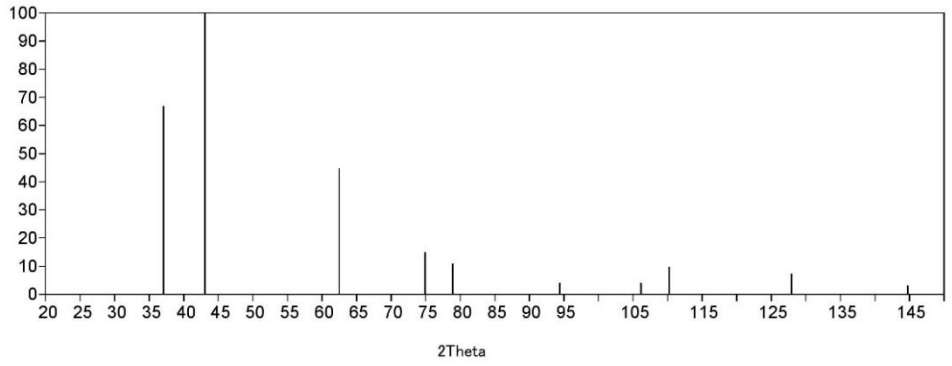

No.	2Theta	d-Value	Intensity	h	k	l	No.	2Theta	d-Value	Intensity	h	k	l
1	37.04	2.425	66.7	1	1	1							
2	43.04	2.100	100.0	2	0	0							
3	62.49	1.485	44.5	2	2	0							
4	74.93	1.266	14.8	3	1	1							
5	78.89	1.212	10.7	2	2	2							
6	94.38	1.050	3.9	4	0	0							
7	106.15	0.964	3.9	3	3	1							
8	110.21	0.939	9.6	4	2	0							
9	127.92	0.857	7.1	4	2	2							
10	144.72	0.808	2.9	5	1	1							

Note: 2theta are calculated with wavelength = 1.54056

1/1

Go to Top

Nickel (JCPDS No. 00-004-0850) for XRD analysis

PDF Card No.: 00-004-0850 Quality:S

Sub-File Name:	Inorganic, Mineral, Alloy&Metal, Common Phase, Educational Pattern, Forensic,...
Formula:	Ni
Name:	Nickel, syn — I/Ic (RIR)= ---
Crystal System:	Cubic — Space Group: Fm-3m(225) — Dmeas:
Cell Parameters:	a= 3.5238 b= 3.5238 c= 3.5238
	Alpha= 90.000 Beta= 90.000 Gamma= 90.000
	Volume= 43.756 Z= 4
Reference:	Swanson, Tatge. Natl. Bur. Stand. (U. S.), Circ. 539I(1953)13.
Radiation:	CuKa1 — Wavelength= 1.54050
2Theta range:	44.51 - 155.65
Database comments:	Additional Patterns: See PDF 01-087-0712. ANX: N. Analysis: Spectrographic analysis show <0.01% each of Mg, Si and Ca. Sample Source or Locality: Sample obtained from Johnson Matthey Company, Ltd. Temperature of Data Collection: 299 K. Unit Cell Data Source: Powder Diffraction.

Relative Intensity

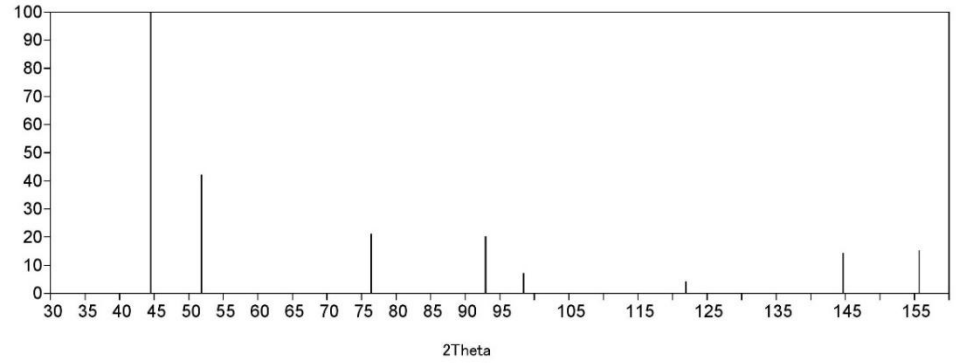

No.	2Theta	d-Value	Intensity	h	k	l	No.	2Theta	d-Value	Intensity	h	k	l
1	44.51	2.034	100.0	1	1	1							
2	51.85	1.762	42.0	2	0	0							
3	76.37	1.246	21.0	2	2	0							
4	92.94	1.062	20.0	3	1	1							
5	98.45	1.017	7.0	2	2	2							
6	121.93	0.881	4.0	4	0	0							
7	144.67	0.808	14.0	3	3	1							
8	155.65	0.788	15.0	4	2	0							

Note: 2theta are calculated with wavelength = 1.54056

1/1

Go to Top

Graphite (JCPDS No. 00-041-1487) for XRD analysis

PDF Card No.: 00-041-1487 Quality:I

Sub-File Name:	Inorganic, Mineral, Alloy&Metal, Battery Material, Common Phase, Educational ...
Formula:	C
Name:	Graphite-2H I/Ic (RIR)= 7.78
Crystal System:	Hexagonal Space Group: P63/mmc(194) Dmeas: 2.160
Cell Parameters:	a= 2.4704 b= 2.4704 c= 6.7244
	Alpha= 90.000 Beta= 90.000 Gamma= 120.000
	Volume= 35.540 Z= 4
Reference:	Sanc, I., Polytechna, Foreign Trade Corporation, Panska, Czechoslovakia. ICDD...
Radiation:	CuKa1 Wavelength= 1.54051
2Theta range:	26.38 - 93.59
Database comments:	Additional Patterns: To replace 00-001-0640, 00-001-0646, 00-002-0456, 00-003-0401, 00-023-0064, 00-025-0284 and 00-034-0567 and validated by calculated pattern 00-025-0284. ANX: N. Sample Source or Locality: Specimen from Netolice, Czech Republic. Temperature of Data Collection: 298(1) K. Warning: Lines with abs(delta 2Theta)>0.06 DEG. Unit Cell Data Source: Powder Diffraction.

Relative Intensity

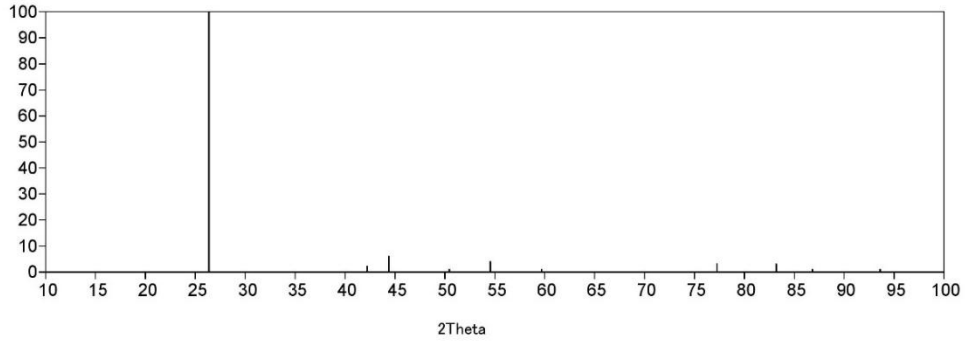

No.	2Theta	d-Value	Intensity	h	k	l	No.	2Theta	d-Value	Intensity	h	k	l
1	26.38	3.376	100.0	0	0	2							
2	42.22	2.139	2.0	1	0	0							
3	44.39	2.039	6.0	1	0	1							
4	50.45	1.807	1.0	1	0	2							
5	54.54	1.681	4.0	0	0	4							
6	59.69	1.548	1.0	1	0	3							
7	77.24	1.234	3.0	1	1	0							
8	83.18	1.160	3.0	1	1	2							
9	86.82	1.121	1.0	0	0	6							
10	93.59	1.057	1.0	2	0	1							

Note: 2theta are calculated with wavelength = 1.54056

1/1

Go to Top

Hematite (JCPDS No. 00-033-0664) for XRD analysis

PDF Card No.: 00-033-0664 Quality:S

Sub-File Name:	Inorganic, Mineral, Alloy&Metal, Common Phase, Educational Pattern, Forensic,...							
Formula:	Fe2 O3							
Name:	Hematite, syn						I/Ic (RIR)=	2.40
Crystal System:	Trigonal		Space Group:	R-3c(167)		Dmeas:	5.260	
Cell Parameters:	a=	5.0356	b=	5.0356		c=	13.7489	
	Alpha=	90.000	Beta=	90.000		Gamma=	120.000	
	Volume=	301.926	Z=	6				
Reference:	Natl. Bur. Stand. (U. S.) Monogr. 2518(1981)37.							
Radiation:	CuKa1		Wavelength=	1.54060				
2Theta range:	24.14 - 147.96							

Database comments: Additional Patterns: To replace 00-013-0534 and validated by calculated pattern 00-024-0072. See PDF 01-079-0007. General Comments: Pattern reviewed by Syvinski, W., McCarthy, G., North Dakota State Univ., Fargo, North Dakota, USA, ICDD Grant-in-Aid (1990). Agress well with experimental and calculated patterns. Additional weak reflection (indicated by brackets) was observed. Melting Point: 1623-1633 K. Opaque Optical Data: Opaque mineral optical data on

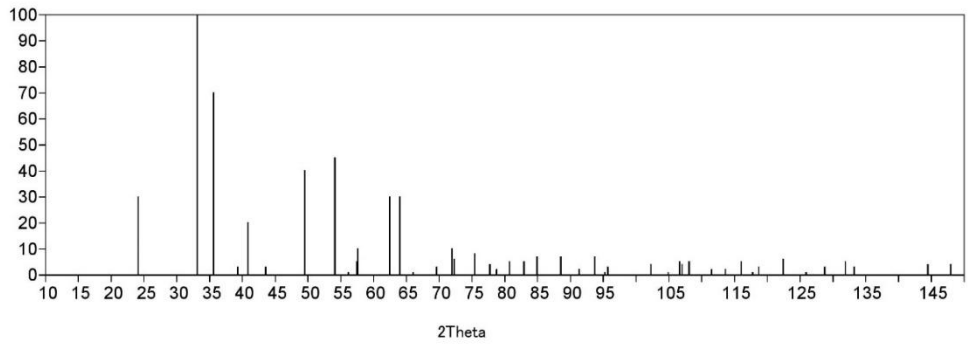

No.	2Theta	d-Value	Intensity	h	k	l	No.	2Theta	d-Value	Intensity	h	k	l
1	24.14	3.684	30.0	0	1	2	21	80.71	1.190	5.0	1	2	8
2	33.15	2.700	100.0	1	0	4	22	82.94	1.163	5.0	0	2	10
3	35.61	2.519	70.0	1	1	0	23	84.91	1.141	7.0	1	3	4
4	39.28	2.292	3.0	0	0	6	24	88.54	1.104	7.0	2	2	6
5	40.85	2.207	20.0	1	1	3	25	91.34	1.077	2.0	0	4	2
6	43.52	2.078	3.0	2	0	2	26	93.71	1.056	7.0	2	1	10
7	49.48	1.841	40.0	0	2	4	27	95.24	1.043	1.0	1	1	12
8	54.09	1.694	45.0	1	1	6	28	95.66	1.039	3.0	4	0	4
9	56.15	1.637	1.0	2	1	1	29	102.28	0.989	4.0	3	1	8
10	57.43	1.603	5.0	1	2	2	30	104.91	0.971	1.0	2	2	9
11	57.59	1.599	10.0	0	1	8	31	106.62	0.961	5.0	3	2	4
12	62.45	1.486	30.0	2	1	4	32	107.02	0.958	4.0	0	1	14
13	63.99	1.454	30.0	3	0	0	33	108.09	0.952	5.0	4	1	0
14	66.03	1.414	1.0	1	2	5	34	111.51	0.932	2.0	4	1	3
15	69.60	1.350	3.0	2	0	8	35	113.59	0.921	2.0	0	4	8
16	71.94	1.311	10.0	1	0	10	36	116.04	0.908	5.0	1	3	10
17	72.26	1.306	6.0	1	1	9	37	117.75	0.900	1.0	3	0	12
18	75.43	1.259	8.0	2	2	0	38	118.69	0.895	3.0	2	0	14
19	77.73	1.228	4.0	3	0	6	39	122.43	0.879	6.0	4	1	6
20	78.76	1.214	2.0	2	2	3	40	125.92	0.865	1.0	2	3	8

Note: 2theta are calculated with wavelength = 1.54056

1/2

PDF Card No.: 00-033-0664 Quality:S

No.	2Theta	d-Value	Intensity	h	k	l	No.	2Theta	d-Value	Intensity	h	k	l
41	128.75	0.854	3.0	4	0	10							
42	131.87	0.844	5.0	1	2	14							
43	133.23	0.839	3.0	3	3	0							
44	144.45	0.809	4.0	3	2	10							
45	147.96	0.801	4.0	2	4	4							

Note: 2theta are calculated with wavelength = 1.54056

2/2

Go to Top

Magnetite (JCPDS No. 01-073-9877) for XRD analysis

PDF Card No.: 01-073-9877 Quality:S

Sub-File Name:	Inorganic, Mineral, Alloy&Metal, Battery Material, Common Phase, Forensic, Ph...
Formula:	Fe3 O4
Name:	iron diiron(III) oxide, magnetite I/Ic (RIR)= 5.07
Crystal System:	Cubic Space Group: Fd-3m(227) Dmeas:
Cell Parameters:	a= 8.3199 b= 8.3199 c= 8.3199
	Alpha= 90.000 Beta= 90.000 Gamma= 90.000
	Volume= 575.910 Z= 8
Reference:	Finger, L.W., Hazen, R.M., Hofmeister, A.M. Phys. Chem. Miner.13(1986)215.
Radiation:	CuKa1 Wavelength= 1.54060
2Theta range:	18.46 - 148.37
Database comments:	ANX: AB2X4. Analysis: Fe3 O4. Formula from original source: Fe3 O4. ICSD Collection Code: 77591. Pressure of Datacollection: 3900 MPa. Wyckoff Sequence: e d a. Unit Cell Data Source: Single Crystal.

Relative Intensity

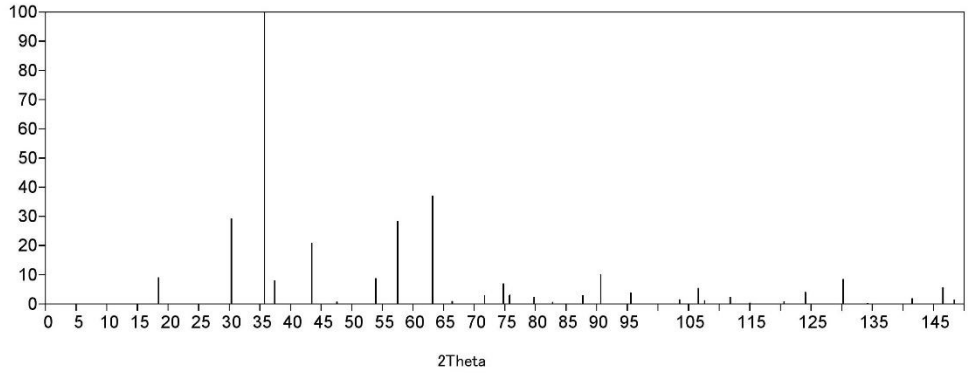

No.	2Theta	d-Value	Intensity	h	k	l	No.	2Theta	d-Value	Intensity	h	k	l
1	18.46	4.804	8.8	1	1	1	21	107.63	0.954	1.1	6	6	2
2	30.36	2.942	29.1	2	2	0	22	111.81	0.930	2.2	8	4	0
3	35.76	2.509	100.0	3	1	1	23	115.02	0.913	0.2	9	1	1
4	37.41	2.402	7.8	2	2	2	24	120.57	0.887	0.6	6	6	4
5	43.47	2.080	20.7	4	0	0	25	124.06	0.872	3.9	9	3	1
6	47.60	1.909	0.6	3	3	1	26	130.22	0.849	8.3	8	4	4
7	53.94	1.698	8.6	4	2	2	27	134.20	0.836	0.1	7	5	5
8	57.51	1.601	28.3	5	1	1	28	141.53	0.816	1.7	10	2	0
9	63.17	1.471	36.9	4	4	0	29	146.55	0.804	5.4	9	5	1
10	66.42	1.406	0.8	5	3	1	30	148.37	0.801	1.2	10	2	2
11	71.68	1.315	2.8	6	2	0							
12	74.76	1.269	6.8	5	3	3							
13	75.78	1.254	2.9	6	2	2							
14	79.80	1.201	2.2	4	4	4							
15	82.78	1.165	0.4	5	5	1							
16	87.71	1.112	2.8	6	4	2							
17	90.66	1.083	9.9	7	3	1							
18	95.58	1.040	3.7	8	0	0							
19	103.55	0.981	1.3	8	2	2							
20	106.60	0.961	5.3	7	5	1							

Note: 2theta are calculated with wavelength = 1.54056

1/1

Go to Top

Cellulose (JCPDS No. 00-056-1718) for XRD analysis

PDF Card No.: 00-056-1718 Quality:S

Sub-File Name:	Organic, Pharmaceutical, Polymer
Formula:	(C6 H10 O5)n
Name:	Cellulose Iß — I/Ic (RIR)= 8.27
Crystal System:	Monoclinic — Space Group: P21(4) — Dmeas:
Cell Parameters:	a= b= c=
	Alpha= Beta= Gamma=
	Volume= Z= 4
Reference:	Kaduk, J., BP Chemical, Naperville, IL, USA. Private Communication(2005).
Radiation:	CuKa1 — Wavelength= 1.54063
2Theta range:	13.81 - 60.15
Database comments:	Additional Patterns: To replace 00-050-2241. See See PDF 00-060-1502. Sample Preparation: The sample was a sheet of Whatman No.42 filter paper. Structures: Crystal structure optimized by a density functional plane wave pseudopotential quantum mechanical calculation, with fixed experimental lattice parameters.

Relative Intensity

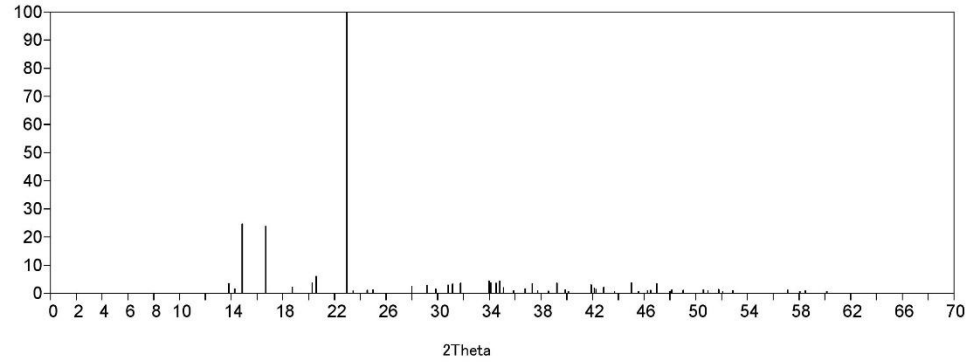

No.	2Theta	d-Value	Intensity	h	k	l	No.	2Theta	d-Value	Intensity	h	k	l
1	13.81	6.409	3.4	0	1	1	21	34.80	2.576	4.2	-1	3	1
2	14.27	6.201	1.5	1	0	1	22	35.10	2.554	1.9	-1	2	3
3	14.86	5.959	24.5	-1	1	0	23	35.87	2.502	0.8	3	0	1
4	16.67	5.314	23.7	1	1	0	24	36.78	2.442	1.5	1	2	3
5	18.74	4.730	2.1	1	1	1	25	37.33	2.407	3.3	1	3	1
6	20.27	4.377	3.5	0	1	2	26	37.75	2.381	0.9	3	1	0
7	20.59	4.309	5.9	1	0	2	27	38.58	2.332	0.7	1	1	4
8	22.98	3.867	100.0	2	0	0	28	39.24	2.294	3.5	-2	3	1
9	23.44	3.792	0.7	0	2	1	29	39.90	2.258	1.1	-2	2	3
10	24.55	3.623	1.0	2	0	1	30	40.12	2.246	0.5	-3	2	1
11	25.01	3.557	1.2	-1	2	1	31	41.89	2.155	2.9	2	0	4
12	27.99	3.185	2.3	2	1	1	32	42.14	2.142	1.7	-2	3	2
13	29.17	3.059	2.7	-1	2	2	33	42.27	2.136	1.3	0	3	3
14	29.84	2.991	1.4	-1	1	3	34	42.87	2.108	2.0	2	2	3
15	30.81	2.900	2.8	1	1	3	35	43.70	2.070	0.5	2	3	1
16	31.15	2.869	3.2	1	2	2	36	45.00	2.013	3.6	1	3	3
17	31.78	2.814	3.5	2	1	2	37	45.55	1.990	0.5	-1	4	1
18	33.97	2.637	4.3	0	2	3	38	46.25	1.961	0.8	3	1	3
19	34.10	2.627	3.6	0	3	1	39	46.51	1.951	1.0	-3	3	1
20	34.53	2.595	3.5	0	0	4	40	46.96	1.933	3.3	1	1	5

Note: 2theta are calculated with wavelength = 1.54056

1/2

PDF Card No.: 00-056-1718 Quality:S

No.	2Theta	d-Value	Intensity	h	k	l	No.	2Theta	d-Value	Intensity	h	k	l
41	48.01	1.893	0.6	-2	4	0							
42	48.14	1.888	1.1	-1	4	2							
43	49.03	1.857	1.0	2	2	4							
44	50.59	1.803	1.1	2	3	3							
45	50.94	1.791	0.8	1	3	4							
46	51.77	1.764	1.3	2	1	5							
47	52.09	1.754	0.5	3	1	4							
48	52.89	1.730	0.9	4	1	2							
49	57.12	1.611	1.0	-3	4	2							
50	58.05	1.587	0.6	-4	3	2							
51	58.48	1.577	0.8	3	3	3							
52	60.15	1.537	0.6	2	1	6							

Note: 2theta are calculated with wavelength = 1.54056

2/2

Go to Top

Stearic Acid (JCPDS No. 00-038-1923) for XRD analysis

PDF Card No.: 00-038-1923 Quality:S

Sub-File Name:	Organic, Common Phase, Educational Pattern, Forensic, Pharmaceutical
Formula:	C18 H36 O2
Name:	Stearic acid I/Ic (RIR)= ---
Crystal System:	Monoclinic Space Group: P21/c(14) Dmeas:
Cell Parameters:	a= 39.9600 b= 4.9540 c= 9.3780
	Alpha= 90.000 Beta= 94.810 Gamma= 90.000
	Volume= 1849.948 Z= 4
Reference:	Welton, J., McCarthy, G., North Dakota State Univ., Fargo, ND, USA. ICDD Gran...
Radiation:	CuKa Wavelength= 1.54178
2Theta range:	2.23 - 52.33
Database comments:	Additional Patterns: To replace 00-009-0618. General Comments: All peaks (153 total) with 2-theta angles greater than 30° and intensities of less than three were omitted. Average relative standard deviation in intensity of the 10 strongest reflections for three specimen mounts = 12.8%. Melting Point: 342.6 K. Sample Source or Locality: Sample obtained from Fisher Scientific Company. Structures: C form. Unit Cell: Cell parameters refined from original Crystal

Relative Intensity

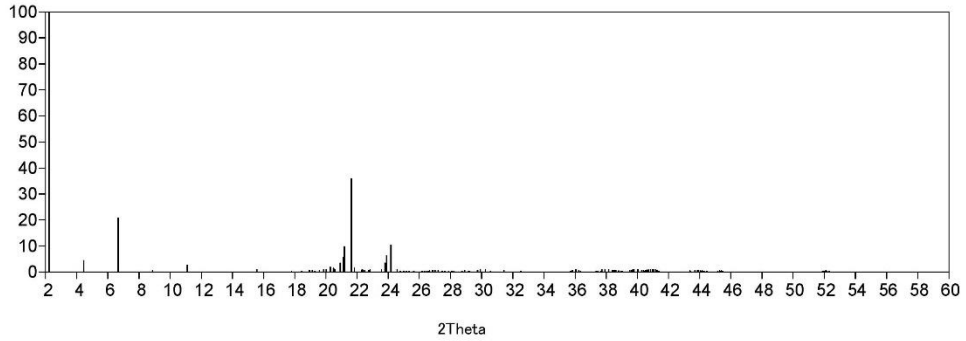

No.	2Theta	d-Value	Intensity	h	k	l	No.	2Theta	d-Value	Intensity	h	k	l
1	2.23	39.620	100.0	1	0	0	21	21.63	4.105	35.8	3	1	1
2	4.45	19.856	4.4	2	0	0	22	21.84	4.066	1.4	-4	1	1
3	6.67	13.251	20.6	3	0	0	23	22.31	3.981	0.7	10	0	0
4	8.87	9.958	0.6	4	0	0	24	22.37	3.971	0.7	-6	1	0
5	11.11	7.957	2.6	5	0	0	25	22.49	3.950	0.6	4	1	1
6	15.57	5.687	0.7	7	0	0	26	22.77	3.902	0.6	-5	1	1
7	17.79	4.983	0.2	8	0	0	27	22.84	3.890	0.7	5	0	2
8	18.45	4.806	0.3	-2	1	0	28	23.57	3.771	0.9	5	1	1
9	18.95	4.680	0.5	-1	0	2	29	23.80	3.735	3.4	-7	1	0
10	19.12	4.639	0.5	-2	0	2	30	23.89	3.722	6.1	-6	1	1
11	19.30	4.596	0.3	1	0	2	31	24.18	3.678	10.2	6	0	2
12	19.59	4.527	0.4	-3	0	2	32	24.57	3.620	0.7	11	0	0
13	19.86	4.466	0.8	2	0	2	33	24.78	3.590	0.3	6	1	1
14	20.02	4.431	0.9	-4	1	0	34	25.00	3.559	0.3	-8	0	2
15	20.29	4.374	1.7	0	1	1	35	25.16	3.537	0.2	-7	1	1
16	20.49	4.332	1.4	1	1	1	36	25.34	3.512	0.2	-8	1	0
17	20.59	4.311	0.9	-2	1	1	37	25.65	3.470	0.2	7	0	2
18	20.93	4.240	3.3	2	1	1	38	26.15	3.405	0.2	7	1	1
19	21.11	4.206	5.5	-5	1	0	39	26.20	3.399	0.2	0	1	2
20	21.20	4.187	9.7	-5	0	2	40	26.31	3.385	0.3	-2	1	2

Note: 2theta are calculated with wavelength = 1.54059

1/2

PDF Card No.: 00-038-1923 Quality:S

No.	2Theta	d-Value	Intensity	h	k	l	No.	2Theta	d-Value	Intensity	h	k	l
41	26.43	3.370	0.2	1	1	2	101	44.05	2.054	0.4	6	2	2
42	26.55	3.355	0.3	−9	0	2	102	44.16	2.049	0.4	8	0	4
43	26.65	3.342	0.4	−3	1	2	103	44.28	2.044	0.3	−11	2	0
44	26.85	3.318	0.4	12	0	0	104	44.46	2.036	0.3	4	1	4
45	27.00	3.300	0.6	−9	1	0	105	45.16	2.006	0.3	−18	1	1
46	27.20	3.276	0.5	−4	1	2	106	45.28	2.001	0.4	−8	1	4
47	27.46	3.246	0.3	3	1	2	107	45.38	1.997	0.4	9	0	4
48	27.64	3.225	0.2	8	1	1	108	45.47	1.993	0.3	−9	2	2
49	27.88	3.198	0.3	−5	1	2	109	51.88	1.761	0.3	−14	1	4
50	28.09	3.174	0.3	−9	1	1	110	51.97	1.758	0.3	15	2	1
51	28.21	3.161	0.2	−10	0	2	111	52.04	1.756	0.3	−16	2	0
52	28.74	3.104	0.3	−10	1	0	112	52.10	1.754	0.4	−2	1	5
53	28.91	3.086	0.4	9	0	2	113	52.17	1.752	0.3	−3	1	5
54	29.15	3.061	0.3	13	0	0	114	52.33	1.747	0.3	16	1	3
55	29.24	3.052	0.2	9	1	1							
56	29.74	3.002	0.5	−10	1	1							
57	29.91	2.985	1.0	−11	0	2							
58	30.24	2.953	0.9	6	1	2							
59	30.56	2.923	0.3	−11	1	0							
60	31.43	2.844	0.4	−11	1	1							
61	32.51	2.752	0.3	11	0	2							
62	35.71	2.512	0.3	−6	1	3							
63	35.82	2.505	0.5	4	1	3							
64	36.06	2.489	0.8	16	0	0							
65	36.24	2.477	0.5	0	2	0							
66	36.34	2.470	0.3	13	0	2							
67	37.34	2.406	0.3	11	1	2							
68	37.46	2.399	0.3	−4	2	0							
69	37.65	2.387	0.3	1	2	1							
70	37.72	2.383	0.7	−2	2	1							
71	37.92	2.371	0.8	2	2	1							
72	38.16	2.357	0.7	−5	2	0							
73	38.42	2.341	0.6	−1	0	4							
74	38.52	2.335	0.5	0	0	4							
75	38.61	2.330	0.5	7	1	3							
76	38.80	2.319	0.4	1	0	4							
77	38.94	2.311	0.3	−15	1	1							
78	39.03	2.306	0.3	−5	2	1							
79	39.51	2.279	0.5	5	2	1							
80	39.64	2.272	0.6	−10	1	3							
81	39.71	2.268	0.8	−6	2	1							
82	39.78	2.264	1.0	−6	0	4							
83	40.04	2.250	0.9	−14	1	2							
84	40.28	2.237	0.4	6	2	1							
85	40.38	2.232	0.4	4	0	4							
86	40.45	2.228	0.3	15	0	2							
87	40.53	2.224	0.5	−7	2	1							
88	40.64	2.218	0.7	−8	2	0							
89	40.74	2.213	0.9	18	0	0							
90	40.84	2.208	1.0	13	1	2							
91	40.97	2.201	1.0	−16	1	1							
92	41.03	2.198	1.0	9	1	3							
93	41.17	2.191	0.7	7	2	1							
94	41.25	2.187	0.5	0	2	2							
95	41.29	2.185	0.4	−2	2	2							
96	41.38	2.180	0.3	1	2	2							
97	43.38	2.084	0.4	2	1	4							
98	43.69	2.070	0.5	−10	2	1							
99	43.85	2.063	0.4	3	1	4							
100	43.94	2.059	0.5	−6	1	4							

Note: 2theta are calculated with wavelength = 1.54059

2/2

Go to Top

APPENDIX 3

Supplementary Video (V2)

Demonstration of HGPG device performance across varying humidity levels (40%–90% RH)

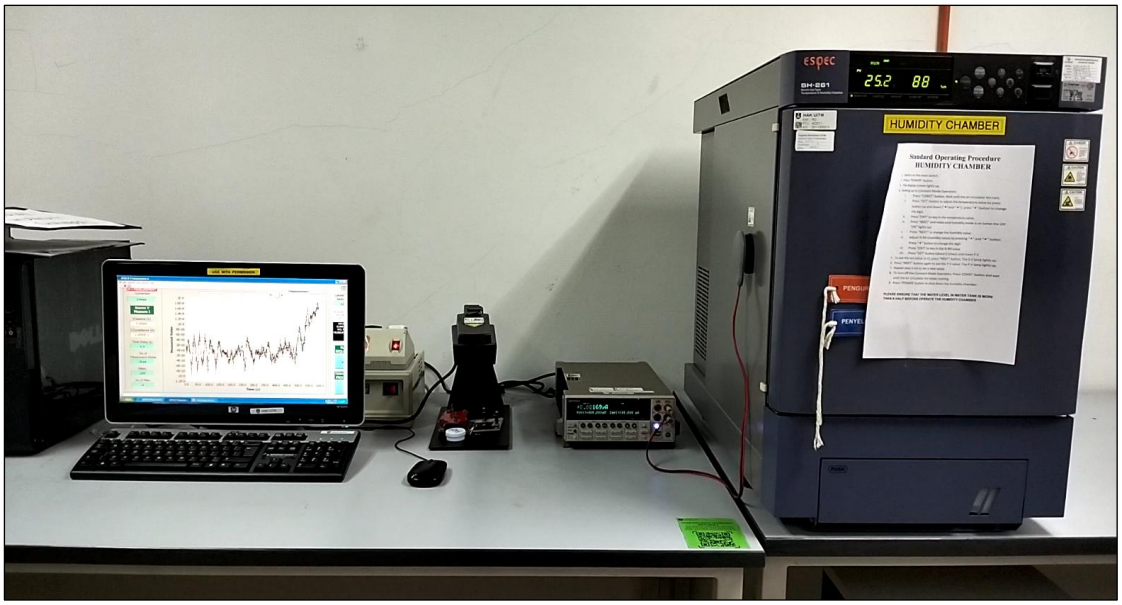

https://youtu.be/qYaSPhgaV-k

Go to Top

APPENDIX 4

Supplementary Video (V3)

Demonstration of HGPG device performance across varying humidity levels (90%–40% RH)

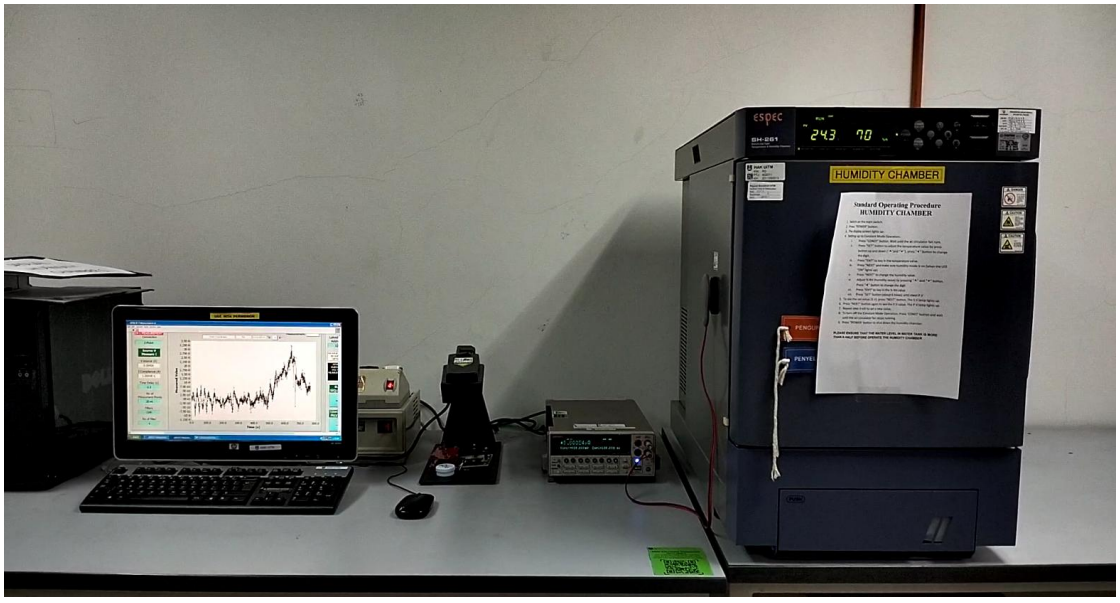

https://youtu.be/wol0MKSr0bQ

Go to Top

APPENDIX 5

Supplementary Video (V4)

Humidity Response of S-HNG-Hydrogel/RP-based HGPG to Humidity Changes Under Blowing Conditions

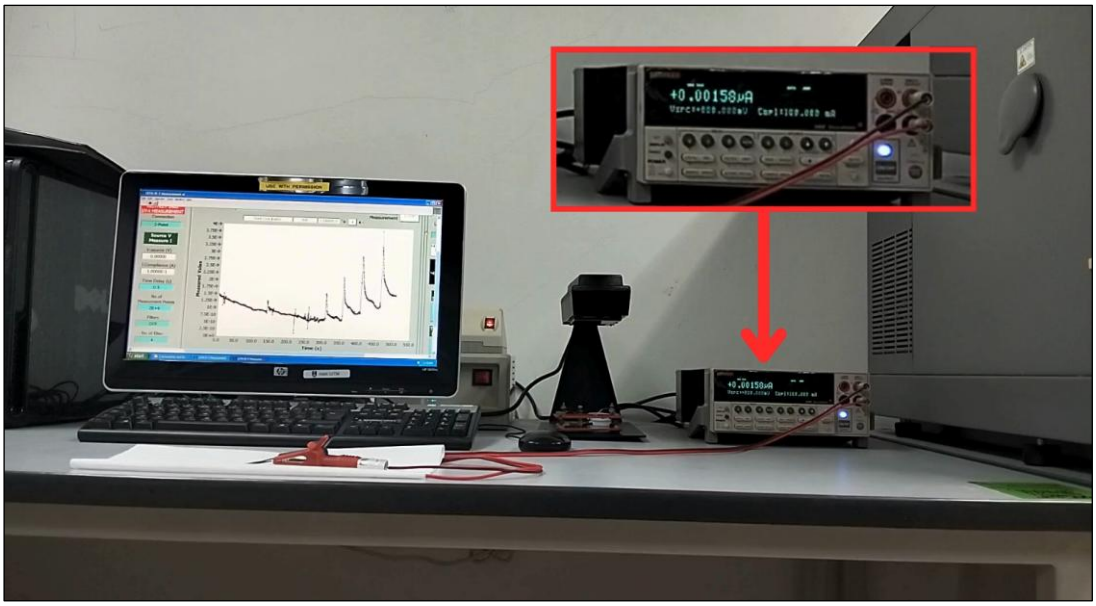

https://youtu.be/Px8mn-pDkD8

Go to Top

APPENDIX 6

Supplementary Video (V5)

Demonstration of the S-HNG-Hydrogel/RP-based PENG Under Full-Hand Tapping

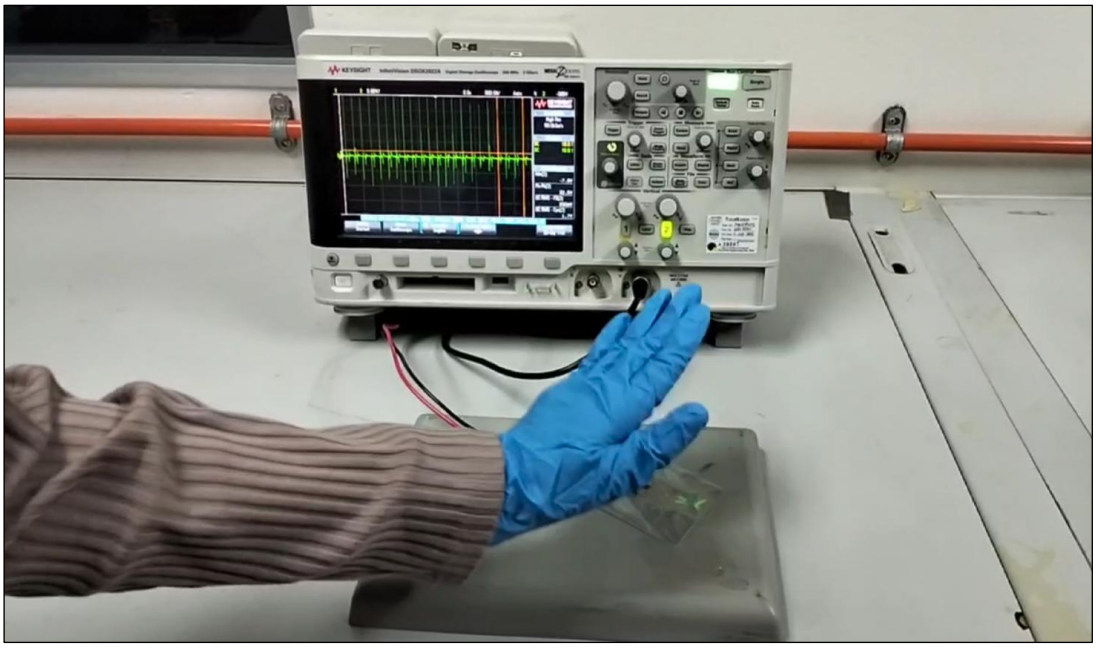

https://youtu.be/TMykPxY9mgc

Go to Top

APPENDIX 7

Supplementary Video (V6)

S-HNG-Hydrogel/RP-based PENG Under 2 N Solenoid Tapping, Successfully Powering LED

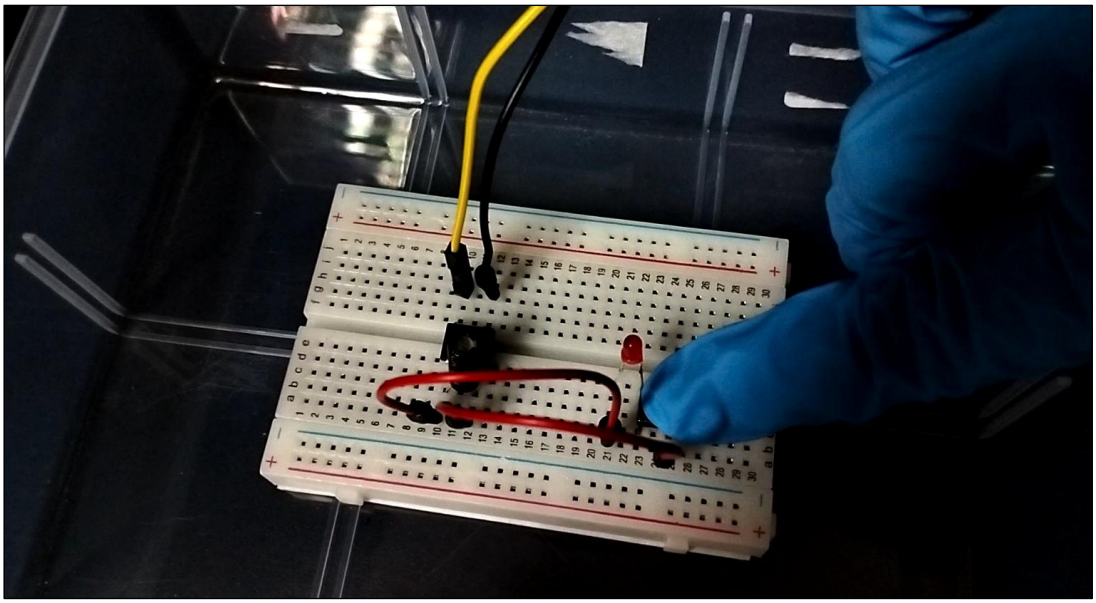

https://youtu.be/rHdOsLXywWs

Go to Top

AUTHOR'S PROFILE

Nurul Syafiqah Mohamed Mustakim, currently pursuing her Doctorate in Electrical Engineering at the Nano-Electronic Centre, Faculty of Electrical Engineering, Universiti Teknologi MARA (UiTM), Shah Alam. She holds a Master of Science (MSc) degree in Renewable Energy from the Solar Energy Research Institute at Universiti Kebangsaan Malaysia (UKM), Bangi, which she completed in 2019. Prior to that, she earned her bachelor's degree with Honors in Electronics Engineering, specializing in Microelectronics, from Universiti Tun Hussein Onn Malaysia (UTHM), Johor, in 2015. Her research interests encompass a wide range of topics, including nanogenerators specifically Piezoelectric Nanogenerators (PENG), energy harvesting devices such as Humidity Gradient Power Generation (HGPG), and advanced solar cell technologies including Dye-Sensitized Solar Cells (DSSCs) and Quantum Dot-Sensitized Solar Cells (QDSSCs). In addition, she focuses on the fabrication of nanomaterials and semiconductor devices, contributing to the advancement of innovative solutions in these emerging fields.

LIST OF PUBLICATIONS:

1. **Nurul Syafiqah Mohamed Mustakim**, Dayana Kamaruzaman, Norfarariyanti Parimon, Mohd Khairul Ahmad, Suriani Abu Bakar, Mohamad Hafiz Mamat, "Hematite/NiO/Graphene Composites: Enhancing Humidity Energy Harvesting Through Temperature Variations," Baghdad Science Journal, Vol. 23: Iss. 1,

Article 8, (2026). https://doi.org/10.21123/2411-7986.5134 (Q2 WoS indexed – Published)

2. **Nurul Syafiqah Mohamed Mustakim**, Dayana Kamaruzaman, A Shamsul Rahimi Bin A Subki, Mohd Hanapiah Abdullah, Mohd Firdaus Malek, Norfarariyanti Parimon, Mohd Khairul Ahmad, Suriani Abu Bakar, Nagamalai Vasimalai, Mohamad Hafiz Mamat, "Green Energy Solutions: Humidity-Driven Power Generation Using NiO/G Composites on Recycled Paper," AIP Conf. Proc. 9 October 2025; 3322 (1): 040006.
   https://doi.org/10.1063/5.0290075 (WoS & Scopus indexed – published)
3. **Nurul Syafiqah Mohamed Mustakim**, Mohamad Hafiz Mamat, Dayana Kamaruzaman, Mohd Hanapiah Abdullah, Mohd Firdaus Malek, Norfarariyanti Parimon, Mohd Khairul Ahmad, Nagamalai Vasimalai, Suriani Abu Bakar, (2025). "Sustainable Energy Harvesting: From Waste to Energy using NiO Nanoparticles with Recycled Paper," Journal of Advanced Research in Micro and Nano Engineering, 40(1), 130–140.
   https://doi.org/10.37934/armne.40.1.130140 (Q2 Scopus indexed – published)
4. **Nurul Syafiqah Mohamed Mustakim**, Wan Muhammad Dzhahirul Wan Muhamad Zamri, Mohd Hanapiah Abdullah, Mohd Firdaus Malek, Norfarariyanti Parimon, Shazleen Ahmad Ramli, Mohd Khairul Ahmad, Suriani Abu Bakar, Nagamalai Vasimalai, Mohamad Hafiz Mamat, "Actinomorphic-structured Nickel Oxide/Graphene Composites Treated with Stearic Acid on Cellulose-Based Substrate for Humidity-to-Energy Harvesting Applications," Materials Today Sustainability, (2026).
   https://doi.org/10.1016/j.mtsust.2026.101336 (Q1 WoS; Q1 Scopus indexed – Published) (IF: 7.9)
5. **N. S. Mohamed Mustakim**, D. Kamaruzaman, M. Hanapiah, M. F. Malek, N. Parimon, M. K. Ahmad, S. Abu Bakar, N. Vasimalai, S. Ramakrishnai, and M. H. Mamat, "Review of recent advances in piezoelectric material for nanogenerator application: preparation methods, material selection, performance, applications, and future outlook," J Mater Sci 59, 19380–19423 (2024).
   https://link.springer.com/article/10.1007/s10853-024-10293-4 (Q2 WoS; Q1 Scopus indexed – published) (IF: 3.5)

6. **N. S. Mohamed Mustakim**, K. Dayana, A. S. R. Bin A Subki, A. Mohd Hanapiah, M. Mohd Firdaus, P. Norfarariyanti, A. Mohd Khairul, B. Suriani Abu, V. Nagamalai, and M. H. Mamat, "Optimizing Hydrophilicity in NiO/Graphene Composites Via Stearic Acid Treatment for Humidity-to-Energy Applications," International Journal of Integrated Engineering, vol. 16, no. 7, pp. 266-279, (2024). https://publisher.uthm.edu.my/ojs/index.php/ijie/article/view/19095 (Q4 WoS; Q3 Scopus indexed - published) (IF:0.4)
7. **N. S. Mohamed Mustakim**, D. Kamaruzaman, A. S. R. A Subki, M. H. Abdullah, M. F. Malek, N. Parimon, M. K. Ahmad, S. Abu Bakar, N. Vasimalai, and M. H. Mamat, (2025). "Fabrication of Nanosheet-Assembled Flower-like NiO for Energy Harvesting from Humidity," Journal of Advanced Research in Micro and Nano Engineering, 38(1), 37–48. https://doi.org/10.37934/armne.38.1.3748 (Q2 Scopus indexed – published)
8. Kamaruzaman, D., **Mohamed Mustakim, N. S.**, A Subki, A. S. R., Abdullah, M. H., Parimon, N., Yaakob, M. K., Mamat, M. H. (2025). "Investigating the ZnO Effects on the Performance of ZnO/Waste Polystyrene Nanocomposite Film Based Triboelectric Nanogenerator," Journal of Advanced Research in Micro and Nano Engineering, 37(1), 50–61. https://doi.org/10.37934/armne.37.1.5061 (Q2 Scopus indexed – published)
9. D. Zamri, N. H. Nik Ali, **N. S. M. Mustakim**, N. K. Mohd, N. Azis and M. H. Mamat, "Advanced Transformer Insulating Fluids: Morphological and Dielectric Performance of Hybrid Hematite-Zinc Oxide Nanofluids," 2025 IEEE 5th International Conference in Power Engineering Applications (ICPEA), Bandar Baru Bangi, Malaysia, 2025, pp. 287-291, doi: 10.1109/ICPEA65539.2025.11198553. (WoS & Scopus indexed – published)
10. Kamal Ariffin, N. I., Kamaruzaman, D., **Mohamed Mustakim, N. S.**, Parimon, N., Malek, M. F., Yaakob, M. K., Mamat, M. H. (2025). Effect of Ni Doping on the Structural Characteristics of ZnO for Nanocomposite ZnO Film-Based Nanogenerator Application. Journal of Advanced Research in Micro and Nano Engineering, 37(1), 112–127. https://doi.org/10.37934/armne.37.1.112127 (Q2 Scopus indexed – published)
11. Dayana Kamaruzaman, Nurul Syafiqah Mustakim, A. Shamsul Rahimi A. Subki, Norfarariyanti Parimon, Muhamad Kamil Yaakob, Nagamalai

Vasimalai, Zakiah Ahmed, Sabu Thomas, Mohamad Hafiz Mamat; A triboelectric nanogenerator utilizing recycled polystyrene-ZnO nanocomposite film with high humidity resistance. AIP Conf. Proc. 9 October 2025; 3322 (1): 040009. https://doi.org/10.1063/5.0290080 (WoS & Scopus indexed – published)

12. D. Kamaruzaman, **N. S. Mohamed Mustakim**, A. S. R. A Subki, N. Parimon, M. K. Yaakob, M. F. Malek, N. Vasimalai, M. H. Abdullah, S. Abu Bakar, M. K. Ahmad, S. Thomas, and M. H. Mamat, "Polystyrene Waste-ZnO nanocomposite film for energy harvesting via hydrophobic triboelectric nanogenerator: Transforming waste into energy," Materials Today Sustainability, vol. 26, p. 100726, (2024), https://doi.org/10.1016/j.mtsust.2024.100726 (Q1 WoS; Q1 Scopus indexed – published) (IF: 7.1)
13. D. Kamaruzaman, M. H. Mamat, A. A. Aziz, A. S. R. A Subki, N. I. K. Ariffin, **N. S. M. Mustakim**, N. Parimon, N. Vasimalai, M. H. Abdullah, N. D. M. Sin, M. K. Ahmad, S. A. Bakar, and S. P. Krishnan. "Triboelectric Nanogenerator Based on Tin Doped Zinc Oxide and Polyvinyl Alcohol Composite Thin Film for Energy Harvesting Applications." Journal of Advanced Research in Applied Mechanics,126(1)(2024):165–177. https://doi.org/10.37934/aram.126.1.165177 (Q4 Scopus index - published)
14. K. Dayana, M. Mohamad Hafiz, A. S. R. A. Subki, A. Nurul Izzati Kamal, Z. Megat Danial Aizat Megat, M. **Nurul Syafiqah Mohamed**, P. Norfarariyanti, Y. Muhammad Kamil, M. Mohd Firdaus, V. Nagamalai, A. Mohd Hanapiah, S. Nor Diyana Md, B. Suriani Abu, and A. Mohd Khairul, "Nanosheet Zinc Oxide Synthesized by Solution-Immersion Method for Triboelectric Nanogenerator," Journal of Advanced Research in Applied Sciences and Engineering Technology, vol. 34, no. 2, pp. 88-98, (2023). https://doi.org/10.37934/araset.34.2.8898 (Q2 Scopus indexed – published)

LIST OF PRESENTATIONS:

1. Collaborative Community Research, Education, and Technology Exchange Symposium 2025 (Co-CREATES 2025), GReeNiCell Hybrid: Converting Ambient Moisture and Mechanical Motion into Energy Using Waste-Based

Hydrogel Material, 18 – 19 November 2025 **(First place winner for Best Paper Award and First place winner for Best Presenter Award)**

2. International Conference on Discoveries in Applied Science and Advanced Technology (DASAT) 2025, "Hematite/NiO/Graphene Composites: Enhancing Humidity Energy Harvesting Through Temperature Variations," Resort World Awana, Genting Highland, 6 – 7 February 2025 **(Best Poster Award)**
3. 6th Malaysia-Japan International Conference on Nanoscience, Nanotechnology, and Nanoengineering 2025 (MJIC 2025), "Sustainable Energy Strategies: Actinomorphic Nickel Oxide/Graphene Composite on Hydrogel-Based Recycled Paper for Renewable Energy Generation," DoubleTree by Hilton Hotel, Melaka, 21 – 23 February 2025 **(Best Poster Award)**
4. 3rd International Conference on Advanced Science and Engineering (ICASE) 2024, "Sustainable Energy Harvesting: From Waste to Energy Using NiO Nanoparticles with Recycled Paper," Resorts World Langkawi, 16 - 17 November 2024 **(Best Paper Award)**
5. Nanotechnology Malaysia Annual Symposium (Nanosym) 2024 by MOSTI, "Advanced H2E GreenCell: Innovative Hydrogel Device for Sustainable Electricity Generation from Humidity and Waste," Bangi Resort Hotel, Bangi, Selangor, 10 - 11 October 2024 **(Jury Award)**
6. Symposium of Engineering, Technology & Industrial Applications (SETIA) 2024, " Green Energy Solutions: Humidity-Driven Power Generation Using NiO/G Composites onRecycled Paper", Mardhiyyah Hotel, Shah Alam, 4 – 5 September 2024 **(Gold Award)**
7. International Conference on Advances in Electrical and Electronic Engineering (ICAEEE-ICET) 2024, "Optimizing Hydrophilicity in NiO/Graphene Composites Via Stearic Acid Treatment for Humidity-to-Energy Applications," Mardhiyyah Hotel, Shah Alam, 4 – 5 September 2024 **(Best Paper Award)**
8. 4th International Conference on Technology, Engineering and Sciences (ICTES) 2024, "Fabrication of Nanosheet-Assembled Flower-like NiO for Energy Harvesting from Humidity," Avillion Hotel, Tanah Rata, Cameron Highlands, 27- 28 June 2024

LIST OF RESEARCH PITCHING, INNOVATION AND INVENTION COMPETITION/ACHIEVEMENT

MAIN:

1. **Platinum Medal** – "H2E GreenCell: Innovative Device to Generate Electricity from Humidity and Waste for Future Sustainable Energy," International Conference on Discoveries in Applied Science and Advanced Technology (DASAT 2025) Innovation Competition, Resort World Awana, Genting Highland, 6 – 7 February 2025
2. **Excellence Award –** "H2E GreenCell: Innovative Device to Generate Electricity from Humidity and Waste for Future Sustainable Energy," International Conference on Discoveries in Applied Science and Advanced Technology (DASAT 2025) Innovation Competition, Resort World Awana, Genting Highland, 6 – 7 February 2025
3. **Gold Medal –** "Dual Energy GreenCell : A Hybrid Device Integrating Humidity Harvesting and Piezoelectric Nanogenerator for Sustainable Energy Using Hematite/NiO/Graphene Composites on Hydrogel-Based Recycled Paper," 6th Malaysia-Japan International Conference on Nanoscience, Nanotechnology, and Nanoengineering 2025 (MJIC 2025) International Innovation Competition, DoubleTree by Hilton Hotel, Melaka, 21 – 23 February 2025
4. **Diamond Award** – "P2E GreenCell : Transforming Waste into Sustainable Energy through Hydrogel Innovation," Young Inventor Postgraduate in the Invention, Innovation, Design Exposition (iiDEX) 2024, UITM Puncak Alam, Selangor , 4 - 8 November 2024
5. **Gold Award** – "P2E GreenCell : Transforming Waste into Sustainable Energy through Hydrogel Innovation," Invention, Innovation, Design Exposition (iiDEX) 2024, UITM Puncak Alam, Selangor , 4 - 8 November 2024
6. **First place winner** – Industrial Awards, Research Pitch on Chemical Engineering & Sustainable Energy 2024 by Energy Institute Malaysia, " Green Energy Solutions: Humidity-Driven Power Generation Using NiO/G Composites on Recycled Paper", Mardhiyyah Hotel, Shah Alam, 4 September 2024
7. IEEE EDS Postgraduate Award 2024, "H2E GreenCell: A Sustainable NiO-Based Device for Generating Electricity from Humidity Using Recycled Paper"

MEMBER:

1. **Gold award & 1st runner-up** – Research Pitch on Chemical Engineering & Sustainable Energy 2024 by Energy Institute Malaysia (4 September 2024)
2. **Gold Award** – Invention, Innovation, Design Exposition (iiDEX) 2023, "Enhanced Electricity Generation of ZnO/Waste PS Based Nanogenerator Using Eco-modifier Treated Hydrophobic Triboelectric Layer," 12-15 December 2023
3. **Green & Sustainability Special Award** – lnnovation & lnvention Challenge in Engineering and Technology 2023 (llCET2023), "Turning Waste Into Energy: Utilization of Recycled Polystyrene Waste Material to Fabricate ZnO-based Triboelectric Nanogenerator For Energy Harvesting," 5-6 September 2023
4. **Gold award** – Invention, Innovation, Design Exposition (iiDEX) 2022, "NT22:Generating Electricity From Recycled Polystyrene Material Based Zinc Oxide Nanocomposite Triboelectric Nanogenerator," 21-25 November 2022
5. **Gold Award & Special Award** – SDG lnternational lnnovation Awards & Expo (MTE2022), "NT22:Generating Electricity From Recycled Polystyrene Material Based Zinc Oxide Nanocomposite Triboelectric Nanogenerator," 17-21 October 2022 (by lndonesia lnvention and lnnovation Promotion Association)

LIST OF ATTENDED INTERNATIONAL PROGRAMME/CONFERENCE:

1. Selected to participate in Future Energy Leader (FEL) 2023 organized by PETRONAS at PETRONAS Leadership Center, Bangi, 23-25 Jun 2023 **(appointed as team leader)**
2. Turkey 5th International Conference on Advanced Engineering Technologies 2024 "Exploring Nickel Oxide (NiO) Deposition on Recycled Paper: A Preliminary Characterization Study", 25 – 27 September 2024 **(presenter)**

LIST OF IP/COPYRIGHTS:

1. **N.S.M. Mustakim**, M.H. Mamat, M.H. Abdullah, M.F. Malek, N. Parimon, D. Kamaruzaman, and A.S.R.A. Subkie, "Fabrication of Fe3O4/NiO/Gr composites with hydrogel-based cellulose substrate for piezoelectric nanogenerator application", Malaysia Copyright CRLY2024W07072, 2024

2. **N.S.M. Mustakim**, M.H. Mamat, M.H. Abdullah, M.F. Malek, N. Parimon, D. Kamaruzaman, and A.S.R.A. Subkie, "Synthesis of NiO/Gr powder using sonicated solution immersion method", Malaysia Copyright **CRLY2024W01212**, 2024
3. **N.S.M. Mustakim**, M.H. Mamat, M.H. Abdullah, M.F. Malek, N. Parimon, D. Kamaruzaman, and A.S.R.A. Subkie, "Stearic acid treatment on Fe doped NiO/Gr for hydrophilicity properties modifications for humidity-to-electricity conversion technology", Malaysia Copyright **CRLY2024W01213**, 2024
4. **N.S.M. Mustakim**, M.H. Mamat, M.H. Abdullah, M.F. Malek, N. Parimon, D. Kamaruzaman, and A.S.R.A. Subkie, "Fabrication of Fe doped NiO/Gr-based device for energy harvesting from humidity technology", Malaysia Copyright **CRLY2024W01214**, 2024
5. **N.S.M. Mustakim**, M.H. Mamat, M.H. Abdullah, M.F. Malek, N. Parimon, D. Kamaruzaman, and A.S.R.A. Subkie, "Application of Fe doped NiO/Gr powder in energy harvesting from humidity technology", Malaysia Copyright **CRLY2024W01215**, 2024

OTHERS RESEARCH CONTRIBUTION/INVOLVEMENT:

1. International Congress of Engineering & Technology (ICET) 2024 (Chairperson)
2. STEM Program, Karnival Kimia Malaysia Zon Utara 2024, Penang Public Library, Penang, 24 August 2024 (Exhibitor)
3. Biz.Spotlight 2024, UiTM Puncak Alam, 7 November 2024 (Exhibitor)
4. Industry visit at SIRIM Kulim (AMREC) (Industrial Center of Innovation), Kedah, 23 August 2024
5. Seminar on Micro – XRF Characterization on FESEM, 8 August 2024, Faculty of Applied Science, UITM Shah Alam
6. XPS Workshop, MIMOS Berhad, 12 July 2023